



Dublin City University
Ollscoil Cathair Bhaile Átha Cliath

**NMR STUDIES OF CONDUCTION
MECHANISMS IN ELECTROLYTE
MATERIALS FOR FUEL CELLS**

by

Eoin Murray, B.Sc.

Thesis submitted for the Degree of Doctor of Philosophy

Supervisor:

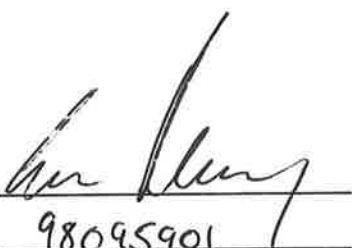
Dr. Dermot Brougham

School of Chemical Sciences

February 2007

Declaration

I hereby certify that this material, which I now submit for assessment on the programme of study leading to the award of PhD, is entirely my own work and has not been taken from the work of others save and to the extent that such work has been cited and acknowledged within the text of my work.

Signed: 
ID no.: 98095901
Date: 18/5/07

Dedication

To Mamo.

Acknowledgments

First and foremost I would like to express my gratitude towards my supervisor Dr. Dermot Brougham for his untiring support and assistance in shaping this thesis from its inauspicious start to its hopefully successful conclusion. His knowledge of so many areas of physical and analytical sciences was an inspiration and a huge advantage as we sought to derive order and meaning from this jumbled chaos.

I would like to thank my lab-mates, Sarah, Swapan, Carla, Darren, Galya, Jacek and Tracey, for their in-depth scientific discussions and constant abuse. I would also like to thank the lunch crew both under- and post-grad, Siobhan, Stephen, Aileen, Pauline, Paula, Lynda, Jimmy, Ciaran, Sarah Mc and others (you know who you are). These are the people who kept me (just about) sane. While I'm at it I would like to thank everyone who has ever been involved in DCU Olympic Handball Club and with the Irish national team. It's your fault it's taken this long!

I wish to thank our many collaborators who made this work a possibility, Dr. Isaac Abrahams in Queen Mary London, Dr. Peter Innis and Dr. Gordon Wallace in Wollongong University Australia, Dr. Sarah Brady in DCU and Prof. Sossina Haile in Caltech USA. I would also like to thank the technical staff in DCU for their unceasing support and advice.

I would especially like to thank my family, my parents and sisters (and the spud), who cultivated a home environment of learning and independent thinking which lead all of us to pursue our dreams. I wouldn't be writing this without them. Finally, ein großes vielen dank to Nicole, whose patience, love and support astounds me every day – HDL!

Abstract

NMR Studies of Conduction Mechanisms in Electrolyte Materials for Fuel Cells

Fuel cells are clean and efficient electrochemical energy conversion devices which have garnered much scientific attention in recent years as clean renewable sources of energy. However, development is currently restrained by materials limitations, particularly those associated with the electrolyte. A number of liquid electrolytes are currently in use in commercial applications but solid electrolytes are preferable as they are more robust, more efficient and less susceptible to corrosion. In this work, a number of solid conducting materials which have potential to be applied in fuel cells were studied by NMR techniques. By gaining detailed mechanistic insight into charge transport we hope to contribute to the development of these materials.

In the first part of this thesis charge conduction mechanisms is investigated in ionic conductors. In Chapter 3 ^{19}F NMR relaxometry is applied to investigate fluoride ion dynamics in the fluoride conducting superionic material, PbSnF_4 and in Chapter 4 ^1H NMR relaxometry is used to examine proton motions along hydrogen bonds in the novel superprotonic material, $\text{Cs}_6(\text{HSO}_4)_3(\text{H}_2\text{PO}_4)_4$. The results of the NMR analysis show good agreement with bulk physical properties from diffraction and conductivity techniques for both materials and a new mechanism for fluoride ion conduction in PbSnF_4 is proposed.

In the second part of this thesis, the synthesis and analysis of conducting polyaniline is presented. In Chapter 5 the synthesis of amorphous polyaniline samples with varying dopant content is presented and in Chapter 6 a number of methods for the synthesis of nano-structured doped polyaniline are examined. Both amorphous and semi-crystalline polymers are analysed by ^{19}F and ^1H NMR relaxometry and show similar dependence on the dimensionality of charge carriers through the heterogeneous regions of the material. The dimensionality of this motion is shown to be dependent on both the conductivity and the relative dopant concentration.

In an appendix, preliminary NMR relaxometry results on molecular dynamics in ionic liquids are presented.

Table of Contents

Declaration	II
Dedication	III
Acknowledgments	IV
Abstract	V
Table of Contents	VI
List of Abbreviations	X
CHAPTER 1 -INTRODUCTION	2
1.1 Thesis Overview	3
1.2 Nuclear Magnetic Resonance	4
1.2.1 Principles of Nuclear Magnetic Resonance	4
1.2.2 Relaxometry and NMR	6
1.2.3 Spectral Density Functions	9
1.3 Electrical Conductivity	20
1.3.1 Principles of Electrical Conduction	20
1.3.2 Conduction Mechanisms	21
1.3.3 Fuel Cells	28
CHAPTER 2 - EXPERIMENTAL	30
2.1 Introduction	31
2.2 FFC-NMR	31
2.2.1 Historical development	31
2.2.2 Field-cycling	32
2.2.3 Practical considerations	35
2.2.4 High field measurements	37
2.3 Conductivity	38
2.3.1 The 4-point probe method	38
2.3.2 Apparatus development	38
2.3.3 Practical considerations	41
2.4 Microscopy	42
2.4.1 Scanning Electron Microscopy	42
2.4.2 Atomic Force Microscopy	42
2.5 Differential Scanning Calorimetry	42
2.6 Raman	43
	VI

CHAPTER 3 – FLUORIDE SUPERIONIC CONDUCTORS	44
3.1 Introduction	45
3.1.1 Electrical conduction in solids	45
3.1.2 Solid Electrolytes	45
3.1.3 PbSnF ₄ structure and properties	46
3.1.3 NMR of Solid Electrolytes	48
3.2 Experimental	50
3.2.1 Synthesis	50
3.2.2 Diffraction	50
3.2.3 NMR	50
3.3 Results	52
3.3.1 Diffraction	52
3.3.2 ¹⁹ F NMR	53
3.4 Discussion	55
3.4.1 ¹⁹ F NMR	55
3.4.2 Proposed Mechanism	66
3.4.3 Assessment of the Mechanism	69
3.5 Conclusion	70
 CHAPTER 4 – SUPERPROTONIC CONDUCTORS	 72
4.1 Introduction	73
4.1.1 Fuel Cells	73
4.1.2 Solid Acids – Cs _x (HSO ₄) _y (H ₂ PO ₄) _{x-y}	73
4.1.3 Proton Conduction in Solid Acids	77
4.1.4 NMR Studies of Solid Acids	79
4.2 Experimental	80
4.2.1 Synthesis	80
4.2.2 Differential Scanning Calorimetry	81
4.2.3 ¹ H NMR	81
4.3 Results	82
4.3.1 Differential scanning calorimetry	82
4.3.2 ¹ H NMR	83
4.4 Discussion	87
4.4.1 ¹ H NMR	87
4.5 Conclusion	97
 CHAPTER 5 – AMORPHOUS CONDUCTING POLYANILINE	 99
5.1 Introduction	100
5.1.1 Inherently conducting polymers	100
5.1.2 Conductivity	100

5.1.3	Polyaniline	101
5.1.4	NMR Studies of Conducting Polymers	105
5.2	Experimental	113
5.2.1	Synthesis of Polyaniline HPF ₆	113
5.2.2	Synthesis of Polyaniline TFSA	114
5.2.3	Conductivity measurements	115
5.2.4	FFC-NMR	115
5.3	Results	117
5.3.1	¹ H NMR of Polyaniline HPF ₆	117
5.3.3	¹ H NMR of Polyaniline TFSA	120
5.3.4	¹⁹ F NMR of Polyaniline TFSA	124
5.3.5	Dopant Concentration (y-values)	125
5.3.6	Conductivity Measurements	125
5.3.7	Raman Spectroscopy	126
5.3.8	Scanning electron microscopy (SEM)	128
5.4	Discussion	129
5.4.1	Bulk Analysis (y-values and conductivity)	129
5.4.2	¹ H NMR Analysis	130
5.4.2	¹⁹ F NMR Analysis	140
5.5	Conclusions	142
CHAPTER 6 – CRYSTALLINE CONDUCTING POLYANILINE		144
6.1	Introduction	145
6.1.1	Synthesis of Nanocrystalline Polymers	145
6.1.2	Nanosynthetic Routes to Polyaniline TFSA	151
6.2	Experimental	152
6.2.1	Ultrasonicated chemical synthesis	152
6.2.2	Electrochemical Synthesis	153
6.2.3	Surfactant synthesis	155
6.2.4	Interfacial synthesis	156
6.2.5	AFM	159
6.3	Results	160
6.3.1	Review of Synthetic Methods	160
6.3.2	Analysis of ICP's produced by interfacial synthesis	164
6.4	Discussion	175
6.4.1	¹⁹ F NMR	175
6.4.2	¹ H NMR	176
6.5	Conclusions	181
Overall Conclusions and Future Work		183
Bibliography		185
Appendix 1 – Ionic Liquids		206

Appendix 2 – Publications	221
Appendix 3 – Presentations and Posters	252

List of Abbreviations

1/3-D	One/three dimensional
AFM	Atomic force microscopy
APS	Ammonium persulphate
APSR	Aperiodic saturation recovery pulse sequence
B_{acq}	Acquisition field
BP	Bipolaron
B_{pol}	Polarisation field
BPP	Bloembergen-Purcell-Pound
B_{rlx}	Relaxation field
CSA	Camphor sulphonic acid
CTAB	Cetyl trimethylammonium bromide
\bar{d}	Spectral dimensionality of motions
$D_{ }/D_{\perp}$	Intra-/inter-chain diffusion rate
DBSA	Dodecylbenzene sulphonic acid
d_f	Fractal dimensionality of spatial distribution
DQ	Double quantum
DSC	Differential scanning calorimetry
EDAX	Energy dispersive X-ray spectroscopy
ENMR	Activation energy from NMR measurements
ESR/EPR	Electron spin/paramagnetic resonance
EXAFS	Extended x-ray absorption fine structure
E_{σ}	Activation energy from conductivity measurements
FFC	Fast-field cycling
FID	Free induction decay
ICP	Inherently/intrinsically conducting polymer
ID	Internal diameter
IR	Inversion recovery pulse sequence
MAS	Magic angle spinning
MW	Molecular weight
MWNT/SWNT	Multi-/single- wall carbon nanotubes
NAFION	Sulfonated tetrafluoroethylene copolymer
NASICON	Sodium-based superionic conductor

nMP	n-methyl pyrrolidone
NMR	Nuclear magnetic resonance
NP	Non-polarised pulse sequence
PAFC	Phosphoric acid fuel cell
PCS	Photon correlation spectroscopy
PDI	Polydispersity index
PEM/PEFC	Polymer electrolyte membranes/polymer electrolyte fuel cells
PP	Pre-polarised pulse sequence
PSS	Poly(sulphonated styrene)
PTFE	Teflon
PWRA	Population weighted rate average
Q-1D	Quasi-one-dimensional
R_1	Spin-lattice relaxation rate
RD	Recycle delay
RF	Radio frequency
$r_{FF}/r_{HH}/r_{HP}/r_{HCs}$	Internuclear (jump) distances
RTIL	Room temperature ionic liquid
S1P	Single pulse sequence
SDS	Sodium dodecyl sulphate
SEM	Scanning electron microscopy
SOFC	Solid oxide fuel cell
T_1	Spin-lattice relaxation time
T_2	Spin-spin relaxation time
T_c	Phase transition temperature
TEM	Transmission electron microscopy
TFSA	Trifluoromethane sulphonic acid
VFT	Vogel-Fulcher-Tamman
XRD	X-ray diffraction
σ_{DC}	Conductivity (dc)
σ_{NMR}	Conductivity from NMR measurements

Chapter 1 -Introduction

1.1 Thesis Overview

The first chapter of this thesis is an introduction to the field of magnetic resonance and charge transport in solid materials. In the first section of the chapter the principles underpinning NMR techniques are described and the interpretation of relaxation data to yield information on molecular dynamics is examined. As the thesis focuses on charge transport in solids the mechanisms of transport in a number of classes of conducting materials are then summarised.

In Chapter 2 the main experimental techniques employed throughout the thesis are described. These include nuclear magnetic resonance relaxometry, conductivity measurements, and microscopy. The construction of a home built four-point probe for solid conductivity measurements is also described. Experimental details specific to individual chapters are described as they arise, through the thesis.

In Chapter 3 a study of ion dynamics in the fluoride conducting superionic material, PbSnF_4 using NMR relaxometry is described. Two dynamic processes, on different timescales, were observed. These motions could be assigned to in-plane diffusive motions that were directly related to charge transfer and out-of plane motions which, while facilitating charge transfer were non-translational. On the basis of this analysis a mechanism for fluoride ion conduction is proposed which is consistent with both the diffraction analysis and conductivity measurements.

In Chapter 4 a study of the novel superprotonic material, $\text{Cs}_6(\text{HSO}_4)_3(\text{H}_2\text{PO}_4)_4$ by ^1H NMR relaxometry is presented. A single dynamic process was observed by NMR, due to correlated proton motions along hydrogen bonds through a highly ordered three-dimensional network. The NMR analysis yielded diffusion coefficients and conductivities consistent both with bulk conductivity measurements and diffraction analysis.

The synthesis and analysis of amorphous conducting polyaniline is presented in Chapter 5. Polyaniline with varying dopant content was synthesised and analysed by a number of techniques including both ^1H and ^{19}F NMR relaxometry and conductivity.

The relaxation data showed a dependence on both the diffusion and dimensionality of the polaronic charge carriers which could be related to both the conductivity and the relative dopant content.

In Chapter 6 a number of methods for the synthesis of nano-structured doped polyaniline were examined. It was shown that by using interfacial synthesis the degree of crystallinity could be controlled. A number of samples with varying crystalline content were analysed using a range of characterisation techniques. The NMR relaxation showed little dependence on bulk crystallinity but a similar dependence on dopant concentration to that observed for amorphous polyaniline.

Some preliminary results on dynamics in ionic liquids studied by NMR methods are included as an appendix. The NMR data could be used to calculate thermally activated changes in viscosity similar to published viscosity data obtained from traditional bulk measurements on related compounds.

1.2 Nuclear Magnetic Resonance

1.2.1 Principles of Nuclear Magnetic Resonance

The existence of nuclear spin was originally postulated by Pauli in 1924 [1] and the first NMR experiments were developed by Bloch and Purcell soon after in the early 1940's. [2, 3] The spin angular momentum is the sum of all individual spins (n) of nucleons, so nuclei with both even mass and charge numbers (e.g. ^{12}C , ^{16}O etc.) have zero spin, nuclei with an odd mass numbers have half-integral spins (eg ^1H , ^{15}N) and nuclei with even mass number but odd charge numbers have integral spins (e.g. ^2H , ^{14}N). ^1H nuclei, which possess non-zero spin, generate electromagnetic fields due to their inherent charge and so possess a characteristic dipolar magnetic moment (μ). The moment is related to the spin angular momentum (I) in classical terms by the equation

$$\mu = \gamma I \quad [1.1]$$

where γ , a constant is called gyro-magnetic ratio, is related to the charge and mass number of the nuclei, which determines the resonant frequency of the nucleus.

When these (non-zero) spins are placed in an external magnetic field (of magnetic flux density, B_0) a Zeeman interaction occurs, and the spins orient in $2I+1$ directions. In the case of ^1H ($I = 1/2$) and the individual spins align against or along the B_0 field

with net magnetisation, M , of $1/2$. The equilibrium distribution of the spins between the Zeeman levels is given by Boltzmann statistics.

$$\frac{n_\alpha}{n_\beta} = e^{h\gamma B_0 / 2\pi kT} = e^{\Delta E / kT} \quad [1.2]$$

where n_α and n_β are the populations of the Zeeman levels α and β respectively, h is Planck's constant, k is the Boltzmann constant, T is temperature in Kelvin and ΔE the difference in energy between the states. As the energy difference is very low, $\approx 10^{-25}$ J, at thermal equilibrium the lower level is only slightly more populated, n_α/n_β is c 1.000007 for attainable fields at room temperature. In a system with many non-synchronised spins, the component of the average spin vector in the xy-plane is zero. So given the small population difference there is a weak net magnetisation vector M_0 , the sample magnetisation, along the field direction. As this magnetisation is small, NMR is an intrinsically insensitive technique and there is ongoing interest in attaining higher external fields.

In the vector model of NMR these spins precess at the Larmor frequency (ω_0), according to the equation

$$\omega_0 = \gamma B_0 \quad [1.3]$$

so that the average spin vector in the xy-plane is zero, while along B_0 there is a net vector M , the sample magnetisation. The manipulation of spin distribution by a radio-frequency pulse results in rotation of the magnetisation towards xy-plane. The RF pulse synchronises the spins, producing a condition called phase coherence where the resulting net magnetisation, in the α and β states, now rotates around the z-axis at the Larmor frequency. The angle that the net magnetisation vector rotates by is commonly called the 'flip' or 'tip' angle.

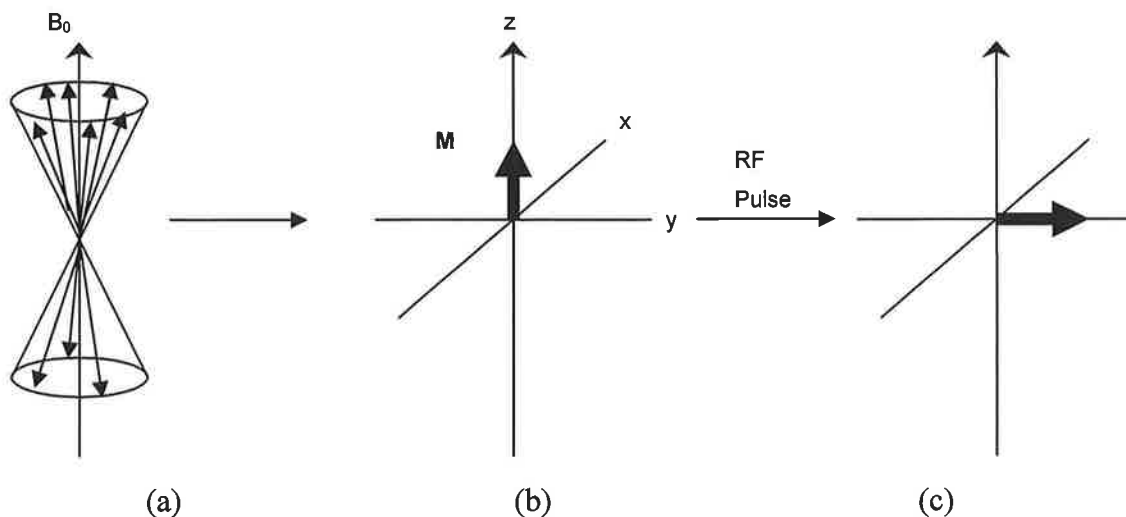


Figure 1.1 Schematic of the progress of a simple NMR experiment showing (a) alignment of spins along B_0 , (b) the resultant net magnetisation vector, M , and (c) perturbation of the spins by an 90° RF pulse.

Following perturbation by an RF pulse, the magnetisation starts to return towards its equilibrium state through the process of relaxation. During this time, the precessing magnetisation in the xy -plane induces a time dependent current in the RF coil producing the measured signal, the free induction decay (FID).

1.2.2 Relaxometry and NMR

The perturbed state of magnetisation induced by the RF pulse is thermodynamically unstable and thus, magnetisation “relaxes” back to the thermal equilibrium with characteristic time constants. The process by which the excess energy is dissipated is called relaxation. There are two different processes by which the excited nucleus may return from the high energy state to the ground state; spin-spin or transverse relaxation and spin-lattice or longitudinal relaxation.

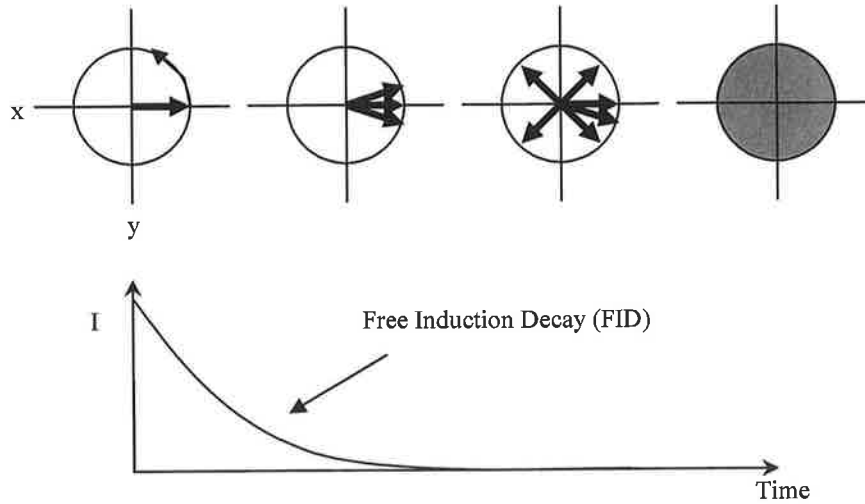


Figure 1.2 The spin-spin relaxation process: coherently precessing spins in the xy plane, with subsequent energy exchange and loss of phase coherence. The characteristic time of decay is T_2 .

The characteristic time with which the phase coherence of the transverse magnetisation, M_{xy} , decays to zero is defined by the spin-spin or transverse relaxation time T_2 , or transverse relaxation rate ($R_2 = 1/T_2$), which is a random process. It is exponential with time, τ , and is described by

$$M_{xy} = M_0 e^{-\tau/T_2} \quad [1.4]$$

where M_0 is the equilibrium magnetisation. In the T_2 process, spin-spin relaxation occurs when spins in the high and low energy states exchange energy, thus the energy of the spin system is unchanged. The phases are lost, hence the driving force for the loss of the transverse magnetisation is entropic. In real systems, there are minor differences in chemical environment which can lead to a distribution of resonance frequencies around the ideal frequency. The dephasing of the magnetisation in the xy plane including effects due to magnet inhomogeneity is known as T_2^* and can be related to a sample's intrinsic T_2 by the equation:

$$\frac{1}{T_2^*} = \frac{1}{T_2} + \gamma\Delta B_0 \quad [1.5]$$

where $\gamma\Delta B_0$ is the variation in Larmor frequency. If the homogeneity is improved T_2^* will increase until dephasing is due to T_2 . However, if dephasing is dominated by magnet inhomogeneity very little information on sample relaxation is obtained.

Spin-lattice relaxation, T_1 , is the return of spin system from a perturbed state to the equilibrium Boltzmann distribution of spins among Zeeman levels. In order to

facilitate the dissipation of this disturbance the 'lattice' (surrounding environment) acts as a heat sink absorbing the energy from the hot spin system. Relaxation occurs through interactions of the magnetic moments of nuclei with random fluctuating magnetic fields caused by the motion of the nuclei in a molecule. The relaxation process, T_1 , by which the excess energy is dissipated into the lattice is also a random process. Thus the magnetisation recovery is exponential with time, τ , and is described by;

$$M_z = M_0(1 - e^{-\tau/T_1}) \quad [1.6]$$

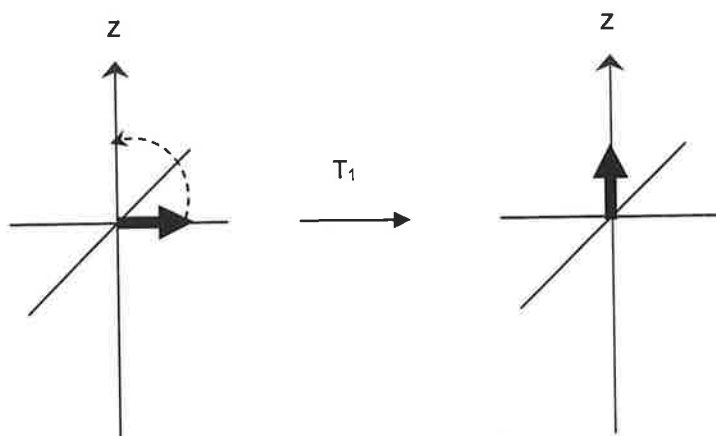


Figure 1.3 The time taken for the full recovery of magnetisation along the z-axis following RF pulse is the characteristic timescale of T_1 .

After the time $\tau = T_1$ where T_1 is the spin lattice relaxation time, the difference in spin population has grown to 63 % of its value at thermal equilibrium and at $\tau = 5T_1$ the difference is 98 % of its thermal equilibrium value. A number of mechanisms can contribute to spin-lattice relaxation. Dipolar relaxation results from fluctuating local fields caused by modulation of the dipole-dipole interactions between neighbouring nuclei due to motion of the spins. The efficiency of this mechanism is dependent on both the gyromagnetic ratio of the nuclei and the proximity of the dipoles. Spin-rotation relaxation, which arises in the gas phase only, is due to molecules being rotating charge systems and the tumbling of the molecule modulates local magnetic fields. Chemical shift anisotropy is due to the nature of the magnetic shielding of nuclei by the electrons that surround the nucleus which gives rise to fluctuating secondary fields. This is averaged by free rotation in liquids but can be significant in solids.

Where $J(\omega)$ is the spectral density function which relates to the spectrum of fluctuations and G is the correlation function of H' and is described by:

$$G_{\alpha\beta} = \langle \alpha | H'(t-\tau) | \beta \rangle \langle \beta | H'(t) | \alpha \rangle \quad [1.13]$$

In a simple system as described above there are two states accessible to the nuclear spin, α and β , and these two, along with the Zeeman interaction with the time-dependent magnetic field, B_n , are the solution to $H'(t)$.

$$H'(t) = -\hbar\gamma B_n(t) I_n \quad [1.14]$$

where $B(t)$ is the time dependent magnetic field. The equation which can also be written as $H'(t) = -\hbar\gamma B I f(t)$ where $f(t)$ contains the time dependent fluctuations. Substituting $H'(t)$ into equation 1.13 yields;

$$G_{\alpha\beta} = \hbar^2 \gamma^2 B_x^2 \langle \alpha | I_x | \beta \rangle \langle \beta | I_x | \alpha \rangle \overline{f(t-\tau) f(t)} \quad [1.16]$$

where:

$$\langle \alpha | I_x | \beta \rangle = \langle \beta | I_x | \alpha \rangle = \frac{1}{2} \quad [1.17]$$

The overlined part of equation 1.16 describes the fluctuating time dependent components and the rest of the equation can be moved outside the integral. Therefore, equation 1.12 becomes:

$$\overline{W}_{\alpha\beta} = \frac{1}{\hbar^2} \hbar^2 \gamma^2 B_x^2 \frac{1}{2} \frac{1}{2} \int_{-\infty}^{+\infty} f(t-\tau) f(t) \exp(i\omega_{\alpha\beta}\tau) d\tau = \frac{\gamma^2 B_x^2}{4} J(\omega) \quad [1.18]$$

Thus $G(\tau) = f(t-\tau)f(t)$ is now known as the auto-correlation function and describes the time-dependence of fluctuations. For random fluctuations $G(\tau)$ is exponential, and has the form;

$$G(\tau) = \exp\left[\frac{-|\tau|}{\tau_c}\right] \quad [1.19]$$

where τ_c is the rotational correlation time which is the average time taken to tumble through an angle of ~ 1 radian, or τ_c is the average time taken for the root-mean-square deflection of the molecules for ~ 1 radian. τ_c^{-1} is the rotational correlation rate and describes the number of radians through which a molecule will tumble per second. Longitudinal relaxation processes are sensitive to motions with τ_c^{-1} of tens to hundreds of MHz.

The spectral density $J(\omega)$ can be considered the power available for relaxation at the frequency ω , or as being proportional to the probability of finding a fraction of spins

in the system in random motion at a particular frequency. If the dynamic process is random $G(\tau)$ is exponential, then the spectral density, $J(\omega)$, which is the Fourier transform of the correlation function will have a Lorentzian form. Using the exponential form of $G(\tau)$, $J(\omega)$ can be calculated:

$$\begin{aligned}
 J(\omega) &= \int_{-\infty}^{+\infty} G_{\alpha\beta}(\tau) \exp(i\omega_{\alpha\beta}\tau) d\tau \\
 &= \int_{-\infty}^{+\infty} \exp\left[-\frac{|\tau|}{\tau_c}\right] (\tau) \exp(i\omega_{\alpha\beta}\tau) d\tau \quad [1.20] \\
 &= \frac{2\tau_c}{1 + \omega^2\tau_c^2}
 \end{aligned}$$

When the mechanism of spin-lattice relaxation is due to the dipolar interaction a pair of homonuclear spin $I = \frac{1}{2}$ nuclei, separated by distance, r , undergo random motions, and the dipolar interaction between them fluctuates randomly. There are four spin states (N_{-1} , N_0 and N_{+1}) N_0 is doubly degenerate and a number of relaxation pathways with associated transition probabilities arise (figure 1.5). The relaxation pathways A and B are secular for homonuclear relaxation, in that their eigenvalues are the same as the static Hamiltonian (H_0), and only contribute to the frequency of the lines in the spectrum. The pathways C and D contain spin operators that can flip a single spin and are represented by transition probabilities $W_{\pm 1}$, while pathways E and F can flip two nuclear spins and are represented by transition probabilities $W_{\pm 2}$. Pathways C, D, E and F are non-secular and are responsible for relaxation.

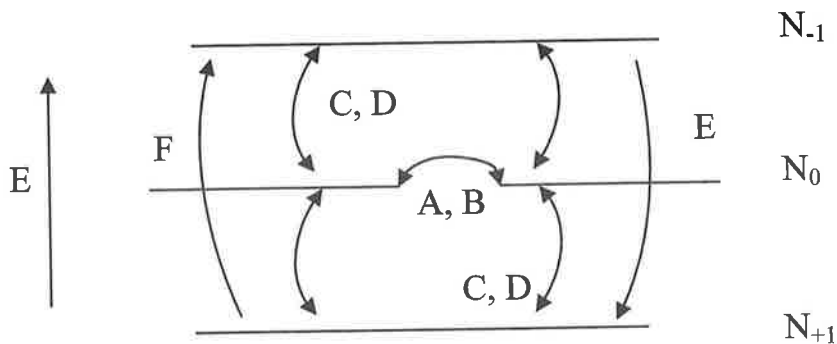


Figure 1.5 Schematic of a two spin system with three energy states, showing the relaxation pathways for zero spin flips (A, B), one spin flip (C, D) and for two spin flips (E, F).

The transition probabilities obey a Boltzmann distribution where:

$$\begin{aligned} W_{\pm 1} &= W_1 \left[1 \pm \frac{1}{2} \left(\frac{\gamma_N B_N H}{kT} \right) \right] \\ W_{\pm 2} &= W_2 \left[1 \pm \left(\frac{\gamma_N B_N H}{kT} \right) \right] \end{aligned} \quad [1.21]$$

Time dependent perturbation theory shows that W_1 and W_2 are proportional to the dipolar time dependent Hamiltonian operator at ω and 2ω respectively:

$$\begin{aligned} W_1 &= \frac{1}{\hbar^2} \left| \langle t_0 | H'_D | t_1 \rangle \right|^2 \frac{2\tau_c}{1 + \omega^2 \tau_c^2} \\ W_2 &= \frac{1}{\hbar^2} \left| \langle t_{-1} | H'_D | t_1 \rangle \right|^2 \frac{2\tau_c}{1 + 4\omega^2 \tau_c^2} \end{aligned} \quad [1.22]$$

The time dependent Hamiltonian operator for dipolar interactions, H'_D , can be described as;

$$H'_D = \gamma_N^2 B_N^2 \left(\frac{I_1 I_2}{r^3} - \frac{3(I_1 r)(I_2 r)}{r^5} \right) \quad [1.23]$$

where I_1 and I_2 are the magnetic moments of nuclei 1 and 2, respectively. The vector products from the previous equation are:

$$\begin{aligned} I_1 I_2 &= I_{1x} I_{2x} + I_{1y} I_{2y} + I_{1z} I_{2z} \\ I_1 r &= I_{1x} x + I_{1y} y + I_{1z} z \\ I_2 r &= I_{2x} x + I_{2y} y + I_{2z} z \end{aligned} \quad [1.24]$$

Following calculation and substitution of Cartesian for polar coordinates ($x = r \sin\theta \cos\phi$, $y = r \sin\theta \sin\phi$, $z = r \cos\theta$), the Hamiltonian operator for dipolar interactions may be written:

$$H_{dd} = \frac{\mu_0}{4\pi} \frac{\gamma^2 \hbar^2}{r^3} [A + B + C + D + E + F] \quad [1.25a]$$

$$\begin{aligned}
A &= -I_{1z}I_{2z}(3\cos^2\theta - 1) \\
B &= \frac{1}{4}[I_1^+I_2^- + I_1^-I_2^+](3\cos^2\theta - 1) \\
C &= -\frac{3}{2}[I_{1z}I_2^+ + I_1^+I_{2z}]\sin\theta\cos\theta\exp(-i\phi) \\
D &= -\frac{3}{2}[I_{1z}I_2^- + I_1^-I_{2z}]\sin\theta\cos\theta\exp(+i\phi) \\
E &= -\frac{3}{4}I_1^+I_2^+\sin^2\theta\exp(-2i\phi) \\
F &= -\frac{3}{4}I_1^-I_2^-\sin^2\theta\exp(2i\phi)
\end{aligned}
\tag{1.25b}$$

As $1/T_1 = (W_1+W_2)$, following calculation the T_1 equation for random fluctuations due to dipolar interactions is:

$$\frac{1}{T_1} = \frac{3}{20} \frac{\gamma^4 B_n^4}{\hbar^2 r^6} \left[\frac{2\tau_c}{1 + \omega^2\tau_c^2} + \frac{8\tau_c}{1 + 4\omega^2\tau_c^2} \right]
\tag{1.27}$$

or more generally for non-random motions:

$$\frac{1}{T_1} = \beta[c_1J(\omega) + c_2J(2\omega)]
\tag{1.28}$$

where c is a constant and β is the dipolar coupling constant. Calculating T_1 involves the analysis of the fluctuating local fields to determine the power available at the relevant nuclear spin transition frequencies. For a random process the spectrum of these frequencies, $J(\omega)$, plotted as a function of frequency shows that the power available is roughly constant up to a frequency $\omega \approx \tau_c^{-1}$, after which it falls off, eventually as $(\omega^2\tau_c)^{-1}$ (figure 1.6). The integral of $J(\omega)$ over all frequencies is a constant, independent of τ_c . The frequency of the dispersion in $J(\omega)$ is determined by the rate of the dynamic process driving relaxation. The motional rate, τ_c^{-1} , can be extracted directly from the half-width of the spectral density function. For smaller molecules or higher temperatures the correlation time is shorter (faster tumbling) and the spectral density extends to higher frequencies.

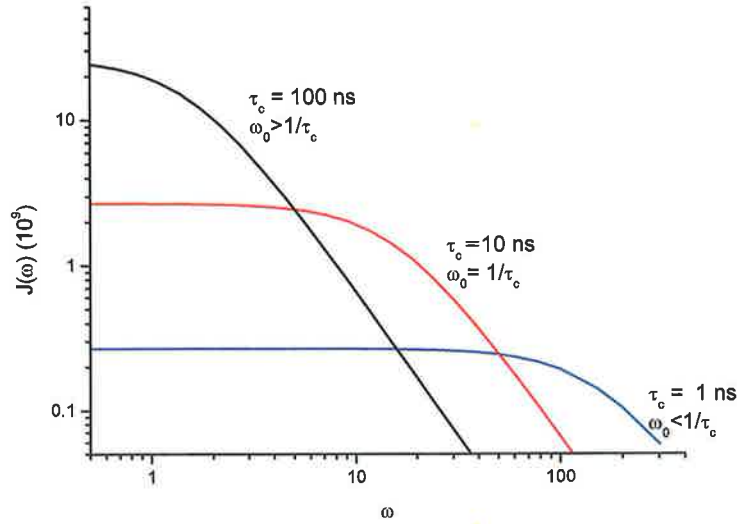


Figure 1.6 Simulation of BPP spectral density function curves showing $J(\omega)$ as a function of frequency for three values of rotational correlation time (τ_c).

1.2.3.1 Bloembergen-Purcell-Pound

A common starting point in the analysis of relaxation data was introduced by Bloembergen, Purcell and Pound (BPP). [4] Relaxation is due to isotropic rotational diffusion of molecules modulating the intra-molecular interaction of two-spin $\frac{1}{2}$ nuclei with fixed inter-nuclear distances. The correlation function is monoexponential, and the spectral density is a Lorentzian.

$$J(\omega) = \frac{2\tau_c}{1 + \omega_0^2 \tau_c^2} \quad [1.29]$$

Therefore, the full BPP spin-lattice relaxation rate equation for dipolar relaxation is:

$$\frac{1}{T_1} = \left(\frac{\mu_0}{4\pi} \right) \frac{3}{10r^6} \gamma^4 \hbar^2 \left[\frac{\tau_c}{1 + \omega_0^2 \tau_c^2} + \frac{4\tau_c}{1 + 4\omega_0^2 \tau_c^2} \right] \quad [1.30]$$

where μ_0 is the magnetic field constant, γ is the gyromagnetic constant, \hbar is planck constant divided by 2π , r the internuclear separation. It is assumed that the dynamic process is in the weak collision limit where $\tau_c \ll T_1$.

The correlation time can be assumed to have an Arrhenius relationship with temperature;

$$\tau_c = \tau_\infty \exp\left(\frac{E_a}{kT}\right) \quad [1.31]$$

where τ_∞ is a weakly temperature dependent or temperature independent parameter. The parameter E_a is the apparent or effective activation energy [5] which can be related to a physically relevant activation energy. Fixed field relaxation experiments measure relaxation times at multiple temperatures at a single usually high field. The activation energy for the process may then be calculated from the slope of the T_1 against inverse temperature curve.

For more complex systems the BPP approach is not sufficient to describe the spectral density. The motions may not be random or independent and the autocorrelation function may not be exponential or there may be multiple motions. There are a number of more complex spectral density functions available for describing such situations. [5] Many of these are derived from functions used to interpret dielectric relaxation measurements, as the two techniques are similar.

Dielectric spectroscopy (sometimes called impedance spectroscopy) measures the dielectric properties of a medium as a function of frequency. It is based on the interaction of an external field with the electric dipole moment of the sample. Dielectric relaxation experiments involve the perturbation of electric dipoles by an external electric field and the recovery to equilibrium on removal of the field is measured. Relaxation is as a result of the movement of dipoles and electric charges due to an applied alternating field, in the frequency range 10^2 - 10^{10} Hz.

1.2.3.2 Havriliak-Negami

In the late 1970's Dissado and Hill [6] formulated a general spectral density function for dielectric relaxation which assumed the presence of a distribution of correlated motions. This was a complex adaptation of a spectral density function developed by Havriliak and Negami [7] to describe electrical and mechanical properties. Adapting the Havriliak-Negami model for NMR spectral densities gives:

$$J_{HN}(\omega) = \frac{2}{\omega} \sin \left[\varepsilon \arctan \left(\frac{(\omega\tau)^\delta \sin\left(\frac{\delta\pi}{2}\right)}{1 + (\omega\tau)^\delta \cos\left(\frac{\omega\tau}{2}\right)} \right) \right] \left[1 + 2(\omega\tau)^\delta \cos\left(\frac{\delta\pi}{2}\right) + (\omega\tau)^{2\delta} \right]^{-\varepsilon/2} \quad [1.32]$$

where ω is the angular resonance frequency and τ is the correlation time. The correlation of motions is represented by $0 < \delta < 1$ where $\delta = 1$ indicates uncorrelated

motions and $\delta = 0$ highly correlated motions. The distribution of motional barriers is represented by $0 < (1-\delta\varepsilon) < 1$, where $\delta\varepsilon = 1$ indicates a unique barrier height and $\delta\varepsilon = 0$ is a maximal number of allowed barrier heights.

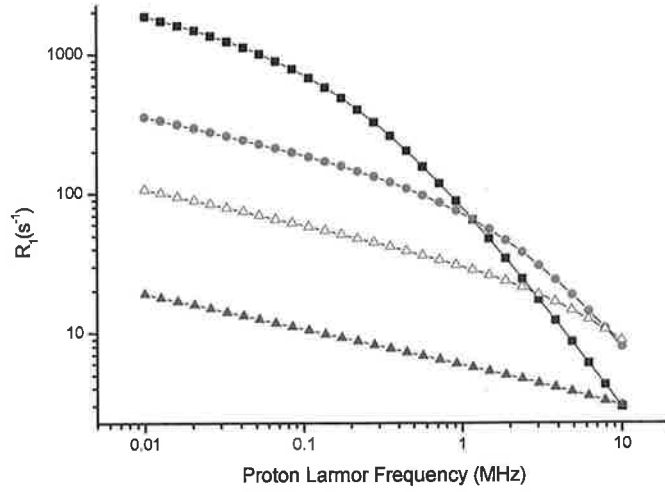


Figure 1.7 Simulation of a relaxation profile showing the dependence on τ_c of the Havriliak-Negami spectral density function with $\tau_c = 5 \times 10^{-7}$ s (■), $\tau_c = 5 \times 10^{-8}$ s (●), $\tau_c = 1 \times 10^{-9}$ s (▲) and $\tau_c = 2.5 \times 10^{-9}$ s (△) ($\varepsilon = \delta = 0.75$).

1.2.3.3 Cole-Cole

The Cole-Cole spectral density [8] was also developed to describe dielectric relaxation which takes into account correlated motions. This model is equivalent to the Havriliak-Negami spectral density equation when $\varepsilon = 1$ and is represented by:

$$J_{CC}(\omega, \tau_c, \delta) = \frac{2}{\omega} \sin\left(\frac{\delta\pi}{2}\right) \left[\frac{(\omega\tau_c)^\delta}{1 + (\omega\tau_c)^{2\delta} + \{2 \cos(\delta\pi/2)\}(\omega\tau_c)^\delta} \right] \quad [1.33]$$

In this case δ is a measure of the degree of correlation and, as $\varepsilon = 1$, the distribution of correlation times is represented by $(1 - \delta)$. Therefore, $\delta = 1$ is indicative of uncorrelated motions and a unique barrier height, and $\delta = 0$ is indicative of high degree of correlation and maximum barrier distribution. This function has been used quite frequently in interpreting dielectric spectroscopy of complex macromolecules [9] and more recently in analysing NMR data from biological protein and colloidal suspensions. [10-12]

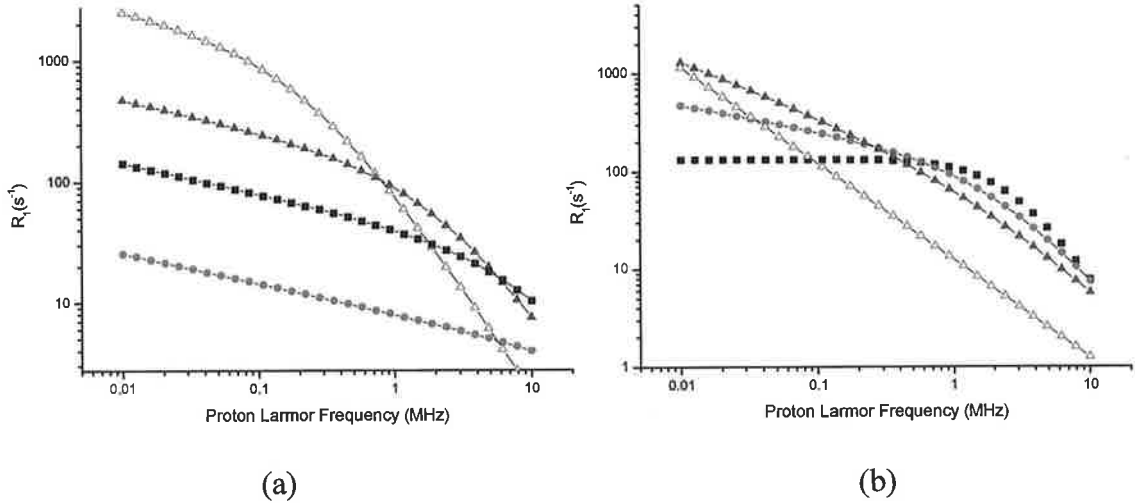


Figure 1.8 Simulations of relaxation profiles showing the dependence of the Cole-Cole function on (a) τ_c where $\tau_c = 2.5 \times 10^{-9}$ s (\blacksquare), $\tau_c = 1 \times 10^{-9}$ s (\bullet), $\tau_c = 5 \times 10^{-8}$ s (\blacktriangle) and $\tau_c = 5 \times 10^{-7}$ s (\blacktriangledown) and (b) δ where $\delta = 1$ (\blacksquare), $\delta = 0.75$ (\bullet), $\delta = 0.5$ (\blacktriangle) and $\delta = 0.1$ (\blacktriangledown) ($\tau_c = 5 \times 10^{-8}$ s).

1.2.3.4 Cole-Davidson

The Cole-Davidson function [13] was again developed to model dielectric relaxation data and takes into account the distribution of barrier heights to uncorrelated motions. The Havriliak-Negami spectral density equation can be reduced to the Cole-Davidson function when $\delta = 1$. The Cole-Davidson function is represented by:

$$J_{DC}(\omega) = \frac{2}{\omega} \left[\frac{\sin(\varepsilon \arctan(\omega\tau))}{(1 + \omega^2\tau^2)^{\varepsilon/2}} \right] \quad [1.34]$$

In this case as $\delta = 1$ there are no correlated motions and the distribution of correlation times is represented by $(1-\varepsilon)$. Therefore, $\varepsilon = 1$ is indicative of a single barrier and $\varepsilon = 0$ is indicative of the maximum allowable number of barriers. This model has found applications in the interpretation of simple systems e.g. methyl and *t*-butyl rotations in solids and rearrangements in ethane. [14, 15] Privalov *et al* [16] used a similar model that described a log-Gaussian distribution of barrier heights when interpreting his NMR relaxation data for the fluorine ion conductor, LaF_3 (equation 1.34).

$$T_1^{-1} = \beta \int_{-\infty}^{\infty} \left[\frac{\exp(z - z^2/2\delta^2)}{1 + \omega^2\tau_c^2 e^{2z}} + \frac{4\exp(z - z^2/2\delta^2)}{1 + 4\omega^2\tau_c^2 e^{2z}} \right] \quad [1.34]$$

Where $z = \ln(\tau/\tau_c)$, τ_c is the centre of the distribution and δ is the width of the barrier distribution. This model exhibits similar behaviour to the Cole-Davidson function but the log-Gaussian model introduces another parameter and hence extra degrees of

complexity to the fit. There are several similar analytical functions describing other statistical distributions of correlation time. [5]

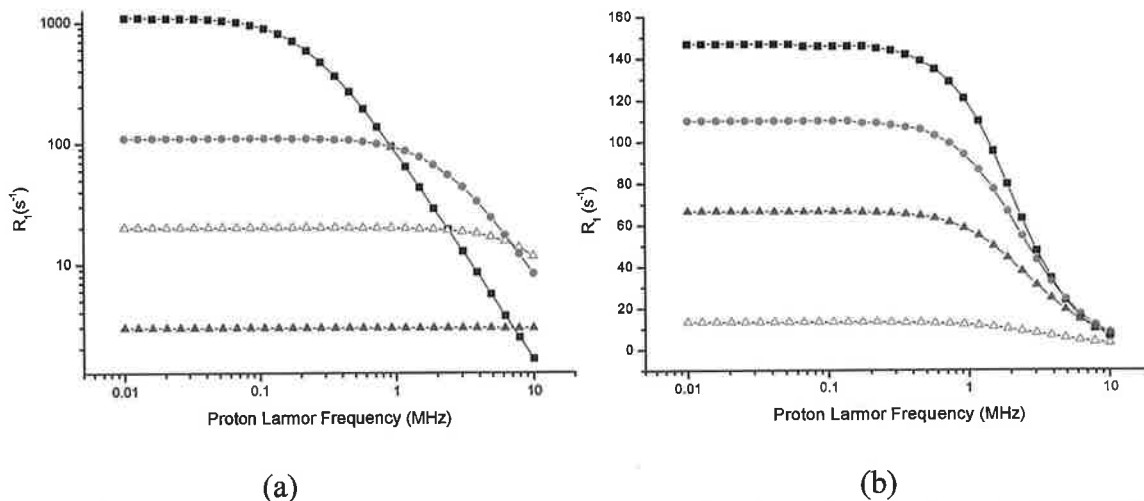


Figure 1.9 Simulations of relaxation profiles showing the dependence of the Cole-Davidson function on (a) τ_c where $\tau_c = 5 \times 10^{-7}$ s (■), $\tau_c = 5 \times 10^{-8}$ s (●), $\tau_c = 1 \times 10^{-9}$ s (▲) and $\tau_c = 2.5 \times 10^{-9}$ s (△) ($\epsilon = \delta = 0.75$) and (b) ϵ where $\epsilon = 1$ (■), $\epsilon = 0.75$ (●), $\epsilon = 0.5$ (▲) and $\epsilon = 0.1$ (△) ($\tau_c = 5 \times 10^{-8}$ s).

When $\delta = 1$ for any of the spectral density functions described above, the motions described are not correlated. This also indicates that the distribution of barriers is described by $(1-\epsilon)$. When $\epsilon = 1$, the system has a single barrier and hence a single correlation time. Thus, when $\delta = \epsilon = 1$, the Havriliak-Negami, Cole-Cole and Cole-Davidson reduce to a simple independent motion described that may be described by a BPP spectral density function.

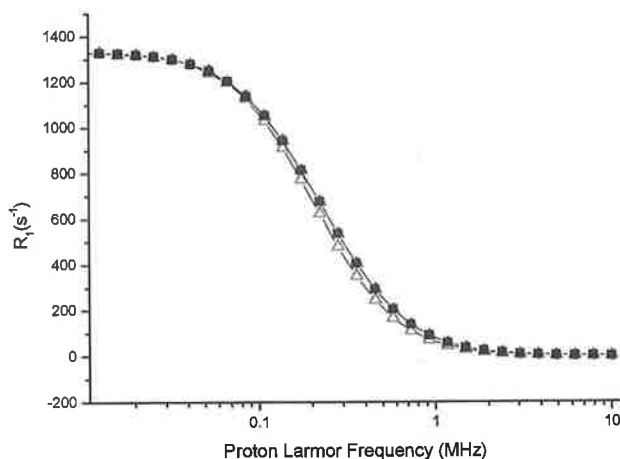


Figure 1.10 Simulation of relaxation profiles of Havriliak-Negami (●), Cole-Cole (▲), Cole-Davidson (△) and BPP (■) spectral density functions with $\delta = \epsilon = 1$.

Whenever possible the Cole-Cole and Cole-Davidson functions are used in preference to the Havriliak-Negami function which introduces another parameter and hence extra degrees of complexity to the fit. Figure 1.11 shows a ^1H relaxation profile for a solid acid which was typical of the data sets analysed by stretched Lorentzian functions in this thesis. Traditional BPP dynamics models are not applicable to this system so the data was fitted using both the Cole-Cole, Cole-Davidson and log-Gaussian functions. The Cole-Cole fit showed good agreement with the data and the resulting $\delta = 0.95$ indicates a non-correlated motion and/or a narrow distribution of correlation times. However, the data could not be fitted using a Cole-Davidson function, which demands the presence of a low-frequency plateau, indicating that a Cole-Davidson or log-Gaussian model for the distribution of correlation times is not applicable in this case. Therefore, it can be assumed that the deviation from simple random motions as described by BPP spectral density theory is due to the presence of correlated motions. Thus in this thesis the δ -value obtained from Cole-Cole fits is referred to as the degree of correlation.

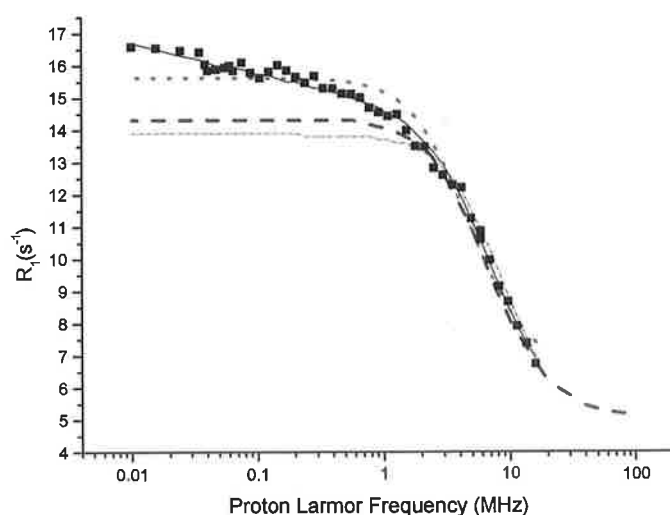


Figure 1.11 Relaxation profile of $\text{Cs}_6(\text{HSO}_4)_3(\text{H}_2\text{PO}_4)_4$ at 390 K (■ chapter 4) fit with Cole-Cole (-), Cole-Davidson (---), log-gaussian (-.-) and BPP (···) spectral density functions.

1.3 Electrical Conductivity

1.3.1 Principles of Electrical Conduction

Electrical conduction arises from the movement of electrically charged particles through a material and conductivity is a measure of the materials ability to conduct these charges. The transport of charges results in an electric current in response to an electric field. The underlying mechanism for transport depends on the material. Conductivity is defined by Ohms law which states that in a conductor the current is proportional to the applied electric field

$$\sigma = R \cdot I \quad [1.35]$$

where I is the current across a resistor (in Amps) and σ is the drop of potential (in Volts). R is a constant called resistance (in Ohms, Ω). The reciprocal of resistance is conductance. Resistance is proportional to the length, l, and inversely proportional to the cross-sectional area of the conductor, A:

$$R = \frac{\rho \cdot l}{A} \quad [1.36]$$

Where ρ is the materials resistivity (Ωm). The inverse of resistivity is the conductivity. The unit of conductance is the Siemen ($1 \text{ S} = 1 \Omega^{-1}$) and conductivity is usually expressed in S cm^{-1} .

The electrical conductivity arises due to transport and hence the bulk conductivity is related to microscopic measures of the transport processes. The diffusion coefficient, D, is defined as the carrier current (number of carriers crossing $1 \text{ cm}^2 \text{ s}^{-1}$) per unit concentration gradient. The conductivity can be related to the charge transfer diffusion co-efficient in the material by the Einstein relationship:

$$\sigma = \frac{Ne^2 D}{k_B T} \quad [1.37]$$

where N is the density of mobile charge carriers, e is the effective charge, T is the absolute temperature and k_B is the Boltzmann constant. From this the mobility of charge carriers may also be calculated. The mobility, μ , is defined as the drift velocity developed by a carrier in an electric field per unit electric field and is a measure of the relative ease with which the carrier moves in an electric field.

$$\mu = \frac{eD}{k_B T} \quad [1.38]$$

The diffusion coefficient, D , can also be related to charge carrier hop distances (r_{CC}) and the mean residence time of the charge carrier (τ) by the relationship

$$D = \frac{r_{CC}^2}{n\tau} \quad [1.39]$$

where n is the number of possible sites to which the charge carrier can hop.

1.3.2 Conduction Mechanisms

1.3.2.1 Electronic Conduction in Metals and Semi-Conductors

In simple molecular systems the interaction of atomic orbitals causes the formation of molecular orbitals with discrete energy levels. However, because of the large number of atoms that interact in a solid material, the energy levels are so closely spaced that they form bands. The highest energy filled band, which is analogous to the highest occupied molecular orbital in a molecule (HOMO), is called the valence band. The next higher band, which is analogous to the lowest unoccupied molecular orbital (LUMO) in a molecule, is called the conduction band. The energy separation between these bands is called the energy gap.

Metals exhibit high conductivity, of the order of 10^6 Scm^{-1} , due to the presence of delocalised electrons which are shared with all atoms in the solid. Metals have overlapping valence and conduction bands (no band gap) meaning there is little barrier to conductivity. Non-metallic covalent materials have localised valence electrons and so are insulators. Only when electrons are excited to the conduction band can current flow in these materials. Hence no conduction takes place. Semi-conductors have similar band-structure to insulators but the energy gap is much smaller, and on doping, mid-gap holes can be created which assist conductivity.

Electrical conductivity is temperature dependent in both semi-conductors and metals. In metals, electrical conductivity decreases with increasing temperature, whereas in semiconductors, electrical conductivity increases with increasing temperature. Over a limited temperature range, the electrical conductivity can be approximated as being directly proportional to temperature.

1.3.2.2 Electronic Conduction in Conducting Polymers

Inherently conducting polymers, ICP's, are polymers with conjugated backbones facilitating charge carrier transport. Conductivity is of the order of 10^{-8} S cm⁻¹ which rises towards metal-like conduction (>10 Scm⁻¹) on the addition of dopant molecules, generally organic acids. All known conducting polymers are semiconductors in their unperturbed or pristine state. To become electrically conductive a polymer must become metal-like in that its charge carriers must have a mean free path significantly greater than the internuclear distance. A key property of conductive polymers is the presence of conjugated double bonds along the backbone of the polymer. In conjugation, there are alternately single and double bonds between adjacent carbon atoms. The single bonds are localised σ -bonds which form a strong chemical bond. In addition, every double bond is a less strongly localised π -bond which is weaker. However,, the presence of conjugation is not enough to make the polymer material highly conductive.

The conductivity of conducting polymers spans a very wide range ($<10^{-12}$ to 10^5 Scm⁻¹) depending on oxidation state, pH, counterion type and concentration and physical morphology. [17] The source of this variety is the quasi-one-dimensional (Q-1D) nature of the materials. The chain deformation that results from adding electrons (or consequently holes) to a chain produces a variety of 'particles'; polarons, bipolarons and solitons. Generally the conductivities of the pristine electronic polymers are transformed from insulating to conducting through the process of doping, with the conductivity increasing as the doping level increases. Both n-type and p-type dopants have been used to induce an insulator-to-conductor transition in electronic polymers. [18] Dopants induce a 'hole' on the conduction band side of the band gap which facilitates electron motion.

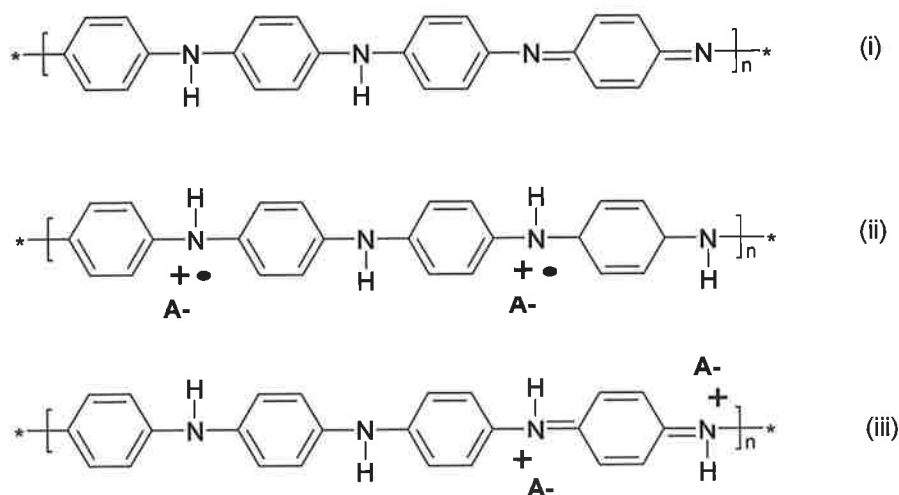


Figure 1.12 Three of the oxidation states of polyaniline (i) undoped emeraldine base, (ii) and (iii) doped emeraldine salt where ii) is the metallic delocalised polaron lattice and iii) the initial bipolaron form where • represents a mobile radical polaron.

Charge transport in conducting polymers occurs via electron transfer between localised states. [19] The conduction mechanism of conducting polymers has been explained as the interchain hopping of polarons and bi-polarons. When an electron is added to a perfect chain (a pristine polymer), either by oxidation or reduction by the dopants, it causes a characteristic bond deformation in the chain about 20 monomer sites long and the electron plus the deformation 'pattern' constitute a polaron (spin = $1/2$, charge = $\pm e$). [20] In the case of conducting polyaniline this conformational change generally takes the form of a switch between single and double bonds. If an electron is removed from the top of the valence band of a semiconductive polymer, such as polyacetylene or polyaniline, the vacancy created does not delocalise completely, as expected from band theory. An electron is removed locally from one carbon atom, and a radical cation is obtained. This radical cation is generally localised due to its attraction to its counterion. However, it may diffuse freely along the polymer chain at the on-chain diffusion rate, D_{\parallel} . At high dopant levels the polaron may hop occasionally between chains at the inter-chain diffusion rate, D_{\perp} , [21] as it can move in the field of other close counterions. Along with the deformation there is an associated change in the energy level structure. In order to form an electron polaron, P^- , an electron is added to the upper (conduction level), or conversely to form a hole polaron, P^+ , an electron leaves the lower level. [22] As a half-filled level remains in either case the polaron has spin $1/2$.

If a second electron is removed from an already oxidised section of the polymer, either a second independent polaron may be created or, if the unpaired electron of the first polaron that is removed, a bipolaron (BP^{2+}) is formed. The two positive charges of the bipolaron are not independent, but move as a pair. [19] A bipolaron is formed by the union of two polarons of like sign and because the combination of two polarons yields two electrons in each level the BP^{2+} has spin, $I = 0$. It is thought that mobile BP's are unstable due to repulsion of like charges, but BP's resulting from doping are stabilised by counterions.

A polymer undergoing isomerisation by protonation and charge carrier motion may create a defect and release a stable free radical; a soliton. This neutral soliton can propagate down a chain but it does not carry a charge. However, it may contribute to charge transfer by assisting charge transfer between chains. [23] Bulk conductivity is limited by the transfer of charge between chains. One mechanism to account for conductivity due to charge-hopping between chains is intersoliton hopping. [24] However, in real polymers charge transport is not simple, due to the presence of finite chain lengths, chain defects, non-crystalline morphology etc.

1.3.2.3 Conduction in Ionic Materials

Ionic solids generally show poor conductivity in the range e.g. NaCl $\sigma \sim 10^{-4} \text{ Scm}^{-1}$. The conduction of ions in the solid state requires the presence of defects in the ionic lattice. In most ionic solids the defect concentration is very low. However, there is a class of solid compounds where defect concentrations are extremely high and these materials often exhibit conductivities which can rival those of electrolyte solutions ($< 10^2 \text{ Scm}^{-1}$). Solid ionic conductors are defined as solid materials that exhibit high electrical conductivity, wholly or mainly due to the motion of ions. For solids to exhibit fast ion conduction there are two general requirements. Firstly, the solid should contain a high concentration of defects; vacancies or interstitials, and secondly the defects should be connected by continuous low energy pathways.

In some solid electrolytes at low temperatures, ions are fixed in the lattice and the solid exhibits low conductivity. On increasing the temperature, thermal energy results in disorder in the lattice, i.e. in the formation of defects. In the absence of an applied electrical field the vibrational motion of ions allows for random hopping of charge carriers between sites. On application of an electric field, current flows through the

migration of ions within the solid, with a compensating flow of electrons in the external circuit of the electrochemical cell.

In perfect crystals all regular lattice points are occupied by atoms and there are no interstitial atoms. Ionic conduction in solids arises through ions hopping from one site to a vacant site in the crystal lattice. There are three types of conduction mechanisms; (i) vacancy mechanisms, where an ion hops to an intrinsic or extrinsic vacancy; (ii) interstitial mechanisms, where an interstitial ion hops onto a neighbouring vacant interstitial site; and (iii) interstitialcy mechanisms, a cooperative motion where an interstitial ion pushes a neighbouring ion in a normal lattice site into an interstitial vacancy and then takes its place on the normal lattice site. [25]

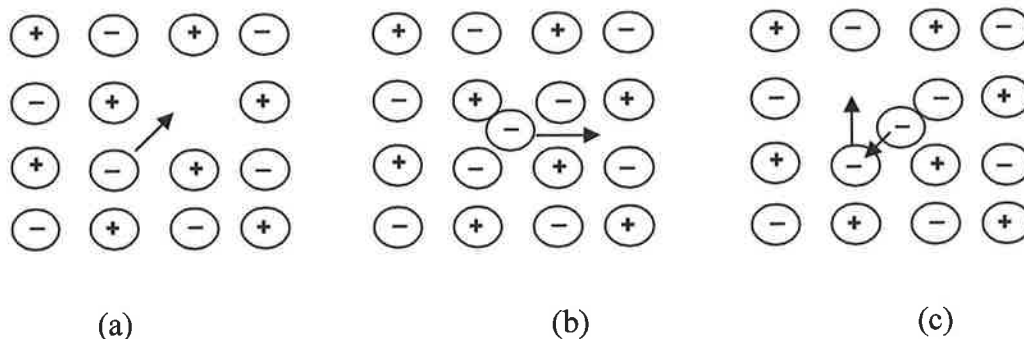


Figure 1.13 Schematic representation of (a) a vacancy mechanism (b) an interstitial mechanism and (c) interstitialcy mechanism.

Due to the complexity of most solid electrolyte materials there are many types of defects or disorder that can affect the conductivity. However, due to electric neutrality the number of positive charges must equal the number of negative charges, and as a result only three combinations of defects are possible. The first is the Schottky defect which is a pair of vacancies comprising a cation and an anion vacancy. [26] The others are Frenkel and anti-Frenkel defects [27], which are comprised of an anion vacancy accompanied by an interstitial anion, or a cation vacancy with an interstitial cation respectively.

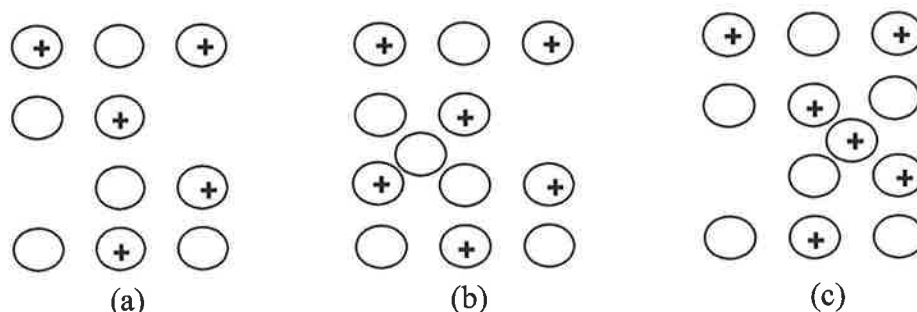


Figure 1.14 Schematic representation of (a) a Schottky defect, (b) a Frenkel defect and (c) an anti-Frenkel defect.

In most ionic conductors there is also a sublattice of immobile ions which do not leave their lattice sites and, while not involved in the conduction process, are important for the extent of conduction as they provide a lattice for the mobile ions to move through. The polarizability of these static ions can influence conductivity. Generally the larger the ionic radius of the ion the greater its polarizability. [28] This fact is often used in the development of improved ionic conductors.

There are three general types of superionic conductors. Type I have well-defined first-order phase transitions into the superionic phase with a subsequent jump in the conductivity. For example the halide conducting material AgI, whose conductivity jumps by four orders of magnitude at T_c . Type III materials, such as Na- β -Al₂O₃ display an exponential increase in conductivity with no definite conversion point.

Type II conductors, such as PbSnF₄, show a gradual change from the insulating state to the conducting state. For example, in PbF₂, the conductivity increases exponentially up to ~ 720 K, above this temperature it only increases slightly up to melt temperature, >1000 K. [29] Type II materials typically exhibit second order phase transitions of the disordering mobile sublattice, with no change in the immobile cation sublattice.

1.3.2.4 Conduction in Protonic Materials

There are a number of mechanisms of proton transport in solid protonic conductors. These include the transport of protons between relatively stationary host atoms (H⁺) and the transport of proton carriers (OH⁻, H₂O, H₃O⁺, NH₄⁺). The former is known as the Grotthuss mechanism while the latter are termed vehicle mechanisms.

The vehicle mechanism is observed in materials that have liquid or liquid like layers and in solids with open channels which allow the passage of large ions. [30] In the

1.3.3 Fuel Cells

The conducting materials examined in this thesis have potential for application in fuel cells. Fuel cells essentially consist of an anode and a cathode separated by an electrolyte. In a simple hydrogen cell hydrogen gas diffuses to the anode catalyst where it dissociates into protons and electrons. The protons are conducted through the electrolyte to the cathode, but the electrons are forced to travel in an external circuit. At the cathode catalyst, oxygen molecules react with both migrating species to form water.

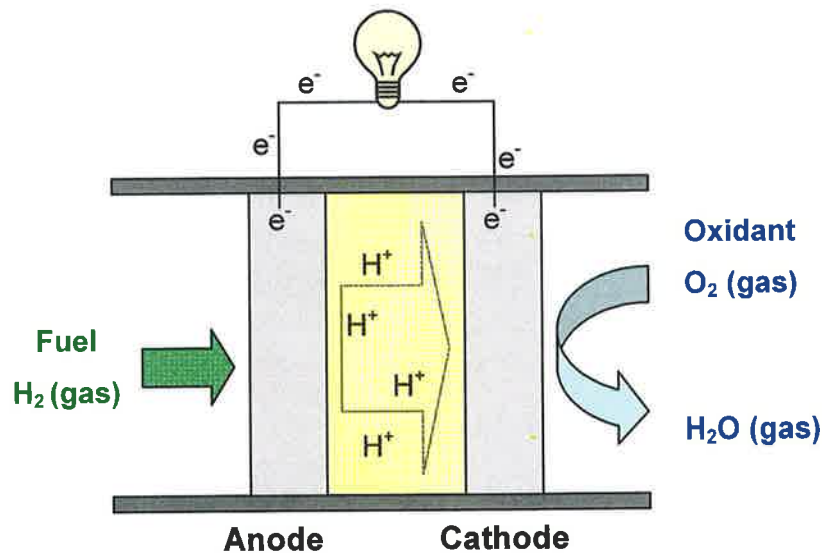


Figure 1.16 Schematic diagram of the operation of a simple hydrogen fuel cell.

It is expected that this technology will find uses in diverse field such as transport, for large-scale power sources in remote places and as portable electronic applications. However, development is currently restrained by materials limitations of the electrolyte. The electrolytes used may be solid or liquid and each has its own advantages and disadvantages. At the present time there are a number of liquids used in a wide variety of fuels cells including:

- i) Phosphoric acid fuel cells (PAFC) use aqueous phosphoric acid as the electrolyte and operate at ~ 470 K. The main advantages of this type of fuel cell are their efficiency and that they can use impure hydrogen as fuel. The mobile ion in this aqueous cell is the hydronium ion, H_3O^+ .
- ii) Alkaline fuel cells operate at relatively low temperatures and use potassium hydroxide as the electrolyte and OH^- as the mobile ion.

iii) Molten carbonate fuel cells use an electrolyte composed of a molten carbonate salt mixture suspended in a porous, chemically inert matrix, and operate at high temperatures, usually ~ 1000 K. The mobile ion in this case is CO_3^{2-} . [30]

Solid electrolytes are often preferable as they are more robust, more efficient and less susceptible to corrosion. The solid electrolyte materials closest to full commercial application at the present time are:

- (i) Solid oxide fuel cells (SOFC), which use a hard, non-porous ceramic compound as the electrolyte, and operate at very high temperatures (> 800 K). The mobile ion in this case is the O_2^- ion. The main drawback is the high operating temperature which makes them only suitable for stationary or large scale processes. [30]
- (ii) Polymer electrolyte fuel cells (PEFC) or polymer electrolyte membranes (PEM) contain liquid-like regions between sulphonated polymer membranes. Their high efficiency and low operating temperature, < 373 K, make them ideal for portable applications. However,, they have a number of drawbacks including low permeability to fuels. More significantly they require humid conditions and hence have a maximum operating temperature of 373 K. [29, 30] The mobile ion is H_3O^+ .

Of the materials examined in this thesis, the Cs based superprotonic materials are closest to commercial use as electrolytes in fuel cells. Haile *et al* [32] have shown that caesium mixed sulphate/phosphate materials show good efficiency and stability as electrolytes at elevated temperatures (< 400 K) in hydrogen fuel cells. Polyaniline is attractive as an electrolyte material as it exhibits high conductivity and can be fabricated at low cost by simple methods. HCl-doped films of polyaniline showed good conductivity. However, it has poor stability compared to the industry standard Nafion when used as polymer electrolyte membrane in a halide fuel cell. [35] More encouragingly when combined with polyethers in a methanol fuel cell, polyaniline showed good stability and very low methanol permeation. [36] PbSnF_4 has yet to be tested as a fuel cell electrolyte but closely related superionic fluoride conductors in the LiF-MgF class shown high conductivity and stability under the conditions at which hydrogen fuel cells operate. [37, 38] Ionic liquids due their thermal stability and low toxicity have frequently been used as supporting electrolytes in fuel cell applications. [39, 40]

Chapter 2 - Experimental

2.1 Introduction

In this experimental section the characterisation techniques which were applied throughout the work are described. The synthesis or sources of the materials themselves are described in the relevant chapters. Fast-field cycling NMR (FFC-NMR) and conductivity measurements are the two most extensively used techniques in this work and are described in detail. A short description of some other techniques also used in this project, including scanning electron and atomic force microscopy, differential scanning calorimetry, and raman spectroscopy is also provided.

2.2 FFC-NMR

2.2.1 Historical development

Fast field cycling relaxometry is the preferred [11, 41, 42] method for measuring the dependence of NMR relaxation times on the magnetic field strength. The use of a field-switchable magnet has a number of advantages over traditional field dependent relaxation measurements; (i) conventional fixed field measurements require the use of more than one spectrometer which makes it prohibitively expensive to record field dependent data; (ii) relaxation data can be measured at low fields, where T_1 is sensitive to slow motions; (iii) it can be difficult to extrapolate measured relaxation times from one field to another; (iv) variable-field electromagnets experience problems associated with very high B_0 such as sample heating and transmitter phase shifts during long pulse sequences.

The field cycling NMR technique was developed in 1953 by Packard and Varian [43], who used a basic field cycling device to observe nuclear magnetism in the earth's field. In the late 1950's Abragam and Proctor [44] used a similar technique to study the concept spin temperature. In these early experiments, the magnetic field was cycled by extracting the sample from the magnet at the polarisation field and moving it by hand to another magnet at the relaxation field. The relaxation times of the studied samples had to be extremely long, of the order of minutes to hours. This design was significantly improved by Edmonds in the early 1970's, [45] by including a carriage mounted on a rod between the two magnets, the movement of which was controlled pneumatically. The main advantage of this approach is that the detection

magnet can have high sensitivity and homogeneity which results in resolution comparable to a modern fixed field spectrometer, from which they are usually constructed. However, there are obvious weaknesses to this approach; it is difficult to reduce the switching time to <0.2 s and precise temperature control is not possible.

The alternative to manual switching is electronic field switching in a single magnet. In the late 1950's A. G. Anderson [46] used a simple single magnet field cycling apparatus to study the absorption of RF radiation by local fields. In Germany during the 1960's, Noack introduced the concept of "relaxation spectroscopy" and the first electronically field cycled NMR instrument was constructed by Kimmich in Noack's laboratory soon after. The design of the magnet currently used today is based on a design by Noack and Schweikert, where each coil is cut from a single cylinder of metal with a variable step of the helix. [47] However, the use of field cycling was limited to research groups able to build their own field cycling instruments. An Italian company, Stelar SRL, developed a commercial FFC relaxometer in the early 1990's. It is now possible to measure relaxation times in the entire range from 10 kHz to 40 MHz. [48] The development of field cycling devices has not stopped; new magnets with improved homogeneity, and extended field range continue to emerge. [49]

2.2.2 Field-cycling

The basic field cycling experiment consists of three steps:

- (i) The sample is polarised to obtain reproducible initial magnetisation in a relatively high field, B_{pol} , (usually 10-14 MHz) for a time, T_{pol} , until the nuclear magnetisation achieves saturation ($\sim 5T_1$) at that field. This is called a 'pre-polarised' (PP) sequence. For high relaxation fields, >6 MHz, the difference between the magnetisation at the polarisation and the relaxation fields is insufficient, so the field is switched from zero field to the relaxation field in what is termed a 'non-polarised' (NP) sequence.
- (ii) After the switching time, swt , the magnetic field is switched to the relaxation field, B_{rlx} , for a time, τ , during which the magnetisation relaxes back to equilibrium.
- (iii) The magnetic field is switched to the acquisition field, B_{acq} , (typically 9.25 MHz for ^1H and 9.81 MHz for ^{19}F) and a 90° RF pulse is applied followed by acquisition of the free induction decay (FID) in the xy-plane. This is followed by a

recycle delay (RD) of generally $5T_1$ to allow the magnet to cool and all magnetisation to dissipate.

As the detection field is reproduced in subsequent cycles, phase sensitive detection is feasible. Quadrature detection allows further compensation for the effects of the field switch, by using the signal magnitude for evaluation of the magnetisation intensity. It also means that signals can be accumulated to improve the sensitivity. [50] The experiment is repeated for a set of τ values; generally 16 values are used ranging from four times the estimated T_1 to 0.001 s. When τ is short the intensity of the magnetisation will reflect the polarisation period, when τ is long compared to T_1 at B_{rlx} , the intensity of the magnetisation will reflect the equilibrium magnetisation at B_{rlx} . From the dependence of the magnetisation on τ , the T_1 value at B_{rlx} , can be determined by least squares fitting. For mono-exponential recovery, a three-parameter model with a strict statistical estimate of confidence intervals is applied. A new B_{rlx} can then be selected and a new T_1 value measured. This process can be repeated automatically for the desired number of fields, creating a relaxation profile. The profile can be recorded at various temperatures in the accessible range.

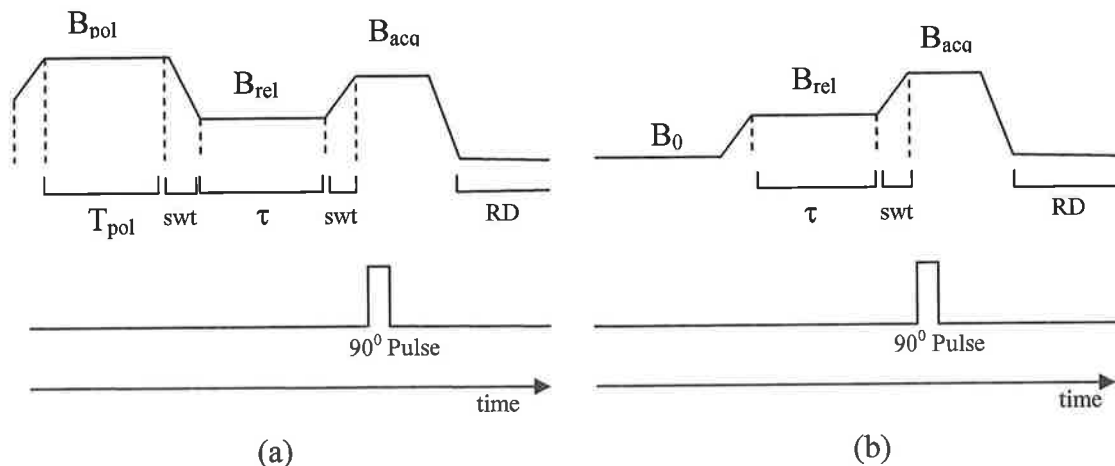


Figure 2.1 The basic (a) pre-polarised (PP) and (b) non-polarised sequences used in field cycling NMR.

It is necessary to remove some of the early points of the FID to eliminate instrumental artefacts including magnet field settling and probe ringing. In order to get reliable results the signal must be kept on resonance for all evolution times. When a large current passes through the magnet coils during the experiment, the resulting heat causes thermal expansion of the coil resulting in a shift in the magnetic field. The

magnet temperature may fall as much as 20-30° C between polarisation and evolution for long time pulses. This is compensated for by a circuit that senses the magnet temperature and adds a current proportional to the temperature increase to stabilise the magnetic field. The magnet temperature compensation factor is one of the adjustable parameters in an FFC experiment. The cooling-heating cycle is normally less than couple of seconds due to the efficient cooling system, so the magnet temperature always equilibrates during the relaxation delay.

The effective lower limit for T_1 using the FFC equipment is approximately 1ms ($R_1 = 1000 \text{ s}^{-1}$). This is due to the minimum magnet switching time of 1ms with a switching rate (slew rate) of 24 MHz/ms. Any measured T_1 shorter than this limit is unreliable as it may contain contributions from the residual magnetisation from the polarisation field and only the later part of the magnetisation recovery can be sampled. Figure 2.2 shows relaxation profiles of aqueous solutions of GdCl_2 at different concentrations with low frequency T_1 plateaus expected close to the measurable limit. The samples with T_1 values close to 1ms show a marked increase in scatter and associated increase in errors, and the onset of systematic errors for $R_1 > 1000 \text{ s}^{-1}$.

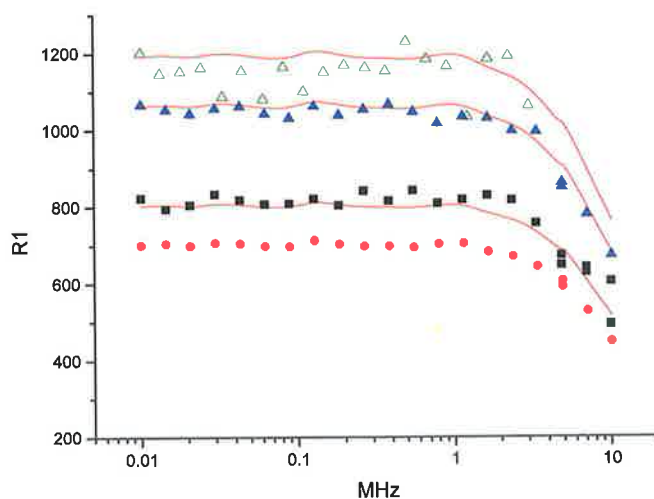


Figure 2.2 Relaxation profiles of aqueous GdCl_2 solutions at 45 mM (Δ), 40 mM (\blacktriangle), 30 mM (\blacksquare), and 25 mM (\bullet) The solid lines show the expected relaxation rates for each concentration calculated from the measured R_1 value at 25 mM using the equation $R_{1(\text{obs})} = R_{1(\text{H}_2\text{O})} + r_1[\text{Gd}]$, where r_1 is the relaxivity given in units of $\text{s}^{-1}\text{mM}^{-1}$.

The typical duration of the 90° pulse was 6-7 μs . The spectral window width (Nyquist frequency) was generally of the order of 1 MHz with a cutoff frequency from 120-930 kHz. The maximum magnetisation dephasing time, T_2^* , due to the B_0 inhomogeneity of the field cycling magnet is approximately 250 μs .

One of the major limitations of field-cycling NMR is the poor sensitivity and resulting low signal-to-noise ratio. If the detection field can be reproduced accurately then signals may be accumulated but this averaging is less successful than in high-field NMR measurements spectrometers due to the limited stability of field-cycling systems. [50] As the polarisation and detection fields have different flux densities in fast-field cycling applications the standard NMR signal-to-noise ratio relationship is modified to [50-52]

$$\frac{S}{N} \propto B_p \xi \sqrt{\frac{nQV_s}{k_B T} \left(\frac{\nu_d}{\Delta\nu} \right)} \quad [2.1]$$

where B_p is the flux density of the polarisation field, n is the filling factor of the RF coil, Q is the quality factor of the coil, V_s is the sample volume, k_B is Boltzmanns constant, T is the absolute temperature, $\Delta\nu$ is the bandwidth of the receiver filtering system, ξ is the reciprocal noise level of the receiver (<1) and ν_d is the detection larmor frequency ($= \gamma B_d/2\pi$ where γ is the gyromagnetic constant for the nuclei in question and B_d is the detection flux density). From this it can be seen that signal to noise is proportional to $B_0^{3/2}$ and high polarisation and detection densities are crucial for good sensitivity but are restrained by heating effects. Also large samples, high Q coils, low-noise receivers and narrow RF filters can all be employed to maximise the sensitivity of the instrument. Despite this the sensitivity is poor, but errors in T_1 of less than 1% can be achieved for ^1H T_1 measurements on aqueous solutions of paramagnetic materials (eg MnCl_2). Unfortunately for this project the situation is much worse for solids than liquids, due to shorter T_2 and is worse again for nuclei other than ^1H .

2.2.3 Practical considerations

Samples are maintained at a constant temperature during the experiments. The Spinmaster Variable Temperature Controller (VTC) allows setting of the sample temperature from 113-433 K with control of about ± 0.1 K. Temperatures above

ambient (>293 K) are easily and rapidly achieved using a resistive heating element and an airflow of 4 ml/min. For low temperature measurements a liquid nitrogen dewar equipped with a controllable resistive heating device, which can control the extent of evaporation of cold N_2 , is used to control the sample temperature. The practical lower temperature limit using this apparatus is close to 200 K due to the relatively long uninsulated path of the cold vapour N_2 from the dewar to the sample.

In a typical experiment the cooling pump for the B_0 magnet and RF transmitter are turned on. Then the sample, in a 10 mm diameter NMR tube, is placed in the probe. The measurement starts with the setting of acquisition field (B_{ACQ}) normally 9.25 MHz for 1H and 9.81 MHz for ^{19}F . The probe is tuned to be resonant at 9.25 MHz. The optimal acquisition parameters are found by trial and error and due to the vastly different characteristics of the samples studied in this thesis there were no standard parameters. To record a relaxation profile, successive T_1 measurements as a function of field are performed using a software macro in which most of the parameters are preset. The general procedure is:

- The sample temperature is set and the sample is equilibrated at this temperature for the required time usually 30 min.
- Using the NP sequence all the parameters concerning the magnet cycle (switching time, slew rate, pre-scan delay etc.), RF (90° pulse width, receiver gain etc.) and acquisition (scan size, spectral width, etc.) at the maximum desired Larmor frequency of the profile are optimised and fixed.
- The optimum magnet temperature compensation factor is determined. In practice this parameter is stable for weeks at a time.
- The maximum expected T_1 , polarisation time and pre-scan delay are then set in the loaded NP/S sequence (normally for the profile range 20 to 0.01 MHz). T_1 is measured and saved in a pre defined data and results file.
- When all these parameters are optimised, the macro is started to acquire the profile automatically.

Some parameters, e.g. the estimate for T_1 which determines the range of τ values used, and frequency offsets, are updated by the software after each measurement.

2.2.4 High field measurements

Measurements were also carried out on a reconditioned Bruker WP80 variable field magnet. This magnet extended the available maximum field range from 20 MHz up to 80 MHz. It also has greater sensitivity and increased magnet homogeneity, although this is not sufficient for ^1H spectroscopy. This is not a field cycling machine so traditional relaxation experiments were carried out using both inversion recovery and modified saturation recovery pulse sequences which involve the application of RF pulses to generate non-equilibrium magnetisation. The inversion recovery pulse sequence (IR) is used at a fixed field and involves the application of a 180° pulse then a relaxation time, τ , followed by a 90° acquisition pulse. The τ value is varied from 0 s to four times the maximum expected T_1 value. The magnetisation recovery is plotted as a function of τ and the T_1 value is determined as before. The aperiodic pulse saturation recovery sequence (APSR) is similar but instead of a 180° initial pulse there is a train of preparatory 90° pulses with linearly decreasing interpulse separation, which serves to saturate the sample magnetisation, prior to the recovery time τ .

In a typical WP80 experiment the procedure is:

- The sample temperature is set and the sample is equilibrated at this temperature for the required time usually 30 min.
- The magnetic field is set to the appropriate value and the probe is tuned to the appropriate frequency (between 20 and 80 MHz usually in 5 MHz steps)
- A single pulse sequence (S1P) is started on continuous mode and the current in the B_0 magnet is adjusted until the signal is on-resonance
- Using the S1P sequence all the parameters concerning the magnet cycle (switching time, slew rate, pre-scan delay etc.), RF (90° pulse width) and acquisition (spectral width, receiver gain, receiver phase etc.) are optimised.
- An inversion recovery sequence or saturation recovery sequence is used to measure T_1 and the process is repeated at the next field

There are limitations associated with the WP80 system; the temperature is more difficult to control than in the case of field cycling due to the probe design. Low temperatures are not possible due to the distance from the dewar to the sample. The field range is limited and the measurements, especially for solid samples, are very time-consuming.

2.3 Conductivity

2.3.1 The 4-point probe method

Bulk resistivity or conductivity measurements are perhaps the most critical characterisation method for conducting and semi-conducting materials. The four-point, or Kelvin probe method is the most common way to measure a semiconducting materials resistivity. This technique involves bringing four equally spaced points into contact with the material as in figure 2.3. Two of the points are from the current source and the other two points are used to measure voltage. Using four points eliminates measurement errors due to the probe resistance, the spreading resistance under each probe, and the contact resistance between each metal probe and the semiconductor material. [53]

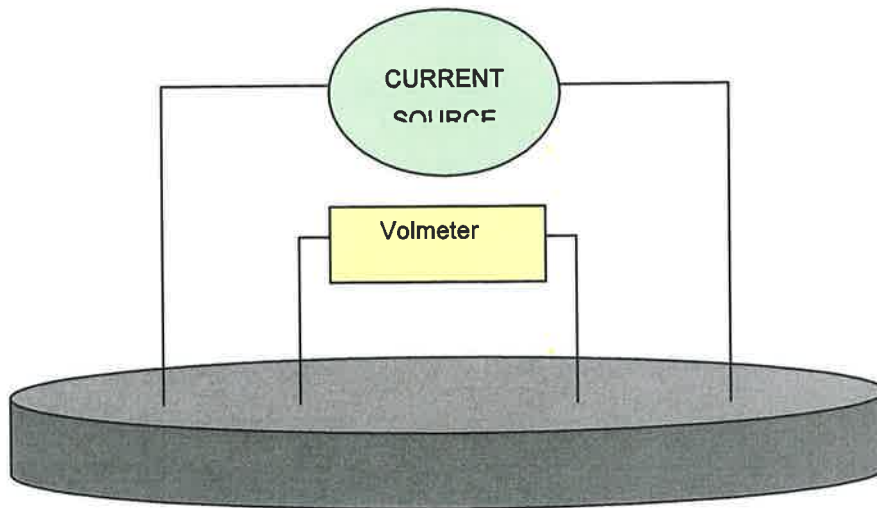


Figure 2.3 Schematic representation of the pin configuration in the four-point probe head

The volume resistivity is then calculated with this equation [54]:

$$\rho = s \frac{\pi V}{\ln 2 I} \quad [2.2]$$

where ρ is the resistivity ($\Omega \text{ cm}^{-1}$), s is the pin spacing (cm), V is the measured voltage (volts) and I is the source current (Amperes). The conductivity is simply the inverse of the resistivity and is measured in Scm^{-1} .

2.3.2 Apparatus development

The conductivity meter used in most of this work was developed with assistance with Dr Darren Carty. A number of considerations were taken into account when

constructing the system. Firstly a good quality current source was obtained. Given the conductivities and typical inter-point spacing, this had to be accurate for sub-milliamp currents while emitting a constant current. The Time Electronics 1044 Current calibrator was sourced from Radionics Ltd, it has a μA -mA range and nA resolution. A comparably accurate voltmeter was sourced also from Radionics Ltd, a Goosen Metrawatt MetraHit 22S which has a voltage measuring range from mV-1000 V and μV precision.



Figure 2.4 Four-point probe apparatus.

The most critical aspect of the design was the construction of the probe head. The four pins must have a small enough outer diameter to be placed very close together (ideally $<1\text{mm}$ apart to ensure applicability to different sample sizes) but it must be possible to easily connect them to the voltmeter and current source. They also must be strong enough to withstand the pressure of the probe forcing them into the samples (pellets) without distortion, and to ensure there are no resistivity artefacts from the pins. Pins were sourced from Radionics which have tungsten carbide sleeves that ensured similar depth of penetration for all the pins and which made it easier to wire the voltmeter and current source to the probe head.

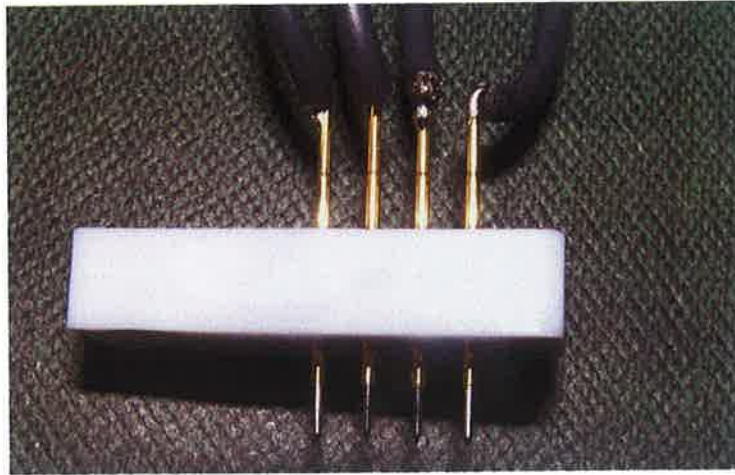


Figure 2.5 Four-point probe pin head.

The pins had to be electrically isolated from the rest of the apparatus and from each other. To achieve this four holes 0.9 mm in diameter and exactly 0.9 mm apart from each other were drilled into a block of Teflon and the pins were secured in the holes. The probe head was mounted on a frame with a screw with a locking nut that ensured that the distance the pins travel into each sample pellet could be accurately reproduced.

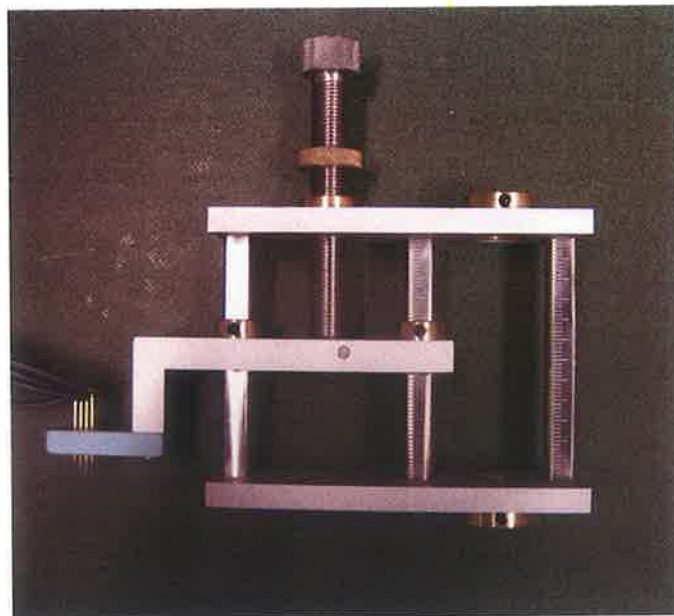


Figure 2.6 Four-point probe pin head and mount.

For temperature control the apparatus was mounted on a standard lab hotplate. In order to electrically isolate the sample from the metal top of the hotplate but allow thermal contact a thin Teflon block was placed between the sample and the hotplate. Two small holes were drilled in the block, one just below the surface of the sample and one just above the surface of the heat source. A t-type thermocouple, with a Microtherma 2 thermometer, was inserted into each of these holes to monitor the temperature of the sample, and separately of the hotplate, to ensure heat transfer was efficient. The temperature was found to vary across the hot plate surface probably due to air currents so the entire apparatus was encased in a plexi-glass case with a hinged door to allow sample access.

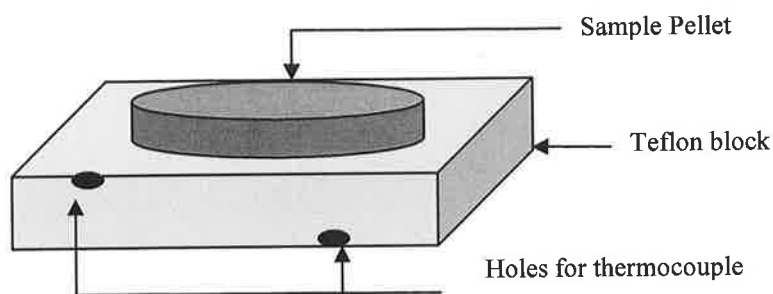


Figure 2.7 Schematic representation of the Teflon block used as a sample holder.

2.3.3 Practical considerations

Powder samples of conducting polymers were pressed into pellets ~0.7-1 cm in diameter and <0.1 mm thick. The first pellets were made using a hydraulic press while later pellets were made using a small manual press. The pressure used to form the pellets did not affect the measured conductivity. The temperature was kept constant during all experiments. The temperature was set on the hotplate and after twenty minutes equilibration time, the exact temperature of the sample was measured using the thermocouple in the top of the Teflon block. The experiment involves measuring the voltage at a certain current and then using equation 1 calculate the resistivity and hence conductivity. This was repeated a number of times across a wide range of currents from 0.1-20 mA and from -0.1 to -20 mA. For conducting polyaniline samples, the resulting V/I curves were all linear ($R^2 > 0.99$) and passed through the origin proving the validity of both the method and our home-built equipment for use in this application. The conductivity values calculated were also all repeatable at room temperature over the expected lifetime of the samples.

However, there were problems using the apparatus for measurements of the thermal dependence of conductivity in conducting polymers. Plotting the conductivity against time at an elevated temperature typically showed an initial increase in the measured conductivity followed by a constant decrease. It is likely that the thermal expansion of the material when the pins are embedded causes distortions in the pellet. An alternative explanation could be that the pins cause localised excess heating at their points resulting in dedoping. The situation was improved slightly if the probe was removed from the sample during heating or if the sample was maintained at an elevated temperature for an extended period.

2.4 Microscopy

2.4.1 Scanning Electron Microscopy

Scanning electron microscopy, SEM, was performed on a general purpose Hitachi S-3000N Scanning electron microscope. Conducting polymer samples were mounted by drying a drop of suspended aqueous solution on the carbon pad on a sample stub but not gold ablated. High magnification SEM pictures were taken with a typical acceleration voltage of 20 kV and suitable filament current/ emission.

2.4.2 Atomic Force Microscopy

All AFM measurements were carried out using a Digital Instruments D3000 Atomic Force Microscope in Dr Tony Cafollas lab in DCU. Samples were analysed in air in a number of physical forms including; pellets of powder samples similar to the pellets used in conductivity experiments; aqueous suspensions drop- and spin-coated onto the surface of plain glass slides; aqueous suspensions drop-coated onto the carbon pad on an SEM sample stub. Usually the contact mode was used for the samples, and the images were recorded at a number of magnifications in the range of 20-0.5 μm

2.5 Differential Scanning Calorimetry

Thermal analysis was performed using a Polymer Labs PL-DSC differential scanning calorimeter. Each sample was lightly ground and approximately 20 mg was placed in an open sample pan under flowing nitrogen (5 mL/min). The reference was air in each

case. The measurements were conducted using a heating rate of 1, 2 or 5 K/min, in the temperature range of 223-500 K depending on the sample.

2.6 Raman

Raman spectra were recorded with a Perkin Elmer 1700 raman spectrometer. The excitation wavelength was 514.5 nm from an Ar⁺ Ion laser with a typical laser power of ~20 mW in order to avoid excessive heating. The incident and scattered beams were focussed using a microscope with 100× objective lens and a laser spot of approximately 4-5 μm diameter. All measurements were carried out at room temperature using powdered samples.

Chapter 3 – Fluoride Superionic Conductors

3.1 Introduction

3.1.1 Electrical conduction in solids

Ionic solids generally show poor conductivity as the conduction of ions in the solid state requires the presence of defects in the ionic lattice and in most cases the defect concentration is very low. However,, there is a class of solid compounds where defect concentrations are extremely high and these materials often exhibit conductivities which can rival those of electrolyte solutions. This class of materials are collectively known as solid electrolytes, superionic conductors or fast ion conductors.

The field of solid ionic conduction dates back to the 19th century. In 1897 Nernst developed a resistive-heating light source using stabilised zirconia. He correctly believed the induced current was due to the flow of oxide anions. In the early part of the 20th century cationic conduction in alkyl halides was extensively studied. Initial interest focussed on the abnormally high conductivity of AgI, which increases by four orders of magnitude at 386 K at a first order phase transition. [55, 56] Since that time the field of solid electrolytes has expanded rapidly and materials such as the Na⁺ superionic conductor NASICON [57] and fluorite-based solid electrolytes have found applications in electrochemical devices including sensors, solid state batteries and fuel cells. [58-60]

3.1.2 Solid Electrolytes

Solid electrolytes are solids that exhibit high electrical conductivity, wholly or largely due to the motion of ions. There are three general types of superionic conductors. Type I have well-defined first-order phase transitions into the superionic phase with a subsequent jump in the conductivity. Type III materials display an exponential increase in conductivity with no definite conversion temperature.

Type II anion conductors show a gradual change from the insulating state to the conducting state and typically exhibit second order phase transitions of the disordering mobile sublattice with no change in the immobile cation sublattice. Most of the conductors in this group have the fluorite structure which consists of a face-centered cubic arrangement of cations with anions occupying the tetrahedral positions. On heating, the anion sublattice exhibits increased Frenkel disorder and

anions begin to populate the octahedral interstitial sites leaving vacancies on the tetrahedral sites.

3.1.3 PbSnF₄ structure and properties

Much of the early work on solid electrolytes was on oxide and metal halide systems. Recently focus has turned to fluoride ion conductors as the fluoride ion is in general more conductive than the oxide ion. Low-temperature fluoride conductors have been used more extensively in sensing devices while oxide materials are generally more suited to fuel cells due to their high temperature stability.

PbSnF₄ is a Type II fluoride ionic conductor related to β -PbF₂. It exhibits high, purely ionic conductivity and low activation energy for conduction. PbSnF₄ has attracted much interest due to its promising practical potential including its recent use in amperometric oxygen gas sensors. [59] Detailed investigations of its structural, thermal, electrical and dynamic properties have been carried out. It has a room temperature conductivity of $\sim 10^{-3} \text{ Scm}^{-1}$ [61] and the reported activation energy for conductivity at room temperature is between 0.41 to 0.52 eV. PbSnF₄, and other β -PbF₂ based materials, have shown higher conductivity than other fluoride conductors due to the disorder in the anion sublattice and the high polarisability of the Pb²⁺ ions. [61]

PbSnF₄ (α -PbSnF₄) was first synthesised by Donaldson *et al* [62] by precipitation from aqueous solution and by the high-temperature reaction between SnF₂ and PbF₂. There are three main polymorphous phases of PbSnF₄; low-temperature α -PbSnF₄, intermediate temperature β -PbSnF₄ and high temperature the γ -PbSnF₄. [63] The structure of β -PbSnF₄ is based on a tetragonal unit cell, and can be described as cation ordering of a pseudo cubic fluorite subcell. The ionic conductivity of this phase was found to be in the order of 10^{-2} Scm^{-1} at 437 K, with an activation energy of ~ 0.31 eV. [62] The exact temperature of the α to β phase transition appears to differ depending on sample history and experimental conditions, but is generally observed between 530 and 560 K. [57, 63] The γ -phase, which occurs between 653 K and 663 K, is isostructural with β -PbFSnF₄.

α -PbSnF₄ is the most studied of the three phases as it has the highest room temperature anionic conductivity. There is dispute over the structure of α -PbSnF₄ which has been described as monoclinic, orthorhombic and tetragonal. [62-64] These differences have been explained by the high sensitivity of the structure to small

changes in synthesis conditions which can introduce Sn or Pb deficient minor phases with altered symmetry. Indeed Perez reported further possible orthorhombic phases with the acidification of the SnF_2 aqueous solution during synthesis. [64]

The structure of $\alpha\text{-PbSnF}_4$ is similar to other fluorite based materials with mobile fluoride and stationary cation sublattices. The structure may be described as being based on a tetragonally ordered fluorite (CaF_2), with cubic close packed cations (Sn^{2+} and Pb^{2+}) and two of the fluoride ions occupying tetrahedral sites (F2 and F3), while the third is slightly distorted away from the ideal site to an almost octahedral site (F4). [65] This cation ordering over distorted fluorite related supercells is the cause of the high ionic conductivity as it can accommodate Frenkel defects. The remaining tetrahedral site (F1) which lies between adjacent Sn layers shows no measurable occupancy at 298 K (figure 3.1). From X-ray powder diffraction the cation ordering has been elucidated. The immobile cation sublattice has an order along c as follows: Pb Pb Sn Sn Pb Pb, which results in a supercell with a doubling of c . [66]

Mössbauer spectroscopy has provided evidence that the lone pair of Sn electrons are stereochemically active, and therefore they are localised around the Sn atoms and do not contribute directly to conductivity. This is consistent with the observation of purely ionic conductivity. [66] Between the Pb and Sn layers there are mobile fluoride ions. The exact location of fluoride ions and local structure was determined by EXAFS and neutron diffraction studies which showed that disorder of the fluoride ions is more pronounced near to Sn rather than Pb atoms. [66]

The neutron diffraction study of $\alpha\text{-PbSnF}_4$ of Castiglione *et al* [65] was carried out on a carefully prepared, relatively phase pure, sample and revealed full occupation of only three of the four fluoride ion sites, two of which show large anisotropic thermal parameters indicative of positional/vibrational disorder. The structure remains tetragonal above 340 K, but there is increased fluoride disorder, with greater anion density linking the F2 and F4 sites. Also at higher temperatures the sample exhibits partial occupancy in the F1 site.

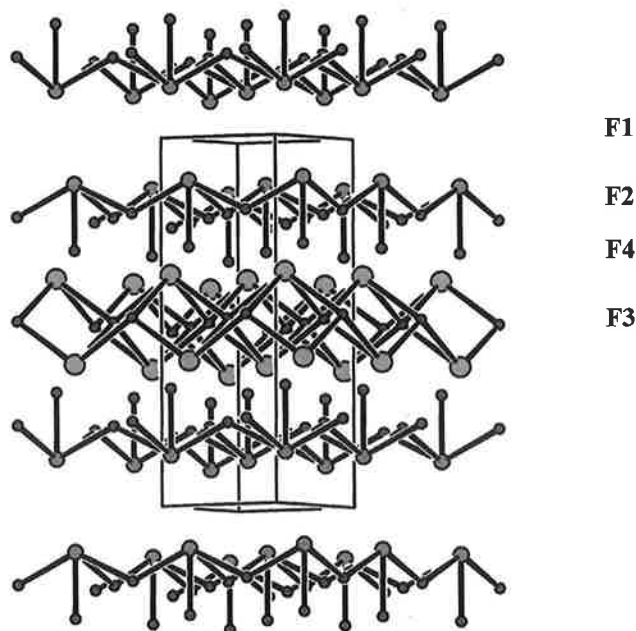


Figure 3.1 Supercell structure of PbSnF₄ showing the Pb (●) and Sn (●) layers and the four fluoride sites (●); F1 (vacant); F2 and F4 (mobile) between the Sn and Pb layers; and F3 (static) between two Pb layers.

3.1.3 NMR of Solid Electrolytes

NMR spectroscopy is commonly used in conjunction with conductivity measurements to obtain insight into ionic transport. NMR has advantages in that it can be used on single crystals, polycrystalline and powder samples and it can be used on both highly conducting and insulating samples. A number of NMR methods have been applied to obtain structural and dynamic information for these materials. [67]

The Type I alkyl halides (CuI and AgI) have been extensively studied by NMR above and below their transition temperatures, using both linewidth and relaxation measurements. [29, 67] Dynamic parameters from BPP analysis of the relaxation data showed good agreement with those obtained from conductivity measurements.

Fluoride ion conductors have also been extensively studied, especially PbF₂. Rao *et al* [68] determined an activation energy for fluoride motion of 0.35 eV in the α -phase using linewidth analysis, a finding which supported a relaxometry study by Hwang. [69] Hwang *et al* [70] also used spin-spin relaxation measurements to show that fluoride ions are more mobile in the β -phase of PbF₂ than in the α -phase. Boyce [29] measured relaxation rates for β -PbF₂ across a wide temperature range. The results were consistent with the BPP model indicating a single mechanism for motion below

520 K. This was attributed to a vacancy diffusion mechanism with an activation energy of 0.74 eV which is similar to that obtained previously and with conductivity measurements (0.6-0.72 eV). Above the first order phase transition temperature, 520 K, the activation energy in PbF_2 , derived from NMR, increases in a similar fashion to the conductivity, due to sublattice melting. Similar measurements were made with BaF_2 [71], which has a related structure but much lower conductivity. Once again there was good agreement between NMR relaxation and conductivity measurements, both of which indicated a relatively high activation energy of 1.7 eV.

Privalov [16] used ^{19}F NMR relaxometry to measure fluoride dynamics in LaF_3 across wide frequency (60 kHz to 284 MHz) and temperature (303-1400 K) ranges. He observed non-BPP dynamics and, by applying a spectral density model describing a log Gaussian distribution of correlation times, obtained activation energies for two motions. A faster motion with $E_a = 0.36$ eV and a slower motion with $E_a = 0.57$ eV, which were attributed to F_1 hops and F_1 - $F_{2,3}$ hops, respectively. [72] A third contribution to the relaxation from fixed paramagnetic centres is observed at high temperatures but does not correspond to a fluoride motion.

More recently ^{19}F NMR techniques have been used to study the complex ionic motion in PbSnF_4 and BaSnF_4 . Grey et al [73] used magic angle spinning solid-state NMR to examine the fluoride mobility in BaSnF_4 . They observed two fluoride sublattices which they attributed to specific sites on the lattice. The first is a rigid sublattice in the Ba^{2+} double layer. The second is a sublattice comprised of highly mobile fluorides between the Ba^{2+} and Sn^{2+} layers which rapidly exchange with the fluorides in the less-populated Sn^{2+} - Sn^{2+} layer. On the basis of their ^{19}F results these authors proposed a new mechanism involving rapid two-dimensional anisotropic conduction of fluorides between the Ba and Sn layers.

Ahmed et al [74] compared activation energies extracted from temperature dependent conductivity measurements on PbSnF_4 with those extracted from NMR line-width analysis. They observed a change in the activation energy for conductivity at approximately 355 K, which they attributed to an orthorhombic to tetragonal phase change. This change was also observed in the NMR data as a second narrowing which began at approximately 300 K. The activation energies obtained from NMR and conductivity of 27 and 30 kJmol^{-1} (0.28 and 0.32 eV respectively) were similar.

3.2 Experimental

3.2.1 Synthesis

In this work two samples of the solid electrolyte PbSnF_4 ($\text{PbSnF}_4\text{_a}$ and $\text{PbSnF}_4\text{_b}$) were examined by relaxation. The samples were synthesised by our collaborators in the group of Dr. Isaac Abrahams at Queen Mary, University of London. Samples were prepared by conventional solid-state methods. Stoichiometric amounts of SnF_2 and PbF_2 were ground as a slurry in methylated spirits using an agate mortar and pestle. After drying, the mixture was sealed in an evacuated pyrex tube and heated in a tube furnace at 523 K for ~18 h. In the case of $\text{PbSnF}_4\text{_b}$ a second processing step was included. The cooled sample was reground as a slurry in methylated spirits and dried at 353 K for 3 h. The dry sample was then resealed in a Pyrex glass tube and heated for a further 18 h at 523 K, before being cooled to room temperature.

3.2.2 Diffraction

X-ray powder diffraction data were collected at room temperature on an automated Philips PW1050/30 X-ray diffractometer, using Ni filtered $\text{CuK}\alpha$ radiation ($\lambda = 1.5418 \text{ \AA}$), in flat plate $\theta/2\theta$ geometry. Data were collected in the range $5\text{-}120^\circ 2\theta$, in steps of 0.02° , with a scan time of 7 s per step. Calibration was with an external Si standard.

Neutron diffraction data were collected on the Polaris diffractometer at the ISIS facility, Rutherford Appleton Laboratory, UK. Data were collected on back-scattering and low angle detectors over the respective time of flight ranges 1.0 to 20 and 0.5 to 20 ms. 200 μA or greater were collected in each case. The samples were contained in cylindrical 11 mm vanadium cans located in front of the back-scattering detectors.

The structure of PbSnF_4 was refined using data in the 2θ range 20 to 120° by the Rietveld method using the GSAS suite of programs. [75] The structure described by Castiglione *et al* [65] was used a starting model for refinement.

3.2.3 NMR

The ^{19}F NMR relaxometry measurements were carried out on a Stellar spinmaster FFC-NMR 2000 relaxometer using pre-polarised and non-polarised sequences. The magnetisation recovery curves were mono-exponential at all fields, at all temperatures for all samples (figure 3.2).

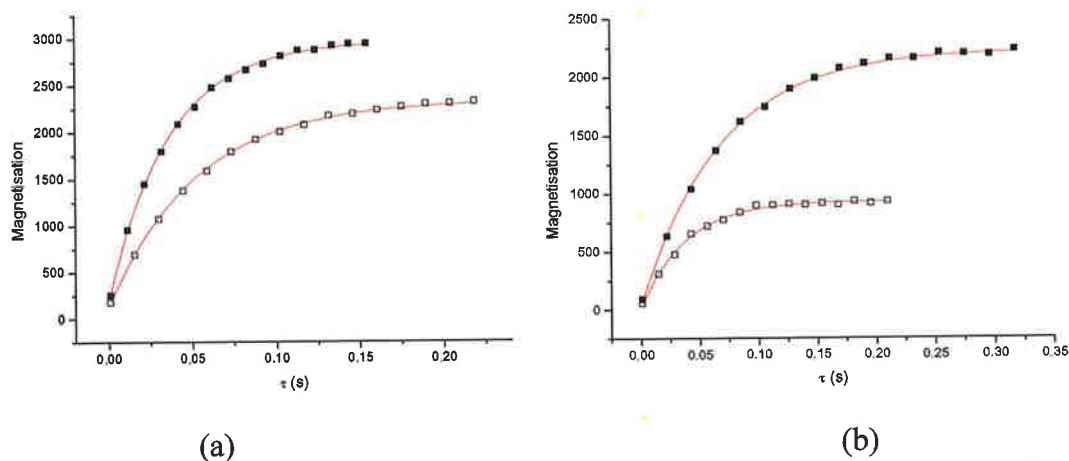


Figure 3.2 Magnetisation recovery curves at 16 MHz for a) $\text{PbSnF}_4\text{_a}$ (■) and $\text{PbSnF}_4\text{_b}$ (□) at 297 K and b) $\text{PbSnF}_4\text{_b}$ at 273 K (□) and 383 K (■) with single exponential fits (-) to the data.

The magnetisation was sampled by summing the intensity in the time range indicated by dashed lines (3-30 μs) in figure 3.3. The extracted T_1 was always insensitive to the interval used for this summation, although extending the interval to longer times (greater than 30 μs) increased the error in T_1 .

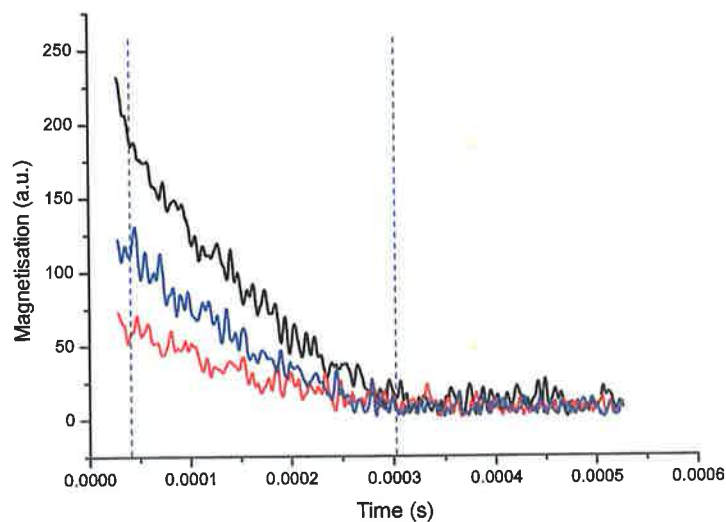


Figure 3.3 FIDs of sample $\text{PbSnF}_4\text{_b}$ at 373 K (-), 348 K (-) and 248 K (-) showing monoexponential decays normalised to one scan.

3.3 Results

3.3.1 Diffraction

The crystallographic and refinement parameters for sample PbSnF₄_b are summarised in Table 3.1. The refined structural parameters are presented in Table 3.2, with the corresponding fitted X-ray diffraction profile in figure 3.4 and the significant contact distances are given in Table 3.3.

Table 3.1 Crystal and refinement parameters for PbSnF₄_b

Chemical formula	PbSnF ₄
Formula weight	401.88
Crystal system	Tetragonal
Space group	<i>P4/nmm</i>
Unit cell dimensions	$a = 4.2158(4) \text{ \AA}$ $c = 11.396(1) \text{ \AA}$
Volume	$202.53(5) \text{ \AA}^3$
Z	2
Density (calculated)	6.592 g cm^{-3}
Absorption coefficient μ (CuK α)	130.13 mm^{-1}
F(000)	336
Sample description	Beige powder
R-factors*	$R_p = 0.1131$, $R_{wp} = 0.0897$, $R_{ex} = 0.0308$, $R_F2 = 0.1405$
Total no. of variables	30
No of profile points used	4999

*For definition of R-factors see reference [75]

Table 3.2 Refined Parameters for PbSnF₄

Atom	Mult.	x	y	z	$U_{iso} (\text{\AA}^2)^a$
Pb	2	0.25	0.25	0.3742(7)	0.003(2)
Sn	2	0.25	0.25	0.8630(9)	0.007(3)
F(1)	4	0.75	0.25	0.237(6)	0.090(9)
F(2)	2	0.75	0.25	0.5	0.090(9)
F(3)	2	0.25	0.25	0.658(6)	0.090(9)

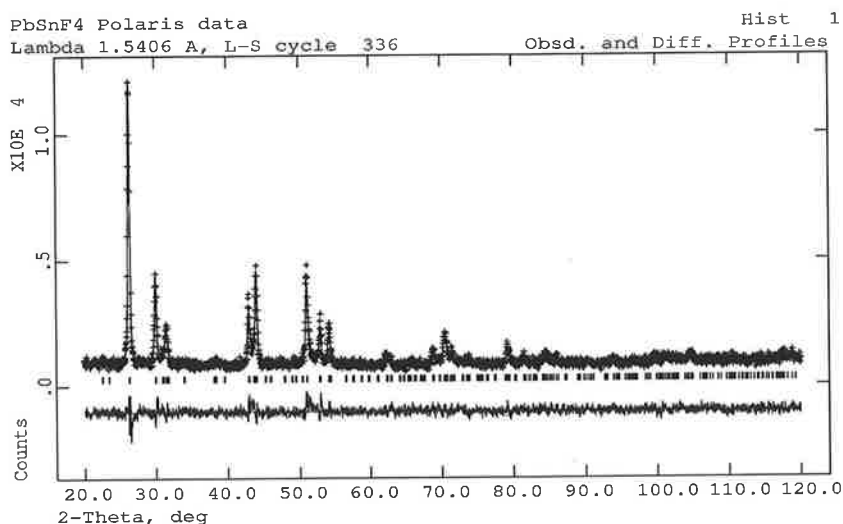


Figure 3.4 Fitted X-ray diffraction profile for PbSnF₄, showing observed (points), calculated (line) and difference (lower) profiles. Reflection positions are indicated by markers.

Table 3.3 Significant contact distances (Å) in PbSnF₄, at 298 K

Pb-F(2)	2.800(6)	Pb-F(4)	3.079(2)
Sn-F(2)	2.321(4)	Sn-F(4)	2.0062(9)
F(1)-F(2)	2.476*	F(2)-F(2)	2.992(1)
F(2)-F(3)	3.237(8)	F(2)-F(4)	2.388(5)

*not refined on basis of scattering; set to ideal position

3.3.2 ¹⁹F NMR

For samples PbSnF₄_a and PbSnF₄_b, approximately 1 cm³ of the sample was placed in a 10 mm ID NMR tube under nitrogen and sealed. A relaxation profile was collected initially at 297 K. The experiment was repeated after a week in order to check stability. Following this period the sample was heated and cooled in order to obtain profiles at different temperatures. After each heating/cooling cycle the profile at 297 K was recorded and was found to show no significant differences to the original profile at this temperature (figure 3.5).

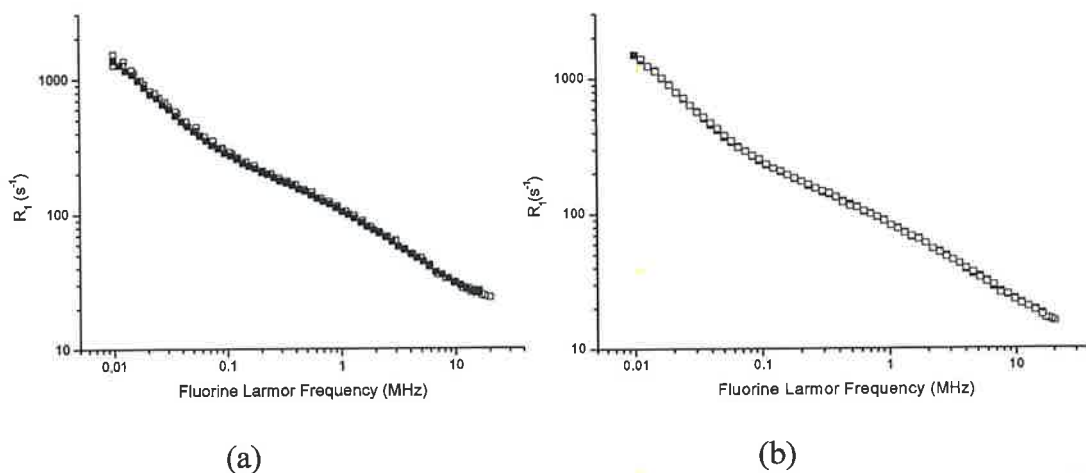


Figure 3.5 ^{19}F relaxation profiles at 297 K, initially (■) and following heating to 423 K (□), showing the stability of (a) sample PbSnF_4a and (b) sample PbSnF_4b .

Relaxation profiles for PbSnF_4a were recorded at a number of temperatures from 243K to 398 K and are presented in figure 3.6.

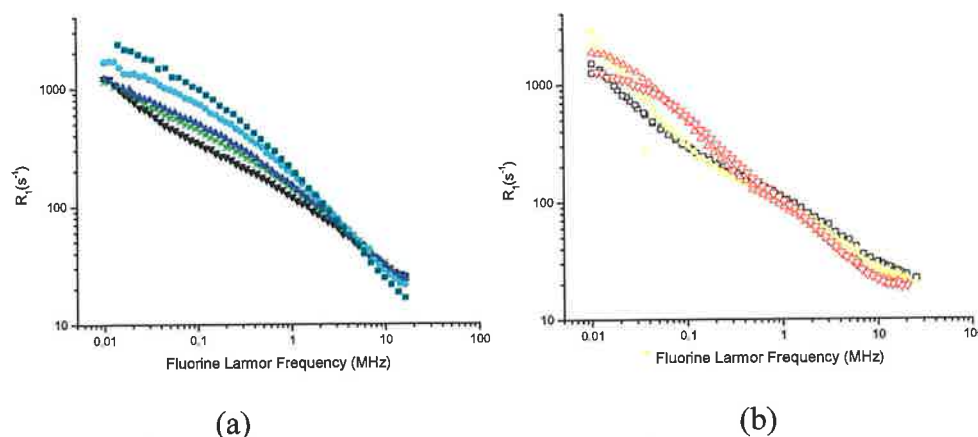


Figure 3.6 ^{19}F NMR data for sample PbSnF_4a , showing the change in relaxation at (a) reduced temperature (■ 243 K, ● 253 K, ▲ 263 K, * 273 K, ▼ 283 K), and (b) elevated temperatures (□ 297 K, ● 323 K, ▲ 373 K and ▼ 398 K).

Relaxation profiles for sample PbSnF_4b were collected at various temperatures from 223 K to 423 K and are presented in figure 3.7. Both samples showed significant dependence of spin-lattice relaxation on temperature across the frequency range 0.01-20 MHz. At low temperatures (< 273 K) it appears there is a single broad dispersion in the measurable frequency range. However, above 273 K a second motion becomes apparent at low field which shifts to higher frequency with increasing temperature

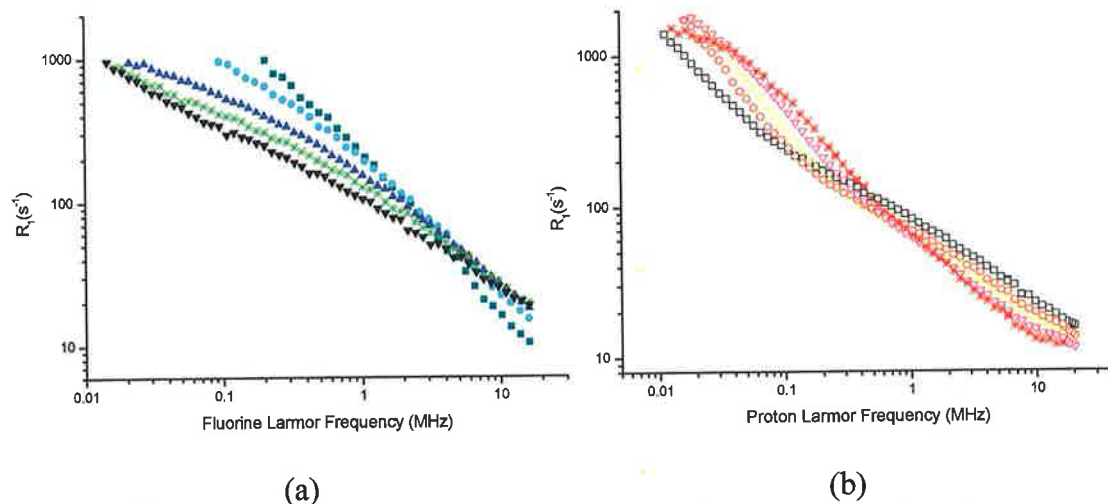


Figure 3.7 ^{19}F NMR data for sample $\text{PbSnF}_4\text{_b}$, showing the change in relaxation at (a) reduced temperature (\blacksquare 228 K, \bullet 248 K, \blacktriangle 263 K, $*$ 273 K, \blacktriangledown 283 K), and (b) elevated temperatures (\square 298 K, \circ 323 K, \triangle 348 K, \triangledown 373 K and $*$ 398 K).

It is possible to measure R_1 values greater than 1000 s^{-1} by field-cycling techniques. However,, given the magnetic field slew rate used, 20 MHz ms^{-1} , the conservative approach of removing all R_1 values in excess of 1000 s^{-1} ($T_1 < 1\text{ ms}$) was adopted to avoid possible systematic errors.

3.4 Discussion

3.4.1 ^{19}F NMR

Comparison of the relaxation profiles for samples $\text{PbSnF}_4\text{_b}$ and $\text{PbSnF}_4\text{_a}$ reveals that while the overall shape of the profiles is similar the curves are non-superimposable at all temperatures. Both samples exhibit small amounts of phase impurity caused by unreacted SnF_2 . $\text{PbSnF}_4\text{_b}$ exhibits higher purity (c. 5% phase impurity) than sample $\text{PbSnF}_4\text{_a}$ (c. 9% phase impurity) from diffraction measurements. It is thought that the second phase is a closely related Pb-deficient phase.

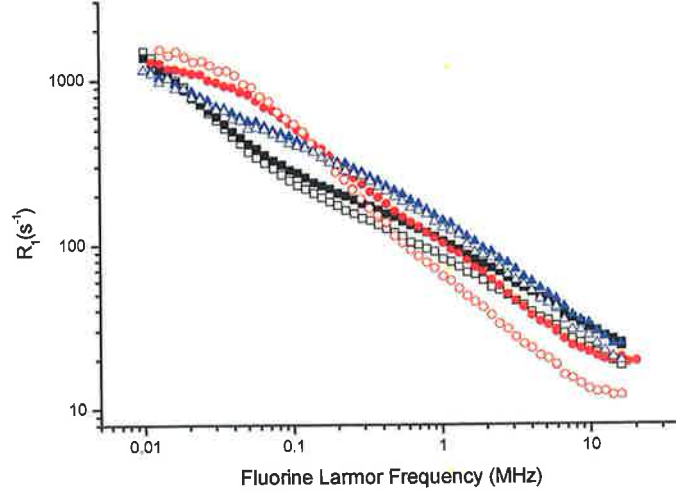


Figure 3.8 ^{19}F relaxation profiles of samples $\text{PbSnF}_4\text{_a}$ and $\text{PbSnF}_4\text{_b}$ at 273 K (■,□), 297 K (●,○) and 398 K (▲,△).

3.4.1.1 Multi-Lorentzian model

The observation of mono-exponential relaxation at all frequencies and temperatures strongly supports the assumption that the measured relaxation rates are representative of the bulk material and that all motional fluoride ions are at a common spin temperature due to fast spin diffusion. [52] In analysing the data, it was assumed that the relaxation is driven by modulation of the homonuclear dipolar ^{19}F - ^{19}F interactions arising from anion dynamics. Calculations based on the crystallographic data show that, given the low isotopic abundance (7.7, 8.6 and 22.10 % for ^{117}Sn , ^{119}Sn and ^{207}Pb respectively) and low gyromagnetic ratios of these nuclei, the heteronuclear ^{19}F - ^{117}Sn , ^{19}F - ^{119}Sn and ^{19}F - ^{207}Pb interactions are too weak to contribute significantly to the observed fast ^{19}F relaxation. The Bloembergen, Purcell and Pound [BPP] theory of relaxation in polycrystalline solids can therefore be applied and the spin-lattice relaxation rate, R_1 , is given by:

$$\frac{1}{T_1} = \beta_{FF} \left[\frac{\tau_c}{1 + \omega_0^2 \tau_c^2} + \frac{4\tau_c}{1 + 4\omega_0^2 \tau_c^2} \right] \quad [3.1]$$

Where ω_0 is the ^{19}F angular resonance frequency and τ_c is the correlation time. β_{FF} is the dipolar coupling constant for the ^{19}F - ^{19}F interactions, which is given by;

$$\beta_{FF} = \frac{3}{5} \gamma_F^4 \hbar^2 \mu_0 (\mu_0 + 1) r_{FF}^{-6} \quad [3.2]$$

μ_0 is the magnetic field constant, γ_F is the gyromagnetic constant for the ^{19}F nucleus, \hbar is Planck constant divided by 2π , r_{FF} is the fluoride ion jump distance.

It is possible to fit the NMR data successfully using spectral density functions based on a multi-Lorentzian or a modified Lorentzian model using the software routine developed by Halle *et al.* [76] At intermediate temperatures it was possible to fit the data to a model comprising of three Lorentzians. This can be interpreted as indicating that there are three independent fluoride motions and is consistent with the diffraction analysis which shows that presence of three crystallographically distinct fluoride ion sites. However, at higher (> 350 K) and lower (< 263 K) temperatures, merit function analysis demonstrated that only two Lorentzians are required to fit the data.

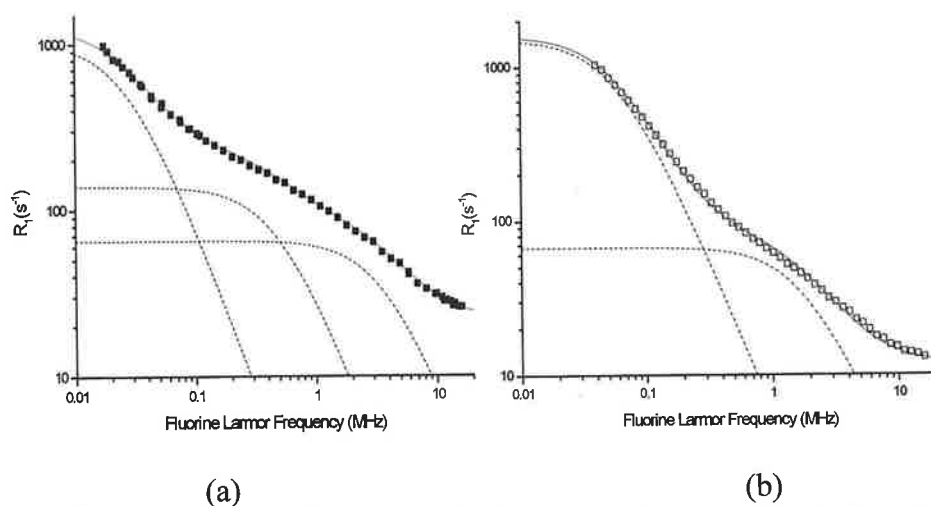


Figure 3.9 ^{19}F relaxation profile of sample PbSnF_4_b at (a) 297K (\blacksquare) fit with a three Lorentzian model (-) and (b) 373K (\square) fit with a two-Lorentzian model (-). The dashed lines are the contributions from each Lorentzian.

Correlation times (τ_c) and dipolar coupling coefficients (β) were extracted for each Lorentzian spectral density contribution and the results for PbSnF_4_b are summarised in Table 3.4.

Table 3.4 Table of correlation times and β values from the multi Lorentzian fits of relaxation profiles of PbSnF_4 at multiple temperatures.

Temp (K)	β_1 ($\times 10^8 \text{ s}^{-2}$)	τ_{c1} ($\times 10^{-8} \text{ s}$)	β_2 ($\times 10^8 \text{ s}^{-2}$)	τ_{c2} ($\times 10^{-8} \text{ s}$)	β_3 ($\times 10^8 \text{ s}^{-2}$)	τ_{c3} ($\times 10^{-8} \text{ s}$)
228			32.90	32.70	37.20	3.93
238			30.20	33.70	39.80	3.71
248			21.80	44.00	41.80	4.28
263	3.50	208.00	15.20	31.90	34.80	2.87
273	2.30	449.00	10.70	23.80	30.20	2.67
283	2.33	459.00	8.29	25.20	25.70	2.63
297	3.05	498.00	5.27	21.60	19.80	2.57
308	5.46	433.00	3.60	22.30	16.00	2.91
323	7.44	412.00	3.21	23.40	14.50	3.31
338	6.75	283.00	2.69	23.30	13.40	3.46
348	8.11	180.00			13.70	4.97
353	8.21	167.00			13.50	5.08
358	9.24	164.00			12.70	5.29
373	9.94	109.00			12.10	5.18
383	10.70	94.20			11.40	5.40
398	11.60	58.80			12.80	5.68

The three independent spectral density functions can be classified as fast (τ_{c3}), intermediate (τ_{c2}) or slow (τ_{c1}) depending on their relative correlation times. The temperature dependence of β is represented graphically in figure 3.10. The β value corresponding to a fast process, β_3 , is present at all temperatures. However, the contribution from the slowest component, β_1 , decreases with decreasing temperature until it becomes insignificant and is no longer required to fit the data at approximately 263K. Conversely, the contribution from the intermediate component, β_2 , decreases with increasing temperature until it disappears at approximately 358K. In the temperature range where both contributions are a significant fraction of the total spectral density the data can be fitted to a three-Lorentzian model.

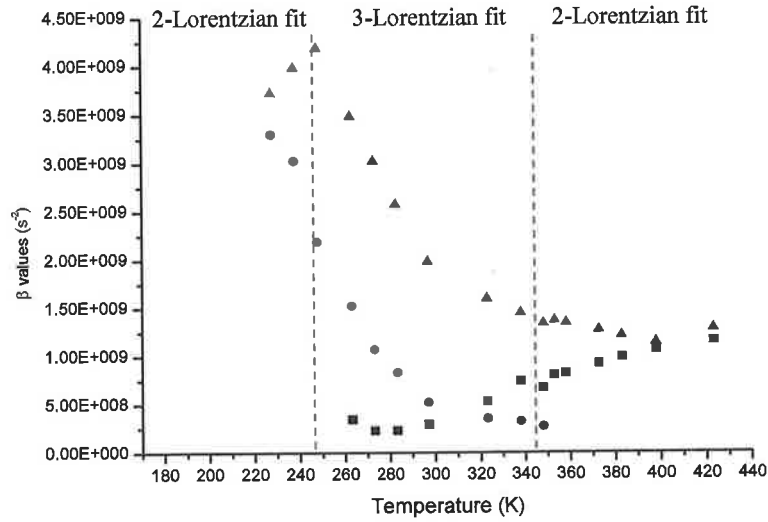


Figure 3.10 Temperature dependence of the β values from the multi Lorentzian fits of ^{19}F NMR profiles of $\text{PbSnF}_4\text{-b}$ showing the two-Lorentzian to three-Lorentzian crossover.

The multi-Lorentzian or model free approach assumes that the motions associated with the three spectral density functions are independent. If this assumption is correct then an Arrhenius temperature dependence of the rate ($1/\tau_c$) is expected (Eq.1)

$$\tau_c^{-1} = \tau_0^{-1} \exp\left(\frac{-E_{Act}}{RT}\right) \quad [3.3]$$

The Arrhenius law predicts a straight line dependence of the $\ln(\tau_c^{-1})$ as a function of inverse temperature, with a negative slope proportional to the activation energy of the process. However,, as can be seen in figure 3.11 non-Arrhenius behaviour is observed for all three processes. This suggests that a multi-Lorentzian model is not appropriate in this case.

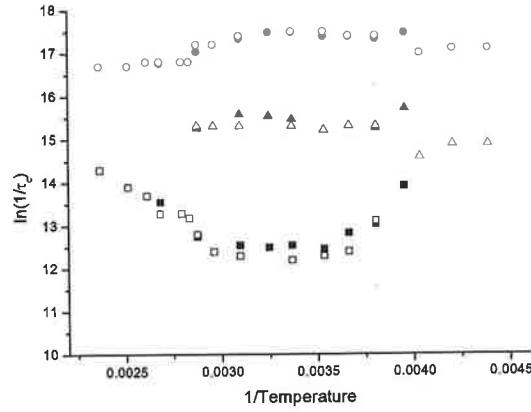


Figure 3.11 Arrhenius plot of $\ln(\tau_c^{-1})$ against inverse temperature from the three-Lorentzian fits (lor1 (■□), lor2 (▲△), and lor3 (●○)) of relaxation profiles of both PbSnF_4_a and PbSnF_4_b respectively.

3.4.1.2 Cole-Cole model

The Cole-Cole model is based on a stretched Lorentzian function with another parameter which is taken to be the degree of correlation of the relaxing system. The Cole-Cole function is given by:

$$T_{1d}^{-1} = \beta_{FF} \left(\left(\frac{2}{\omega} \sin\left(\frac{\sigma\pi}{2}\right) \left[\frac{(\omega\tau_c)\delta}{1 + (\omega\tau_c)^{2\delta} + \left(2 \cos\left(\frac{\delta\pi}{2}\right)(\omega\tau_c)^\delta}\right)} \right] \right) + \left(\frac{1}{\omega} \sin\left(\frac{\sigma\pi}{2}\right) \left[\frac{(2\omega\tau_c)\delta}{1 + (2\omega\tau_c)^{2\delta} + \left(2 \cos\left(\frac{\delta\pi}{2}\right)(2\omega\tau_c)^\delta}\right)} \right] \right) \right) \quad [3.4]$$

Where τ_c is the correlation time for fluoride motion, ω is the angular resonance frequency for ^{19}F and δ is the degree of correlation. β_{FF} is the dipolar coupling constant for the relaxation of the dipolar interactions of ^{19}F - ^{19}F . This is related to the fluoride jump distance by equation 3.2.

Attempts were made to fit the data to a spectral density model based on a single Cole-Cole function but this was only successful below 273 K. The 297 K data was then fit to a similar model consisting of two Cole-Cole functions. By adopting this approach it was possible to fit the profiles at all temperatures, which indicates that there are two motional processes on different timescales driving relaxation. However, the δ -values extracted for the slower process were greater than one (in the range 1.08-1.90) which is not physically realistic. The inflection point at about 0.08 MHz apparent in figure 3.12 strongly supports the interpretation that there are two processes, but a better model for the spectral density of the slow motion is required.

3.4.1.3 Cole-Cole and Lorentzian model

It was then assumed that the faster motion had a Cole-Cole form and the slower motion had a Lorentzian form. It was possible to fit the data from all of the temperatures using this approach. However,, at lower temperatures (<273 K), the spectral density contribution from the slower motion moved out of the measurable frequency window and the data can be fitted to a single Cole-Cole function.

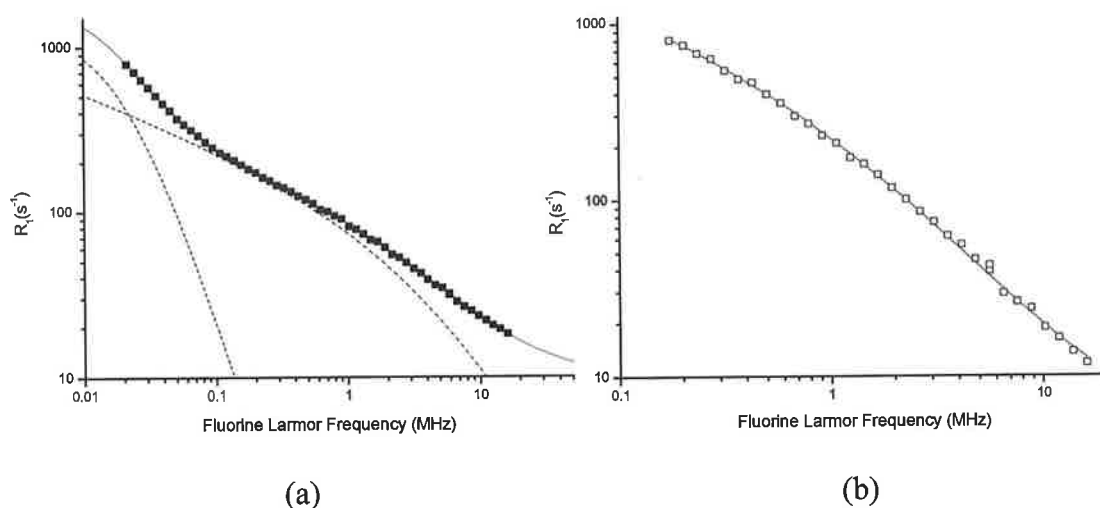


Figure 3.12 ^{19}F NMR profiles of sample PbSnF_4b at (a) 297 K (■) fitted with a Cole-Cole/Lorentzian spectral density function (-) and (b) 238 K (□) fitted with a Cole-Cole spectral density function (-). The dashed lines are the individual contributions from the Cole-Cole and Lorentzian components.

Table 3.5 Table of correlation times, β values, and δ -values from Cole-Cole/Lorentzian fits of relaxation profiles of PbSnF_4b at multiple temperatures.

Temp (K)	$\beta_{(\text{cole})}$ ($\times 10^8 \text{ s}^{-2}$)	$\tau_c (\text{cole})$ ($\times 10^{-7} \text{ s}$)	$\delta_{(\text{cole})}$	$\beta_{(\text{lor})}$ ($\times 10^8 \text{ s}^{-2}$)	$\tau_c (\text{lor})$ ($\times 10^{-7} \text{ s}$)
228	38.00	1.15	0.54		
238	31.60	0.84	0.62		
248	30.80	0.56	0.61		
263	21.20	0.46	0.67		
273	18.40	0.34	0.67	1.38	200.00
283	16.50	0.25	0.65	1.38	66.60
297	13.80	0.19	0.68	3.03	50.10
308	10.50	0.27	0.74	4.39	30.70
323	14.90	0.11	0.65	6.98	40.90
338	9.80	0.23	0.73	8.71	25.70
348	10.60	0.18	0.70	8.48	21.60
353	13.10	0.13	0.65	11.00	23.20
358	13.80	0.11	0.61	10.30	21.50
373	20.20	0.04	0.52	9.27	14.40
383	22.90	0.02	0.37	7.86	13.30
398	26.20	0.01	0.32	7.04	8.80

Assuming that the correlated and uncorrelated motions are independent, the two processes can be shown to be thermally activated as they conform to the Arrhenius law (figure 3.13).

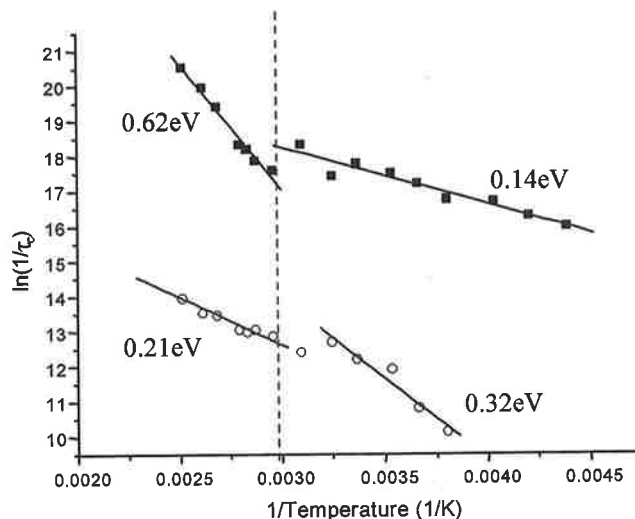


Figure 3.13 Arrhenius plot of dynamic parameters extracted from the two-process model analysis of the NMR data for sample PbSnF₄_b showing the rates extracted for the Cole-Cole (■) and Lorentzian (○) processes. The solid curves are linear fits to the data. The activation barriers are included. The dashed line indicates the temperature at which the fluoride sublattice disorder increases, ~340 K. [29]

Several authors have reported phase transitions at ~345 K in PbSnF₄. Reau and Chadwick [61] suggested a transition from a monoclinic (α) to a tetragonal (β) phase, with a discontinuity in the conductivity temperature curve at around 350 K. Kanno attributed the discontinuity in conductivity to a diffuse phase transition. [67] The Arrhenius plot of the rate data from our NMR analysis (figure 3.13) shows a similar discontinuity in both the Cole-Cole (fast) and Lorentzian (slow) processes. The Arrhenius activation energies and pre-factors obtained from the NMR data above and below the discontinuity temperature (T_c), are given in Table 3.6.

Table 3.6 Dynamic information from Arrhenius analysis of the PbSnF_4 _b rate data from the two-process model

	E_{act} (kJmol^{-1})	E_{act} (eV)	τ_0^{-1} (s^{-1})
Fast, above T_c	59(3)	0.62(3)	$5.29(3) \times 10^{16}$
Fast, below T_c	13(1)	0.14(1)	$1.15(1) \times 10^{10}$
Slow, above T_c	20(2)	0.21(2)	$4.61(6) \times 10^8$
Slow, below T_c	30(3)	0.32(3)	$4.46(2) \times 10^{10}$

In a previous study, by Ahmad *et al* [74], on the temperature dependence of conductivity of PbSnF_4 , the DC conductivity showed a gradual change in slope at around 350 K with $E\sigma = 30 \text{ kJmol}^{-1}$ and $E\sigma = 22 \text{ kJmol}^{-1}$ at high and low temperature respectively.

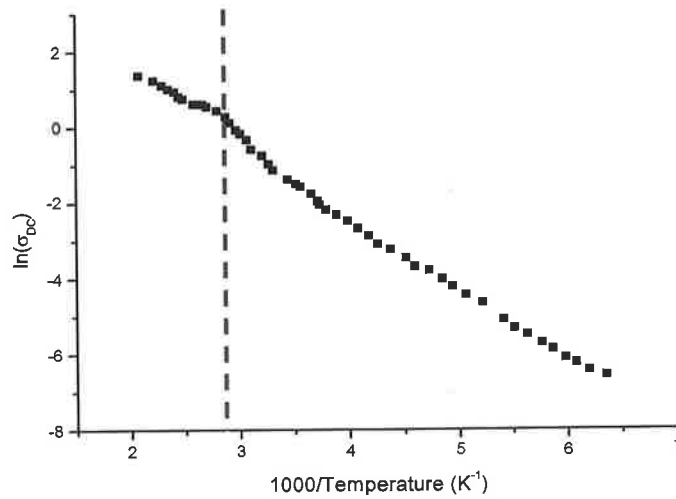


Figure 3.14 Arrhenius plot of bulk dc conductivity against inverse temperature, redrawn from [29].

The activation energies obtained for the slow fluoride motion, E_{NMR} , of $30(3) \text{ kJmol}^{-1}$ and $20(2) \text{ kJmol}^{-1}$ above and below 340 K, respectively, show very good agreement with the reported barriers to conductivity. This result strongly suggests that the slower motion observed on a microscopic level by NMR is the process that limits the bulk conductivity. This assignment also implies that the faster motion, observed by NMR, does not correspond to a translational motion of anions through the lattice, it must therefore be a local exchange process.

The Arrhenius pre-factor, or attempt frequency, derived from the NMR analysis, for the slower (Lorentzian) motion in the ordered-lattice temperature range is $\tau_0^{-1} = 4.46 \times 10^{10} \text{ s}^{-1}$. This is slightly lower than the rate of vibration of an ion trapped in a normal lattice site (10^{12} s^{-1}). [29] However, low pre-factors are often observed in superionic materials, and there has been much speculation on their causes. [29] Significantly, the pre-factor is smaller, by more than three orders of magnitude, than that expected for the generation of a Frenkel defect. This strongly suggests that even when the fluoride lattice is relatively ordered, there are large numbers of vacancies available, a situation consistent with the presence of a faster independent process generating the required vacancies. Above 350 K, where the fluoride lattice is disordered, the pre-factor for the slower process is smaller, $\tau_0^{-1} = 4.69 \times 10^8 \text{ s}^{-1}$. This may be due to additional broadening of the potential well for anion dynamics, associated with an increase in disorder. The barrier to this slower motion is lower as might be expected. The pre-factor for the faster (Cole-Cole) motion in the ordered-lattice temperature range, $\tau_0^{-1} = 1.15 \times 10^{10} \text{ s}^{-1}$, is also close to the timescale expected for anion motion into a pre-existing vacancy. Above 350 K, the pre-factor for this motion is much larger at $\tau_0^{-1} = 5.29 \times 10^{16} \text{ s}^{-1}$ and the activation energy is higher. This strongly suggests that, for the non-translational fluoride exchange process, the onset of fluoride disorder is associated with the requirement for defect generation. [29]

The degree of correlation, the δ value, is extracted from the Cole-Cole spectral density component. When plotted against inverse temperature it shows a discontinuity at around 340 K. Below this temperature the δ value appears to be weakly temperature dependent (figure 3.15). However, the relaxation data can also be fitted successfully by fixing the δ value to the average value, 0.68, in this region without significantly altering the extracted rate at a given temperature. Above 340 K different behaviour is observed and the δ value decreases with temperature, indicating an increase in correlation. In this range it is not possible to fit the data by assuming a constant δ value, this is indicative of an increase in the extent of correlation in the motional process.

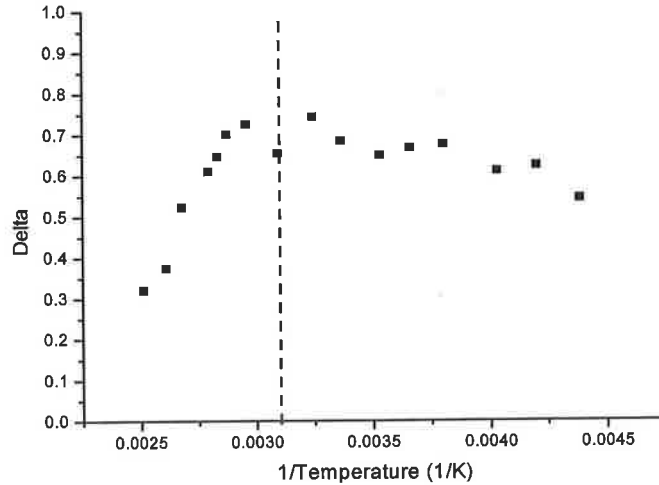


Figure 3.15 Plot of the δ -value against inverse temperature (■), extracted from the Cole-Cole part of the multi-process model fits, showing the discontinuity at ~ 340 K as a dashed line.

The β -value is proportional to the inverse sixth power of the fluoride ion jump distance, r_{FF} . The jump distances were calculated from the relaxation analysis for each motion and are compared to the distances from diffraction analysis [65] at various temperatures in figure 3.16.

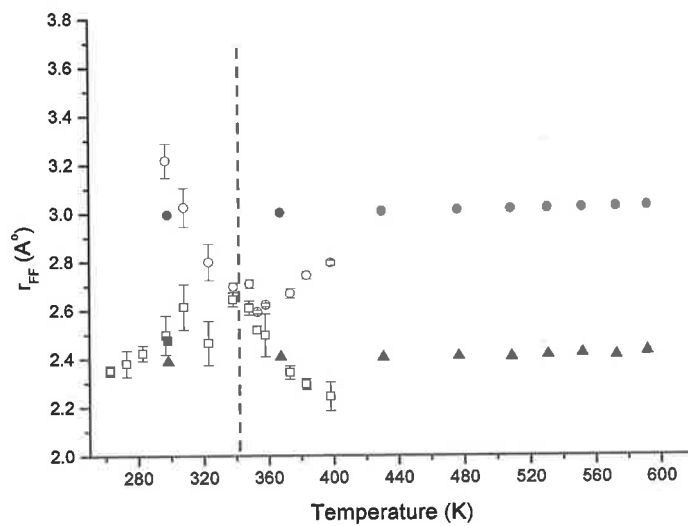


Figure 3.16 Comparison of the r_{FF} values of the fast process (□) and slow process (○) derived from the NMR data, with the fluorine-fluorine contact distances for F2-F1 (■), F2-F2 (●) and F2-F4 (▲) from the published diffraction study. [65]

The r_{FF} value for the slower uncorrelated motion is 3.0 ± 0.2 Å, in the low temperature range, and reduces to 2.7 ± 0.2 Å above the discontinuity. For the faster

motion, the r_{FF} value is 2.4 ± 0.2 Å over the full temperature range. By comparing the crystallographic and NMR data recorded at 298 K, the slow (Lorentzian) motion is assigned to F2-F2 in-plane hops. As the temperature increases the r_{FF} values decrease to a value between the F2-F2 and F2-F4 crystallographic contact distances. Analysis of the neutron diffraction data demonstrated increased anion density linking the F2 and F4 sites with increased temperature, [65] indicative of increased disorder between these sites.

From the r_{FF} values at 298 K, the fast (Cole-Cole) motion can be assigned to F2-F1 out-of-plane hops or possibly F2-F4 in plane motion. The low activation energy and pre-factor for this motion indicate that this motion does not require the formation of a defect. This is consistent with the motion being into vacant F1 sites. As the temperature increases, both the activation energy and the extent of correlation of the motional process increase, indicating partial occupancy of F1. This is consistent with observations from diffraction of detectable anion density on the F1 sites at high temperature (> 700 K). Indeed low F1 occupancies are expected, as the F1 residence time would be very short, given that the barrier to reverse F1-F2 hops must be significantly lower than for F2-F1 hops.

The good agreement between the extracted fluoride jump distance and the crystallographic structure, suggests that the fluoride atoms in the F3 sites are not part of the dynamic fluoride lattice, and that our experiments are not sensitive to their relaxation. It is assumed the T_2 of this rigid sub-lattice is very short, so the magnetisation contribution from F3 dephases completely during the short switching time required for field stabilisation at the detection field. In BaSnF_4 the timescale for exchange between the mobile and static lattices was shown by NMR [73] to be milliseconds. Processes on this ultra-slow timescale fall outside the dynamic range of the field-cycling experiment.

3.4.2 Proposed Mechanism

In summary, a consistent picture of the fluoride dynamics emerges from the relaxometry study as show in figure 3.17. There are two processes on quite different timescales modulating the ^{19}F relaxation times in the accessible temperature and frequency range. There is a slower uncorrelated motion and a faster correlated motion. The barriers to both of these motions change at ~ 340 K which matches a transition

reported in published conductivity data. The barrier to the faster motion increases while the barrier to the slower motion decreases, indicating an increase in disorder in the anion layer.

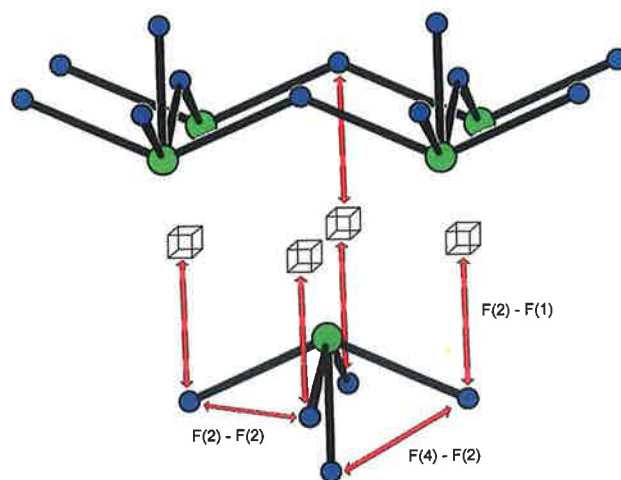


Figure 3.17 Lead tin layer of PbSnF₄ showing the proposed motion of F2-F2 and F2-F4 translational motions and F2-F1 local hops.

In the low temperature regime, the uncorrelated motion may be unambiguously assigned to F2-F2 translational motions on the basis of the β values at room temperature. The prefactor associated with this motion at $4.46 \times 10^{10} \text{ s}^{-1}$ is of the order expected for an anion motion into a pre-existing vacancy. In this temperature range, the β values for the faster correlated motion are consistent with both the F2-F1 and F2-F4 jump distances. However,, an F2-F4 jump would require the formation of a Frenkel defect. The prefactor for this motion is $1.15 \times 10^{10} \text{ s}^{-1}$, which is also in the expected range for motion of an anion into a pre-existing vacancy. However,, it is not consistent with an F2-F4 jump, so this process can be assigned to F2-F1 fluoride exchange. The occupancy of the F1 site remains low due to F1-F2 return jumps, which are expected to be faster than F1-F2 due to the relative energies of these sites. The predicted short residence time for fluoride ions on the F1 site is consistent with the diffraction data which only showed detectable occupancy of this site at high temperature. [65] The F2-F1 motion gives rise to vacancies on the F2 site through formation of an anion Frenkel defect, and hence low pre-factors are observed for the slower motion

At ~340 K a clear change is observed for both motional processes. The faster correlated process shows an increase in activation energy and the prefactor for this process increases to $5.29 \times 10^{16} \text{ s}^{-1}$ due to increased occupancy of F1 necessitating the formation of a Frenkel defect on a significant proportion of the F1 sites, prior to an F2-F1 jump.

In the high temperature regime, the activation energy for the slower Lorentzian process decreases and a lower prefactor value of $4.69 \times 10^8 \text{ s}^{-1}$ is observed. This motion is still associated with the F2-F2 jump, however at these temperatures there is a significant concentration of vacancies of the F2 site which facilitates F2-F4 hops. Evidence for this change is provided by the jump distance for this process which decreases to a value intermediate between F2-F2 and F2-F4. F2-F4 jumps are consistent with the observation of partial occupancies of F2 and F4 sites at elevated temperatures in the diffraction data, [65] which was interpreted as being due to shared anion density. This is also consistent with a reduced pre-factor as observed in the NMR analysis. Thus the observed transition in dc conductivity at 350K, to a phase of lower activation energy arises from F2-F4 mixing of the translational anion motions. The disorder arises due to an excess of F2 vacancies, driven by an increasing number of rapid correlated F2-F1 hops.

It is possible to calculate the charge carrier diffusion co-efficient, D , and hence the 'NMR' conductivity, σ_{NMR} , from the mean residence times, τ_c , and the fluoride jump distances, r_{FF} , extracted from the NMR fits, using equations 3.5a and 3.5b:

$$D = \frac{r_{\text{FF}}^2}{n\tau_c} \quad [3.5a]$$

$$\sigma = \frac{Ne^2D}{k_B T} \quad [3.5b]$$

where N is the density of mobile charge carriers, e is the effective charge, T is the absolute temperature and n is the number of possible sites to which the charge carrier may hop. However, in PbSnF_4 there are in effect multiple anion jump distances, as the increase in r_{FF} with increasing temperature is as a result of F2-F2 and F2-F4 mixing. "NMR" diffusion coefficients and conductivities, are dependent on the square of the jump distance, and hence are very sensitive to the value used. So this approach is probably not appropriate for this material.

3.4.3 Assessment of the Mechanism

3.4.3.1 Sample purity

Interpreting the relaxation data from a sample with a greater extent of phase impurity, $\text{PbSnF}_4\text{_a}$, with the same two-process model yields very similar results. The similarity of the extracted rate information for the two samples indicates that phase purity is not required to extract meaningful dynamic information. It is likely that the second phase does not contribute significantly to the conductivity, fluoride dynamics or NMR relaxation. Such a phase is likely to contain static fluoride ions only. Indeed our studies on the related salt BaF_2 indicate that the ^{19}F T_2 is extremely short. The magnetisation of the static fluoride component in these samples probably lies outside the portion of the FID sampled for the determination of T_1 .

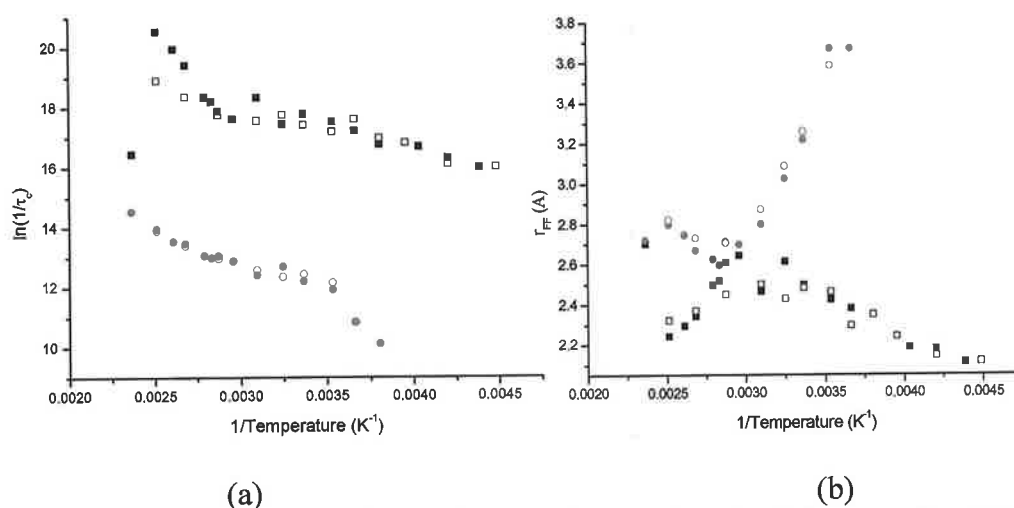


Figure 3.18 Arrhenius plot of (a) τ_c^{-1} and (b) r_{FF} determined for samples $\text{PbSnF}_4\text{_a}$ (○, □) and $\text{PbSnF}_4\text{_b}$ (●, ■), from the analysis of the NMR data using the two-process model.

3.4.3.2 Extended field range

Both samples were also examined at higher field using a reconditioned Bruker WP80 NMR variable field magnet in conjunction with the FFC-NMR spectrometer. Relaxation profiles were extended up to 80 MHz at a number of temperatures above and below the transition temperature. These were then fitted using the same spectral density model. The τ_c and β values obtained were similar to those obtained over the reduced frequency range. This confirms that there is no faster motion in the accessible frequency range (< 100 MHz). As the WP80 could not be used over the entire temperature range, the high frequency data has been omitted from the analysis.

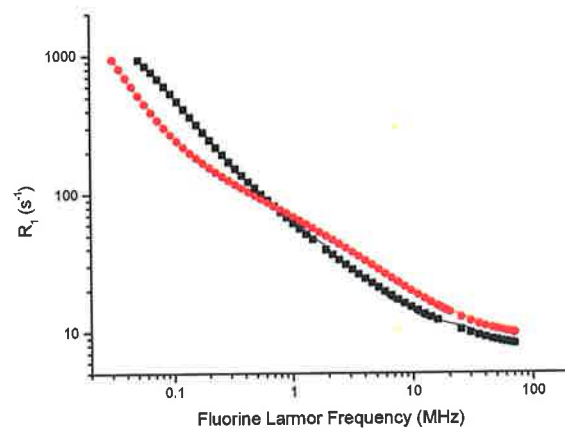


Figure 3.19 Extended range ^{19}F NMR profiles of $\text{PbSnF}_4\text{-b}$ at 323 K (■) and 393 K (●). The solid lines are fits to a Cole-Lorentzian spectral density function.

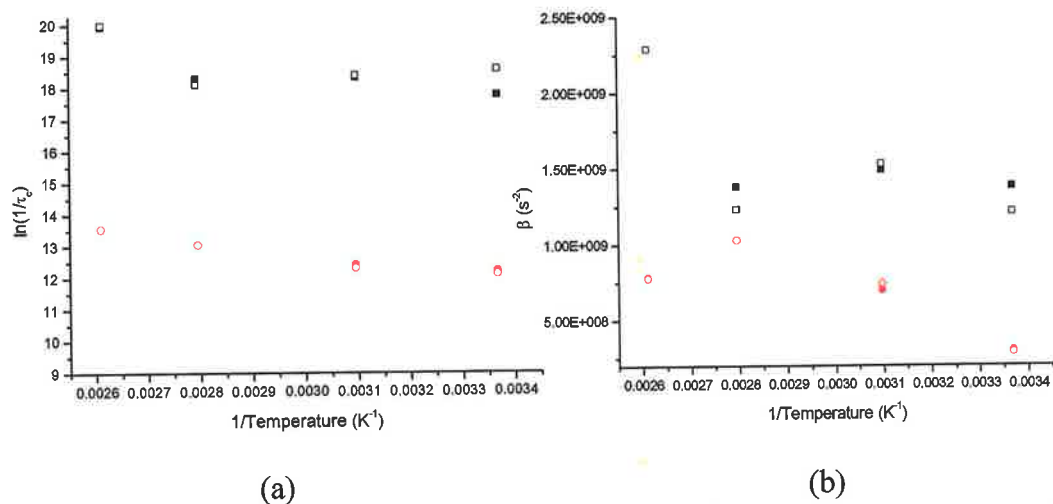


Figure 3.20 (a) $\ln(1/\tau_c)$ and (b) β values as a function of inverse temperature extracted from Cole-Lorentzian spectral density model of the NMR profiles of $\text{PbSnF}_4\text{-b}$ using normal (■, ●) and extended frequency (□, ○) ranges.

3.5 Conclusion

The aim of this study was to examine whether ^{19}F relaxometry could add to the understanding of the mechanism of conductivity in this important material. In this we were successful; from our NMR analysis we can propose a detailed mechanism for conduction that is consistent with the diffraction and conductivity measurements.

The data conformed very well to a model comprising a Cole-Cole spectral density function for fast correlated motions and a Lorentzian spectral density function for a slower process in the fluoride sublattice. Using the fluoride jump distances and

Arrhenius prefactors extracted from the analysis, the faster motion was assigned to non-translational fluoride jumps from the F2 position to the vacant F1 sites. The slower motion was assigned to F2-F2 translational motion which, at higher temperatures, was mixed with F2-F4 jumps. The proposed mechanism indicates that conductivity in PbSnF_4 is due to translational diffusion in the F2-F4 plane which is assisted by fast F2-F1 hops creating vacancies in the F2 sublattice which act as Frenkel defects. The quenching of the highly disordered lattice, associated with a loss of mobility through the F4 sites, results in conductivity of approximately 0.25 Scm^{-1} , which otherwise would be closer to 1 Scm^{-1} .

Future work could involve investigation into the fluoride conduction mechanisms in related fluoride ion conductors such as BaSnF_4 , which has a similar structure, and PbF_2 , which has a less complex tetrahedral fluorite structure. The possibility of gaining similar insights into superprotonic conductors prompted the study which is presented in the next chapter. Other possibilities including studies of conducting lithium solid electrolytes could be of tremendous scientific importance, as many of the electrolytes used today are based on lithium. However, such studies may be beyond the capabilities of the current generation of field-cycling relaxometers, for which poor sensitivity remains a significant problem.

Chapter 4 – Superprotonic Conductors

4.1 Introduction

4.1.1 Fuel Cells

Fuel cells are clean and efficient electrochemical energy conversion devices which have garnered much attention in recent years as the search for clean renewable energy storage and transformation technologies intensifies. However,, the development of fuel cells and batteries is currently restrained by materials limitations especially those associated with the electrolyte. The solid acid CsHSO₄ has been known for a number of years as a proton conductor but was not applied to fuel cell technology, due to its water solubility and ductile mechanical properties. Recently Haile and co-workers demonstrated that operation at a slightly elevated temperature of ~400 K ensured that water was present only as steam which is harmless to the electrolyte. [32] Elevated temperatures have several other advantages; the activity of the catalysts increases, the excess heat is useful in practical devices and less pure fuels can be used. [77] Since its initial success the range of Cs-based solid acids with potential for use in fuel cells has grown to include CsH₂PO₄ [78] and a group of caesium mixed sulphate/phosphate materials. [79-82]

4.1.2 Solid Acids – Cs_x(HSO₄)_y(H₂PO₄)_{x-y}

Solid acids are a unique class of compounds which are intermediate in character between acids and salts and are formed by the introduction of acid protons into a crystalline salt, for instance CsHSO₄:



A number of mixed sulphate-phosphate solid acids in the Cs_x(HSO₄)_y(H₂PO₄)_{x-y} series have been developed. These materials have a well defined crystal structure and consist of a cation sublattice and an anion sublattice consisting of tetrahedral oxyanions such as phosphate or sulphate. Above a transition temperature, T_c, the value of which varies depending on stoichiometry and structure, these materials transform into a superprotonic phase with conductivity two or three orders of magnitude greater than below T_c.

Table 4.1 Physical properties of materials in the CsHSO₄-H₂PO₄ series

	T _c (K)	Decomp. (K)	Structure (RT)	Structure (HT)	H-bond network	E _{act} (kJ/mol)
CsHSO ₄ ^[83]	415	473	monoclinic	tetragonal	1-D	6.2
Cs ₂ (HSO ₄)(H ₂ PO ₄) ^[84]	358	458	monoclinic	cubic	2-D	8.3
Cs ₃ (HSO ₄) ₂ (H ₂ PO ₄) ^[81]	377	421	monoclinic	cub/tetr	2-D	10.7
Cs ₅ (HSO ₄) ₃ (H ₂ PO ₄) ₂ ^[85]	369	453	monoclinic	cubic	3-D	9.2
Cs ₆ (HSO ₄) ₃ (H ₂ PO ₄) ₄ ^[86]	374	473	cubic	cubic	3-D	15.1
CsH ₂ PO ₄ ^[84]	503	476	monoclinic	cubic	2-D	11.3

The material studied in this work, Cs₆(HSO₄)₃(H₂PO₄)₄, has unusual stoichiometry and crystal structure. As a result it is an anomalous material in the sequence. As written this material is not charged balance and hence, can also be represented by the formula Cs₆(H₂SO₄)₃(H_{1.5}PO₄)₄. This may account for the poorly defined structure from diffraction.

4.1.2.1 Low Temperature Structure

Most of the CsHXO₄ based solid acids possess similar structures at room temperature. For the simplest materials in this class, CsHSO₄ and CsH₂PO₄, the anion sublattice consists of zigzag rows of hydrogen bonded tetrahedra, while the cation sublattice is similarly formed of zigzag rows of Cs⁺¹ atoms. [87] In CsH₂PO₄ the two hydrogen atoms in the phosphate groups result in the tetrahedra being crosslinked giving a three-dimensional hydrogen-bond network compared to the one-dimensional network of CsHSO₄.

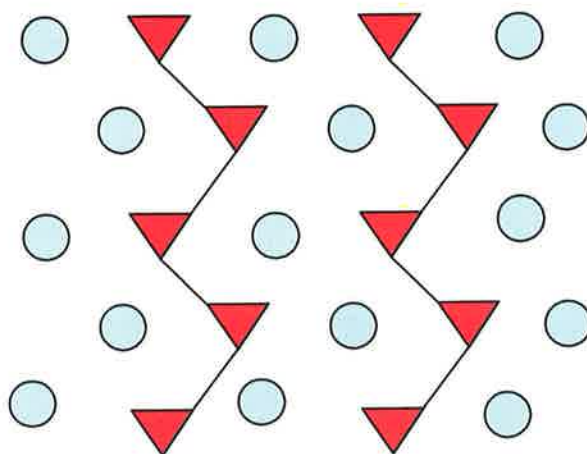


Figure 4.1 Schematic representation of the basic structure of room temperature simple Cs-based solid acids; HSO_4 (\blacktriangledown) tetrahedra linked by hydrogen bonds (-) in a one-dimensional network, caesium atoms (\bullet).

Very similar low temperature structures are formed across this class of materials irrespective of the stoichiometry. $\text{Cs}_2(\text{HSO}_4)(\text{H}_2\text{PO}_4)$, $\text{Cs}_3(\text{HSO}_4)_2(\text{H}_2\text{PO}_4)$, and $\text{Cs}_5(\text{HSO}_4)_3(\text{H}_2\text{PO}_4)_2$ are all monoclinic with a similar arrangement of the anion and cation sublattices. The only difference is that as the phosphate content is increased the anion sublattice becomes more cross-linked giving rise to different topology in the hydrogen bonded networks. [78, 84, 85]

4.1.2.2 High Temperature Structure

At T_c CsHSO_4 undergoes a phase transition from monoclinic to a tetragonal body-centred cubic structure. On the other hand CsH_2PO_4 adopts a cubic structure at high temperature which is related to the cubic CsCl system, with the Cl atoms being replaced by freely rotating H_2PO_4 tetrahedra. The intermediate compounds, including $\text{Cs}_2(\text{HSO}_4)(\text{H}_2\text{PO}_4)$, $\text{Cs}_3(\text{HSO}_4)_2(\text{H}_2\text{PO}_4)$, and $\text{Cs}_5(\text{HSO}_4)_3(\text{H}_2\text{PO}_4)_2$, exhibit either a mixture of both tetragonal and cubic structures or, at higher phosphate content, the cubic structure alone.

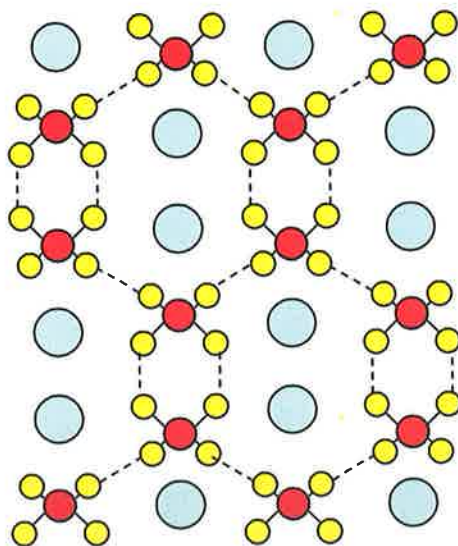


Figure 4.2 High temperature tetragonal structure of CsHSO_4 with (●) Cs, (●) S (●) O and (----) hydrogen bonds in highly mobile three-dimensional tetrahedral arrangement.

4.1.2.3 Structure of $\text{Cs}_6(\text{HSO}_4)_3(\text{H}_2\text{PO}_4)_4$

The exception in this series is the solid $\text{Cs}_6(\text{HSO}_4)_3(\text{H}_2\text{PO}_4)_4$, the material examined in this study. This exhibits a cubic structure at ambient temperatures, as opposed to the usual monoclinic structure, and has a unique arrangement of both its anion and cation sublattices. This arises due to the Cs: XO_4 ratio of 6:7, as compared to 1:1 observed for the other Cs-based solid acids. As a result it has a proton taking the place of a Cs^{+1} ion in the cation sublattice. [86]

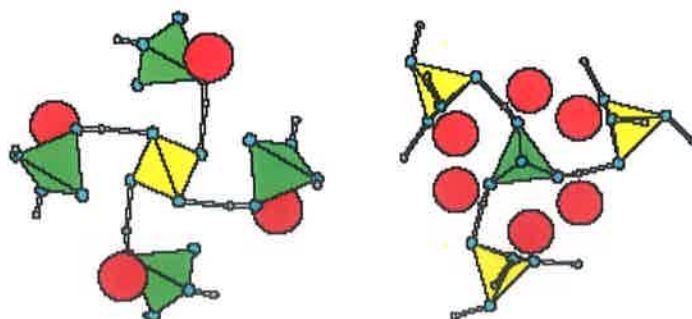


Figure 4.3 Cubic structure of low temperature $\text{Cs}_6(\text{HSO}_4)_3(\text{H}_2\text{PO}_4)_4$; (▼) PO_4 (▼) SO_4 (●) Cs (taken from [17]).

At high temperature, above its T_c , $\text{Cs}_6(\text{HSO}_4)_3(\text{H}_2\text{PO}_4)_4$ adopts a cubic structure similar to that observed in the other phosphate rich materials. However, due to the Cs: XO_4 ratio it is assumed there are vacancies in the cation (Cs^{1+}) sublattice. This is

supported by the observation of the negative thermal expansion of this material [86] which is believed to be due to the Cs ions moving into vacancies.

4.1.3 Proton Conduction in Solid Acids

4.1.3.1 Grotthuss mechanism in solid acids

The Grotthuss mechanism is the accepted mode of proton transport present in solid acids. This is due to the unique structural features of solid acids. The incorporation of the acid proton in the salt results in hydrogen bonded networks linking the anions together. In the Grotthuss mechanism [31] the proton is transferred along a hydrogen bond and there is a subsequent reorientation of the carrier molecule. This allows the proton to diffuse through the material. The rate of conduction is limited by proton transport and/or structural reorientation. [32]

Protonic conduction in solid acids differs from other ionic conduction (for instance from fluoride conduction in PbSnF_4) as hydrogen is the only element with no core electron shell and so it must be coordinated to an electronegative species. In solid acids the coordinating atom is usually oxygen resulting in a normal OH single bond, $\sim 0.9\text{-}1 \text{ \AA}$ long. However, as this pair comes within $2.4\text{-}3 \text{ \AA}$ of another oxygen on a second tetrahedron, a hydrogen bond (O-H...O) is formed. [88] As the proton can never be free from the electron density of its neighbours, it must move by a method where it is bonded to at least one of the oxygen atoms during the entire process. [89, 90]

4.1.3.2 Low Temperature Conduction

Most of the early work on the Cs-based solid acid compounds focused on their behaviour at ambient temperatures. Around this temperature these compounds have conductivity of the order of $10^{-3}\text{-}10^{-5} \text{ Scm}^{-1}$. It is accepted this conductivity is due to a basic Grotthuss mechanism with restricted reorientation of the tetrahedra resulting in relatively low rates of protonic conduction, but the details of the transport remain in dispute. Murphy [91] and Pollock [92] proposed a simple Grotthuss mechanism, as above with proton migration along the hydrogen bonds and reorientation of the tetrahedra. However,, due to the restricted rotation and crystallographic position of the oxyanion groups, this mechanism demands a xO-H H-Ox configuration with an inter-hydrogen distance less than twice the van der Waals radius of hydrogen. This would

result in large repulsive forces. Sharon [93] proposed synchronised reorientation of all of the tetrahedra which, while solving the problem of electrostatic repulsion, requires the breaking of hydrogen-bonds and physically unlikely synchronised reorientation. Baranov [94] proposed the existence of interstitial vacancies similar to Frenkel defects as with other ionic conductors.

4.1.3.3 High Temperature Conduction

In the early 1980's a first order phase transition was observed at 414 K for CsHSO₄ and above which the protonic conductivity increased by over three orders of magnitude. [83, 95] Above T_c the situation is simpler. There is generally an increase in disorder and symmetry in the anion lattice, resulting from rapid free rotation of tetrahedra through multiple equivalent sites. [96] Therefore, there are more conduction sites available than protons to occupy them, leading to very high proton conduction along the hydrogen bonds by a simple Grotthuss mechanism. [90] With extensive conduction through these vacant sites it is not necessary to form defects or to occupy interstitial sites, as is the case for ionic transport in other materials. [97] This discovery led to increased interest in the high temperature behaviour of these materials.

4.1.3.4 Experimental conductivity

The result of the phase transition is an increase in the proton transport rate and a consequent increase in the bulk conductivity. On heating, the conductivity of these materials increases by over three orders of magnitude at the phase transition temperature. On cooling, some of the materials show a rapid return to the non-superprotonic phase while those with a higher PO₄²⁻ to SO₄²⁻ ratio can exhibit long term stability (hours to days) of the superprotonic phase with the conductivity remaining high. [82, 86] While all of the compounds in the caesium-based solid acid series exhibit similar conductivity in the superprotonic phase [80, 81, 98], the onset temperatures and the transition range, from the onset of the phase transition to full conversion, both show some dependence on the phosphate content, although not in a consistent fashion across the range.

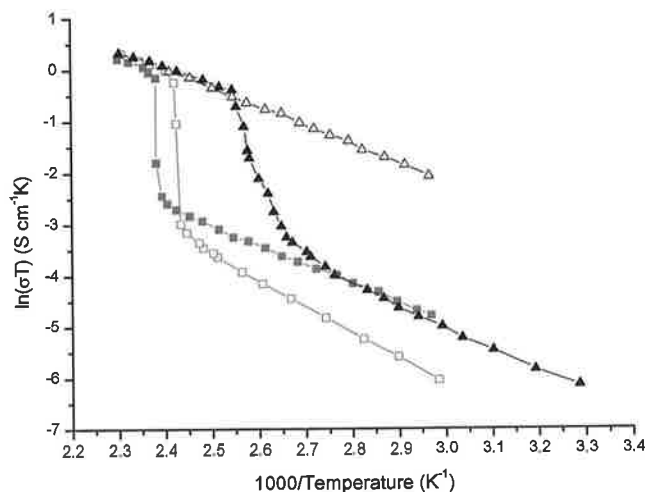


Figure 4.4 Conductivity data on heating (solid markers) and cooling (open markers) of $\text{Cs}_6(\text{HSO}_4)_3(\text{H}_2\text{PO}_4)_4$ (black) and CsHSO_4 (red), reproduced from [86].

4.1.4 NMR Studies of Solid Acids

NMR spectroscopy has been used to study conduction mechanisms in a number of proton conducting materials. Slade *et al* [99] used T_1 data recorded at high temperatures to study the both rotational and translational motion of NH_4^+ vehicles in proton conducting ammonium tungsten bronze. NAFION, one of the most commonly used polymers for PEMs, was studied by pulsed field gradient methods [100], this yielded information about the diffusion mechanism. Matsuo *et al* [101] used the temperature dependence of the ^1H linewidth to extract information on proton dynamics in $\text{Tl}_3\text{H}(\text{SO}_4)_2$, the results were in good agreement with results from bulk measurements of conductivity.

However, in his review of the field of NMR of superionic materials Brinkmann [67] indicated the problem with traditional temperature-dependent NMR experiments is the non-BPP behaviour of these materials, which makes the analysis of fixed frequency data problematic. Ishii [102] went further stating that a number of motional modes, including hopping ion motions and both extended and localised nondiffusive modes, do not contribute to conductivity but do contribute to the spin lattice relaxation. These factors explain why the theoretical conductivity values calculated from the proton hopping rates, extracted from NMR data, do not always agree with the experimentally measured conductivity.

There have been very few published NMR studies of Cs-based solid acids. Lahajner [103] used one and two-dimensional exchange, ^2H NMR spectroscopy of deuterated CsHSO_4 to show there is very slow motion along the $\text{OD}\dots\text{O}$ hydrogen bond at room temperature. ^1H NMR linewidth measurements of the related compound CsHSeO_4 supported the assumption of low temperature proton motion along the hydrogen bonds. In the same study ^{77}Se NMR relaxometry was used to demonstrate that the reorientational motion of SeO_4 tetrahedra is related to the transport of protons below T_c . [104] The temperature dependence of both the ^1H and ^{31}P NMR linewidths in CsH_2PO_4 , above and below the phase transition temperature were measured by Yamada and co-workers. [105] From this it was determined that the reorientation of the anion plays an important role in the proton conduction of CsH_2PO_4 in both the superprotonic and low temperature phases. In the same work, ^{31}P linewidth measurements on single crystals were used to obtain an activation energy of 0.74 eV for the reorientational jump of the H_2PO_4 oxyanion.

Hayashi and coworkers have recently examined a number of materials based on $\text{CsHSO}_4\text{-H}_2\text{PO}_4$ by NMR relaxation methods. [106-108] They were able to demonstrate that the predicted conductivity from microscopic NMR measurements was in good agreement with the experimental values. The conductivity was extracted from second moment analysis and by modelling the temperature dependence of ^1H T_1 , using a relaxation mechanism which involved $^1\text{H}\text{-}^1\text{H}$, $^1\text{H}\text{-}^{31}\text{P}$ and $^1\text{H}\text{-}^{133}\text{Cs}$ dipolar interactions modulated by Lorentzian spectral densities (BPP model). However, the assumption of a single random motional process remains central to this analysis, despite the sophistication of the model used for the dipolar interactions.

4.2 Experimental

4.2.1 Synthesis

The solid acid, $\text{Cs}_6(\text{HSO}_4)_3(\text{H}_3\text{PO}_4)_4$, was synthesised in the research group of our collaborator Prof. Sossina Haile's in the Materials Science Department, California Institute of Technology. The material was grown by slow evaporation of an aqueous solution of metal carbonates and a mixture of mineral salts at room temperatures. After the formation of crystal samples, they were filtered over a porous ceramic filter and washed with acetone or isopropanol and dried.

4.2.2 Differential Scanning Calorimetry

Thermal analysis was performed using a Polymer Labs PL-DSC differential scanning calorimeter. A sample of $\text{Cs}_6(\text{HSO}_4)_3(\text{H}_3\text{PO}_4)_4$ was lightly ground and placed in an open sample pan under flowing nitrogen (5 mL/min). The measurement was conducted using a rate of 2 K/min, from a temperature of 290 K to 500 K.

4.2.3 ^1H NMR

Most of the NMR analysis was carried out on a Stellar Spinmaster FFC-NMR 2000 relaxometer, using pre-polarised and non-polarised sequences as required. The technique is constrained by sensitivity and resolution so the low proton concentration of these samples renders them difficult to study. This is particularly the case below the phase transition temperature, where proton motion is limited and T_2 is apparently very short resulting in a poor signal to noise ratio. The magnetisation recovery curves were mono-exponential at all fields and at all temperatures.

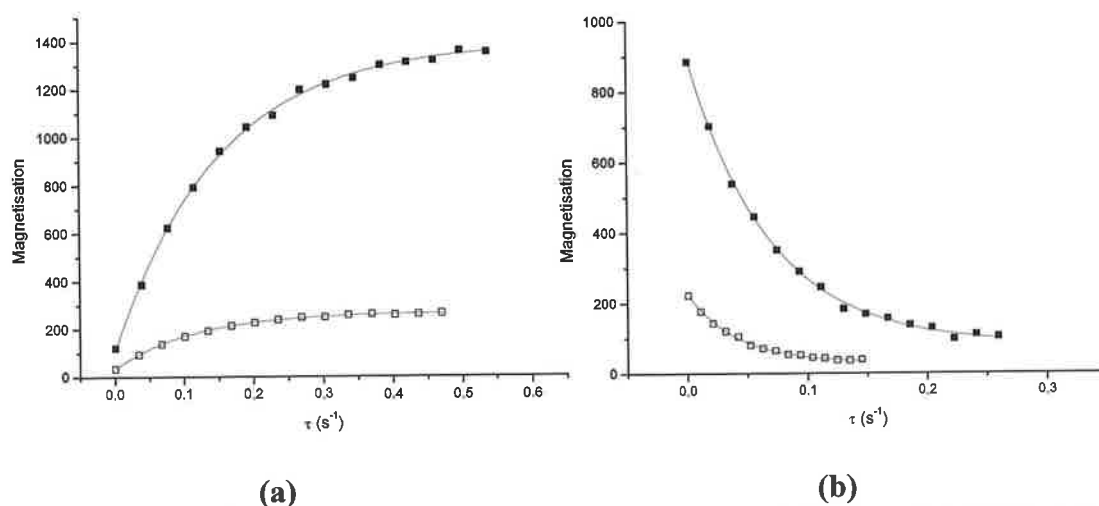


Figure 4.5 Magnetisation recovery curves of $\text{Cs}_6(\text{HSO}_4)_3(\text{H}_2\text{PO}_4)_4$ at (a) 16MHz and (b) 0.1MHz at 398 K (■) and 383 K (□) with single exponential fits (-) to the data.

Intermediate field (20-80 MHz) measurements were undertaken on a reconditioned Bruker WP80 variable field magnet using the multi-block saturation recovery pulse sequence. The WP80 was used for temperatures from 373 - 398 K but due to limitations of the sample temperature control system could not be used for temperatures above 393 K.

Motional information was also obtained by performing measurements of T_1 as a function of temperature, $T_1(T)$, at fixed magnetic field. These high field NMR

experiments were carried out on a 300 MHz Varian Chemagnetics CMX Infinity spectrometer in collaboration with Dr Jeremy Titman in the Solid-State NMR group in the University of Nottingham. T_1 measurements were carried out using both inversion recovery and saturation recovery pulse sequences. The T_1 curves were mono-exponential at all temperatures with both pulse sequences.

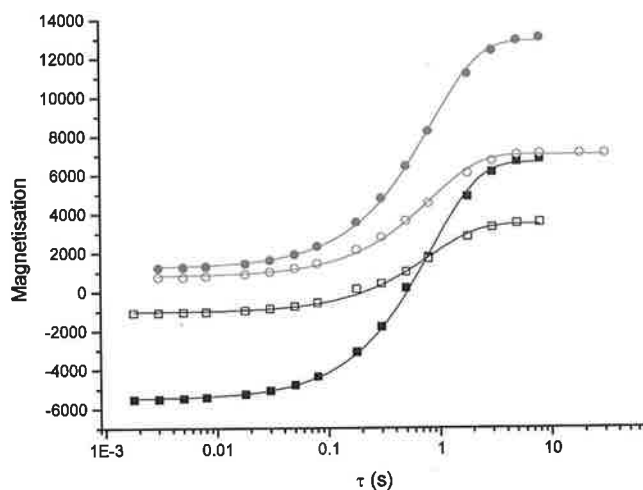


Figure 4.6 Inversion recovery (■, □) and saturation (●, ○) recovery curves of $\text{Cs}_6(\text{HSO}_4)_3(\text{H}_2\text{PO}_4)_4$ at 300 MHz and at 383 K and 453 K, respectively.

4.3 Results

4.3.1 Differential scanning calorimetry

The thermal response of $\text{Cs}_6(\text{HSO}_4)_3(\text{H}_2\text{PO}_4)_4$ as monitored by differential scanning calorimetry (DSC) is shown in Figure 4.7. It is readily apparent that, upon heating, the compound undergoes a sharp transition which begins at 370 K and is complete by 392 K. This has been attributed to a structural phase change into the superprotonic state which is also observed by conductivity measurements and in the diffraction data which is complete at a T_c of 390 K. [86] The second feature between 460 K and 480 K is due to the decomposition of the material.

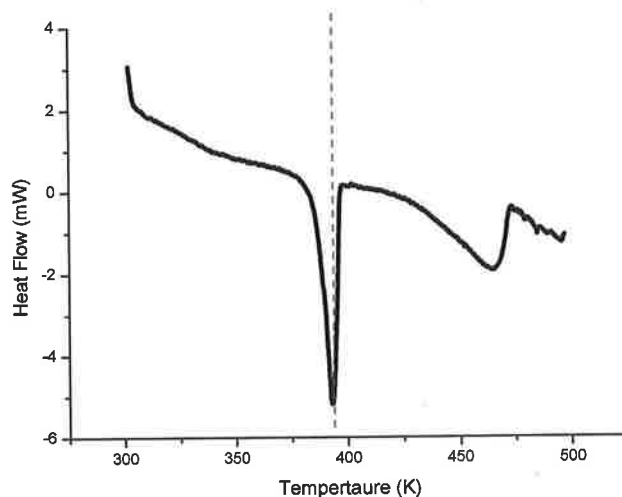


Figure 4.7 DSC curve of $\text{Cs}_6(\text{HSO}_4)_3(\text{H}_2\text{PO}_4)_4$ showing superprotonic phase transition at 373 - 405 K with a T_c at 390 K (represented by a dashed line) and decomposition from 450 K.

4.3.2 ^1H NMR

4.3.2.1 High temperature stability

As can be seen from the DSC curve, decomposition of the material begins at approximately 460 K so all NMR measurements were carried out below this temperature. However, it has been seen that in this class of solid acids prolonged exposure to temperatures above T_c (390 K) can lead to dehydration. [79] It is well known that phosphate groups have the potential to dehydrate producing phosphites and other decomposition products. This process is apparent as a change in the measured T_1 value over a period of hours (figure 4.8b), effectively limiting the temperature range that could be studied by NMR. The saturation recovery curves recorded for a sample maintained at 435 K show an increase in T_1 , in addition to the increase in the short time magnetisation offset which is apparent in figure 4.8a.

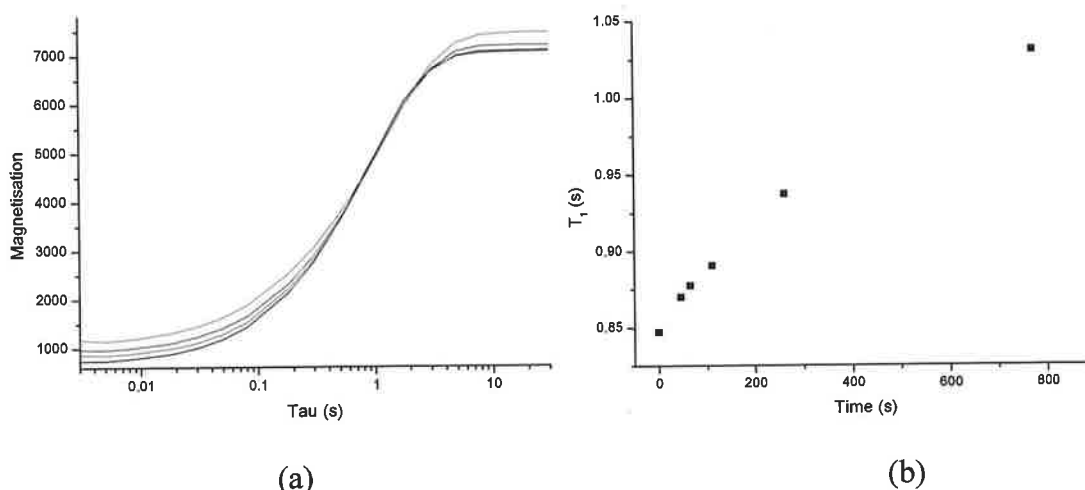


Figure 4.8 (a) Saturation Recovery T_1 curves after 60 (-), 150 (-), 260 (-) and 750 (-) min and (b) T_1 as a function of time calculated from saturation recovery curves at 435 K showing increase of T_1 over 12.5 hours due to dehydration.

The sample was examined by NMR relaxometry in the temperature range from the onset of the phase change at 373 K to 413 K, where the relaxation times were stable. Stability of the sample over a long period of time at a moderate temperature was confirmed using NMR in the following way.

The sample was left at 383 K for two hours to ensure full interconversion into the superprotonic state and a profile was obtained. The sample was left to cool overnight then reheated to 383 K for 2 hours and the profile was recorded again. Another profile was obtained immediately and again the sample was left to cool overnight. The following morning the sample was heated to 383 K and maintained at this temperature for ~54 hours. The T_1 value was measured at 10 and 0.1 MHz at regular intervals over this period to examine longer term stability at elevated temperatures and following this another profile was acquired. The resulting relaxation profiles were reproducible in all cases and the sample appeared to be thermally stable over a long period of time at this temperature. The errors in the measured R_1 values were of the order of 0.5-1.5 %.

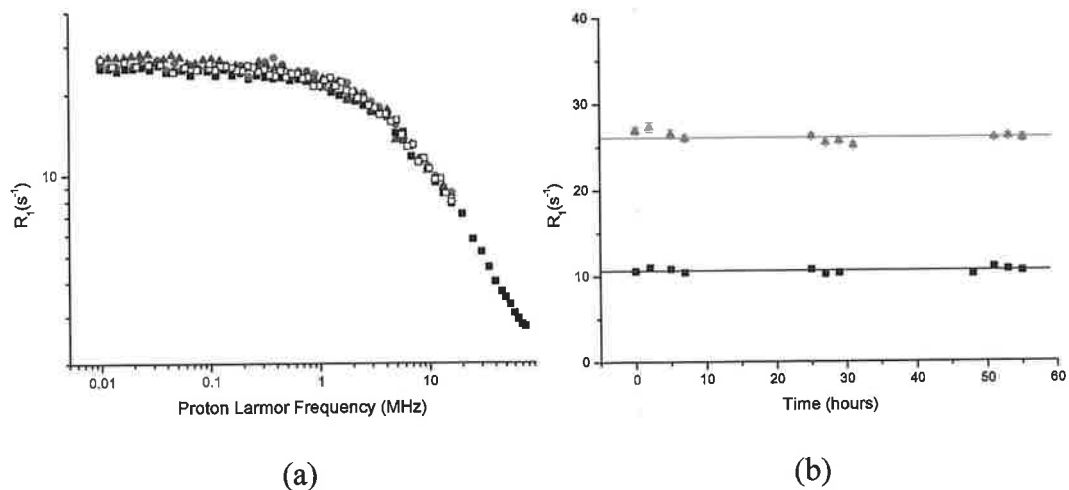


Figure 4.9 (a) ^1H proton relaxation profiles recorded at various times over 54 hours exposure to 383 K and (b) plot of T_1 measured at 10 MHz (\blacksquare) and 0.1 MHz (\blacktriangle) as a function of time spent at 383 K, showing the thermal stability of $\text{Cs}_6(\text{HSO}_4)_3(\text{H}_3\text{PO}_4)_4$ sample at this temperature.

4.3.2.2 Low Temperature NMR

Below the phase transition temperature (T_c) there is very little proton motion and T_1 measurements are challenging. The sample is relatively proton dilute and due to the inherent lower sensitivity and magnet inhomogeneity of the low field fast field cycling NMR technique it is very difficult to make sufficiently accurate T_1 measurements at ambient temperatures. However, an attempt was made using the late-generation two Tesla FFC at Stelar SRL in Italy and with the WP80 variable field magnet. Large errors, lengthy measurements times and non-reproducibility of the data meant that no useful or consistent results were obtained.

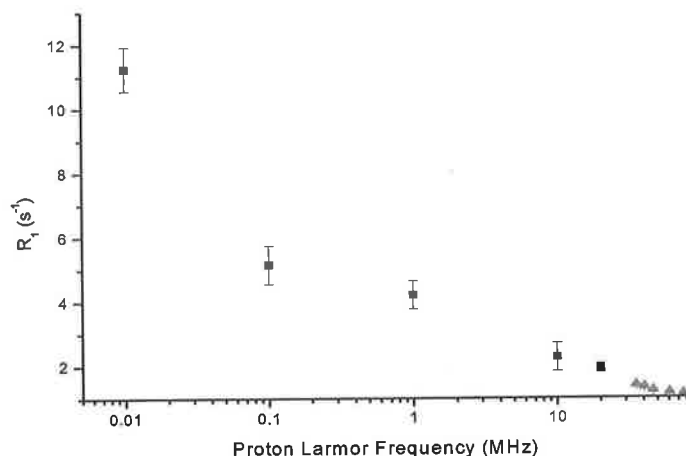


Figure 4.10 ^1H NMRD profile of $\text{Cs}_6(\text{HSO}_4)_3(\text{H}_3\text{PO}_4)_4$ at 298 K using field cycling at 2 T (\blacksquare) and the WP80 magnet (\blacktriangle).

4.3.2.3 High Temperature NMR

Above the superprotonic phase temperature, ($T_c \sim 370$ K), the quality of data is improved as T_2 is longer, see figure 4.11, the signal-to-noise ratio increases greatly, making it possible to record a profile using the fast-field cycling relaxometer. The magnetisation dephasing time is longer, at $\sim 220 \mu\text{s}$, is very similar to the T_2^* of the magnet.

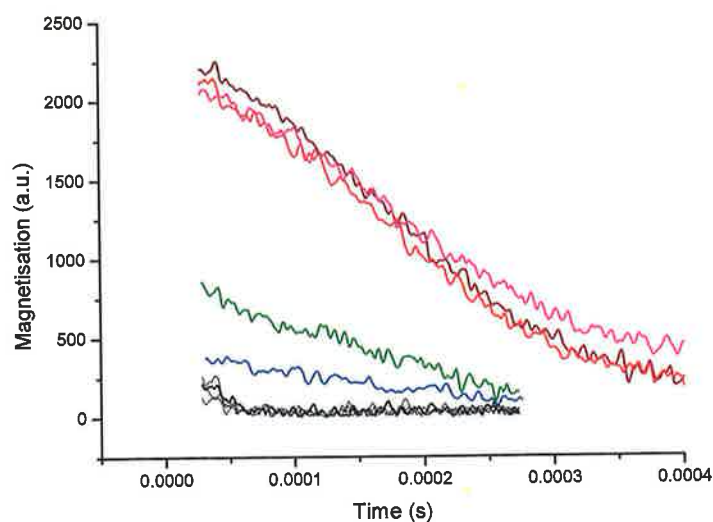


Figure 4.11 Free induction decay curves (128 scans) of $\text{Cs}_6(\text{HSO}_4)_3(\text{H}_3\text{PO}_4)_4$ at 413 K (-), 398 K (-), 391 K (-), 383 K (-), 373 K (-) and a number of temperatures from 298-363 K (-).

Relaxation profiles were recorded from 20-0.01MHz at a number of temperatures. The measurement temperatures were chosen from the DSC curve. All samples were left at the relevant temperature for two hours before measurement to ensure full interconversion. Following the completion of a profile the samples were left to cool for 24 hours to ensure the complete conversion back to the non-superprotonic state before reheating to the next temperature. The profiles show a dispersion that moves to lower frequency as the phase transition reaches completion.

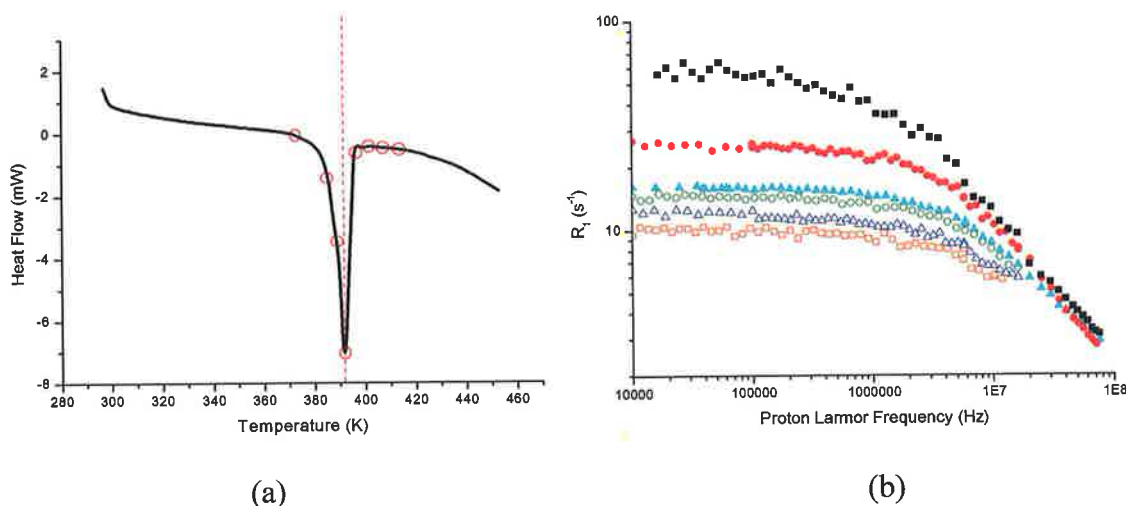


Figure 4.12 (a) DSC curve showing the temperatures chosen for NMR (b) ^1H NMR relaxation profiles of $\text{Cs}_6(\text{HSO}_4)_3(\text{H}_3\text{PO}_4)_4$ at 373 K (■), 383 K (●), 391 K (▲), 398 K (○), 408 K (△) and 413 K (□).

4.4 Discussion

4.4.1 ^1H NMR

4.4.1.1 Lorentzian Model

The mechanism for proton relaxation that is most likely to dominate in solid acids is the fluctuation of dipolar interactions. For high field NMR relaxation in the Cs mixed sulphate-phosphate systems the contribution of ^{31}P and ^{133}Cs , which are both c. 100% natural abundant, to the proton dipolar interaction must be considered. ^{33}S and ^{17}O interactions can be ignored due their integer spin quantum numbers. Hayashi [106-108] showed that high field NMR relaxation data of a number of Cs-based solid acid materials could be fitted using a Bloembergen-Purcell-Pound (BPP) spectral density function. This is a simple spectral density function for random tumbling in an ordered environment which takes into account the homonuclear dipole-dipole interactions between ^1H spins, and the heteronuclear interactions between ^1H and ^{31}P spins, and between ^1H and ^{133}Cs spins. In which case;

$$\begin{aligned}
T_{1d}^{-1} = & \beta_{HH} \left(\frac{0.5\tau_H}{1 + (0.5\omega_H\tau_H)^2} + \frac{2\tau_H}{1 + (\omega_H\tau_H)^2} \right) \\
& + \beta_{HP} \left(\frac{0.5\tau_H}{1 + ((\omega_H - \omega_P)\tau_H)^2} + \frac{1.5\tau_H}{1 + (\omega_H\tau_H)^2} + \frac{3\tau_H}{1 + ((\omega_H + \omega_P)\tau_H)^2} \right) \\
& + \beta_{HCs} \left(\frac{0.5\tau_H}{1 + ((\omega_H - \omega_{Cs})\tau_H)^2} + \frac{1.5\tau_H}{1 + (\omega_H\tau_H)^2} + \frac{3\tau_H}{1 + ((\omega_H + \omega_{Cs})\tau_H)^2} \right) \quad [4.2]
\end{aligned}$$

where τ_H is the correlation time for proton motion, ω_H , ω_P and ω_{Cs} are the angular resonance frequencies for ^1H , ^{31}P and ^{133}Cs respectively. β_{HH} , β_{HP} and β_{HCs} are the dipolar coupling constants for the contributions to the relaxation of the dipolar interactions of ^1H - ^1H , ^1H - ^{31}P and ^1H - ^{133}Cs spin pairs, respectively. These constants are given by:

$$\beta_{HH} = \frac{3}{5} \gamma_H^4 \hbar^2 I_H (I_H + 1) r_{HH}^{-6} \quad [4.3a]$$

$$\beta_{HP} = \frac{4}{15} \gamma_H^2 \gamma_P^2 \hbar^2 I_P (I_P + 1) r_{HP}^{-6} \quad [4.3b]$$

$$\beta_{HCs} = \frac{4}{15} \gamma_H^2 \gamma_{Cs}^2 \hbar^2 I_{Cs} (I_{Cs} + 1) r_{HCs}^{-6} \quad [4.3c]$$

Where γ_H , γ_P and γ_{Cs} are the gyromagnetic constants for the ^1H , ^{31}P and ^{133}Cs nuclei respectively, \hbar is Planck's constant, I_H , I_P and I_{Cs} are the spin quantum numbers which are 1/2, 1/2 and 7/2 for ^1H , ^{31}P and ^{133}Cs respectively. r_{HH} , r_{HP} and r_{HCs} are the distances between the lattice sites for pairs of ^1H nuclei, for ^1H and ^{31}P nuclei and for ^1H and ^{133}Cs nuclei, respectively. By adopting this approach Hayashi found that the extracted correlation times and activation energies were comparable with the bulk conductivity data from impedance spectroscopy.

When this approach is applied to our NMR data it is not possible to fit the relaxation profile. In the BPP approach the contribution from each of the homo- and heteronuclear dipolar interactions, became frequency independent below 1 MHz. The experimental R_1 values are frequency dependent in the observable frequency window, down to 10 kHz. Also the dispersion observed in the NMR data was too broad to be consistent with a BPP spectral density function. This indicates that a more complex spectral density function is required. Brinkmann [67] and Ishii [102] have shown the

presence of non-BPP behaviour in NMR relaxometry studies of other superionic conductors. This result is not surprising and it again demonstrates the critical requirement for T_1 measurements as a function of field, in the study of complex dynamic systems.

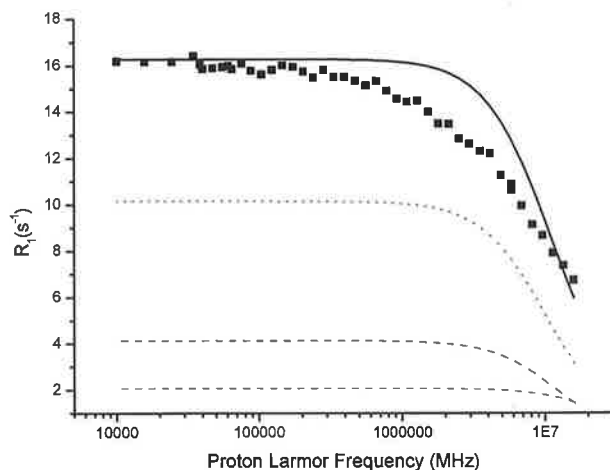


Figure 4.13 Relaxation profile of $\text{Cs}_6(\text{HSO}_4)_3(\text{H}_2\text{PO}_4)_4$ recorded at 391 K (■) fitted using the BPP spectral density function from eqn 1 (-) and the contributions from each of the ^1H - ^1H (···), ^1H - ^{31}P (---) and ^1H - ^{133}Cs (---) dipolar interactions.

4.4.1.2 Homonuclear Cole-Cole model

The Cole-Cole model is based on a stretched Lorentzian with a parameter, delta (δ), taken to be the degree of correlated motion and distribution of correlation times where $\delta = 1$ is uncorrelated motion and $\delta = 0$ is the highest degree of correlation possible. In this first instance the contribution to the spectral density due to heteronuclear dipolar interactions is ignored. Due to the much smaller gyromagnetic ratios of ^{31}P and ^{133}Cs and the large internuclear distance, the contribution to the relaxation of these heteronuclear interactions is much less than that of the homonuclear interactions. The spin-lattice relaxation rate in this “homonuclear-only” model is given by;

$$T_{1d}^{-1} = \beta_{HH} \left(\left(\frac{2}{\omega} \sin\left(\frac{\sigma\pi}{2}\right) \left[\frac{(\omega\tau_c)\delta}{1 + (\omega\tau_c)^{2\delta} + \left(2 \cos\left(\frac{\delta\pi}{2}\right)(\omega\tau_c)^\delta}\right)} \right] \right) + \left(\frac{1}{\omega} \sin\left(\frac{\sigma\pi}{2}\right) \left[\frac{(2\omega\tau_c)\delta}{1 + (2\omega\tau_c)^{2\delta} + \left(2 \cos\left(\frac{\delta\pi}{2}\right)(2\omega\tau_c)^\delta}\right)} \right] \right) \right) \quad [4.4]$$

where τ_c is the correlation time for proton motion, ω is the angular resonance frequency for ^1H , and δ is the degree of correlation. β is the dipolar coupling constant for the ^1H - ^1H dipolar interactions, which is related to the internuclear H-H distance (equation 2a)

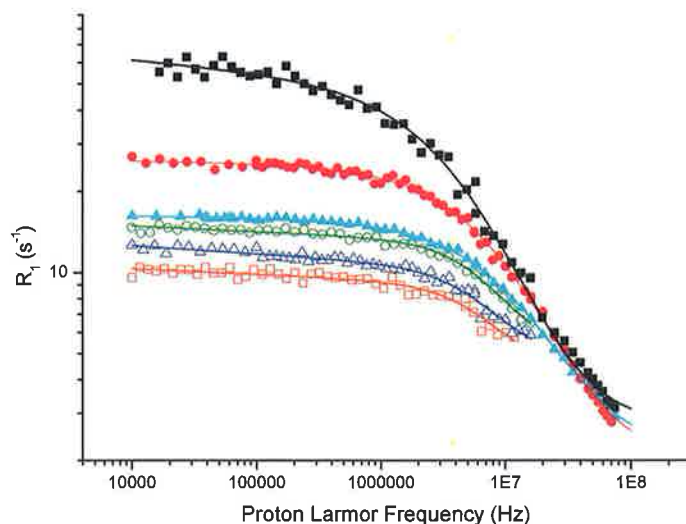


Figure 4.14 ^1H relaxation profiles of $\text{Cs}_6(\text{HSO}_4)_3(\text{H}_2\text{PO}_4)_4$ at various temperatures fit with a Cole-Cole spectral density function (equation 3) at 373 K (■), 383 K (●), 391 K (▲), 398 K (○), 408 K (△) and 413 K (□).

The NMR data at all temperatures were fitted using this approach and correlation times (τ_c), dipolar coupling constants (β values) and correlation co-efficients (δ values) were extracted.

Table 4.2 Table of correlation parameters extracted from Cole-Cole fits of relaxation profiles of $\text{Cs}_6(\text{HSO}_4)_3(\text{H}_2\text{PO}_4)_4$ at multiple temperatures.

Temp (K)	β ($\times 10^8 \text{ s}^{-2}$)	τ_c ($\times 10^{-8} \text{ s}$)	δ	Offset (s^{-1})
413	1.4(3)	1.2(2)	0.96(6)	4.2(5)
408	1.7(3)	1.2(1)	0.95(4)	4.6(4)
403	1.6(4)	1.2(3)	0.97(6)	3.7(5)
398	2.6(2)	1.17(6)	0.96(2)	4.8(2)
390.5	2.8(2)	1.21(6)	0.96(2)	5.1(2)
387	3.1(3)	1.5(2)	0.95(1)	5.2(5)
383	3.7(2)	1.61(8)	0.96(3)	6.4(3)
373	4.9(6)	2.5(3)	0.91(9)	8.4(9)

Inclusion of the higher field data (20-80 MHz) for temperatures <390 K obtained using the WP80 equipment does not significantly affect the fits or the extracted dynamic parameters. Therefore,, as the extended frequency range was not accessible

at all temperatures, it is reasonable to restrict the data analysis to the narrower frequency range.

Table 4.3 Comparison of dynamic parameters from the Cole-Cole spectral density model for NMR data recorded over different frequency ranges

Freq. Range (MHz)	Temp (K)	β ($\times 10^8 \text{ s}^{-2}$)	τ ($\times 10^{-8} \text{ s}$)	δ
0.01-16	373	4.96	2.59	0.91
	383	3.73	1.61	0.96
	391	2.85	1.21	0.96
	398	2.61	1.17	0.96
0.01-80	373	5.46	2.61	0.91
	383	4.00	1.41	0.95
	391	3.38	1.19	0.97
	398	2.61	1.17	0.96

A δ -value of one corresponds to uncorrelated motion and the spectral density function reduces to a Lorentzian, i.e. to a BPP spectral density function. The δ -values of ~ 0.96 obtained for the superprotonic phase, imply that the motional process is only very slightly correlated or that the distribution of correlation times is very narrow. However,, the data cannot be fitted using a BPP function, showing that even slight correlation is important with this model (figure 4.15). At the lower end of the temperature scale (373 K) a lower δ -value at 0.91 was obtained which could be interpreted as indicating that the process is more correlated in the non-superprotonic phase.

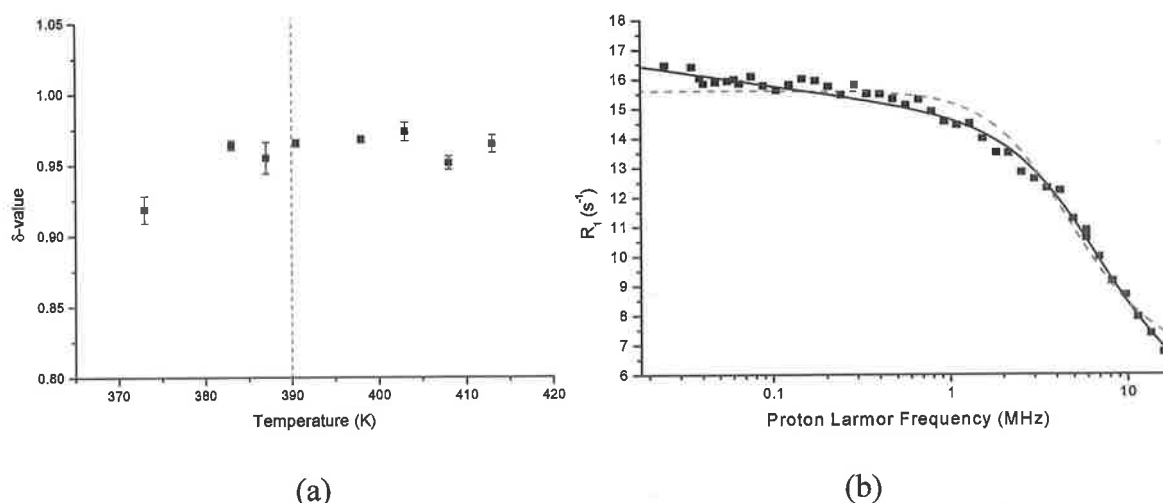


Figure 4.15 (a) Plot of the degree of correlation, δ , against temperature and (b) relaxation profile of $\text{Cs}_6(\text{HSO}_4)_3(\text{H}_2\text{PO}_4)_4$ (■) fit with BPP (---) and with Cole-Cole (-) functions.

The dipole coupling constant, β , shows a decrease with increasing temperature which suggests a surprisingly large increase in the internuclear proton spacing (r_{HH}) with temperature. There appear to be two linear regimes; above and below the full interconversion temperature (390 K). In the high temperature range the structure remains cubic but there is rapid motion of the oxyanion tetrahedra. Above T_c the diffraction data [86] shows a negative thermal expansion of the unit cell due to migration of the caesium cations into vacant sites, which becomes more prevalent with increasing temperature. However, while the overall unit cell contracts by 1-2 % the volume of the oxyanion tetrahedra increases by $\sim 8\%$ between 390 and 420 K. There is a large observed increase in the r_{HH} value from the NMR data of $\sim 10\%$ from $\sim 2.8\text{-}3.3$ Å in the temperature range 370 - 420 K. The $^1\text{H}\text{-}^1\text{H}$ internuclear distance from the diffraction data of the low-temperature phase is ~ 3.2 Å [86] indicating that the internuclear spacing obtained from NMR is a reasonable value. However, on the timescale of the diffraction experiment, proton motion averages the $^1\text{H}\text{-}^1\text{H}$ distances across the oxyanion tetrahedra, even in the low temperature phase.

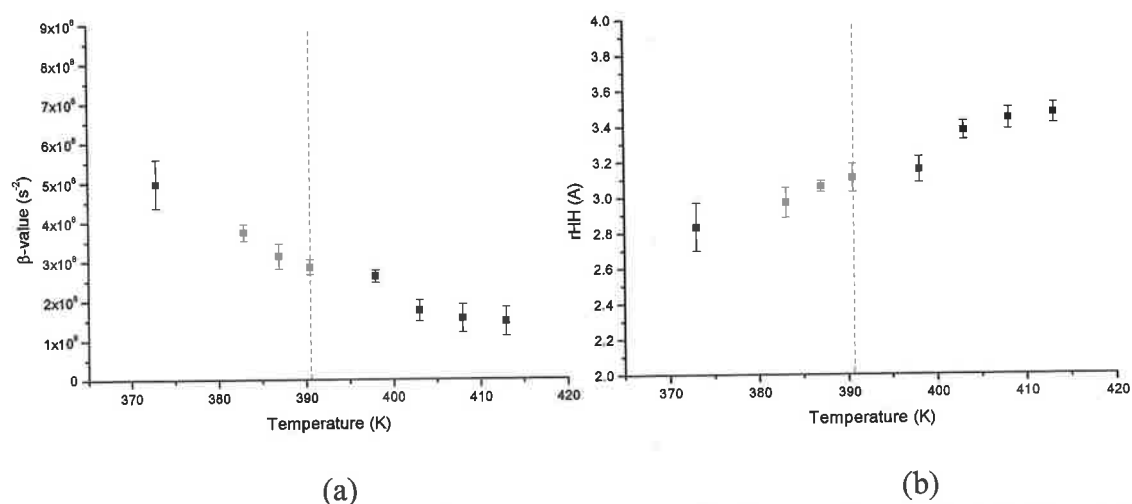


Figure 4.16 Temperature dependence of (a) the dipolar prefactor, β (b) the H-H internuclear jump distance, r_{HH} .

Below T_c the correlation time, τ_c , exhibits a decrease with increasing temperature as expected for a thermally activated process. Above T_c there is no measurable increase in the correlation time. This suggests that in the superprotonic cubic phase the mean ^1H residence time is temperature independent, at least over this narrow temperature range. It also indicates, somewhat surprisingly, that the conductivity is not due to a change in rate of proton hopping, but arises from an increase in the jump distance of the protons.

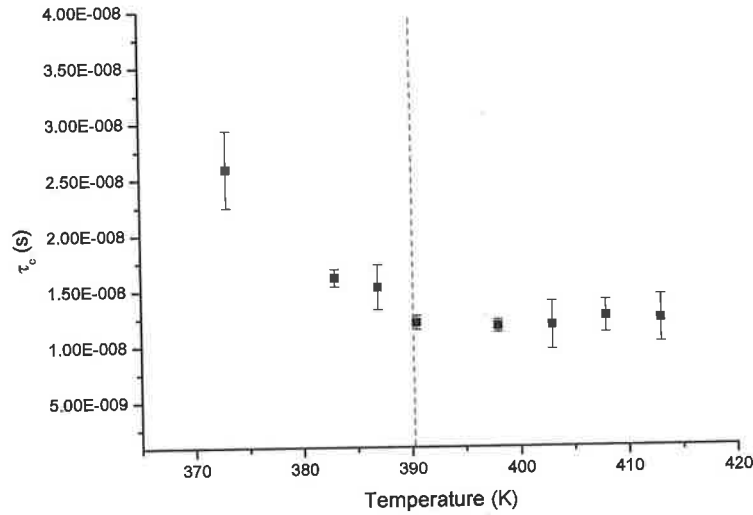


Figure 4.17 Temperature dependence of the correlation time, τ_c extracted from the Cole-Cole fits of the $\text{Cs}_6(\text{HSO}_4)_3(\text{H}_2\text{PO}_4)_4$ NMR profiles.

The charge carrier diffusion coefficient, D , can be related to the correlation times using the equation:

$$D = \frac{r_{\text{HH}}^2}{n\tau_c} \quad [4.5]$$

Where n is the number of possible sites to which the proton can jump and τ_c is the mean residence time. The sample is a three-dimensional conducting powder sample with a cubic structure, so $n=6$. Using the proton-proton internuclear distances and correlation times from the NMR analysis, diffusion coefficients can be calculated. These range from 1.33×10^{-12} to $1.63 \times 10^{-12} \text{ m}^2 \text{ s}^{-1}$ between 391 K and 413 K, values which are comparable to those obtained in other NMR studies on this class of materials (1.2×10^{-12} to $2.7 \times 10^{-12} \text{ m}^2 \text{ s}^{-1}$). [107]

D has an Arrhenius dependence on temperature in the high temperature phase. A plot of $\ln(D)$ against inverse temperature yields a straight line with a negative slope which is related to the activation energy for the diffusion process. The intercept is the temperature independent term, D_0 .

$$D = D_0 \exp\left(\frac{-E_{\text{act}}}{RT}\right) \quad [4.6]$$

For the superprotonic phase, the activation energy, E_{act} , for the diffusive process was calculated as $12.5(9) \text{ kJ mol}^{-1}$ and D_0 was calculated as $4.5(5) \times 10^{-11} \text{ m}^2 \text{ s}^{-1}$.

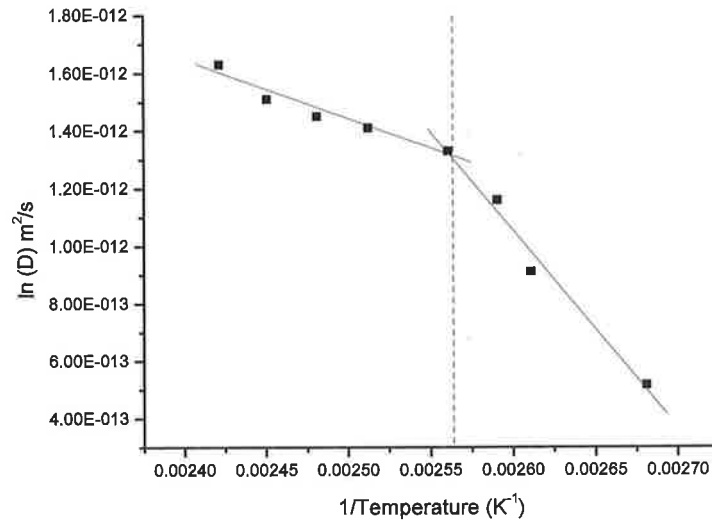


Figure 4.18 Arrhenius plot showing the apparent Arrhenius behaviour of the diffusion coefficient calculated from the parameters extracted from the Cole-Cole fits of the $\text{Cs}_6(\text{HSO}_4)_3(\text{H}_2\text{PO}_4)_4$ ^1H NMR profiles.

The electric conductivity can be related to the proton diffusion coefficient by the Einstein relationship:

$$\sigma = \frac{Ne^2 D}{k_B T} \quad [4.7]$$

Where e is the effective proton charge and k_B is the Boltzmann constant. The N value, which is the density of mobile protons, is estimated at $11 \times 10^{27} \text{ m}^{-3}$ from the proposed crystal structure [17]. The conductivity calculated from the NMR diffusion constant displays an Arrhenius temperature dependence and can be compared with the bulk conductivity data from other methods.

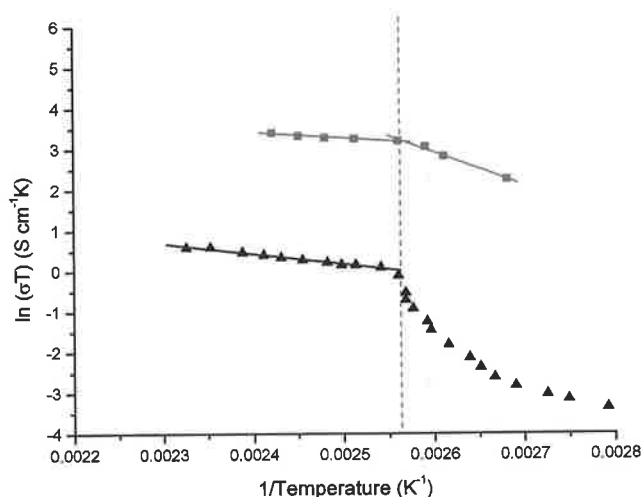


Figure 4.19 Comparing the temperature dependence of conductivities calculated from NMR (■) and impedance spectroscopy (▲) from [86].

Above 390.5 K, where conversion to the superprotonic phase is complete, a linear dependence on inverse temperature is observed and the slope of the straight line fit again yields an activation energy, $E_{a\text{NMR}}$, of 12.4(9) kJmol^{-1} . This is in reasonable agreement when compared to the activation energy derived from the published conductivity data ($E_{a\sigma}$) of 15.1(6) kJmol^{-1} . [86] The intercept from the linear fit is proportional to the temperature independent term, A_0 , and is similar for the Arrhenius conductivity curves for both the NMR and impedance spectroscopy methods, with $A_{0\text{NMR}} = 8.43 \times 10^2 \text{ Scm}^{-1}\text{K}$ and $A_{0\sigma} = 5.66 \times 10^2 \text{ Scm}^{-1}\text{K}$. The actual conductivity derived from NMR is higher than the conductivity obtained from impedance spectroscopy. Systematic overestimates in conductivities derived from NMR were reported by Hayashi in the CsHSO_4 , $\text{Cs}_2(\text{HSO}_4)(\text{H}_2\text{PO}_4)$ and $\text{Cs}_3(\text{HSO}_4)_2(\text{H}_2\text{PO}_4)$ solid acids [106-108] and arise from non-diffusional modes of proton motion. [102]

4.4.1.3 Homo- plus heteronuclear Cole-Cole model

When fitting the NMR data using the Cole-Cole function, the contributions to the ^1H relaxation rate from the heteronuclear interactions were ignored as they are smaller than the homonuclear contribution. To take into account the contribution to the relaxation from the heteronuclear interactions a modified ‘homo- plus heteronuclear’ Cole-Cole function can be used:

$$\frac{1}{T_1} = \beta_{HH} [J(\omega_H) + J(2\omega_H)] + \beta_{HP} [0.5J(\omega_H - \omega_P) + 1.5J(\omega_H \omega_P) + 3J(\omega_H - \omega_P)] + \beta_{HCs} [0.5J(\omega_H - \omega_{Cs}) + 1.5J(\omega_H \omega_{Cs}) + 3J(\omega_H - \omega_{Cs})] \quad [4.8]$$

where

$$J(\omega) = \frac{2}{\omega} \sin\left(\frac{\delta\pi}{2}\right) \left[\frac{(\omega\tau_c)^\delta}{1 + (\omega\tau_c)^{2\delta} + \{2\cos(\delta\pi/2)\}(\omega\tau_c)^\delta} \right] \quad [4.9]$$

Fitting the data with this function yields a single correlation time (τ_c) for a correlated process and also a dipole coupling constants for the homonuclear ^1H - ^1H interactions (β_{HH}) and for both of the heteronuclear ^1H - ^{133}Cs (β_{HCs}) and ^1H - ^{31}P (β_{HP}) interactions. From these coupling constants internuclear distances for the ^1H - ^1H nuclei (r_{HH}), ^1H - ^{133}Cs nuclei (r_{HCs}) and ^1H - ^{31}P nuclei (r_{HP}) can be calculated as above. It should be noted that this is a five parameter fit, while the homonuclear only model is a three parameter fit to the data.

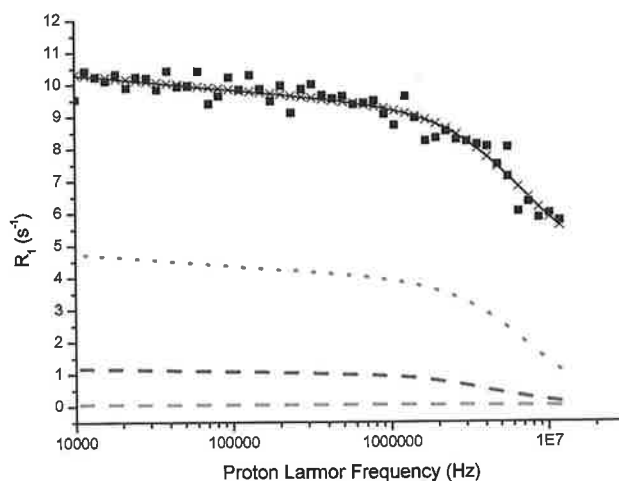


Figure 4.20 Profile of $\text{Cs}_6(\text{HSO}_4)_3(\text{H}_2\text{PO}_4)_4$ at 398 K (\blacksquare) fitted using the homo- plus heteronuclear Cole-Cole fitting function from eqns 6 and 7 (-). The contributions from each of the ^1H - ^1H (\cdots), ^1H - ^{133}Cs ($---$) and ^1H - ^{31}P dipolar interactions ($---$) are shown. The fit from the “homonuclear-only” Cole-Cole model is also shown (X).

The δ and τ_c values extracted from this approach are very similar to those obtained from the homonuclear only model. In this case the correlation times increase very slightly with temperature in the superprotonic phase. Although the effect is weak and close to the limit of what can confidently be claimed from the data.

From these fits the internuclear distances of ^1H - ^1H nuclei (r_{HH}), ^1H - ^{133}Cs nuclei (r_{HCs}) and ^1H - ^{31}P nuclei (r_{HP}) were extracted. The H-Cs dipolar contribution is the weakest

of the interactions, large variations in the extracted r_{HCs} values (2.3-9.2 Å) arise from fitting relatively noisy data so the distances obtained are of no value. Also r_{HH} and r_{HP} values cannot be simultaneously and independently extracted at any frequency. Thus the homo- plus heteronuclear model provides little further insight; the fit to the data is no better than for the homonuclear only model, and no additional information can be obtained.

4.5 Conclusion

The aim of this study was to examine whether field cycling NMR relaxometry can be used to gain insight into the mechanisms of proton conduction in solid acids. The most important result is that the field-cycling data does not conform to the BPP model. The NMR data could not be fitted to a normal BPP function, which is also the case for other superionic conductors. [67] By least squares methods the profiles can be forced to fit to the BPP model, with obvious systematic deviations in the fit. The correlation times obtained are typically 1.5 to 2 times larger than those from the Cole-Cole model. It is very likely that conventional BPP analysis of fixed field T1 data on solid acids, will result in significant systematic errors in the dynamic parameters.

The data could be fitted using a Cole-Cole model for homonuclear ^1H - ^1H dipolar spectral densities only. This indicates that proton motion in these materials is slightly correlated. Using dynamic, τ_c , and structural, r_{HH} , parameters extracted using this model an 'NMR' conductivity could be calculated. This is systematically greater than the conductivity obtained from impedance spectroscopy. However, the activation energy for conduction from NMR is in good agreement. It is surprising that the NMR analysis suggests that the conductivity increase is largely due to expansion of the lattice, and that the correlation time for proton motion is very weakly temperature dependent in this narrow temperature range. It is unfortunate that the accessible temperature range is too narrow to fully explore this finding

The NMR data can also be fitted to a model incorporating heteronuclear ^1H - ^{31}P and ^1H - ^{133}Cs interactions. However, these changes do not significantly improve the fit or alter the τ_c values. Thus the homonuclear only model is preferred to the homo- plus heteronuclear model. The extracted, weak, H-Cs interaction varies spuriously with even minor noise in the data and the r_{HH} and r_{HP} values cannot be independently assigned from these fits. This is unfortunate given the poor quality of the x-ray

diffraction data for this material in the superprotonic phase and the inherent difficulty in accurately determining the proton positions by that technique.

Chapter 5 – Amorphous Conducting Polyaniline

5.1 Introduction

5.1.1 Inherently conducting polymers

Until about 30 years ago all carbon-based polymers were rigidly regarded as insulators. Plastics have been extensively utilised by the electronics industry as inactive packaging and insulating material. This perspective is rapidly changing as a new class of polymers known as inherently conductive polymers (ICP) or electroactive polymers are being developed.

Conductive polymers were discovered by accident. In the early 1970's while working on polyacetylene, Hideki Shirakawa added a large excess of catalyst producing a silvery film; pure trans-polyacetylene. [109] It was found to be possible to control the ratio of cis- and trans- isomers by changing the reaction temperature. Around the same time a chemist Alan MacDiarmid and a physicist Alan Heeger in the USA were experimenting with an inorganic polymer sulphur nitride $(SN)_x$. Shirakawa began a collaboration with MacDiarmid where they modified polyacetylene by oxidation with iodine vapour. [110] Heeger was asked to investigate changes in optical properties of the new material. Conductivity measurements on iodine-doped trans-acetylene showed an increase of ten million times the original conductivity and so the field of conducting polymers was born. [24]

5.1.2 Conductivity

Conductivity depends on the number density of charge carriers (number of electrons) and how fast they can move in the material. To become electrically conductive a polymer must imitate a metal in that its charge carriers have a mean free path significantly greater than the internuclear distance. A key property of conducting polymers is the presence of conjugated double bonds along the backbone of the polymer. In conjugation, there are alternately single and double bonds between adjacent carbon atoms. Every bond contains a localised σ -bond which forms a strong chemical bond. In addition, every double bond also contains a less strongly localised π -bond which is weaker. However, the presence of conjugation is not enough to make the polymer material conductive. All known conducting polymers are semiconductors in their unperturbed or pristine state.

The conductivity of conducting polymers spans a very wide range ($<10^{-12}$ to 10^5 Scm^{-1}) depending on oxidation state, pH, counterion type and concentration and physical morphology. [17] The source of this variety is the quasi-one-dimensional (Q-1D) nature of the materials. The chain deformation that results from adding electrons (or consequently holes) to a chain produces a variety of 'particles'; polarons, bipolarons and solitons. Generally the conductivities of the pristine electronic polymers are transformed from insulating to conducting through the process of doping, with the conductivity increasing as the doping level increases. Both p-type oxidative and n-type reductive dopants have been utilised to induce an insulator-to-conductor transition in electronic polymers. Dopants induce a 'hole' on the conductance band side of the band gap which facilitates electron motion. Charge transport in polaron-doped polymers occurs via electron transfer between localised states either on one chain or between neighbouring chains. [19] The conduction mechanism of conducting polymers arises from the interchain hopping of polarons and bi-polarons, as described in Chapter 1.

5.1.3 Polyaniline

Polyaniline was the first intrinsically conducting polymer (ICP) to be commercially available worldwide. It has achieved importance among conducting polymers due to its ease of processability, environmental stability and of course high conductivity. [111] The polyaniline class of conducting polymer has been widely investigated for potential applications in fuel cells, rechargeable batteries, protection coatings, electrochromic displays, conducting composite materials, gas sensors, corrosion protection, electronic, biosensor and optical devices. [36, 112-115]

Polyaniline is the oxidative polymeric product of aniline under acidic conditions and has been known since 1892 as aniline black. As early as 1862 Letheby obtained a partly conductive material by anodic oxidation of aniline in sulphuric acid which was probably polyaniline. Polyaniline is a typical phenylene based polymer having an secondary amine group flanked either side by phenyl rings. While much work was done at the beginning of the 20th century to elucidate the structure and conformation of polyaniline, it wasn't until 1968 when Jezzard *et al* [116] reported the influence of water on the conductivity in polyaniline that interest was revived in the potential application of these materials. Further development of polyaniline and its derivatives

soared with the ground breaking discovery of the high conductivity in iodine-doped polyacetylene. For their work Shirakawa, Heeger, and MacDiarmid [24] won the Nobel Prize in 2000.

5.1.3.1 Synthesis of polyaniline

Polyaniline is prepared in its protonated form by the polymerisation of aniline in an acidic medium. The acidic medium is necessary as it causes the formation of anilium cations which can undergo polymerisation. Polyaniline can be prepared either by chemical or electrochemical means. One of the key factors in controlling the rate of polymerisation and hence the yield, is the pKa of the acid used. Protonation in polyaniline occurs at the quinone diamine segment which has a $pK_{a1} = 1.05$ and $pK_{a2} = 2.55$ so any acid with pKa within that range is a potential dopant. [117] The most studied synthetic route is the polymerisation of aniline in HCl. The synthesis involves mixing distilled aniline, HCl and ammonium peroxydisulphate (APS) at room temperature, and subsequent filtration and washing, to form polyaniline hydrochloride. [18] It has been suggested that synthesis at reduced temperatures ($\sim 273\text{-}278\text{ K}$) yields higher molar mass polymers. [118] A simple oxidising agent such as APS is used as an oxidant to remove a proton from the aniline molecule in preference to a metal-based oxidant (eg cobalt salts) to avoid the problem of metal coordination. [119] Also the ammonium salt is preferred to its potassium counterpart due to its greater solubility. The optimum stoichiometric peroxydisulphate/aniline ratio is $\sim 1:1.15$, as at higher ratios overoxidation leads to loss of conductivity. [120] The doping process produces a stable nitrogen base salt.

The protonated form is the most common form of polyaniline, it is green coloured (and hence is referred to as the emeraldine salt) and has conductivity in the semiconductor range, of the order of 10 Scm^{-1} . This is many orders of magnitude higher than that of common polymers ($<10^{-9}\text{ Scm}^{-1}$) but is lower than that of typical metals ($>10^4\text{ Scm}^{-1}$). Fully protonated polyaniline doped with HCl was found, on average, to have conductivity of $4.4 \pm 1.75\text{ Scm}^{-1}$. [110] The emeraldine salt can, on addition of most bases, be reduced to the emeraldine base. The blue-coloured corresponding polyaniline base is almost non-conducting with an average conductivity of $1.4 \times 10^{-8}\text{ Scm}^{-1}$. By using a suitably functionalised protonic acid to protonate polyaniline, the counter ion can induce processibility of the resulting doped polymer. Camphor sulphonic acid (CSA) has been used as a solvent in the doping of

polyaniline and the resulting material, following processing, has improved morphology with very high conductivities (100-400 Scm^{-1}). It is thought that this is due to the acid acting as a secondary dopant stabilising the polaron and charge carriers. Also the surfactant counterions render the doped polymer soluble in common non-polar solvents. [121]

There has been significant interest recently in the preparation of polyaniline composites. Composites are conducting polymers incorporated into a suitable insulating or conducting matrix. Composites can help overcome problems with poor processing and mechanical properties. Composites may be prepared by a number of methods; block or graft copolymerisation, by synthesis of conducting polymer within the host matrix or by simple blending. [122-124]

5.1.3.2 Conductivity of Polyaniline

The emeraldine form of polyaniline exists in many oxidation states and specific structures have been proposed for each of the different phases to correlate with electronic and other properties. The non-conducting emeraldine base form (figure 5.1(i)) differs from other conducting polymers in that it is of the A-B type where the A component is the aromatic ring and the B component is the nitrogen heteroatom as compared with the A-A type, observed in polypyrrole and polyacetylene. In polyaniline the B component is involved in the conjugation with the aromatic carbon rings. Also the polymer is not 'charge conjugation symmetric' [125] in that it consists of amine (-NH-) and imine (=N-) sites in equal proportions. Among ICP's polyaniline has a unique doping mechanism, which involves protonation as well as the addition of a p-dopant. [126] Therefore, conductivity is dependent on both the oxidation state of the polymer and the degree of protonation.

In doping to the conducting emeraldine salt, the imine sites are protonated by [127] acids to the bipolaron form (figure 5.1(iii)). However, the polymer chain undergoes further rearrangement to a metallic delocalised polaron lattice (figure 5.1 (ii)) which is the salt of a nitrogen base rather than the carbonium ion present in other ICP's. [126] However,, on the basis of optical [125] and micro-transport [128] studies it was proposed that partial protonation leads to phase segregation between the doped and undoped regions [128] yielding highly conducting domains separated by regions of lower conductivity. In such a scenario the charge transport mechanism is limited by the flow of charge carriers between domains.

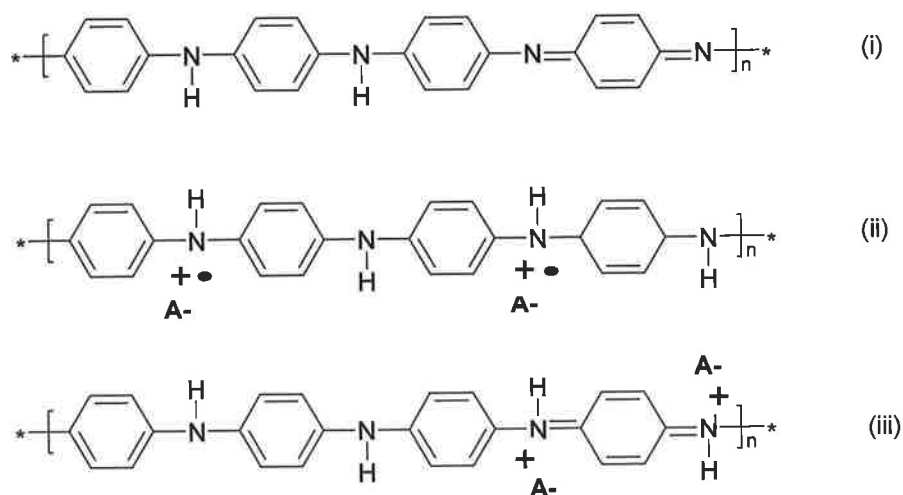


Figure 5.1 Three of the oxidation states of polyaniline (i) undoped emeraldine base, (ii) and (iii) doped emeraldine salt, where ii) is the metallic delocalised polaron lattice and iii) the initial bipolaron form.

Although theoretical calculations have predicted that the bipolaron state is more energetically favoured than the polaron state, [127] it is widely accepted that polarons are the charge carriers responsible for the high conductivity in polyaniline. [17, 129] It has been proposed that coulombic interactions, dielectric screening, and local disorder stabilise the delocalised polaron state. [130]

Polarons may diffuse freely along the polymer chain at the on-chain diffusion rate, D_{\parallel} , so the limiting factor of bulk conductivity is thought to be the polaron inter-chain hopping rate D_{\perp} . Thus the preparation conditions, [131, 132] particularly as they determine structural morphology [133] and structural defects [134] influence conductivity. It has also been reported that the conductivity of polyaniline is dependent on the solvent it is cast from. This phenomenon is known as 'secondary doping'. [121] The solvent is thought to cause a change in the polymer conformation altering the conductivity.

However, the most significant determinant of the conductivity of polyaniline is the proton doping level. [18] Maximum conductivity occurs when polyaniline is 50% doped (one dopant molecule every second monomer unit) to give the full polaron lattice structure. Under these conditions, the conduction mechanism is similar to other polymers with polaron states overlapping to form mid-gap bands facilitating charge transfer between the valance and conduction bands across the band gap.

5.1.4 NMR Studies of Conducting Polymers

5.1.4.1 Spectroscopy

NMR spectroscopy has been applied extensively for polymer characterisation and development. This is due to the short range nature of NMR interactions which are sensitive to different molecular environments in polymers. However, the interpretation of the results is complex and conclusions are generally not definitive, especially with low-resolution NMR.

High-field NMR was used initially for structural determination and elucidation of ICP's. Kaplan and McConwell [135] compared ^{13}C and ^2H solid state NMR MAS spectra to show that the emeraldine base is an alternating copolymer of reduced $[-(\text{C}_6\text{H}_4)\text{-N(H)}\text{-(C}_6\text{H}_4)\text{-N(H)}\text{-}]$ and oxidised $[-(\text{C}_6\text{H}_4)\text{-N}=\text{(C}_6\text{H}_4)=\text{N-}]$ units. These conclusions were supported by ^{15}N solid-state NMR studies by Richter *et al.* [136] Mathew *et al* characterised polyaniline by solid state MAS ^1H NMR. [111] Comparing the spectra of polyaniline in its most reduced (leucoemeraldine base) form with annealed polyaniline, they clearly observed the conversion of quinoid rings to benzenoid rings on heating. This study showed that heating produced a single cross-linked product with a N,N'-diphenylphenazine structure.

In polyaniline the emeraldine base and emeraldine salt forms (see figure 5.1) were studied using ^1H NMR and compared by Kaplan *et al.* [135] The primary chain motion is 180° flips of rings about their 1,4-axes which can be further separated into fast and slow flippers, the ratio of which is an indication of polymer dynamics. For the conducting salt (polyaniline hydrochloride) the ratio of the number of slow to fast flippers is approximately three times the ratio for the non-conducting base (emeraldine base). This decrease in fast flippers can be attributed to steric hindrance by adjacent Cl^- counterions.

5.1.4.2 Polymer Relaxometry

The inherent morphological complexity of solid polymers is an impediment for use of NMR to characterise microscopic events. Complexity arises in several ways; a number of co-operative and/or discrete motions may occur on the same timescale which can lead to a broad distribution of correlation times and spectral densities which can be only dealt with semi-quantitatively. Defects in the polymer chains also promote extraneous motion in their immediate vicinity. Add to this the charge transfer

dynamics of ICP's and it becomes apparent that the range of motions in a polymer sample is large and it is very difficult to isolate individual mechanisms or apply a single spectral density function using, for example, a BPP analysis. [137]

Despite these difficulties a number of idealised models have been devised in an attempt to interpret experimental data in a manner consistent with structural morphology. A two-phase model was proposed by Wilson in 1953 [138] for the differing behaviour of crystalline and amorphous regions in a partially crystalline polymer. This is also applicable to block co-polymers and heterogeneous blends. However, this approach did not take into account the interaction between the phases. [139] Spin diffusion (see section 5.1.4.3) can affect the magnitudes of magnetisation and complicate the quantitative analysis of these systems. T_1 and $T_{1\rho}$ measurements have been used to assess different crystalline phases in the polymer. Glowinkowski *et al*'s [140] study into the change in relaxation times of polyethylene co-polymers with temperature yielded a three-phase structure (crystalline, amorphous and intermediate) and three main relaxation processes (α , β , and γ) observed as multiple minima in the temperature dependence of T_1 . The α -process is observed in the crystalline phase while the γ -process is associated with the glass transition in the amorphous phase. These features have been observed in polymers using other techniques, in particular by differential scanning calorimetry. [141]

The proton frequency range accessible by a combination of FFC-NMR and high-field relaxometry is $\sim 10^2$ - 10^9 Hz. This window matches the dynamic range of chain modes of polymers with molecular masses up to 10^5 . [50] There are three main models for chain motion in polymers; the tube/reptation model [142] the Rouse model [143] and the renormalised Rouse model. [144] The Rouse model reflects chain dynamics below a polymer specific critical molecular weight, M_c , where neighbouring polymer chains effectively form a homogeneous viscous medium. Relaxation is driven mainly by hydrodynamic chain dynamics and can be represented by;

$$\frac{1}{T_1} \propto -\tau_s \ln(\omega\tau_s) \quad [5.1]$$

where ω is the angular frequency and τ_s is the characteristic time for local in-chain motions. [145, 146]

The renormalised Rouse model accounts for entanglements whereby the chain dynamics are hampered by neighbouring chains. The tube/reptation model assumes

the chain in question is in a constraining tube representing these entanglements. Both of these models show power law dependences of relaxation time on frequency;

$$T_1 \propto M_w \omega^x \quad [5.2]$$

where M_w is the molecular weight of the polymer. The power, x , is dependent on whether the motion is in the inter-chain or intra-chain regime and also on the structural morphology.

In their review of ^{13}C and ^2H NMR studies of chain motion Bovey and Jelinski [147] examined different NMR methods for studying molecular motion along a polymer backbone. ^{13}C NMR T_1 and $T_{1\rho}$ (spin-lattice relaxation time in the rotating frame) experiments were used to observe chain motions in polymers. $T_{1\rho}$ is sensitive to molecular motion in amorphous and most glassy materials. Selective deuteration for ^2H NMR experiments was found to sometimes clarify multiple overlapping chain motions and eliminate spin-diffusion and so simplify the NMR interpretation.

5.1.4.2 NMR Studies of Polyaniline

Conducting polymers add further complexity; the motions of mobile charge carriers in highly conducting doped domains provide an additional relaxation mechanism. However,, a lot of work has been carried out to characterise both the morphology and charge carrier dynamics in these polymers.

Metallic conductance is the main goal for producers of conducting polymers. The first condition for metallic behaviour is a high charge carrier density at the Fermi level (band gap), magnetic susceptibility (χ) measurements are used to study this.

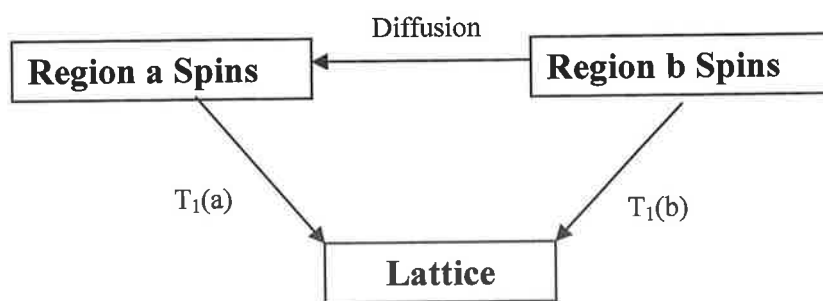
$$\chi_{\text{tot}} = \chi_{\text{curie}} + \chi_{\text{Pauli}} \quad [5.3]$$

χ_{curie} arises from localised spins and χ_{pauli} is proportional to electronic density at the Fermi level. Sariciftci *et al* [148] found evidence that polyaniline doped with CSA yields a material that exhibits metallic-like conduction i.e. with a Pauli susceptibility that was temperature independent as observed for metals. The ^{13}C NMR relaxation rate was observed to increase linearly with temperature obeying a Korringa (metal-like) relationship. However, Wessling *et al* [124] have postulated that this effect may be due to a solvent mediated secondary doping due to processing with *m*-cresol. A similar material using CSA as a dopant synthesised by Lee *et al* [149] using a self-stabilised dispersion technique showed highly crystalline morphology and

conductivity of the order of 1000 Scm^{-1} at room-temperature which increased monotonically with decreased temperature down to 5 K, as observed for metals. Clark *et al* [150] have examined the related conducting polymer polypyrrole- PF_6 , and found that there is a substantial contribution to the temperature dependence of T_1 at very low temperatures ($\leq 10 \text{ K}$) which could only be due to motion of the conducting electrons as is expected in a metallic state.

5.1.4.3 Spin Diffusion

NMR relaxation data of motionally heterogeneous polymers (most conducting polymers) is complicated by magnetic transport via spin diffusion. The measurements can sometimes be internally inconsistent, incompatible with other NMR measurements or disagree with measurements from other sources such as dielectric relaxation. Spin diffusion is the diffusion of coherent magnetisation without diffusion of matter. It occurs among abundant like spins (^1H in polymers) via dipolar coupling and is pronounced in solid-state NMR. Spin diffusion evens out the spatial gradients in magnetisation typically observed in polymers and can average out relaxation information. The gradients are analogous to temperature gradients and can be described in terms of spin temperatures. The spin temperatures describe the deviation from an equilibrium Boltzmann distribution of spin states in a given region of a spin $\frac{1}{2}$ system.



Assuming $T_1(a) \ll T_1(b)$

Figure 5.2 Illustration of the method by which the efficiently relaxing spins in region a can relax the region b spins which are weakly bound to the lattice, redrawn from [151].

NMR spin diffusion measurements can provide information on structural and dynamic heterogeneities in a range of about 10-2000 Å. [152] These measurements are based

on the magnetisation exchange after production of the z-magnetisation gradient by a suitable filter [69]. Variations of this method for measuring spin-diffusion employing double-quantum (DQ) dipolar filters have been used to measure domain sizes in heterogeneous polymers. [153] A method of analysis of motionally heterogeneous polymers proposed by Geppi *et al* [154] is to plot the population weighted rate average (PWRA) of the intrinsic components as a function of temperature. NMR relaxation behaviour is determined both by the intrinsic relaxation behaviour of the different regions in the polymer and by the effects of magnetisation transport. For T_1 relaxation, where intrinsic relaxation times are relatively long, this often leads to the observation of a single exponential decay whose time constant is given by the inverse of the PWRA. However, $T_{1\rho}$ often yields multi-exponential temperature dependence, each component of which is assumed to be due to a motionally heterogeneous region in the polymer. Using a stretched exponential spectral density function the population of each region can be calculated and the motions of processes can be assigned to different sub-phases in the polymer.

5.1.4.5 Spin Dynamics

NMR is also a useful tool in the study of spin dynamics. Spin dynamics studies the motion of spin carriers along the polymer chain. Spin carriers, in this case polarons, are also charge carriers and so the transport properties in conducting polymers may be examined. In conducting polymers the spin-lattice relaxation of nuclear spins is largely due to fluctuations in local fields caused by the nearby moving electronic spins.

The shape of the spectral density, and hence the characteristics of charge carrier dynamics, can be determined from the frequency dependence of T_1 . A straight line dependence of T_1 on $\omega_N^{1/2}$ indicates one-dimensional diffusion of spin carriers along the polymer. The on-chain diffusion rate $D_{||}$ can then be obtained from the slope. [155] T_1 and also T_2 measurements can be used to calculate the intrachain ($D_{||}$) and interchain (D_{\perp}) spin diffusion co-efficients. These parameters characterise the microscopic hopping rates along the chain and between the chains respectively. [18] However, polymers are not perfectly homogeneous along the chain length. Mabboux *et al* [156] studied the proposition that the non-exponential relaxation curves they observed at 15 and 83 MHz in partially doped polyaniline (pH = 3) were due to phase segregation into fully protonated conducting regions and insulated non-protonated

regions. They postulated that the conducting regions have a high concentration of mobile electronic spins and that nuclear spin relaxation is controlled by electron spin dynamics but that the non-protonated region had a low concentration of mobile electronic spins and its relaxation was due to spin diffusion with the doped regions.

Beau *et al* [157] showed that highly conducting polyaniline-CSA is composed of well ordered regions in which spin carriers diffuse quickly and amorphous regions where they diffuse more slowly. Conductivity data shows probable metallic conductance in the well-ordered regions and conductance due to interchain hopping in the disordered region. This hopping motion appeared to be a limiting factor in conduction. The prevalence of the disordered regions is due to a large number of synthetic factors including the effects of different dopants on the electron localisation lengths, dopant size, oxidant/monomer ratio, catalyst type, solution pH, solvent type, secondary doping, and synthesis temperature. [158]

The spectral density for the dynamics and dimensionality of diffusive charge carriers can be developed according to the following argument. [155] In spin dynamics a random walk, or incoherent motion, for the spin carrier is assumed. In a homogeneous space the walker has the same probability $P(t)$ of being at any point within an infinite volume $V(t)$.

$$P(t) \approx \frac{1}{V(t)} \quad [5.4]$$

$V(t)$, is related to the distance covered $r(t)$ and to the dimensionality of the motions, d :

$$V(t) \approx [r(t)^2]^{\frac{d}{2}} \quad [5.5]$$

Therefore, the probability is inversely related to the distance travelled and the dimensionality.

$$P(t) \approx [r(t)^2]^{-\frac{d}{2}} \quad [5.6]$$

For a classical diffusion process the distance travelled increases linearly with time and so there is a direct relationship between $P(t)$ and the diffusion coefficient D :

$$[r(t)^2] = D(t) \Rightarrow P(t) \approx [D(t)]^{-\frac{d}{2}} \quad [5.7]$$

From this relationship the spectral density functions can be derived:

$$J(\omega) \approx (D(\omega))^{-\frac{1}{2}} \quad \text{for } d=1 \quad [5.8a]$$

$$J(\omega) \approx D^{-1} \ln\left(\frac{D}{\omega}\right) \quad \text{for } d=2 \quad [5.8b]$$

$$J(\omega) \approx \text{constant} \quad \text{for } d=3 \quad [5.8c]$$

In nature only quasi-1dimensional rather than the ideal one-dimensional motions exist. This is due to the presence of interchain coupling (the particle has a non-zero probability of hopping to a neighbouring chain), defects and finite chain length, all of which interrupt both $D_{||}$ and D_{\perp} . [155] This results in the probability of the walker coming back to the starting point decreasing rapidly.

There is a discontinuity in the low frequency divergence of $J(\omega)$ which can be interpreted in a crossover from one-dimensional to three-dimensional diffusion with a characteristic crossover frequency (ω_c) which is directly proportional to D_{\perp} . This gives a spectral density function for quasi-1-dimensional diffusion:

$$J(\omega) = \frac{1}{4D_{||}\omega_c} \left[\frac{1 + \sqrt{1 + (\omega/2\omega_c)^2}}{1 + (\omega/2\omega_c)^2} \right]^{\frac{1}{2}} \quad [5.9]$$

Devreux and Lecavalier [159] proposed an anomalous diffusion model to account for relaxation in polypyrrole, a very disordered system. In this theory if the walker is not moving in classical space but on a fractal network, the probability of returning to the starting site is much reduced;

$$P(t) \approx [r(t)^2]^{\frac{\bar{d}}{2}} \quad [5.10]$$

where \bar{d} is the spectral dimensionality of motions within a fractal network, it characterises the anomalous diffusion. The diffusion coefficient is then given by:

$$[r(t)^2] = Dt^{\nu} \quad [5.11]$$

where $\nu = \bar{d}/d_f$, with d_f being the fractal dimensionality of the spatial distribution of protons. \bar{d} is assumed to be less than d_f and so $\nu < 1$. Thus diffusion in a fractal network is anomalous and is less efficient than normal diffusion due to fact that the some of the diffusion paths are unavailable. From this approach the spectral density for a random walk on a fractal network may be obtained:

$$J(\omega) = A\omega^{\frac{\bar{d}}{2}-1} + B \quad \bar{d} < 2 \quad [5.12a]$$

$$J(\omega) = A \ln\left(\frac{B}{\omega}\right) \quad \bar{d} = 2 \quad [5.12b]$$

where A is related to the dipolar coupling strength and B is a constant. Preliminary relaxation measurements on polyaniline by Travers indicated a $\omega^{-1/2}$ dependence of T_1 as expected for one-dimensional charge carrier motion. [140] In a detailed study of spin dynamics in polyaniline by this group in collaboration with Mizoguchi [160] NMR relaxation and ESR data was obtained for a number of polyaniline samples with a range of dopant contents. This is characterised by the y -values, the mole ratio of dopant to monomer units. The theoretical maximum is one dopant molecule every two monomer units (y -value = 0.5). The amine nitrogen cannot normally be protonated as this would disrupt the conjugation along the chain. The spin-lattice relaxation profile from 6-300 MHz showed an increase in relaxation rate at low frequency. This data was fitted with both a quasi-1-dimensional spectral density function (similar to equation 5.9) and a model for anomalous diffusion in a fractal plane (equation 5.12a). [159, 161] The NMR data could be fitted with either function but the ESR data could only be fitted with the quasi-1-dimensional model. Values for $D_{||}$ and D_{\perp} were extracted from the fits. It was observed that $D_{||}$ was independent of dopant concentration and hence the concentration of conducting chains. Therefore, neighbouring chains do not affect the on-chain diffusion as expected. The D_{\perp} values drop rapidly at around $y = 0.2$, suggesting the presence of a percolation threshold. This is supported by the fact that the drop in D_{\perp} was consistent with a decrease in σ_{DC} , which suggests that conductivity is governed by interchain hoppings. However, the extracted $D_{||}$ values are strongly dependent on the dipolar coupling constant used and hence on the internuclear distance (r_{HH}). As there is no crystallographic data available the internuclear spacing between relaxing protons for amorphous polyaniline the value for the coupling constant, and hence $D_{||}$, is subjective. D_{\perp} on the other hand can be obtained from the shape of the spectral density. Mizoguchi [160] also proposed that protonation is not homogeneous and that a conducting domain consists of a single chain surrounded by non-doped non-conducting chains.

Epstein *et al* [162-164] had slightly different interpretation, from x-ray diffraction and low-temperature EPR measurements they describe the system in terms of three-dimensional metallic islands which grow in size with increasing dopant concentration, up to ~ 50 Å at high dopant contents. Below the percolation threshold the slow increase in conductivity is due to the spacing between the polymer chains in the conducting islands decreasing with increasing dopant concentration. Above the

percolation threshold the inter-chain spacing in the islands remains constant but the conducting islands increase in size, decreasing the space between the islands.

5.2 Experimental

5.2.1 Synthesis of Polyaniline HPF_6

5.2.1.1 Oxidative polymerisation of polyaniline using HPF_6

An initial sample of polyaniline doped with hexfluorophosphoric acid (HPF_6) was prepared by our collaborators in Dr Dermot Diamonds group in the NCSR, DCU. The reaction involved the simultaneous polymerisation and doping of distilled aniline by stirring overnight in the oxidant ammonium persulphate (APS) and the dopant HPF_6 at room temperature. A blue to green colour change indicated the presence of a significant proportion of emeraldine salt. The resulting green-black solution was filtered, washed with room temperature distilled water to remove excess free acid and air-dried. The final product was a fine green-black powder (sample HPF_61), which was characterised by FFC-NMR relaxometry

5.2.1.2 Reduced dopant levels by sample washing

In order to obtain a stable compound with a lower dopant level, 0.52 g of the highly doped polyaniline HPF_6 from the previous synthesis was washed with distilled water at room temperature until the pH of the washings was ~ 4 and unchanging. This required approximately 2 L of water. At this point it was assumed that no further dopant was being removed. Following air drying the product was again a fine green powder (sample HPF_62), which was characterised by FFC-NMR.

5.2.1.3 Doping of polyaniline emeraldine base with HPF_6

Due to the unpredictable nature of polymerisation reactions which can give rise to different chain lengths, molecular weights, branching etc., it was thought that by doping undoped polyaniline emeraldine base of known molecular weight, greater control of the sample properties could be obtained. In a typical synthesis, 0.55 g of polyaniline emeraldine base (MW $\sim 65,000$, Aldrich) was stirred overnight in 1 M HPF_6 at room temperature, following the procedure described in Kahol *et al.* [158] The solution was then filtered and washed with ~ 100 ml of distilled water, air-dried

for two hours then oven-dried overnight in a 313 K oven. The product was a fine green powder (sample HPF₆3), which was characterised by FFC-NMR.

5.2.2 Synthesis of Polyaniline TFSA

5.2.2.1 Doping of polyaniline emeraldine base with LiTFSA

A sample of 0.26 g Polyaniline base (MW ~65,000 Aldrich) was dissolved in a minimum (<30 ml) of n-methyl pyrrolidone (nMP) yielding a viscous blue liquid. Polyaniline is insoluble in most organic solvents and only sparingly soluble in nMP. A half-molar equivalent of lithium triflate (0.04 g) was added and the reaction mixture stirred overnight at room temperature. The mixture remained blue so it was assumed that no reaction had occurred. The suspension was left stirring for another 48 hours and no further change was observed. As an attempt to start the reaction ~3 ml of 1 M triflic acid was added to the mixture which was then stirred overnight at room temperature. This suspension turned green on addition of 1 M TFSA but the green colour disappeared on stirring. The apparent doping on addition of acid is consistent with the unique doping mechanism of polyaniline in which doping is by protonation. Finally the resulting blue-black solution was filtered, washed with room temperature distilled water to remove excess free acid/salt and air-dried. The final product was a fine blue-black powder which suggests that the attempt at doping was unsuccessful.

5.2.2.2 Doping of polyaniline emeraldine base with TFSA

The synthetic procedure was adapted from the method of Kahol *et al.* [158] In a typical reaction ~0.55 g polyaniline emeraldine base (Aldrich, MW~65,000) was stirred overnight in 60 ml of 0.5 M aqueous solution of the dopant triflic acid (trifluoromethanesulphonic acid, TFSA) at room temperature. The resulting green-black solution was filtered and washed with ~100 ml of distilled water, air-dried for 4 hours then oven-dried overnight in a 40⁰ C oven. The product was fine green powder. 10 samples were synthesised using a similar synthetic route to produce a range of samples of different dopant concentration. Samples TFSA1, TFSA2, TFSA4, TFSA5, TFSA7, TFSA8 and TFSA10 used ~0.5 M triflic acid while sample TFSA6 used ~0.7 M, TFSA3 used 0.35 M and TFSA9 used 0.2 M triflic acid during the synthesis. These samples were characterised by a number of techniques including FFC-NMR, conductivity, microanalysis, Raman, and SEM.

5.2.2.3 Synthesis of polyaniline with a reduced dopant level

In order to obtain a sample with a lower dopant concentration, ~0.25 g of the highly doped material from the TFSA4 synthesis was washed with distilled water at room temperature until the pH of the washings was ~4 and unchanging. This required approximately 2 L of water. The product was a fine green powder and was labelled TFSA4a. Again this sample was characterised by FFC-NMR, conductivity, microanalysis, raman, and SEM.

5.2.3 Conductivity measurements

Conductivity measurements were performed using the four-point probe method. [54] The four-point probe method is appropriate for measuring resistivity and hence conductivity across a wafer or thin film. The four point probe consists of two current carrying probes (1 and 4), and two voltage measuring probes (2 and 3). Since very little contact and spreading resistance is associated with the voltage probes, one can obtain a fairly accurate calculation of the sheet resistance which is then used to calculate the resistivity. The resistivity (ρ) of a semi-infinite wafer is given by:

$$\rho = s \frac{\pi}{\ln 2} x \frac{V}{I} \quad [5.13]$$

where ρ is the resistivity ($\Omega \text{ cm}^{-1}$), s is the pin spacing (cm), V is the measured voltage (volts) and I is the source current (Amperes). The conductivity is simply the inverse of the resistivity and is measured in Scm^{-1} .

Polyaniline samples were pressed into pellets ~1 cm diameter. For most of the samples the current was varied from -20 to 20 mA and voltages were measured in that range. The pin spacing was 0.1 mm.

5.2.4 FFC-NMR

The NMR measurements were carried out on the Stelar spinmaster FFC-NMR 2000 relaxometer using pre-polarised and non-polarised sequences, as described in Chapter 2. The magnetisation recovery curves were mono-exponential at all fields and at all temperatures for all of the samples.

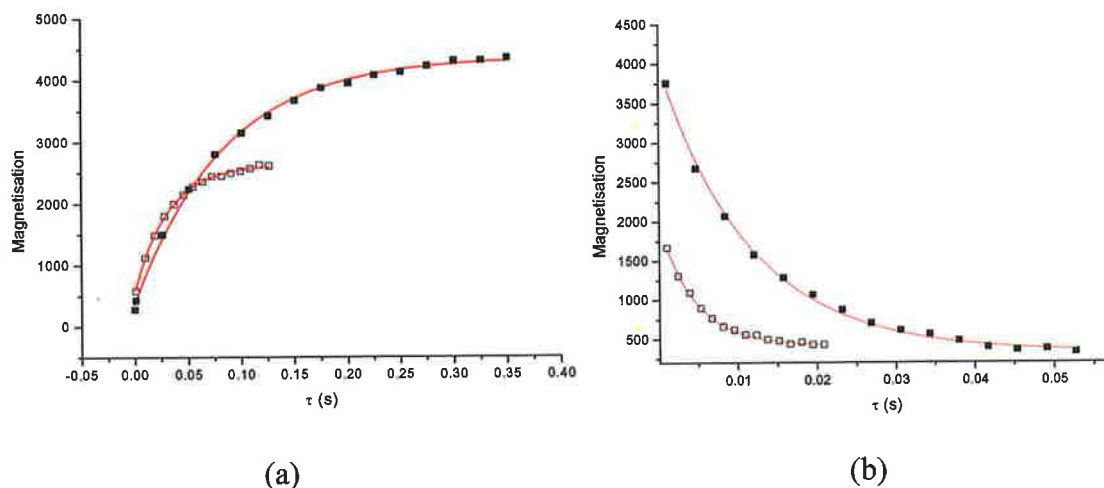


Figure 5.3 Magnetisation equilibration curves for highly doped polyaniline TFSA (sample TFSA2) at 323 K (■) and 263 K (□) at a) 10 MHz and b) 0.1 MHz.

A Bruker minispec is a high resolution single low field spectrometer with much better B_0 homogeneity than the field cycling magnet. A free induction decay recorded for an amorphous polyaniline TFSA (TFSA2) sample at 60 MHz (figure 5.4a) clearly shows two components which may be assigned to contributions from the undoped and doped regions of the polymer. However, the T_2^* of the field cycling magnet is $\sim 250 \mu\text{s}$ so the FID measured for doped polyaniline using this magnet contains contributions from both magnetisation components. However, the fact that the magnetisation is mono-exponential suggests that contributions from both regions are averaged by rapid spin diffusion between the regions. The magnetisation was sampled by summing the intensity in the time range indicated by dashed lines (3-30 μs) in figure 5.4. The extracted T_1 was always insensitive to the interval used for this summation, although extending the interval to longer times (greater than 30 μs) increased the error in T_1 .

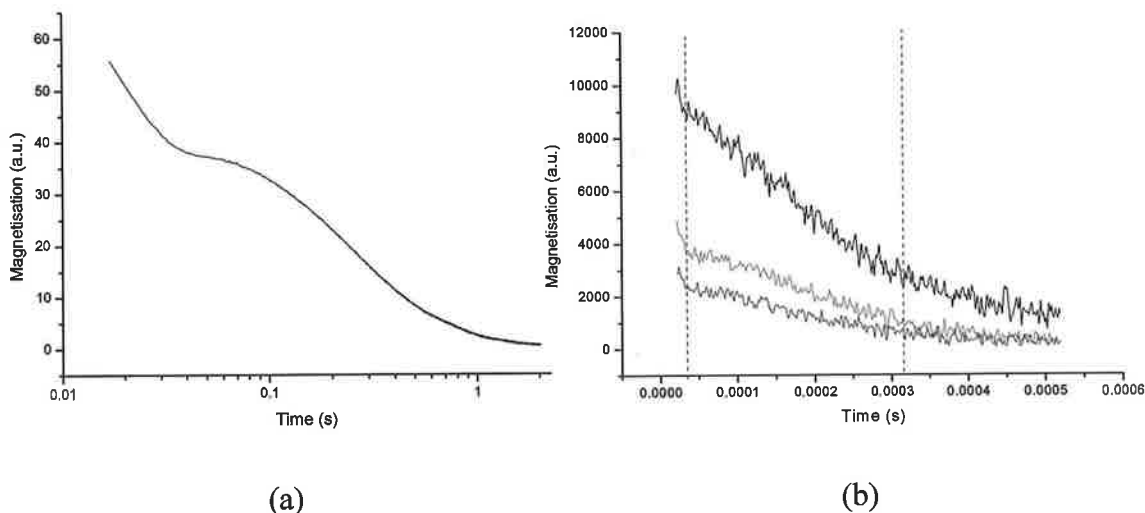


Figure 5.4 (a) Free induction decay of sample TFSA2 recorded using a Bruker minispec showing the crystalline and amorphous parts of the FID and (b) FIDs recorded on the field-cycling magnet for samples TFSA2 (-), TFSA6 (-) and TFSA3 (-), each recorded with 64 scans, showing monoexponential decays.

5.3 Results

5.3.1 ^1H NMR of Polyaniline HPF_6

Preliminary measurements on sample HPF_61 were made at ambient temperature (297 K). The ^1H profile exhibited a pseudo-Lorentzian shape. The measurements were repeated immediately and showed good reproducibility. However, on repeating the measurement a number of days later the profile changed and etching of sample tube was apparent. This was probably due to the dopant, as HPF_6 , leaching from sample into the glass. The observed increase in relaxation rate (figure 5.5) is consistent with reduced dopant levels, as observed in the ^1H profile of a water-washed sample. Heating the sample accelerated the leaching.

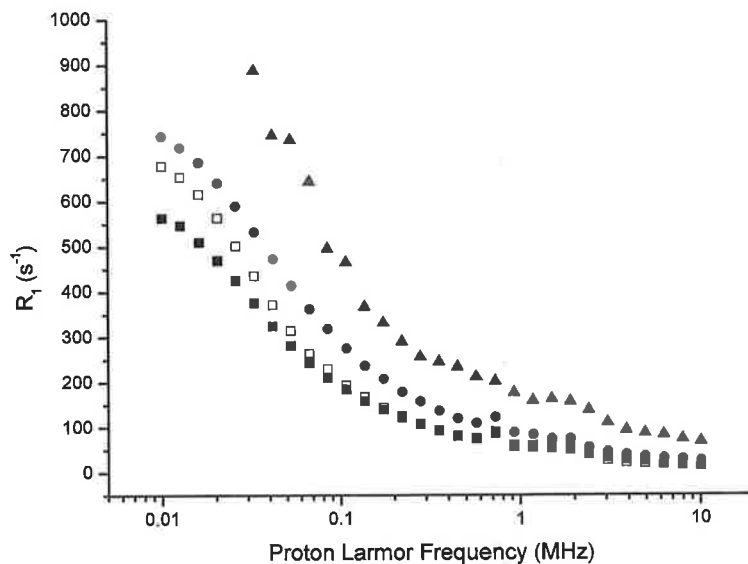


Figure 5.5 ^1H relaxation profiles of highly doped polyaniline PF_6 (HPF₆1) at 297 K recorded shortly after synthesis (■), after heating to 323 K (□) and after 4 weeks (●). Also shown is the relaxation profile of a less doped water-washed sample (▲).

A number of approaches were then taken to try to prevent the loss of dopant. The first involved fitting a drying tube to the NMR tube in order to exclude water. However, NMR experiments conducted over a number of weeks showed that water was not a factor. Another approach involved using a PTFE tube liner inside the glass NMR tube. The sample was placed inside the PTFE tube. This tube is inert to acid and it was hoped that the dopant would not leach out in the liner. Again, however, the NMR experiments showed that over a number of weeks the sample was not stable.

Relaxation profiles were measured over a wide temperature range (233-348 K). Inspection of the profiles recorded above ambient temperature suggests a relaxation mechanism that is temperature activated and where the approximately Lorentzian dispersion moves to higher frequency with increased temperature

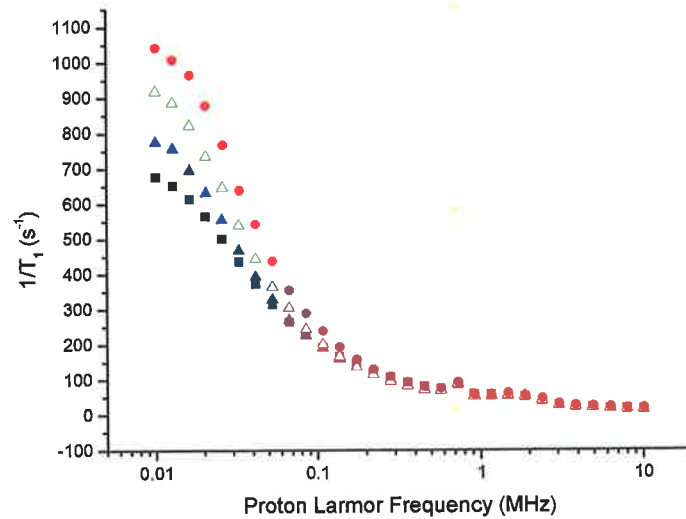


Figure 5.6 ^1H relaxation profiles of sample HPF_61 at 297 K (■), 308 K (▲), 323 K (△) and 348 K (●).

However,, as the material is cooled below room temperature very different behaviour is observed. The spectral density functions shift to higher frequency as the temperature is decreased. Hence they cannot be simply related to a thermally controlled motional process. It is likely that in addition to relaxation due to polymer chain dynamics modulating ^1H - ^1H dipolar interactions a second relaxation mechanism is operating, presumably related to the presence of mobile charge carriers. This is also indicated by the decrease in R_1 on loss of dopant.

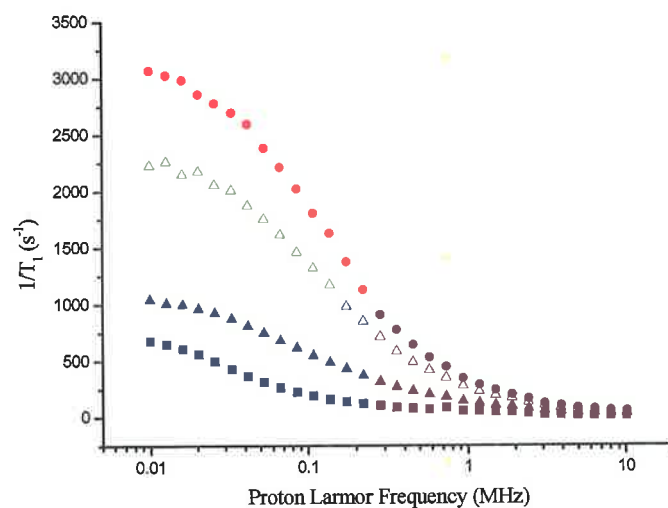


Figure 5.7 ^1H NMR profiles of sample HPF_61 at 297 K (■), 273 K (▲), 263 K (△) and 253 K (●).

However, a sample, prepared by water-washing the highly doped polyaniline HPF₆ to remove dopant, showed very little temperature dependence in the accessible range. All the samples prepared using PF₆ showed continuous gradual leaching of dopant. For this reason this data cannot be analysed further.

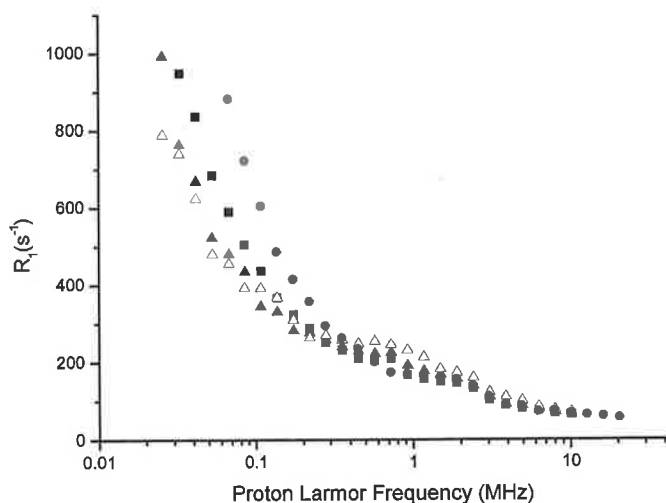


Figure 5.8 ¹H relaxation profiles of water washed sample HPF₆2 at 323 K (●), 297 K (■), 273 K (Δ) and 253 K (▲).

5.3.3 ¹H NMR of Polyaniline TFSA

To prevent dopant leaching a different less mobile dopant was used in the subsequent polyaniline samples. The criteria for choosing an alternative dopant were, as with HPF₆; moderate to high conductivity of the doped polymer, and the dopant should contain fluorine, but no hydrogen atoms, so the ¹H NMR response can be solely attributed to the polymer and the ¹⁹F NMR response to the anion. To this end the dopant trifluoromethanesulphonic acid (triflic acid or TFSA) was chosen. To ensure reproducible polymer structure, the synthesis was by doping of emeraldine base of a known molecular weight (~65,000 MW).

5.3.3.1 High Dopant Content

The first sample, TFSA2, appeared to be stable over a period of a week. Following this time the sample was heated and cooled in order to obtain profiles at different temperatures and after each period of heating the profile at ambient temperature (297

K) was recorded and was found to match the original profile (figure 5.9). Similar thermal exposure had resulted in significant leaching of HPF_6 in the previous samples. The TFSA sample remained stable over a period of several weeks, which was found to be the case for all of the TFSA doped samples regardless of dopant content.

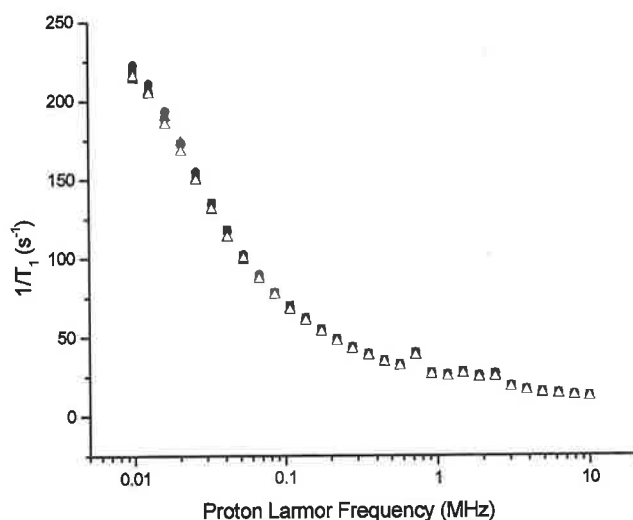


Figure 5.9 ^1H relaxation profiles of sample TFSA 2 at 297 K recorded shortly after synthesis (\blacksquare), after heating to 323 K (\blacktriangle) after cooling to 263 K (\bullet) and after two weeks (\triangle).

The relaxation profiles showed similarly shaped curves to the polyaniline HPF_6 samples but the value of R_1 is substantially different, which may indicate increased dopant content.

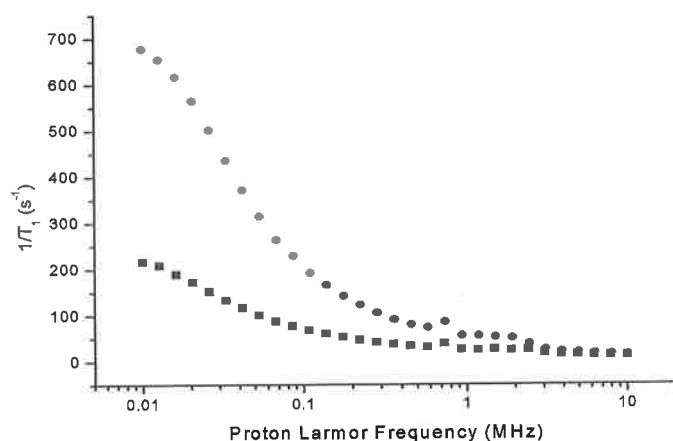


Figure 5.10 ^1H NMR profiles comparing the polyaniline doped with TFSA (TFSA2) (\blacksquare) and HPF_6 (HPF_61) (\bullet).

A number of relaxation profiles were recorded over the temperature range 253 - 348 K. Subsequent microanalysis showed that this sample was relatively highly doped. Its relaxation response showed similar temperature dependence to the highly protonated polyaniline PF₆ sample. The dispersion moved to lower frequency as the temperature was increased, over the whole temperature range. This is strong evidence that relaxation is not due to the modulation of the ¹H-¹H dipolar interaction by molecular motion.

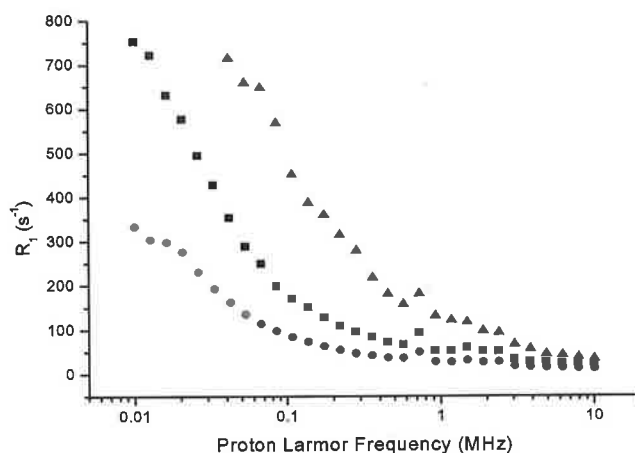


Figure 5.11 ¹H relaxation profiles of the highly doped sample TFSA2 at 253 K (▲), 297 K (■), and 343 K (●).

5.3.3.2 Intermediate Dopant Content

A sample, TFSA3, was synthesised using an acid concentration of 0.35 M as compared to 0.5 M for the previous samples. A number of NMR profiles were recorded over the temperature range 253 - 348 K. Microanalysis showed that this sample had an intermediate dopant content and, as observed previously for lower dopant content samples, the observed NMR response is closer to that of an undoped polymer. The FID shows that T₂ is shorter and as a result the signal-to-noise ratio of the data is poorer. The NMR response is weakly temperature dependent in the accessible temperature range.

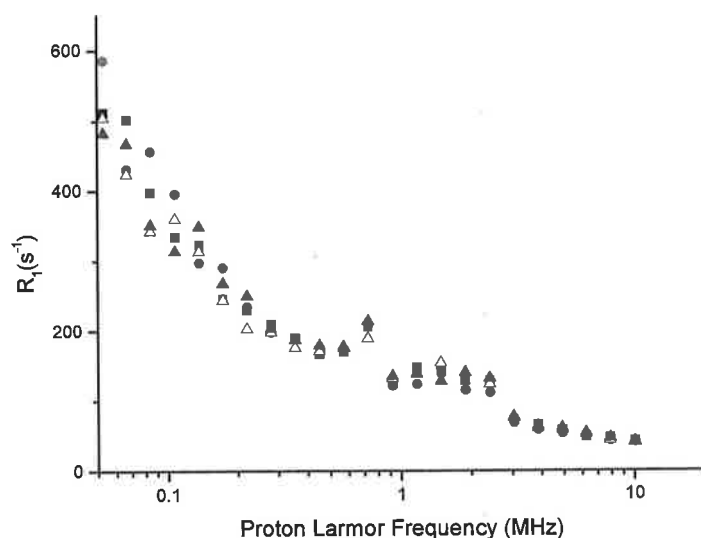


Figure 5.12 ^1H relaxation profiles of the low dopant content sample TFSA3 at 253 K (▲), 268 K (△), 297 K (■), and 323 K (●).

5.3.3.3 Low Dopant Content

Another route to producing samples with lower dopant levels is to dedope the highly doped polyaniline TFSA samples by water washing. The synthesis described for TFSA2 was repeated and yielded a highly doped material (sample TFSA4) with a similar temperature response. This material was then water washed until the washings had a constant pH 4. The resulting green-black solution was then redried and the relaxation profile was recorded. This sample was labelled TFSA4a. The shape and temperature dependence of the ^1H profile of this water-washed sample are different to that of the highly doped sample. There is no measurable temperature dependence of the spin lattice relaxation as expected for a sample of low dopant concentration.

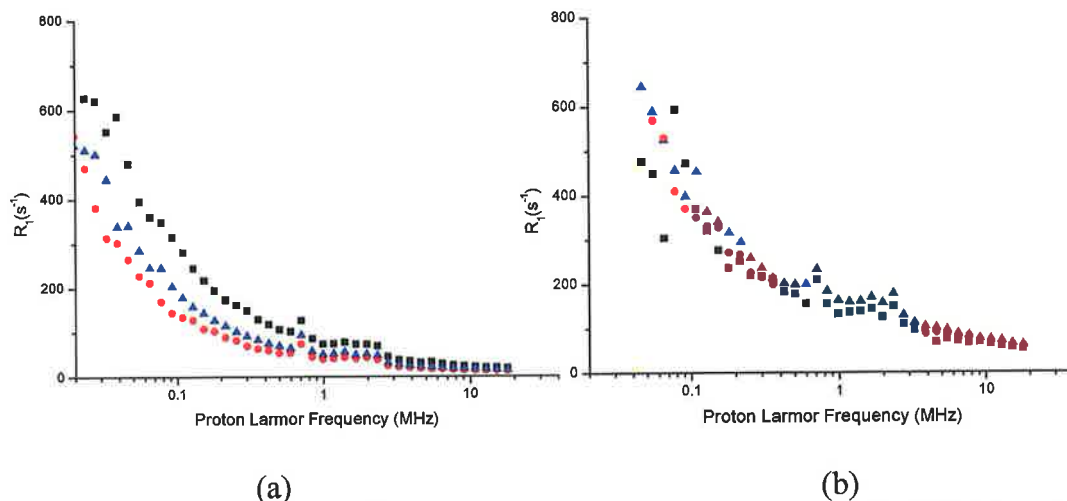


Figure 5.13 ^1H relaxation profiles showing of (a) highly doped sample TFSA4 and (b) reduced dopant content TFSA4a at 297 K (■), 318 K (▲) and 323 K (●).

5.3.4 ^{19}F NMR of Polyaniline TFSA

As only the dopant anion contained fluorine it was possible to use ^{19}F NMR relaxometry to probe dopant mobility. It was found that changing the dopant concentration made little difference to the ^{19}F NMR response. All of the samples gave similar, apparently pseudo-Lorentzian, profiles at ambient temperature. There was little or no temperature dependence measurable in the accessible range.

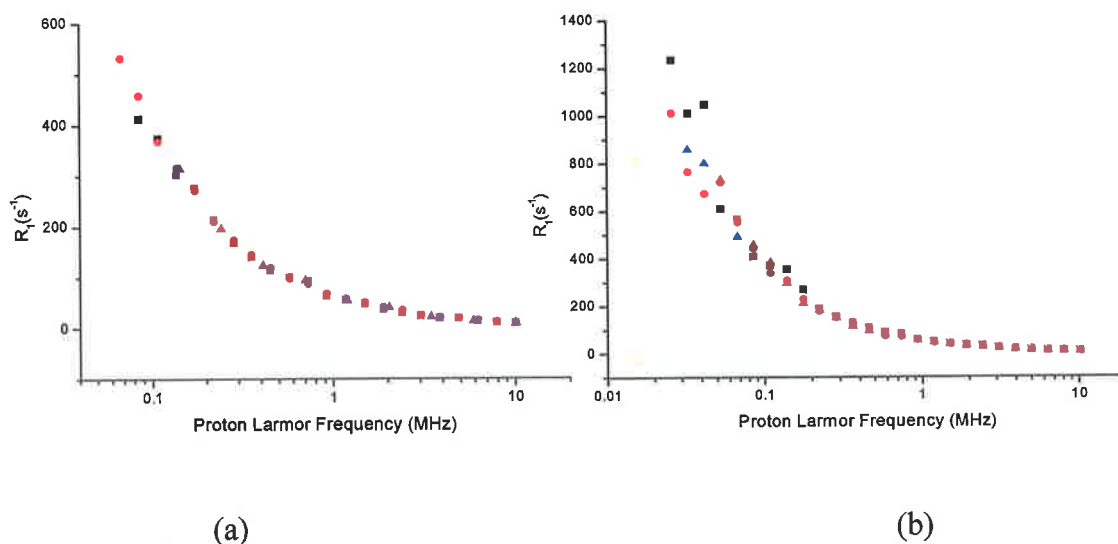


Figure 5.14 ^{19}F relaxation profiles of (a) highly doped TFSA2 (■), reduced acid concentration sample TFSA3 (▲) and water-washed sample 4a (●) at 297 K and (b) highly doped sample TFSA2 at 297 K (■), 318 K (▲) and 323 K (●).

5.3.5 Dopant Concentration (y-values)

The dopant concentration or y-value is the number of dopant molecules per monomer unit along the polymer backbone. The theoretical maximum is one dopant molecule every two monomer units (y-value = 0.5). The imine nitrogen cannot normally be protonated as this would disrupt the conjugation along the chain. The dopant concentration is calculated by CHN elemental microanalysis. This involves the flash oxidation of samples (at ~1000 K) followed by chromatographic separation, detection with a thermal conductivity detector and comparison to a standard. The average error is usually 0.2 % but clearly the sample must be pure and solvent free. From this technique the %weights of C, H and N in each sample were determined. The F content was determined by fluorometric titration. By comparing the %wt of N, one per monomer unit, to the %wt of F, three per dopant anion, and scaling for the atomic weights the number of dopant molecules per monomer unit, or the y-value, can be calculated. Table 5.1 shows the y-values for all of the samples prepared using triflic acid as the dopant and the concentration of acid used in the synthesis.

5.3.6 Conductivity Measurements

Conductivity is the inverse of resistivity and resistivity is proportional to voltage(V)/current(I). The following V/I curves recorded for various TFSA samples are all linear ($R^2 = 0.999$) and pass through the origin, proving the validity of both the method and our home-built equipment for use in this application.

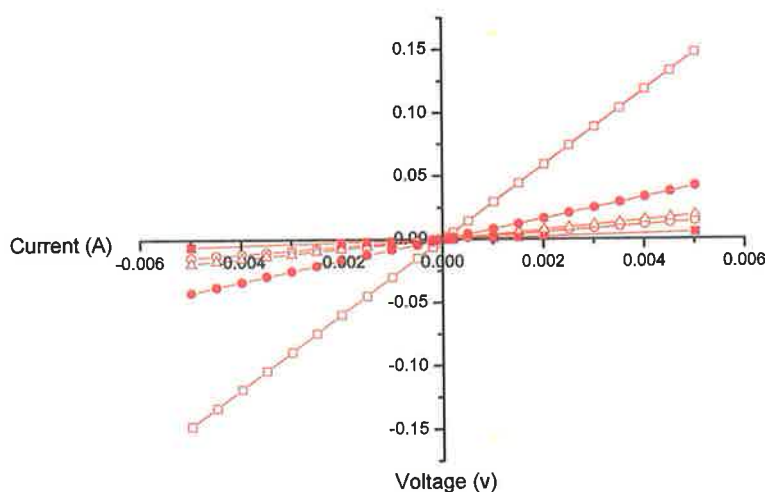


Figure 5.15 Typical V/I curves for samples TFSA5 (Δ), TFSA6 (\blacksquare), TFSA7 (\bullet), TFSA9 (\square) and TFSA10 (\circ).

Using this data and equation 5.5, the conductivity for each of the TFSA samples was determined. As our current source is accurate to nA and the voltmeter to μV the results are accurate to the third decimal place. The table below shows the conductivities for all of the samples prepared using triflic acid as dopant and other relevant parameters. The y-value varies from preparation to preparation, even for those performed with similar reaction conditions, for a number of reasons, one of which was that triflic acid fumes heavily in air and preparing an acid solution with a consistent concentration was difficult.

Table 5.1 Bulk physical properties of polyaniline TFSA samples

Sample	TFSA conc (M)	y-value	Conductivity (Scm^{-1})
Pani TFSA 1	~0.55	0.373	2.50
Pani TFSA 2	~0.55	0.389	4.86
Pani TFSA 3	~0.35	0.346	1.11
Pani TFSA 4	~0.55	0.399	4.35
Pani TFSA 4a	~0.55*	0.268	0.03
Pani TFSA 5	~0.55	0.379	4.18
Pani TFSA 6	~0.75	0.488	11.46
Pani TFSA 7	~0.55	0.360	1.90
Pani TFSA 9	~0.2	0.234	0.53
Pani TFSA 10	~0.55	0.410	5.48

*washed

5.3.7 Raman Spectroscopy

Raman spectroscopy has been used to study the structure of polyaniline in the solid state. [165, 166] The Raman spectra of polyaniline TFSA (figure 5.16) were similar to that presented in the literature for polyaniline doped with HCl and the main features were assigned to the relevant functional groups (table 5.2).

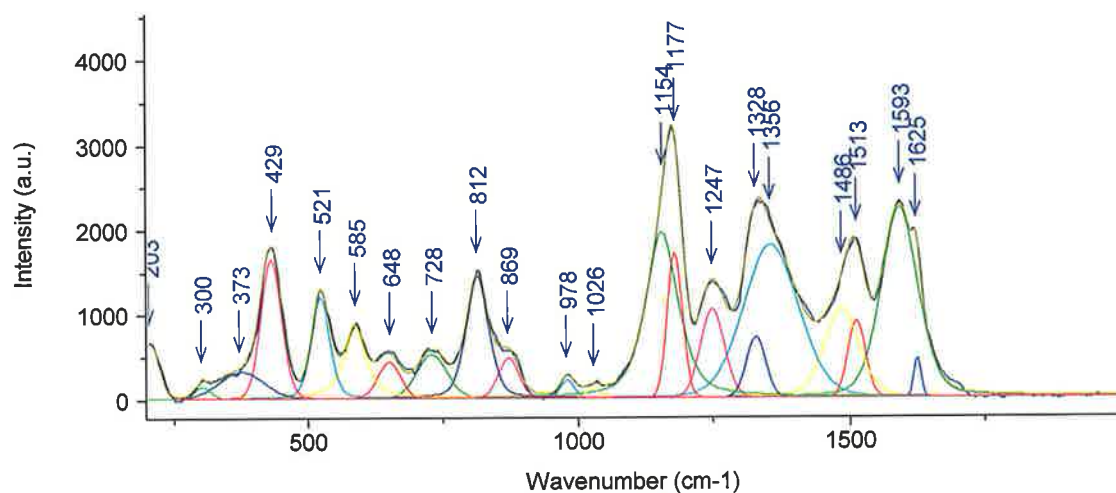


Figure 5.16 Raman spectra of sample TFSA2 showing polymer region ($> 1160 \text{ cm}^{-1}$) and the dopant region ($200\text{-}1160 \text{ cm}^{-1}$).

Table 5.2 Assignment of vibrations from Raman spectra of highly doped polyaniline TFSA (figure 5.16)

Features (cm^{-1})	Assignment
1625	C-C in-plane (ip) stretching of benzoid
1593	C-C ip stretching of benzoid and quinoid
1513	C-C stretching + ip C-H deformation
1485	ip N-H bending
1350	C-N stretching (polaronic radical cation)
1328	C-N stretching (polaronic radical cation)
1247	Ring vibration
1177	ip C-H bending modes of benzoid ring
1154	Symmetric SO stretch
1026	Ring vibration
978	Ring vibration
869	C-S stretch
812	Ring vibration <i>p</i> -disubstituted benzene/ C-S asymmetric stretch
728	Sulphoxide C-S stretch
585	SO ₂ def (covalent sulphonates)
521	SO ₂ deformation
429	C-S-O deformation

The spectra can be divided into two regions; the low wavenumber range (300-1100 cm^{-1}) can be assigned solely to the dopant and the higher wavenumber range (1100-1800 cm^{-1}) to the polymer. The peaks at ~ 1350 and 1328 cm^{-1} can be assigned to the polaronic radical cation and the relative intensity of these peaks has been used as a qualitative monitor of the concentration of charge carriers and hence oxidation levels. [81] The spectra of the polymer region, (figure 5.17), show the relative decrease in intensity of the band at $\sim 1330 \text{ cm}^{-1}$ and an increase in intensity of the band at 1370 cm^{-1} with decreasing dopant content.

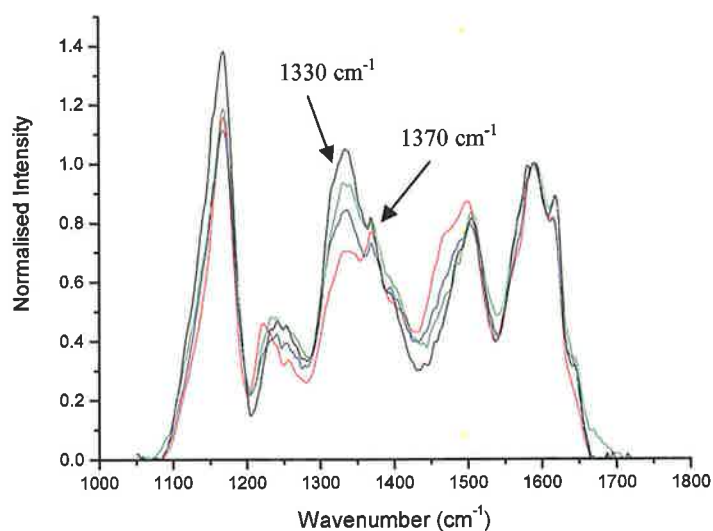
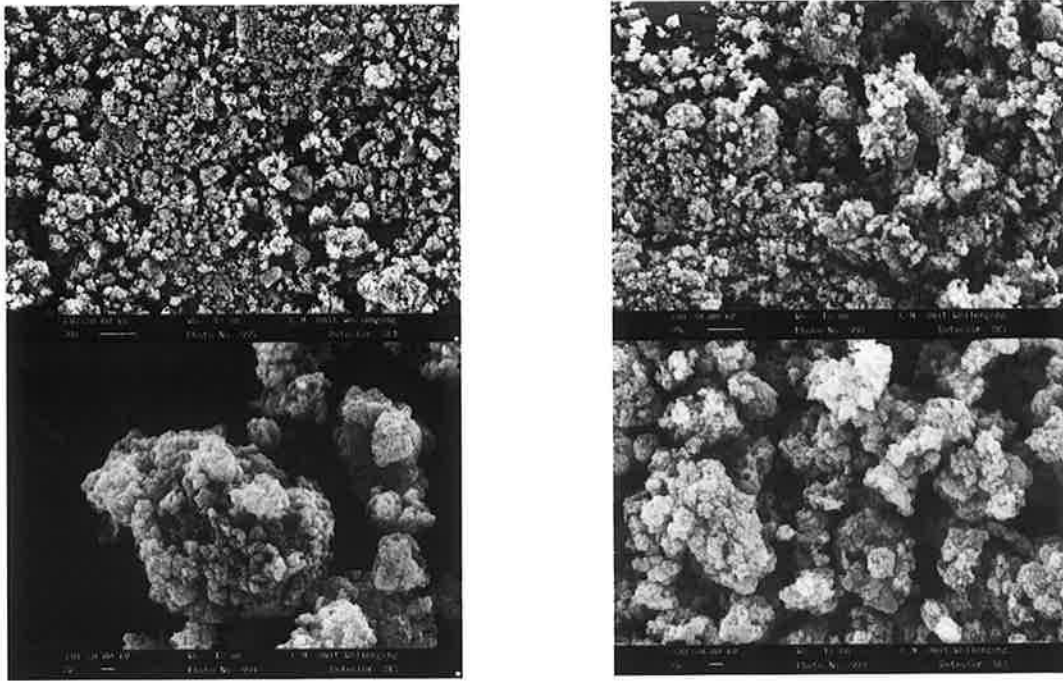


Figure 5.17 Raman spectra of polymer region, normalised wrt the band at 1587 cm^{-1} of samples TFSA4 (black, y-value = 0.399), TFSA2 (green, y-value = 0.389), TFSA3 (blue, y-value = 0.346), TFSA4a (red, y-value = 0.268).

5.3.8 Scanning electron microscopy (SEM)

SEM images of the samples were recorded to ascertain if there was any correlation between the polymer morphology and the conductivity or the NMR response. According to the model for conductivity due to polaron motion, the matrix consists of highly crystalline conducting regions (1-100 nm) which are separated by large regions of amorphous undoped polymer. [18] Transport through the amorphous regions limits the conductivity. Thus if the crystallinity increased one would expect the bulk conductivity to increase. SEM images were recorded on a number of samples across the range of dopant content. However, no increase in crystallinity was observed, the samples were amorphous irrespective of the dopant content.



(a)

(b)

Figure 5.18 SEM images showing consistent amorphous morphology of (a) high dopant concentration sample (TFSA2), and (b) low dopant concentration sample (TFSA4a).

5.4 Discussion

While the NMR results are interesting in their own right, interpretation requires that they are placed in context with other known physical properties. In this section the NMR data and other measurements performed on polyaniline TFSA will be discussed.

5.4.1 Bulk Analysis (γ -values and conductivity)

As expected the γ -values and conductivity were found to be related, an increase in dopant levels generally results in an increase in conductivity. This is due to the fact that the limiting factor in ICP conductivity is thought to be charge carrier motion between conducting regions through the amorphous non-conducting regions. An increase in dopant concentration should result in either an increase in the number of conducting domains and/or their size. Thus, increasing dopant content results in shorter paths through the non-conducting region, and increased conductivity.

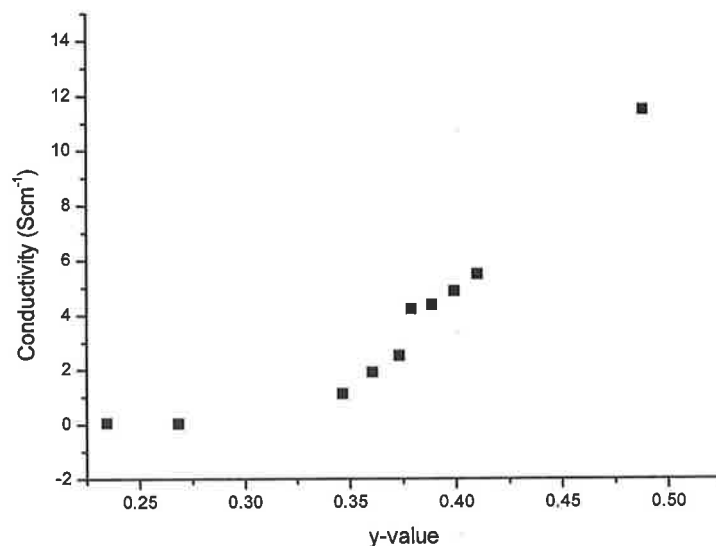


Figure 5.19 Plot showing the dependence of conductivity of polyaniline TFSA on the dopant content.

Plotting conductivity as a function of dopant concentration in this way suggests a dopant level above which the conductivity increases dramatically.

5.4.2 ¹H NMR Analysis

5.4.3.1 *Quadrupolar Dips*

The expected gradual, smooth increase in T_1 with field strength, for doped ICP samples is often superimposed by three pronounced 'dips' (figure 5.20) where the T_1 value drops by 10% or even more over a small range of field strengths at well-defined frequencies (0.74 MHz, 1.56 MHz and 2.30 MHz). These are ¹⁴N quadrupolar dips [77] and occur in the spin-lattice relaxation dispersion when the ¹H magnetisation additionally relaxes to the lattice through a quadrupole transition (¹⁴N) via a level crossing. Spin $\pm 1/2$ nuclei, like ¹H do not have quadrupole moments but nuclei with spin $> 1/2$, like ¹⁴N, almost always do. An $I = 1/2$ spin system such as a ¹H exhibits two Zeeman levels. However, at these level crossings there will be more than the allowed two Zeeman levels and a static electric field gradient will perturb these levels. The ¹H nuclei can undergo a second relaxation process when the resonant frequencies of the ¹H and ¹⁴N spin systems match. The additional quadrupole interactions experienced at these field strengths cause enhanced spin-lattice relaxation. [167] T_1 is

reduced at these field strengths because the nuclear spins of hydrogen atoms on the 'backbone' of the molecules are strongly coupled to the nuclear spins of adjacent nitrogen atoms, and this enhances the efficiency of proton NMR relaxation at the quadrupole resonance frequencies and produces a dip in the T_1 dispersion curve.

Kimmich and Anoardo [50] have shown that the observation of quadrupolar dips in organic macromolecules and biopolymers with restricted side-group motions is due to a relaxation mechanism arising from backbone fluctuations. The observation of a similar effect in doped polyaniline suggests that the relaxation mechanism is at least partially due to backbone fluctuations.

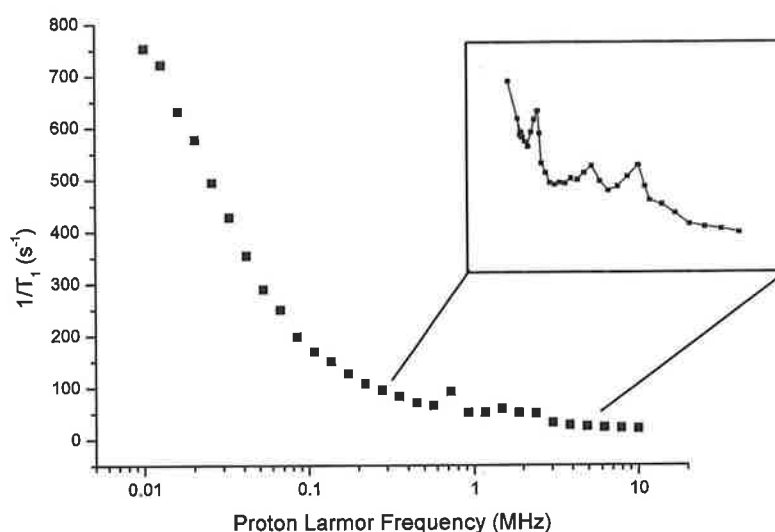


Figure 5.20 ^1H NMR profile of TFSA 2 showing ^{14}N quadrupolar dips.

5.4.3.2 Fractal networks and dimensionality

The rates and characteristics of chain motions in polymers are not determined by local barriers to motion, but are better modelled by scaling laws. As a result the spectral densities conform to power law functions. BPP or even Cole-Cole, spectral density functions usually fail to reproduce the ^1H profile (figure 5.21).

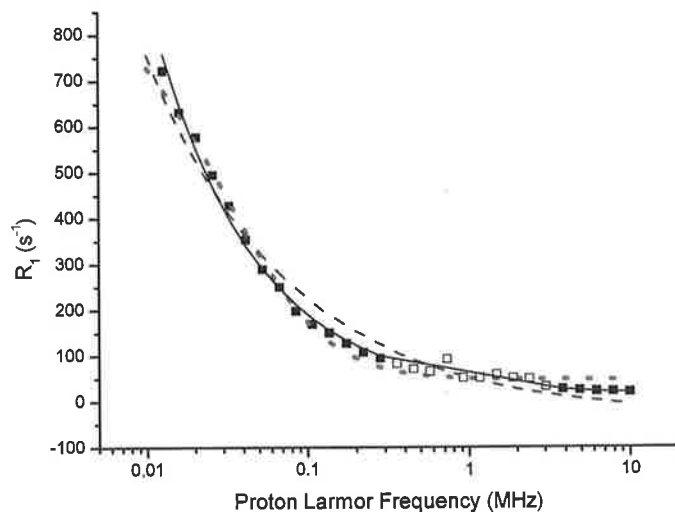


Figure 5.21 ^1H NMR profile of TFSA 2 (■) fitted with BPP (···), Cole-Cole (--) and a power-law (-) spectral density functions. For the purpose of fitting the quadrupolar dip region was omitted (□).

Travers early work on spin dynamics by NMR in polyaniline showed one-dimensional diffusion of spin carriers. [155] However, this paper describes a single polyaniline sample of unknown dopant concentration measured in a limited field range. In a more detailed study of spin diffusion in a range of emeraldine salts with varying dopant levels, Mizoguchi et al [160] observed several low-dimensional features. ^1H relaxation profiles recorded from 6-300 MHz were fitted to both a quasi-1-dimensional model and a power-law model for anomalous diffusion, i.e. a random walk on a fractal network.

Fitting the relaxation profile of a highly doped polyaniline-HCl ($y = 0.62$) sample to the fractal model (equation 5.12b) showed an apparent dimensionality of almost two. It was also possible to fit this data using a model for quasi-1-dimensional behaviour (equation 5.9). The ESR linewidth data suggested quasi-1-dimensional motion of charge carriers, in good agreement with the NMR data. However, a y -value > 0.5 indicates overdoping and there may be partial chlorination of the benzyl rings which may cause structural changes that could alter the morphology and conductivity. [162] The accessible frequency range in our study is from 0.001-20 MHz depending on experimental conditions, whereas the frequency range in Mizoguchi's study was 6-300 MHz. Below the minimum field in the earlier work and in our working field range a further relaxation dispersion is apparent. This can be observed quite clearly from the normalised relaxation plot (figure 5.22b).

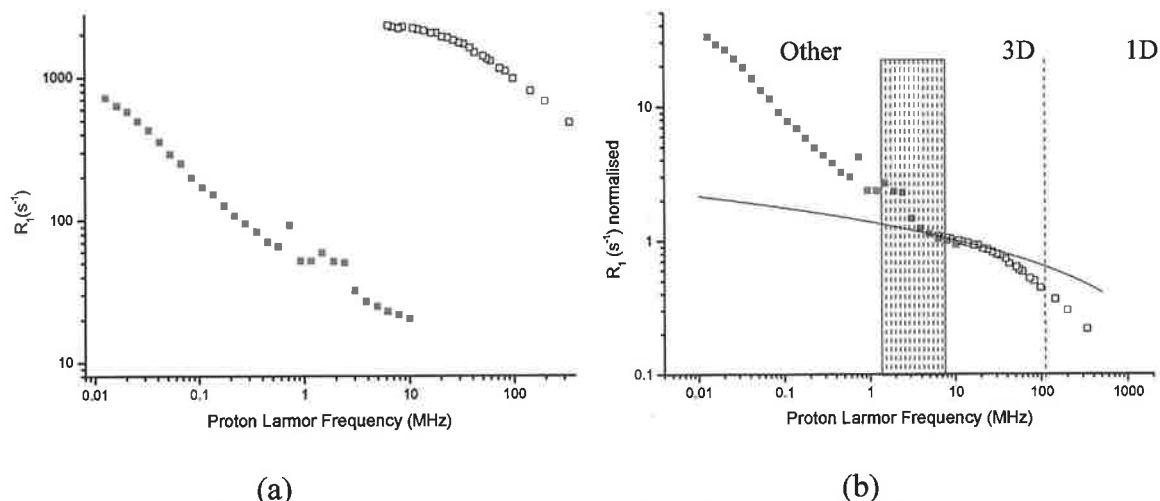


Figure 5.22 (a) ^1H NMR data (\square) for polyaniline doped with HCl ($y = 0.62$) from Mizoguchi *et al*, [160] and data at lower field from this work on polyaniline TFSA (\blacksquare , $y = 0.389$, sample TFSA2) (b) data for both samples normalised to $R_1 = 1 \text{ s}^{-1}$, at 10 MHz. The solid black line is the ideal fit to three-dimensional behaviour.

Mizoguchi *et al* showed that the frequency dependence of the relaxation for all the samples in their study approached $\omega^{-1/2}$ at high frequency, which is characteristic of one-dimensional diffusion. At a cut-off frequency (ω_c) of the order of 10^8 - 10^{11} s^{-1} , a crossover from one-dimensional diffusion at high field to three-dimensional diffusion at lower field was inferred from by a change in the frequency dependence, as indicated in figure 5.22b. This cross-over frequency is outside the frequency window of the field-cycling experiments presented in this thesis (10^4 - 10^8 s^{-1}). Thus the expected one dimensional diffusion regime is not observed and the second low field dispersion is either due to a slower dynamic process or a mechanism, other than diffusion of charge carriers, driving relaxation in this field range.

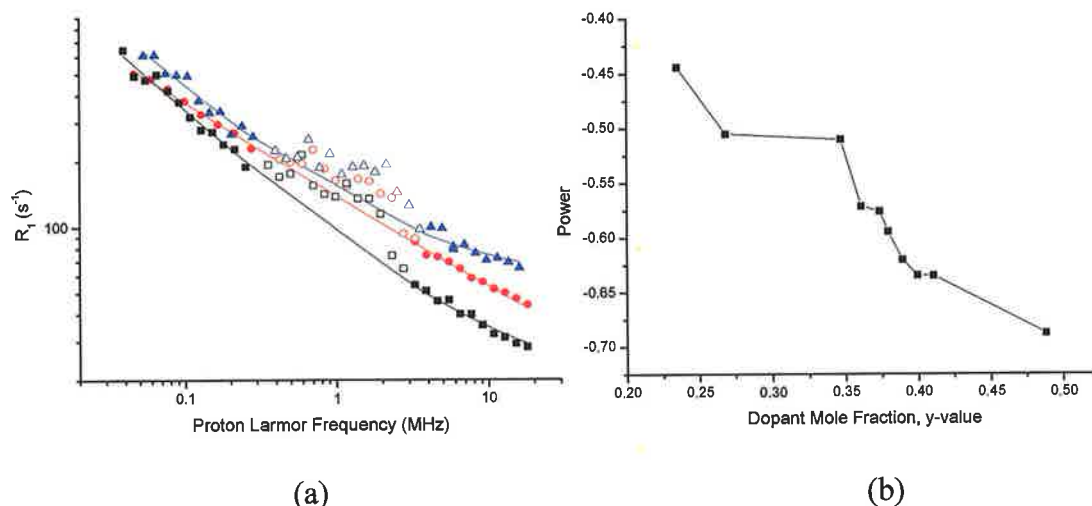


Figure 5.23 (a) ^1H NMR profiles of polyaniline TFSA at selected y -values 0.49 (■), 0.38 (●) and 0.27 (▲) fitted using a power-law spectral density function. The open symbols are the points in the quadrupole dip region which were omitted from the fit, and (b) the powers extracted from the power-law fits as a function of dopant content.

It is possible to fit our field cycling NMR data for polyaniline TFSA to a power law spectral density function (figure 5.23a). The region containing the quadrupolar dips was omitted from the data sets when fitting in order to obtain accurate fits. The highly doped samples conformed well to this model but, due to the smaller signal-to-noise ratio and associated errors, analysing data for samples with low dopant concentrations was more problematic.

Interpreting the power-law dependence of the NMR data by applying the spectral density function used in Mizoguchi's published work (equation 5.12b) yields sub-one-dimensional behaviour. The spatial dimensionality extracted is inversely dependent on the y -value (figure 5.24). Therefore, an alternative interpretation of the power law dependence is required. Addressing the issue remains important as we observe the power law dependence to be related to the doping level and the bulk conductivity.

Interpretation 1. Polaron transport through undoped regions.

The spectral density is given by equation 5.13a, which is a power law that corresponds to fractal dimensionality of charge carriers. Unlike Mizoguchi's published results, the R_1 data for all of our TFSA-doped samples indicates a power law dependence in excess of $\omega^{-1/2}$ at low frequency. Mizoguchi observed similar ($> \omega^{-1/2}$) behaviour over a higher field range in samples with very low dopant levels ($y < 0.02$) and attributed this to nuclear-spin diffusion assisted relaxation due to fixed

paramagnetic centres in the non-conducting part of the matrix. This suggests that the $\sigma > \omega^{-1/2}$ behaviour observed in our materials may be due to the motion of charge carriers through the undoped part of the material. The nuclear spins are relaxed by the nearby mobile electronic spins of the polarons.

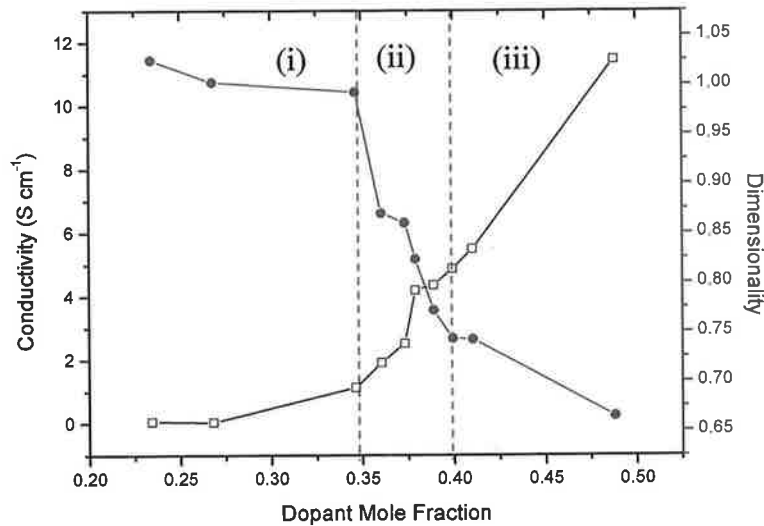


Figure 5.24 Conductivity (○) and fractal dimensionality (■) as a function of dopant mole fraction showing three regimes.

This hypothesis would explain the low spatial dimensionality, d , implied by the power-law fits. Polaron on-chain motion through the undoped regions occurs only through the conjugation of the polymer backbone and inter-chain hopping is restricted. This results in low-dimensionality charge carrier motion, at a much slower rate than through the doped regions. Increasing the dopant content results reduces the spacing between, and connectivity of, the undoped regions. Thus, the dimensionality of charge carrier motion decreases with increasing y -value.

The dimensionality of polaron motion can be related to the data from the bulk conductivity measurements. By plotting both conductivity and dimensionality as a function of dopant concentration, figure 5.24. suggests that the microscopic NMR dimensionality of motion through the undoped region is inversely related to the macroscopic conductivity, as might be expected.

Three distinct regimes depending on dopant concentration, are apparent:

- i) At low dopant concentrations the conductivity is low and the network of undoped regions has relatively high dimensionality.

- ii) At moderate dopant concentrations the conductivity increases dramatically and the dimensionality of charge carriers decreases simultaneously.
- iii) At high dopant concentrations the dimensionality is lower. The dependence of dimensionality of addition of further dopant is weaker. However, the fraction of the material undoped is now very low. In this interpretation, the mechanism for relaxation of the sampled magnetisation is due to fluctuations in local fields caused by the nearby moving electronic spins. The intensity of the FIDs does not decrease in this γ -value range. Therefore, the magnetisation sampled is that of the bulk polymer and there is a common spin temperature across the sample.

Interpretation 2. Backbone fluctuations.

From field-cycling experiments on proteins, Korb and Bryant [168, 169] extracted a spectral density function for relaxation due to the modulation of the homonuclear ^1H dipolar interactions due to structural fluctuations localised along the polymer backbone. This was derived from a model for anomalous diffusion in a fractal network:

$$\frac{1}{T_1} = A\omega^{-b} + c \quad [5.13]$$

where A is related to the dipolar coupling strength and c is a constant. b is related to the fractal dimensionality of the spatial distribution of protons (d_f) and to the spectral dimensionality that characterises the motion due to anomalous diffusion (\bar{d}) by equation 5.14:

$$b = 3 - \frac{2\bar{d}}{d_f} - \bar{d} \quad [5.14]$$

Thus the NMR relaxation can be related to both the structural (d_f) and dynamical (\bar{d}) characteristics of the material studied.

As was discussed in section 5.4.3.1 Kimmich and Ansaldo have shown that quadrupolar dips are an indication of backbone fluctuations in macromolecules. This suggests that the low-field dispersion in our NMR relaxation profiles for polyaniline TFSA is due to structural fluctuations localised along the backbone. The data was again fitted with a spectral density function derived from the model for anomalous diffusion (equation 5.14).

The b-values, of between ~ 0.7 - 0.4 derived from the fits are within the range described by Korb and Bryant. [168, 169] Allowing both dimensionality parameters to go free during fitting results in unphysical fractal dimensionality, d_f , values greater than three. However, for a percolating system with $3N$ degrees of freedom, \bar{d} can be assumed to be $4/3$. [165] The relaxation data was fitted with \bar{d} fixed as 1.33 and the resulting structural fractal dimensionalities, d_f , plotted as a function of dopant mole fraction are presented in figure 5.25. As expected the structural dimensionality, d_f , was always greater than the spatial dimensionality of motion, \bar{d} .

At the minimum possible value of $b = 0$, d_f would be 1.6, which, is indicative of an ensemble of self avoiding chains with no interactions. At the maximum possible value of $b = 0.785$, $d_f = 3$ which corresponds to uniform distribution of protons equivalent to a homogeneously doped material. For very high dopant levels (y-value = 0.49) in polyaniline TFSA, $d_f \sim 2.7$ which is indicative of a very homogeneously doped material. At low dopant concentrations (y-value = 0.23) in polyaniline TFSA, $d_f \sim 2.05$ which is indicative of a more heterogeneous material with greatly reduced interchain interaction.

The parameters extracted from the NMR analysis can be related to the bulk conductivity measurements. From the graph of both conductivity and the fractal dimensionality, d_f , as a function of dopant concentration (y-value), figure 5.25, it is apparent that the microscopic NMR measurements follow the same trend as the macroscopic conductivity measurements. This suggests that the backbone fluctuations in question arise from, or are associated with, polaron motion through the polymer.

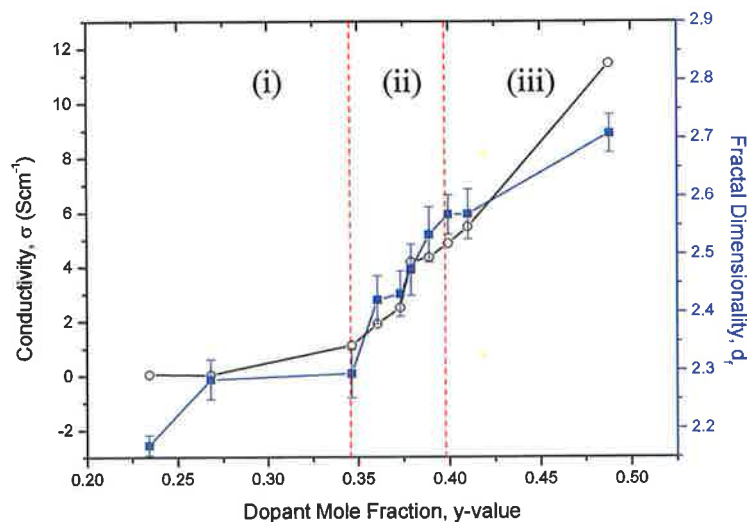


Figure 5.25 Conductivity (\circ) and fractal dimensionality, d_f , (\blacksquare) as a function of dopant mole fraction showing three regimes.

A key aspect of conduction of polyaniline is the presence of conjugated double bonds along the backbone of the polymer. When an electron is added to the chain by addition of dopants, it causes a characteristic bond deformation in the chain about twenty monomer sites long, the electron plus the deformation ‘pattern’ constitute a polaron. [149] In the case of conducting polyaniline this conformational change generally takes the form of a switch between single and double bonds which diffuse freely along the polymer chain at the on-chain diffusion rate, D_{\parallel} and may hop occasionally between chains at the inter-chain diffusion rate, D_{\perp} . It is thought that interchain hopping is the limiting factor in conductivity. The increase in dimensionality with increasing dopant content is probably due to an increase in interchain hopping.

The backbone fluctuations due to polaron motions would be expected to be on the same timescale as the polaron motion and hence to give rise to features at the same frequency range in the NMR relaxation profile. However, the motions driving relaxation in this field range are slow; they are on a timescale close to, but as far as we can tell, below that of the off-chain polaron motion. As the on-chain diffusion must be on the 10^{-12} s timescale, we can infer that the motions observable below 1 MHz arise from the increased polymer mobility due to the introduction of dopants. The increase in T_2 observed for the high dopant concentration samples in figure 5.4 is consistent with this interpretation.

From figure 5.25 it is apparent that at dopant concentration, $y_p = 0.32-0.35$, there is an onset of percolation and the interchain-hopping and hence the conductivity increases. According to this interpretation the three distinct regimes are explainable as follows

- i) At low dopant concentrations (y -value < 0.35) conductivity is low and the dimensionality of the backbone fluctuations is low indicating a rigid heterogeneous material with very little interchain interaction.
- ii) At moderate dopant concentrations (y -value $\sim 0.35-0.4$) both the conductivity and fractal dimensionality increase, indicating increasing homogeneity in proton distribution, increasing interaction with neighbouring chains and increasing polymer backbone motion.
- iii) At high dopant concentrations (y -value > 0.4) the dimensionality becomes less strongly dependent on dopant content as the system approaches the condition for homogeneous doping. It can be assumed that the sample is almost fully doped with one dopant molecule per monomer unit and the percolation network is complete. However, the conductivity continues to rise indicating that there is an increase in charge carrier mobility. This is probably due to the spin system becoming saturated and polarons beginning to form bipolarons and polaron pairs. These will increase the conductivity, but as the bipolarons have spin, $I = 0$, they do not affect the ^1H relaxation.

5.3.4.3 Temperature dependence

For samples in regime i, figure 5.25, there is very little dependence of the NMR response on temperature and the dimensionality does not change significantly on increasing the temperature. However, at higher dopant levels, in regime iii, the relaxation profiles exhibit temperature dependence and the power extracted from the power-law fits decreases approximately linearly with temperature. As has been stated previously a decrease in the extracted power is linked to an increase in conductivity. As the temperature is increased polaron diffusion increases and as a result more of the network is explored by a given polaron. This results in increased conductivity. Previously Mizoguchi [160, 170] observed linear increases in the conductivity of doped polyaniline across a wide temperature range, which he explained as an increase in quasi-1-dimensional diffusion detectable through ESR and NMR. Unfortunately,

due to technical restraints, temperature dependent conductivity measurements could not be performed on our samples.

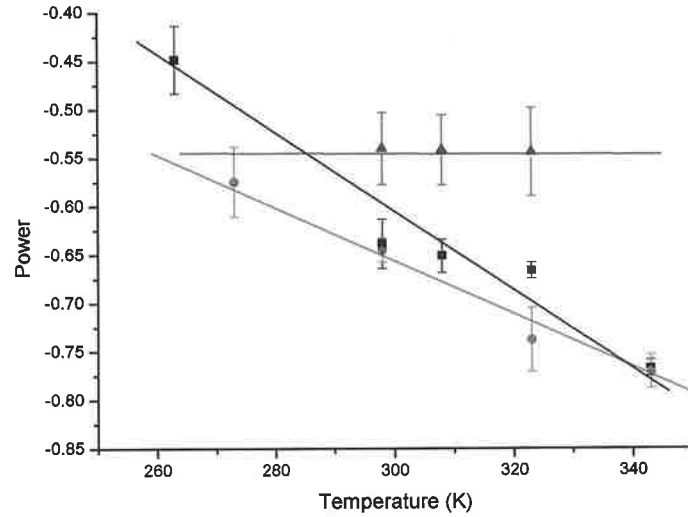


Figure 5.26 Temperature dependence of samples TFSA4a (▲), TFSA4 (●) and TFSA10 (■). The solid lines are linear fits to each data set.

5.4.2 ^{19}F NMR Analysis

The ^{19}F NMR relaxation response of polyaniline TFSA is solely driven by the dopant anion molecular motion and as a result ^{19}F NMR could be used as a probe for dopant dynamics. The ^{19}F NMR profiles exhibited a pseudo-Lorentzian shape and were apparently insensitive to both dopant concentration and temperature change. The relaxation profiles were fitted using the Cole-Cole [5, 8] spectral density (figure 5.27):

$$J_{CC}(\omega, \tau_c, \delta) = \frac{2}{\omega} \sin\left(\frac{\delta\pi}{2}\right) \left[\frac{(\omega\tau_c)^\delta}{1 + (\omega\tau_c)^{2\delta} + 2\cos(\delta\pi/2)(\omega\tau_c)^\delta} \right] \quad [5.16]$$

where ω is the angular frequency in rad s^{-1} and τ_c is the motional correlation time. δ is the degree of correlated motion where $\delta = 0$ is uncorrelated motion and $\delta = 1$ is the highest degree of correlation possible.

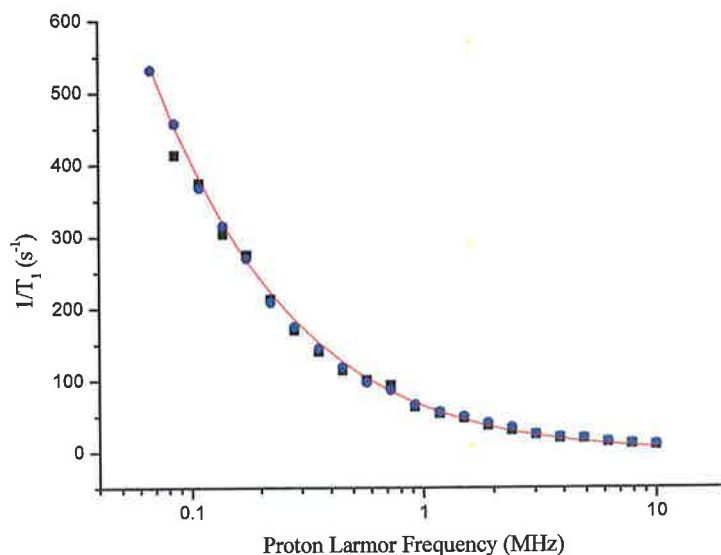


Figure 5.27 ^{19}F relaxation profiles of doped polyaniline with high dopant concentration (■) and low dopant concentration (●) fitted with a model for the Cole-Cole spectral density.

The extracted $3.69(8) \times 10^{-8}$ s correlation time for TFSA anion tumbling is on the expected timescale for molecular tumbling in a moderately restricted environment at this temperature. A δ value of $0.38(8)$ is indicative of a relatively strongly correlated motion. These results were similar to those observed for polyaniline PF_6 indicating that dopant dynamics are similar for dopants of similar size and pK_a .

The most unexpected result from the ^{19}F studies is that the reorientational correlation time of the dopant molecules is independent of dopant concentration. ^{19}F profiles were measured across a wide dopant concentration range, although it was not possible to measure a profile for samples with low dopant content as the fluorine signal was too weak.

The fact that the reorientational correlation time for the anion is independent of concentration suggests that the barrier to motion is locally determined by the interaction of the anion with the adjacent chain. However, the correlation time extracted from the Cole-Cole fit is much slower than the picosecond timescale of on-chain polaron diffusion, indicating that the anion does not directly participate in the conduction process. It is important to note that there are no features in the ^{19}F spectral density in the sub-megahertz range. Thus the dopant concentration dependent low field dispersion observed in the ^1H profiles, is not due to a slow-charge transfer or other dynamical process associated with polymer-anion interactions.

5.5 Conclusions

The aim of this project was to examine whether NMR relaxometry is a suitable tool for the analysis of charge carrier transport in ICP's and to develop experimental methodologies and theoretical models to measure rates and obtain insights into the nature of the motions. In this we have been mostly successful. NMR relaxation data was recorded for a number of polyaniline samples with varying dopant content and compared to results from macroscopic analytical techniques such as conductivity and microanalysis.

The theoretical model describing quasi-one-dimensional diffusion of charge carriers developed for high field NMR relaxometry studies of polyaniline was shown not to be applicable to low-field relaxation profiles. Two new interpretations of the power law frequency dependence of ^1H NMR relaxation profiles were proposed to explain the low-field behaviour. In the first interpretation sub-one-dimensional behaviour is ascribed to restricted charge carrier diffusion through the undoped part of the polymer. The spatial dimensionality of this motion decreases with increasing dopant content as the connectivity of the undoped regions decreases and as expected this change mirrors an increase in conductivity.

In the second interpretation the fractal dimensionality is attributed to backbone fluctuations in the polymer chain. Below the percolation threshold the dimensionality is low, indicating a rigid heterogeneous material with relatively little interaction between chains. Above this threshold the ^1H networks structural dimensionality and conductivity increase, indicating an increase in the homogeneity of the distribution of the protons and increased polymer motions. Increasing the dopant content can also be associated with increasing the rate of charge carrier motion. Approaching the condition for the homogeneous distribution of protons, the dimensionality is less strongly dopant content dependent. The conductivity continues to increase in this range indicating the formation of bipolarons or polaron pairs which, while assisting conductivity do not affect the ^1H relaxation.

Both of these interpretations are consistent with the established model for conductivity of a heterogeneous material with conducting regions and non-conducting regions averaged by spin diffusion. In order to definitively distinguish between these models the undoped part of the material must be removed. In the next chapter

methods for the synthesis of highly crystalline, highly doped polyaniline and the effect of this change in morphology are examined.

One of the major results of this study is the observation that ^{19}F relaxation response is unaffected by dopant levels or changes in temperature. The fact that dopant dynamics are independent of dopant content suggests that the barrier to motion is locally determined by the interaction of the anion with the adjacent chain. It is also interesting to note that the (10^{-9} s) timescale for dopant dynamics are several orders of magnitude less than the on-chain polaron propagation timescale (10^{-12} s) determined by Mizoguchi. [158] Thus, the anion is essentially a bystander to the conductivity.

Chapter 6 – Crystalline Conducting Polyaniline

6.1 Introduction

The production and application of inorganic nano-materials in diverse fields such as optics, electronics and medical imaging has been long established. However, the application of nano-structured ICP's and other related organic semi-conductors to these fields is relatively new. Polyaniline and other ICP nanostructures are of great interest since they combine relatively high conductivity with high surface area. This can lead to enhanced optical, electronic and physical properties [171] resulting in applications such as gas-sensors and biosensors. [172, 173] However, development of these applications is restrained by the poor reproducibility of the materials irrespective of the synthetic route used.

The enhanced attributes in nanostructured ICPs are thought to be due to the fact that increasing the degree of crystallinity results in greater conductivity. The main motivation for this work is that by increasing the crystallinity if possible to 100 %, the interpretation of the NMR profiles of the amorphous polyaniline, presented in the previous chapter, might be clarified.

6.1.1 Synthesis of Nanocrystalline Polymers

There are many synthetic routes to nanostructured ICP's which yield a wide range of morphologies. Synthetic methods of producing nano-structured highly crystalline conducting polymers can be divided into four categories; physical templated methods, steric stabiliser/co-polymer assisted routes, surfactant and microemulsion routes, and other methods. A comprehensive overview of these routes is presented below.

6.1.1.1 Physical Template Methods

One of the simplest and most effective methods to synthesise ICP nanoparticles is to use physical templates. These are generally nanosized inert substances on which the ICP is grown or coated. Physical templates have provided easily accessible and controllable methods for the production of nano-particles.

Nano-sized metal particles are a well-established template for nanoparticulate ICPs. Indeed, one of the first usable nano-structures was created by using a photocatalyst to reduce metals onto TiO₂ particles [174] which were then used as nanoreactors to catalyse redox reactions. The standard route to produce polyaniline nanoparticles using TiO₂ involved the normal oxidative polymerisation of aniline with APS and

acid in the presence of TiO₂ nanocrystals. However, both Li [175] and Qi Wang [176] showed that by polymerisation of aniline under ultrasonic irradiation, in the presence of 20-30 nm nanocrystalline TiO₂, the aggregation of nano TiO₂ can be reduced, and the nanoparticles can be redispersed in the aqueous solution. There is an interfacial interaction between polyaniline and TiO₂, as polyaniline deposits on the surface of the nanoparticle, leading to a core-shell structure. The resulting polyaniline/nano TiO₂ composite particles are spherical, and the sizes vary from 30-45 nm with the content of TiO₂.

Carbon nanotubes exhibit high conductivities and high tensile strength and form one of the easiest and most effective methods for the formation of ICP nanoparticles. Feng *et al* [177] used the oxidative polymerization of aniline in the presence of aligned carbon multi-walled nanotubes (MWNT) to produce MWNTs coated in polyaniline. These structures showed greater conductivity than simple polyaniline and exhibited the temperature dependence expected for semi-conductors. Corio *et al* [178] observed similar behaviour with single-walled carbon nanotubes (SWNT). They reported increased solubility and processability over simple doped polyaniline and increased conductivity over pure SWNT. More recently Wei *et al* [179] used TEM and XRD to show that when the monomer-MWNT ratio <1, polyaniline is formed coated on the MWNT, but if it is >2 filled polyaniline nanotubes form by self-assembly.

Other common syntheses using physical templates are the surface polymerisation of aniline on silica gel. [180] The surface of several types of particle can catalyse aniline polymerisation. These materials act as heterogeneous catalysts for the polymerisation of polyaniline, which form on the surface far more readily than in the suspending media. If a sufficiently large amount of silica with a large specific surface area is added into the reaction mixture, virtually all the polyaniline is produced by surface polymerisation leading to core-shell nanoparticles. Ni nanoparticles have also been used as inorganic templates [181] to produce long polyaniline fibres about ~1 µm long and 50 nm in diameter, usually by an inverse microemulsion polymerization.

ICP's have also been grown in zeolites with pore sizes of >1 nm allowing formation of single molecular wires. [182] Membranes with a specific pore size have been used to grow mats of nano-sized ICP fibres both chemically and electrochemically.[183] Synthetic opals are polystyrene or silica spheres which are arranged on a surface in a close packed template. In the gaps of the opals, ICP's have been produced by chemical polymerisation. The host is then removed to form a polymer inverse opal. [184]

Polyaniline nanotubes have also been obtained by using both chemical and electrochemical synthesis using polycarbonate filtration membranes as templates. [166] Nanowires and nanonetworks have been formed by the polymerisation of polyaniline with fullerene derivatives. [185, 186]

Other syntheses using physical templates include; the intercalation of polyaniline in mesostructured V_2O_5 [187] and the use of V_2O_5 as the oxidising agent in an oxidative polymerisation reaction [188], the preparation of conducting polyaniline-coated barium sulphate nanoparticles in inverse microemulsions [189], and the preparation of uniform and ordered polyaniline nano-fibrils by synthesising within an anodic aluminum oxide (AAO) template. [190]

6.1.1.2 Steric Stabiliser and Co-polymer Methods

One of the major difficulties in developing applications for ICP's is in the materials processing, which can be difficult as the polymers are infusible and insoluble in most common solvents. Although solubility can be increased by doping with CSA or DBSA, toxicity prevents the widespread use of these dopants. In order to enhance the processability, a range of colloidal composites of various polymeric materials have been developed. The conventional approach is the chemical oxidation/polymerisation of the monomer in an aqueous acidic solution containing a suitable polymeric stabiliser to produce stable colloidal dispersions with particle sizes $<100\text{nm}$.

The traditional methods for stabilisation involve long-chain polymer stabilisers such as poly(acrylic acid) (PAA) [191, 192] poly(vinyl alcohol) (PVA) [135, 193, 194] or poly-(sodium 4-styrenesulfonate) (PSSA) [193-195] which act as polymeric stabiliser and doping agent, due to their acidity. This is a simple synthesis involving the dissolution of monomers in an aqueous solution and subsequent oxidative dispersion polymerisation.

Accurate size control of nanostructured polyaniline was demonstrated by Kim *et al* [196] by using polymers as micellar templates. In this approach amphiphilic polymer molecules, hydrophobically end-capped polyethylene oxides (HEURs) of variable length, can be used to produce micelles of controlled size. The HEUR polymers form "flower type" micelles at low concentrations. Since the polymerisation reaction proceeds in the micellar solution, the size of the micelle controls the size and structure of the PANI particles.

A simplified variation of this approach is interfacial synthesis which was used by Hopkins *et al* [197] to produce polyaniline/poly(sulfonated styrene) (Pani-PSS) nanofibre composites. Aniline was dissolved in an organic layer and APS was mixed in the upper aqueous layer with PSS. This in situ polymerisation of polyaniline nanofibres in the presence of PSS produced polyaniline nanostructures embedded in the polymerised sulfonated host.

The morphology of the polyaniline nanoparticles is dependent not only on the dopant but on the synthetic technique. Bannerjee *et al* [198] found that blends of hydrochloric acid-doped polyaniline nanoparticles and poly(vinyl chloride) (PVC), prepared by redispersing sedimented colloidal particles of polyaniline in tetrahydrofuran solutions of PVC using ultrasound, show globular morphology. This is in contrast to the fibre network observed previously for polyaniline-PVC blends prepared by traditional synthesis. [199]

6.1.1.3 Surfactant- based Microemulsion Methods

The self-assembly of surfactant molecules to create structured hydrophobic and hydrophilic domains makes them ideal substrates in the development and synthesis of nano-sized polymers. The main advantage of this approach is that the particle size and shape can be predefined by using the appropriate geometry of the templating micelle. The disadvantage is the insulating effect of the stabilising surfactant detracts from the inherent conductivity of the polymer sample. [200] However, by careful washing the surfactant may be removed.

Formation of ICP nano-particles with sizes in the range 10-30 nm has been achieved by oxidation of aniline with ammonium peroxydisulphate (APS) in sodium dodecyl sulphate (SDS) [201, 202] and dodecylbenzene sulphonic acid (DBSA) [202, 203] micellar solutions. Coalescence and coagulation of the micelles was prevented by electrostatic repulsive interactions between anionic surfactant micelles. Particle morphology is dependent on the initial shape of surfactant aggregates (micelles) and the molar ratio of surfactant to aniline monomer. Spherical particles would be obtained at very low monomer concentration and the shape of particles began to be distorted from the spherical shape as monomer concentration was increased, at constant 0.2 M surfactant concentration. Dynamic light scattering was used to probe the change in the size of SDS micelles in the presence of growing polyaniline. [204] A direct correlation between micelle size and the size of the polyaniline particles was

observed. The conductivities increase with increased surfactant concentration [205] in the range of $\sim 1\text{-}100\text{ Scm}^{-1}$ for materials produced from this route, probably due to the fact that these acidic surfactants are also the dopant for the system.

Modifications to this approach have been suggested with a view to optimising in the resulting particle size. Chemical oxidative polymerization of aniline was performed in a (DBSA)–(2,2,4- trimethylpentane)–(isooctane)–water reversed micelle system. [206] The particles of polyaniline-DBSA obtained had nano-sized (10-30 nm), needle-like morphology and were size monodisperse. The reverse micellar solution was formed by dropping an isooctane solution of DBSA and the oxidant (APS) into an isooctane solution of aniline. A similar technique using horseradish peroxidase has found use as an enzyme biosensor. [207]

Zhang *et al* [208] attempted the chemical oxidative polymerization of aniline in 1.0 M D,L-camphorsulfonic acid (CSA) using APS as the oxidant, and carried out in the presence of added non-ionic surfactant (polyoxyethylene(10) isooctylphenyl ether, Triton-X 100 (TX100)) [209] which resulted in a precipitate of doped emeraldine salt composed almost entirely of nanofibres having average fibre diameter in the range 30–50 nm and a length of $\sim 0.5\text{-}1\text{ }\mu\text{m}$ which exhibited a room temperature DC conductivity of $1\text{ - }5\text{ Scm}^{-1}$. Kim *et al* [210] compared polymerisation of aniline in a conventional aqueous solution and in micellar solutions of sodium dodecyl sulphate (SDS) an anionic surfactant and nonylphenol ethoxylate (NP-9) a nonionic surfactant. Xia and Wang prepared polyaniline nano-particles via an ultrasonic assisted inverse microemulsion technique. [211] They exposed a CTAB/n-hexanol/APS/HCl_{aq} microemulsion to ultrasonic radiation while adding an aniline/n-hexanol solution. This produced spherical nanoparticles 10-50 nm diameter with a conductivity of $\sim 10\text{ Scm}^{-1}$. Polyaniline ‘nanobelts’ with diameter in the range of 40– 50 nm and lengths up to several micrometers were synthesised by chemical oxidative polymerisation of aniline in a surfactant gel (CTAB). [212] Dendritic polyaniline nanofibers with diameters between 60 and 90 nm were formed by chemical oxidative polymerisation of aniline in a surfactant gel, which was formed by a mixture of hexadecyltrimethylammonium chloride (C₁₆TMA), acetic acid, aniline, and water at 265 K. [209] Synthesis of doped polyaniline using lipid bilayers resulted in nanotubes which were on the millimetre scale in length. This reaction involved the preparation of DOPC-cholesterol giant vesicles (30 μm) and the subsequent polymerisation and coating of polyaniline onto these vesicles. [213]

6.1.1.4 Other Methods

There are many other methods for producing nanopolymers. One of the most common methods is by optimising well-known techniques. For instance Chiou *et al* [214] observed that a normal oxidative polymerisation at very dilute aniline concentration (<8 mM) using a aniline/APS ratio of 2:1 yielded nanofibres in the range of 30 – 200 nm depending on the dopant used. Another modification of the simple aniline/APS/aq acid synthesis involves seeding the solution with oligimers. [215] Polymerisation of aniline was carried out in concentrated camphor sulfonic acid (CSA) solutions and aniline oligimers were used to accelerate the polymerisation. TEM showed that 20-40 nm nanoparticles were formed. Similarly, seeding conventional chemical oxidative polymerisation reactions of aniline with very small amounts of biological, inorganic, or organic nanofibers (usually <1 %) dramatically changes the morphology of the resulting doped polyaniline powder. [216]

Some dopants and initiators display tendencies to form specific nanostructures. Synthesis using carboxylic acids yields nanofibres whose diameters increase with increasing numbers of carboxylic functional groups in the acid. This is because long-chain carboxylic acids can form micelles due to their amphiphilic character and polymerisation can occur at the water/micelle interface. [217]

Wang *et al* [52] described a facile route to the synthesis of polyaniline nanofibres by polymerisation of aniline using chloroaurate acid (HAuCl_4) as the oxidant leading to uniform polyaniline nanofibres with a diameter of 35 nm. Use of PAMAM₄[naphthyl(SO₃H)₂]₂₄ or C₆₀(OSO₃H)₆ as protonic acid dopants yields polyaniline nanotubes with a diameter on the order of hundreds of nanometres and a length up to several micrometres. [218] Branched nanofibers of conducting polyaniline buried in crystals of camphor sulfonic acid (CSA) were prepared from an *m*-cresol solution of PANI and excess CSA. [219]

Kaner [220] observed that aqueous polyaniline colloids can be readily prepared by purifying polyaniline nanofibers and controlling the pH without the need for any chemical modification or steric stabiliser. Polyaniline nanofibres were prepared by rapidly mixing a solution of aniline, APS and HCl followed by centrifugation to purify the product. The centrifugation lead to the formation of stable polyaniline colloids. It is thought that these were stabilised by electrostatic repulsion, due to the introduction of a charge to the particle surface, as opposed to steric repulsion, due to the addition of a polymeric or surfactant stabiliser.

Synthesis of nanostructured polymers using chiral molecular templates has been shown to produce optically active polymers with high conductivity. By physical adsorption of aniline monomer onto poly(acrylic acid) particles in the presence of (+) or (-)CSA and subsequent polymerisation, nanoparticles of water-soluble optically active polyaniline were formed. [221]

Electrochemical synthesis is a low yield process which has been used to form oriented nano-wires on substrates including Au and Si, grown galvanostatically without a template. [222] Optically active polyaniline colloids have been generated by the electrohydrodynamic polymerisation of aniline in the presence of CSA, as the dopant, using colloidal silica (5 %wt/wt) as the dispersant, at an applied potential of + 0.8 V vs. Ag/AgCl. [223] There are also a number of non-templated routes using deposition between two nano-electrodes [224] or electron-beam lithography to produce nanopatterns but these are again low yield processes.

The template-free reaction most suitable for this work is an interfacial synthesis whose mechanism is well described by Kaner. [225] In a typical synthesis, aniline is dissolved in an organic solvent, (CCl_4 , benzene, toluene, or CS_2), while APS is dissolved in water with its dopant acid. The two solutions are then carefully transferred to a beaker, generating an interface between the two layers. Polymerisation takes place at the interface [172] and the resulting nanofibers have diameters between 30 and 50 nm, with lengths varying from 500 nm to several μm . The ionic liquid 1-butyl-3-methylimidazolium hexafluorophosphate [C_4mim] PF_6 has been used, in place of the usual organic solvent, in an interfacial polymerisation reaction. This is an interesting approach as ionic liquids have low toxicity. Polyaniline particles with diameters from about 30–80 nm were produced. [226] From this interfacial synthetic technique a general strategy for nanocrystal synthesis of a number of organic and inorganic systems has been devised. This is based on a phase transfer and separation occurring at the interfaces of the liquid, solid and solution phases present during synthesis, it provides a simple and convenient route to a variety of nanosystems. [227]

6.1.2 Nanosynthetic Routes to Polyaniline TFSA

In the work presented in this chapter, several of the approaches to synthetic nanocrystalline polyaniline were applied. In selecting the synthetic routes it became

apparent that many of the electrosynthetic and non-templated routes could not be adapted to yield ~0.5 g of bulk powder required for NMR analysis. The use of steric stabilisers and co-polymers was rejected in this case as the co-polymers, such as PVC and PVA, contain complex NMR signals of their own and contribute significantly to the ^1H NMR response. Similarly approaches involving metallic or superparamagnetic templates were ignored. The following approaches were attempted:

- (i) Optimised standard synthesis: It has been shown that optimising the physical parameters (sonication, temperatures, flow rates, reactant ratios etc) of a standard solution state oxidative polymerisation can yield nano-structures. This would be the simplest and most efficient route.
- (ii) Electrochemical synthesis: Electrochemical synthesis would be a suitable route to nano-structured polymers providing that films could be grown sufficiently thick to yield enough material for NMR analysis.
- (iii) Surfactant synthesis: Surfactant-based synthesis could be useful if the surfactant could be removed by washing from the polymer and replaced with TFSA. This would allow direct comparison of the analysis with that reported for amorphous polyaniline in the previous chapter.
- (iv) Interfacial synthesis: This is a relatively easy approach that has been shown to yield nanostructures on a large scale.

6.2 Experimental

6.2.1 Ultrasonicated chemical synthesis

This preparation is a variation of the procedure by Xia and Wang [36] forming polyaniline nanoparticles by the chemical oxidation of the monomer under ultrasonication. Xia and Wang used dodecylbenzenesulphonic acid (DBSA) as a surfactant and dopant but in order to compare the results with previous work on amorphous polyaniline TFSA (Chapter 5) the synthesis was performed here without the surfactant. The reaction was the chemical polymerisation of distilled aniline monomer in TFSI (bis(trifluoromethane)sulfonimide acid) with very slow addition of the oxidant APS (ammonium persulphate) at 273 K with constant ultrasonication over a number of hours (at least 4 hr) to prevent aggregation of particles.

To form the acid, 74.125 g of LiTFSI was dissolved in 500 ml of H_2O yielding a 0.52 M salt solution. A cation exchange column (Dowex 500W-X2 200-400) was used to

exchange Li for H⁺. The column was reslurried, repacked, and prepared with HCl and LiTFSI solutions. Then 300 ml of the aqueous LiTFSI solution was run through the column resulting in an acidic solution (pH ~1).

150 ml of a 0.2 M aniline solution in 250 ml of 0.5 M TFSI was placed in a slim 250 ml beaker and clamped in a cooling bath at 273 K. An ultrasonication horn was placed in the solution. A micro-pump was set up to deliver 37 ml of a 0.2M APS solution in 250ml 0.5M TFSI at 0.25 ml/min to the aniline solution. The ultrasonicator pulsed at 35 % amplitude with a 50 % workload (to prevent localised heating effects). The addition of the oxidant took 150 mins and the reaction mixture was sonicated for a further 6 hours. Following sonication, the reaction was left stirring overnight at 273 K (~13 hr). A dark green coloured solution indicated that doping/polymerisation had occurred.

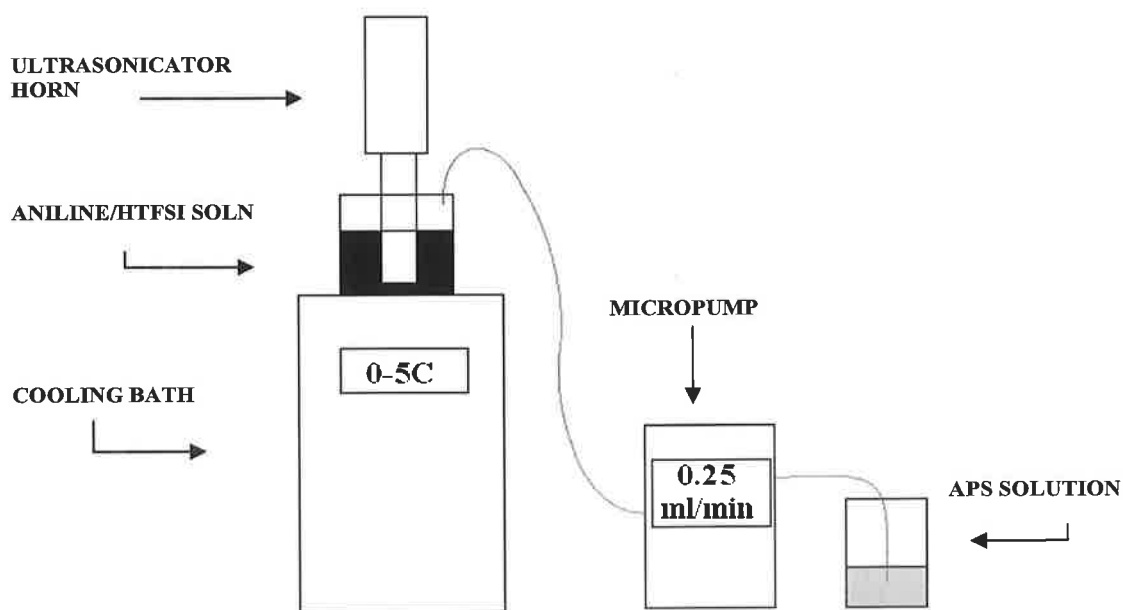


Figure 6.1 Schematic diagram of the apparatus used in the aqueous oxidative polymerisation synthesis.

6.2.2 Electrochemical Synthesis

The electrochemical technique represents one of the simplest and most direct methods of carrying out oxidation or reduction reactions because the removal or addition of electrons can be achieved without the attendant complications involved in the addition of redox reagents. It was thought that a thin film of polyaniline nanoparticles could be grown electrochemically on a large enough scale to be useful for NMR analysis,

providing the plate on which the sample was grown was sufficiently large. Thus a large platinum-coated stainless steel plate, of approximately 10 cm², was used as a working electrode.

6.2.2.1 Potentiostatic growth

The first attempt at electrosynthesis was to grow the polymer potentiostatically. 50 ml of the 0.2 M aniline in 0.5 M TFSI was placed in a 250 ml beaker with a platinum coated plate as working electrode, carbon wetted with deionised H₂O as counter electrode and a double junction Ag/AgCl as the reference electrode. The potential was kept constant at 0.8 V. The plot of voltage against time showed an initial increase but then the curve plateaued and did not increase further. This indicates that the film pacified as it was growing and was not an electroactive/conducting polymer. This was possibly due to increase in hydrophobicity after the first layer of film was deposited which limited further growth. The process was repeated changing both solution concentrations and voltages but invariably produced the same result.

6.2.2.2 Galvanostatic growth

The next attempt at electrosynthesis was to grow the polymer galvanostatically. 50 ml of the 0.2 M aniline in 0.5 M TFSI was placed in a 250 ml beaker with a platinum coated plate as working electrode, carbon wetted with deionised H₂O as counter electrode and a double junction Ag/AgCl as the reference electrode. The sample was grown at a current of 1.8 A. However, the voltage grew to 1.7 V immediately and remained constant throughout. Electrolysis of water occurs at close to this potential and bubbles were apparent in the solution during growth, probably due to splitting H₂O. The solution turned yellow instead of the expected green and this approach was abandoned.

6.2.2.3 Growth by cyclic voltammetry

The final attempt to grow polyaniline TFSI by electrochemical methods was to grow by cyclic voltammetry. This is generally seen as a highly inefficient synthesis in terms of both time and yield. The plot of voltage against time showed consistent growth of redox curve over time, indicating the growth of a conducting polymer. The initial growth on the working electrode was a clear green film and after 10 hours a thicker dark green film was present. The film was thicker than with previous

electrochemical growth methods but did not form in the quantities needed for analysis by NMR methods.

6.2.3 Surfactant synthesis

One of the more established routes to nanoparticulate conducting polymers is through the use of surfactant systems. The use of DBSA as a micellar surfactant to synthesise polyaniline was established by Han *et al* and Moulton *et al* [67, 68]. Both groups reported the production of highly conducting nanodispersions of the order of 20 nm (by TEM and FE-SEM) and in high yield and large quantities.

The synthesis was carried out using the method from Moulton *et al*. [203] 6 ml of aniline (0.65 M) was dissolved in 100 ml of water. This was added to a solution containing 21 ml (0.65 M) DBSA in 100 ml water and stirred for one hour to form a colloidal suspension. 16.5 g APS (0.65 M) was dissolved in 100 ml water and slowly dropped into the micellar solution with vigorous stirring. The solution turned yellow, then on doping turned dark green and was left stirring for 3 hours. A small amount of the resultant solution was retained for particle sizing by photon correlation spectroscopy (PCS) and the remainder was dialysed against deionised water using 12,000-15,000 MW cutoff dialysis tubing to remove small unpolymerised monomers and oligomers. Following dialysis the sample was centrifuged for 20 mins at 4000 rpm and the supernatant was decanted. The precipitate was resuspended in deionised water and a small amount was drop-coated onto an SEM stub. The suspension was then vacuum filtered and water washed and the resultant green-black powder was oven-dried at 323 K overnight. The synthesis was carried out three times using 0.65 M, 0.3 M and 1 M DBSA solutions to yield a number of samples with different dopant concentrations (DBSA1, DBSA2 and DBSA3 respectively). These samples were then analysed using DSC, SEM and NMR methods.

In order to compare these nanostructured materials with the amorphous polyaniline samples from the previous chapter it was necessary to replace all of the DBSA with TFSA. A sample was synthesised using the synthetic route as above with 0.65 M DBSA. The dried powder was resuspended in 0.5 M NaOH and stirred overnight to remove the dopant. The suspension remained green indicating that the material was still doped to some extent. The sample was then filtered, resuspended and stirred

overnight in 1 M NaOH but again the sample still appeared green and was assumed to be still doped with DBSA.

6.2.4 Interfacial synthesis

A recently reported route to producing nanoparticulate conducting polymers is interfacial synthesis. In this approach the monomer aniline is dissolved in an organic solvent (in this case toluene or chloroform) and mixed with the oxidant (APS) which is dissolved in aqueous solution of the dopant acid. This approach has resulted in solutions with high concentrations of polyaniline nanorods on the hundreds of nanometre scale. The optimisation of the syntheses were performed on a small scale (20 ml) and later scaled up to produce sufficient material for NMR analysis (100-200 ml total reaction volume).

6.2.4.1 Acid optimisation

0.285 g (0.125 M) APS was dissolved in 10 ml of 0.5 M hydrochloric acid (HCl) and 0.51 ml (0.5 M) aniline was dissolved in 10 ml of chloroform. The acid solution was poured carefully onto the chloroform solution in a 25 ml glass vial. Within 5 minutes the interface between the two previously clear solutions turned blue/black, indicating polymerisation was taking place. After 10 minutes the blue/black colour had spread throughout the upper aqueous layer and after 2 hours the upper layer had turned green/black indicating the presence of doped polyaniline. The lower organic layer was straw-coloured suggesting the presence of unreacted monomer and partially polymerised oligomers. The sample was left overnight to complete polymerisation then a small amount of the upper green solution was drop-coated onto a stub for SEM analysis. This process was repeated using identical concentrations of APS, aniline and triflic acid (TFSA). SEM images showed the similar concentrations of micro-crystalline rods in an amorphous matrix for both samples.

To examine the effect of the acid concentration on the yield and morphology of the polymerisation reaction, the acid (TFSA) concentration was varied while maintaining the oxidant to monomer ratio constant. Five solutions were made up with varying acid concentration; 0.01M, 0.05 M, 0.10 M, 0.25 M and 0.50 M TFSA. 0.285 g (0.125 M) APS was dissolved in 10 ml of each acid as above and these solutions were added to a solution of 0.51 ml (0.5 M) aniline dissolved in 10 ml of chloroform in a 25 ml glass

vial. Polymerisation occurred more quickly with increased acid concentration and an acid concentration in excess of 0.01 M was required for the reaction to proceed. SEM images of the material from the upper layer showed that increasing the acid concentration had the effect of increasing the concentration of crystalline material in the sample. However,, there was always a large amount of non-crystalline amorphous material in the resulting materials.

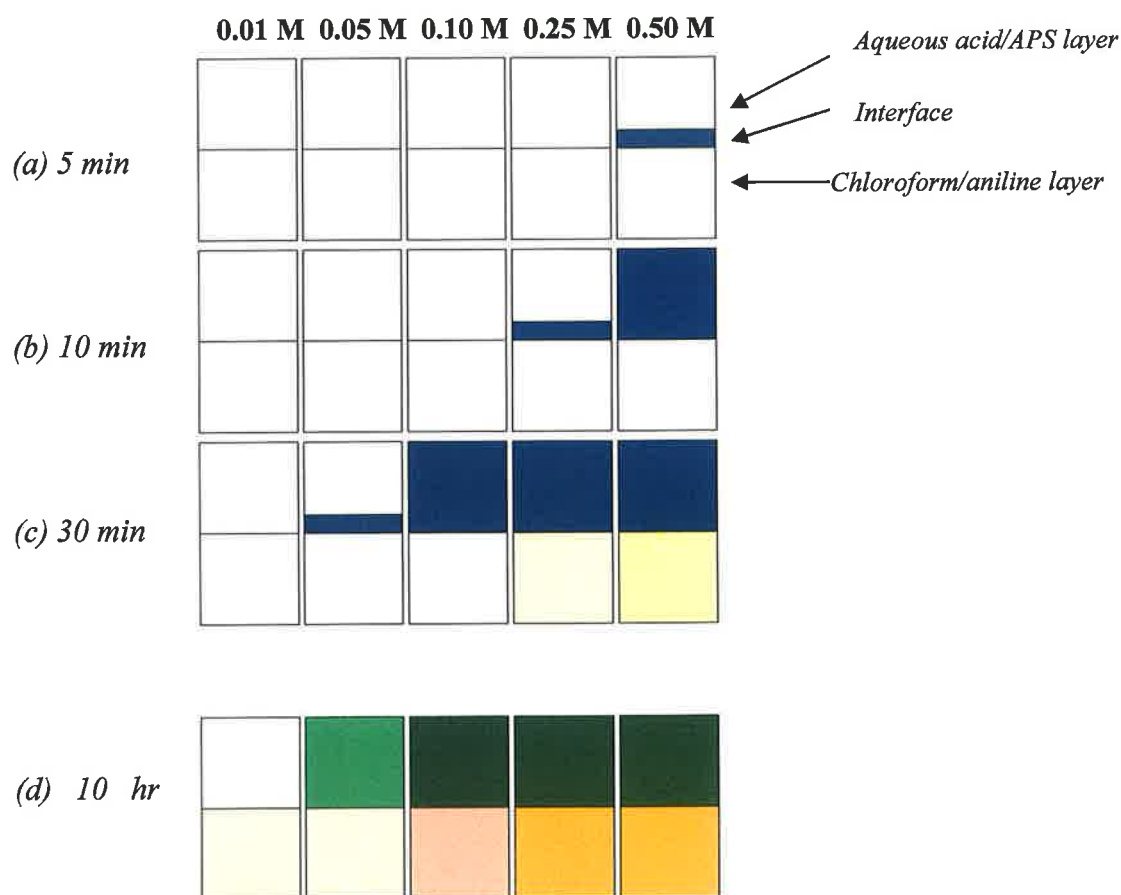


Figure 6.2 Scheme showing the progress of parallel interfacial synthesis with varying acid concentrations. The green colour is indicative of a doped polyaniline suspension.

6.2.4.2 Solvent optimisation

In order to examine the effect of the solvent on the yield and morphology of the polymerisation reaction, the synthesis was repeated using toluene instead of chloroform as the organic layer. Toluene, unlike chloroform, is less dense than water so the polymer migrates to the lower aqueous layer from the interface. 0.285 g (0.125 M) APS was dissolved in 10 ml of 0.5 M TFSA and combined with 0.51 ml (0.5 M) aniline dissolved in 10 ml of toluene and sealed in a 25 ml glass vial. SEM images

showed that changing the solvent to toluene had little effect on the sample morphology.

6.2.4.3 Monomer optimisation

In order to examine the effect of the monomer concentration on the yield and morphology of the polymerisation reaction, the monomer (aniline) concentration was varied while maintaining the oxidant to acid ratio using the optimum acid concentration from the previous experiment (0.5 M). Chiou [214] saw that much reduced aniline concentrations during the oxidative polymerisation reaction can lead to high concentrations of nanofibrous polymer. However, the concentration used (8 mM) was too low to yield sufficient polymer for NMR analysis. A reaction was carried out with reduced aniline concentration: 0.285 g (0.125 M) APS was dissolved in 10 ml of 0.5 M TFSA and combined with 0.051 ml (0.05 M) aniline dissolved in 10 ml of toluene and sealed in a 25 ml glass vial. A similar reaction was carried out with an increased aniline concentration (1.0 M). SEM images showed that altering the aniline concentration, within the range where producing hundreds of milligrams of polyaniline was possible, had no obvious effect on sample morphology.

6.2.4.4 Oxidant optimisation

To examine the effect of the oxidant concentration on the yield and morphology of the polymerisation reaction, the oxidant (APS) concentration was increased to 0.25 M while maintaining the monomer to acid ratio constant using the optimum acid concentration (0.5 M) and the optimum monomer ratio (0.5 M) determined from the previous experiments. Increasing the concentration of the oxidant had the effect of favouring the growth of crystalline flakes instead of crystalline rods in an amorphous matrix. Further increases in oxidant concentration to 0.5 M and 0.75 M resulted in the formation of crystalline flakes in a mixed crystalline/amorphous material, but no crystalline nanon-rods were observed.

6.2.4.5 Polymerisation in a magnetic field

A number of small scale interfacial syntheses was carried out in a large magnetic field in the hope of promoting more ordered polymerisation at the interface and hence the growth of crystalline nanorods over amorphous materials. The reaction was scaled down to fit in a 10 mm ID NMR tube. 0.51 ml (0.5 M) of aniline was dissolved in 10 ml chloroform and 1 ml of this was placed in an NMR tube. To this was added 1 ml of

a solution of 0.125 M APS in 0.5 M TFSA. This was placed in a modified variable field Bruker WP80 NMR magnet at room temperature (293 K) and 0 T field. A blue colour formed at the interface after 5 minutes which spread within 10 minutes to the whole of the upper aqueous layer. The sample was removed from the magnet after 30 minutes and a drop was removed from the upper aqueous layer and drop-coated onto an SEM stub. This process was repeated for two similar fields at 0.5 T and 1 T. SEM images showed no change in the morphology with increasing magnetic field. It also showed no change due to the reduced sample volume.

6.2.4.6 Large scale reactions

In order to obtain samples in the quantities needed for NMR analysis (0.5-1 g) it was necessary to increase the synthesis scale from 20 ml total volume to 150-300 ml total volume. A general synthetic route was followed and only the acid concentration was varied. Acid concentrations of 0.5 M, 0.4 M, 0.2 M and 0.7 M, were used to obtain samples nano2, nano3, nano4 and nano7, respectively, which had different degrees of doping and crystallinity.

In each case 6.59 ml (0.5 M) of aniline was dispersed in 150 ml chloroform and to this was slowly added a solution of 4.27 g (0.125 M) APS in TFSA of varying concentration to form an interface. A blue colour formed at the interface after 5 minutes, which spread within 10 mins to the whole of the upper aqueous layer. After 24 hours the upper layer had turned to a green/black colour, indicating the presence of doped polyaniline. The upper phase was then carefully removed and the by-products were removed by overnight dialysis against deionised water, with 12,000-15,000 MW cutoff dialysis tubing. Some of the resultant dispersion was drop-coated onto an SEM stub. The dialysed sample was filtered, water washed and the resultant green/black fine powder was dried in an oven at 323 K overnight.

6.2.5 AFM

Atomic force microscopy (AFM) was used to probe the nano-crystalline structure of the polymers synthesised using the interfacial synthetic route. It proved difficult to image these heterogeneous powders by AFM, so a number of methods of sample preparation were used. Initially the samples were analysed as pellets ~0.7 mm in diameter and ~0.1 mm thick. These pellets were formed by pressing a small amount

of the dried polymer powder into a small pellet using a hand-press, using the same technique previously described for pressing pellets for conductivity measurements. However, the surface crystalline morphology was lost due to the pressure exerted during pelletisation.

A small aliquot, <1 ml, of the concentrated reaction solution was drop coated onto a glass slide and allowed to air dry. The drop-coated slide was then analysed using AFM but no crystalline material was observed. This is probably due to the fact that the overall sample area was so much larger than the relative area of the crystalline material and the maximum scan area of the AFM that random placement of the tip was unlikely to land on an area containing nano-structures. Spin-coating a glass slide with the same reaction solution produced similar results.

The most effective method of sample preparation was drop-coating onto an SEM stub. A small aliquot, <1 ml, of the concentrated reaction solution was drop-coated onto the carbon-pad covered aluminium stubs used for SEM. These drop-coated stubs were examined using SEM and the position of areas of high concentration of crystalline material was noted. This made AFM tip-placement more efficient.

6.3 Results

6.3.1 Review of Synthetic Methods

A number of synthetic routes to produce nanocrystalline polyaniline were attempted with varying degrees of success.

6.3.1.1 Ultrasound assisted chemical synthesis

By using modifications of published aqueous oxidative polymerisation procedures involving lower temperatures, slower addition rates of oxidant and ultrasonication, large quantities of doped polyaniline could be produced. Raman spectra were, as expected, very similar to the spectra of the amorphous materials from previous syntheses and the main functional groups were similarly assigned. Bulk conductivity measurements showed a DC-conductivity of 1.57 Scm^{-1} .

However these samples were invariably amorphous. Particle sizing of the samples from the ultrasound assisted chemical synthesis using a Malvern Zetasizer showed a particle size of $>1 \mu\text{m}$. Dilution of the concentrated aqueous polymer reaction solution and resizing using the Zetasizer did not result in any change in size. Filtration of the

concentrated reaction solution through a 1.5 μm membrane filter and resizing using the zetasizer showed a bimodal distribution centered on ~ 100 nm and >1 μm . Indeed recent work by Innis [74] shows that rapid addition and vigorous stirring is more effective than slow additions for formation of nanocrystalline material.

6.3.1.2 Electrosynthesis

On the other hand electrochemical synthetic routes did not produce sufficient quantities of polymer. Polymer growth via cyclic voltammetry produced a small amount (< 50 mg) of conducting polyaniline. Raman spectroscopy showed similar response to the amorphous polyaniline and that of the ultrasound assisted chemical synthesis and the bulk conductivity was 0.52 Scm^{-1} . Particle sizing showed a particle size of >1 μm .

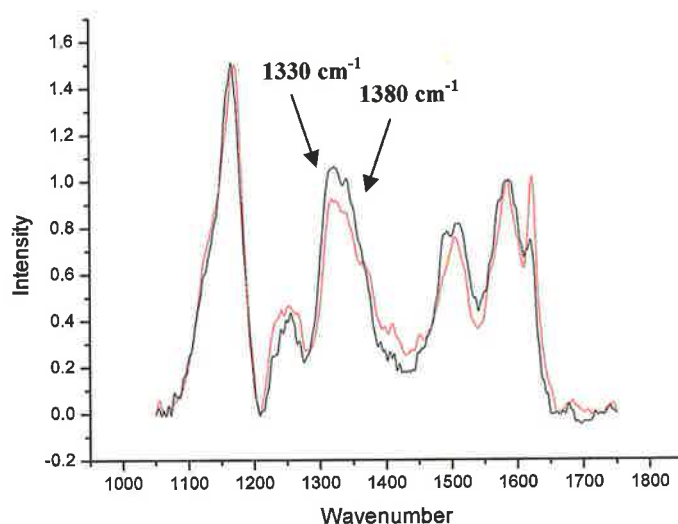


Figure 6.3 Raman spectra of polymer region of the ultrasound assisted chemical synthesis (-) and electrochemical synthesis (-), normalised with respect to the band at 1570 cm^{-1} showing differences in the polaron bands at $\sim 1330 \text{ cm}^{-1}$ and 1380 cm^{-1} .

6.3.1.3 Surfactant based synthesis

Polymerisation from a colloidal microemulsion with DBSA, apparently produced aggregated nanoparticles. Particle sizing by photon correlation spectroscopy (PCS) of the concentrated solution from the centrifugation of the DBSA doped polyaniline showed a broad distribution with a polydispersity index (PDI) of 0.83. Dilution did not change the distribution significantly. Filtration through a 450 nm membrane filter resulted in a broad peak around 138 nm with a PDI of 0.39 indicating a range of

particle sizes of around 138 nm. It is possible that the broad distribution in the concentrated solution was due to the aggregation of the small ~120 nm particles.

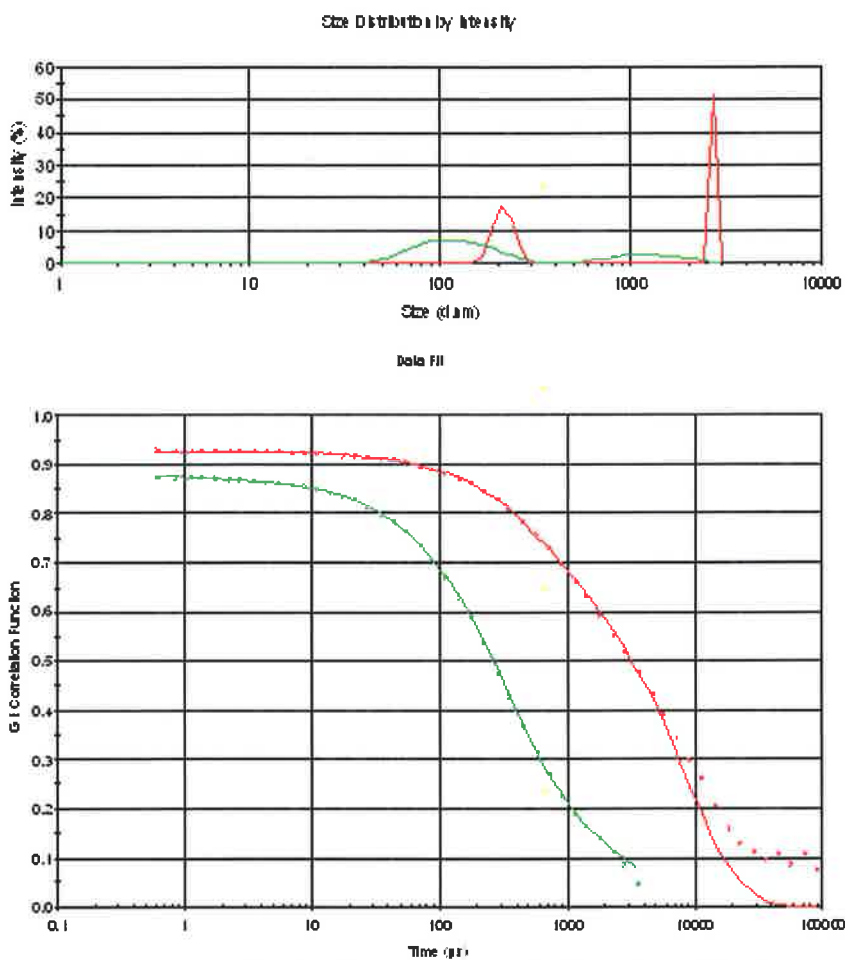


Figure 6.4 The intensity distribution and correlation data fits from PCS for the concentrated polyaniline DBSA with a z-average 959 nm (PDI 0.830) (-) and filtered polyaniline DBSA with a z-average 138 nm (PDI 0.399) (-).

The scanning electron microscopy images of a sample of DBSA doped polyaniline show that it is composed of small spherical particles on the ~100 nm scale and larger aggregates.

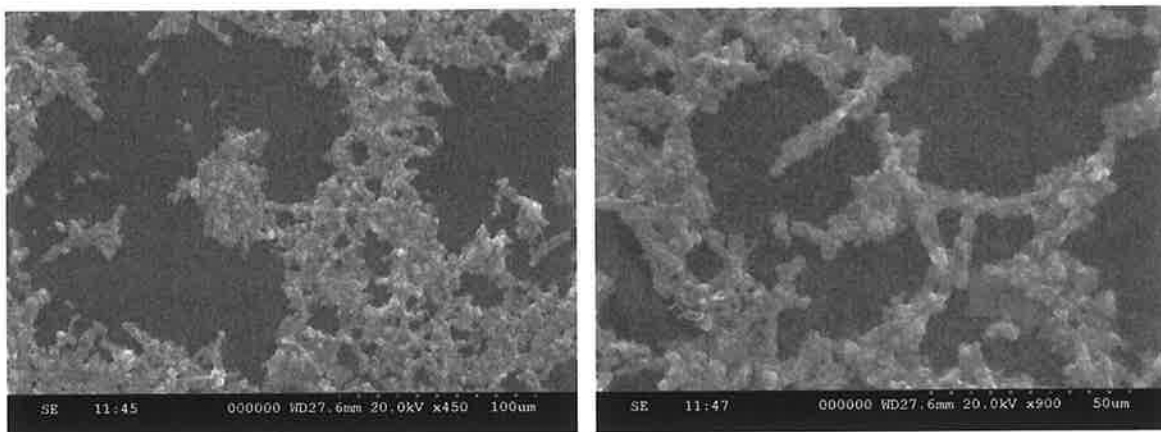


Figure 6.5 SEM images of sample polyaniline DBSA1 showing small spherical nanoparticles (~100nm) and larger clusters.

However, due to the nature of the synthetic route the surfactant DBSA was present as both the surfactant and the dopant. The initial scope of this work was to compare these nanostructured materials with the TFSA doped amorphous polyaniline samples from the previous chapter. For this it was necessary to replace all of the DBSA with TFSA while retaining nanostructure. Normal methods of dopant removal by washing in basic solution were unsuccessful in this case and this synthetic route was not pursued.

Two interesting observations were noted in the NMR profiles of DBSA doped polyaniline; the profiles obtained are not sensitive to dopant concentration and the ^{14}N quadrupolar dips (observed at frequencies between 3.5 and 0.3 MHz) in polyaniline doped with TFSA and HPF_6 are suppressed. Kimmich and Anardo [50] have shown that, for organic macromolecules and proteins, quadrupolar dips arise due to backbone fluctuations. This indicates that doping with DBSA results in a polymer with reduced backbone fluctuations relative to TFSA doped polyaniline. This is probably due to the steric restraints imposed by the larger surfactant molecule. Also the dopant has a large number of protons which may add to the NMR relaxation response.

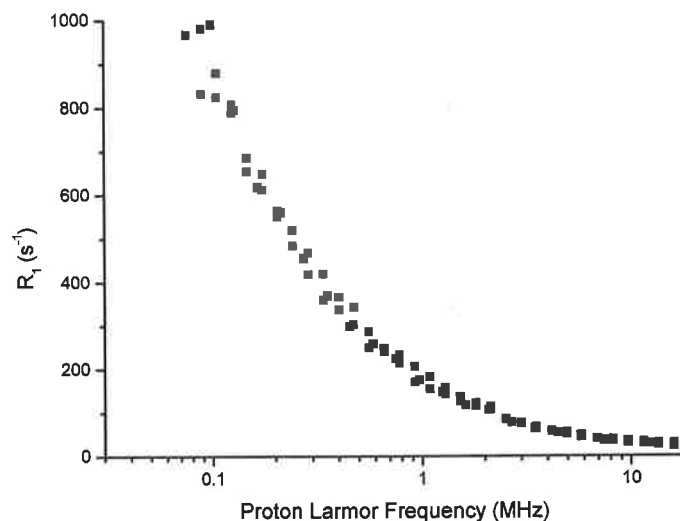


Figure 6.6 Relaxation profiles of polyaniline DBSA samples at 298 K; DBSA1 (■, y-value = 0.59), DBSA2 (●, y-value = 0.46) and DBSA3 (▲, y-value = 0.63).

6.3.1.4 Interfacial synthesis

Interfacial synthesis yielded semi-crystalline materials all of which retained some amorphous component. The goal of a completely nano-structured material was not achieved. However, this synthetic route produced the most consistent and useful nano-structured materials and the following detailed results section and subsequent discussion will therefore, focus on the materials synthesised by interfacial methods.

6.3.2 Analysis of ICP's produced by interfacial synthesis

6.3.2.1 Particle Sizing

Particle sizing by PCS of the concentrated solution of the top layer of the interfacial synthesis showed large particles on the order of $>5 \mu\text{m}$. Dilution and filtration did not change this result significantly. This is probably due to the agglomeration of amorphous material or, as PCS provides the diameter of the sphere of equivalent volume, rod of length $\sim 1 \text{ mm}$ and diameter of $>1 \mu\text{m}$ could be present, which would have the equivalent volume of a very large sphere.

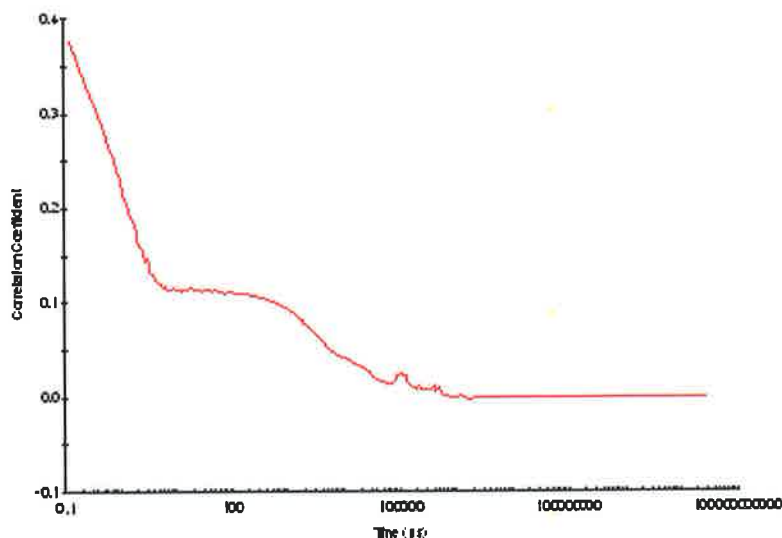
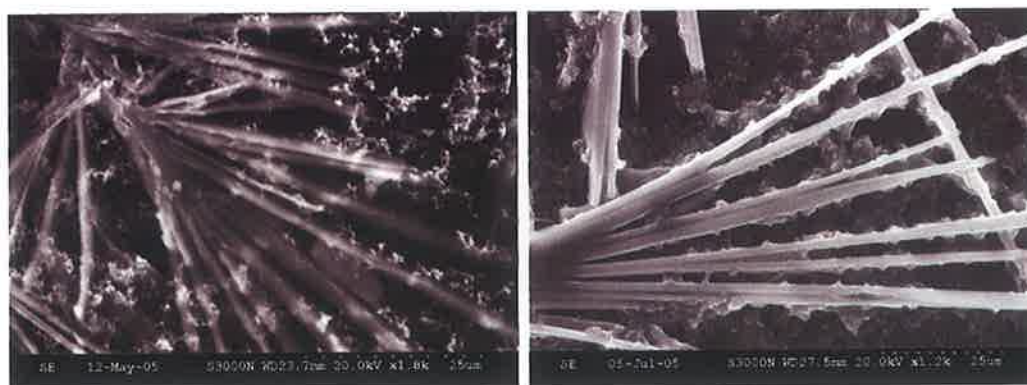


Figure 6.7 The correlation data from PCS for concentrated polyaniline TFSA from interfacial synthesis with a z-average=373 nm (PDI=1) (-). Note the multi-exponential correlation data indicating multiple particle sizes across a wide range.

6.3.2.2 SEM

Scanning electron microscopy was used to estimate the degree of crystallinity of the samples. Imaging was carried out with a general voltage of 20 kV, without gold-coating as the samples are conducting. The major feature of these preparations was the presence of crystalline rods 0.1-2 μm in diameter with length on the order of microns to millimetres. However, it was not possible to synthesise a sample consisting purely of micro-rods, there was always a significant amorphous component detectable by SEM.



(a)

(b)

Figure 6.8 SEM images of (a) polyaniline HCl and (b) polyaniline TFSA showing crystalline rods of the order of 0.1-2 μm in diameter and millimetres in length.

The acid type, solvent type, monomer concentration and the presence of a strong magnetic field during synthesis had little or no effect on the nanorod size, shape or relative content of nanocrystalline to amorphous polymer.

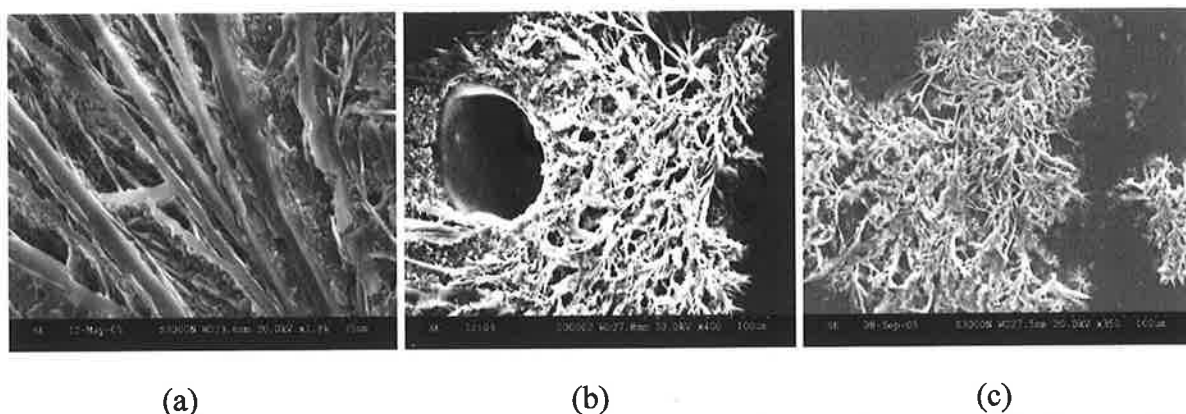


Figure 6.9 SEM images showing nanorods in an amorphous polymer matrix for samples (a) normal conditions (0.5:0.5:0.125 M acid:monomer:oxidant ratio at room temperature) (b) with increased monomer concentration (1 M) and (c) under a 1 T magnetic field.

However, increasing the oxidant concentration resulted in the formation of crystalline flakes $\sim 2 \mu\text{m}$ in diameter, as opposed to the rods produced in the syntheses with monomer:oxidant ratios of 4:1 or less. Figure 6.11 shows SEM images for samples synthesised on a small scale with constant acid and monomer concentrations (0.5 M) but with increasing oxidant concentration.

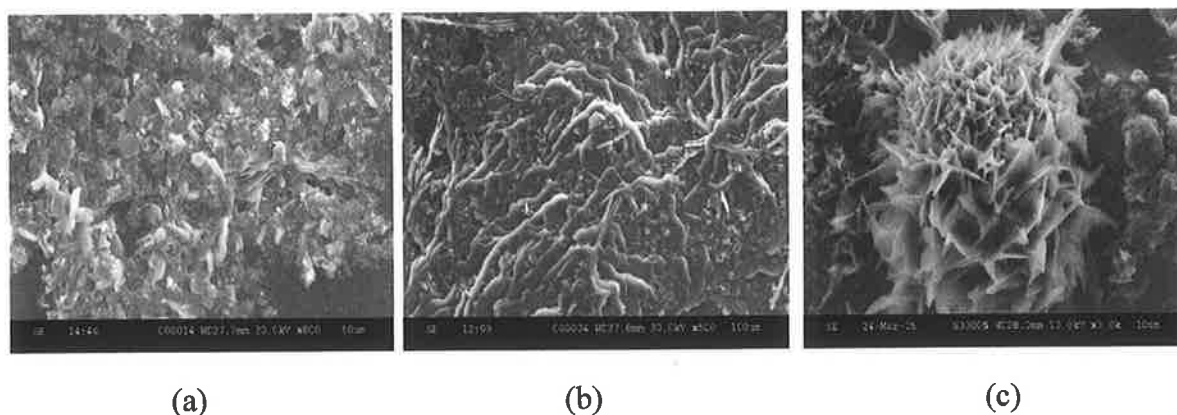


Figure 6.10 SEM images of polyaniline TFSA grown using constant acid and monomer concentrations and an oxidant concentration of (a) 0.25 M, (b) 0.5 M and (c) 0.75 M showing an increase in the proportion of flake-like crystalline phase embedded in amorphous polyaniline.

For both the smaller and larger scale preparations increasing the acid concentration had the effect of increasing the amount of crystalline material in the sample. The sample from large scale synthesis, nano2 was estimated to have $\sim 60\%$ crystalline material, nano3 $\sim 30\%$, nano4 $\sim 20\%$ and nano7 $\sim 70\%$.

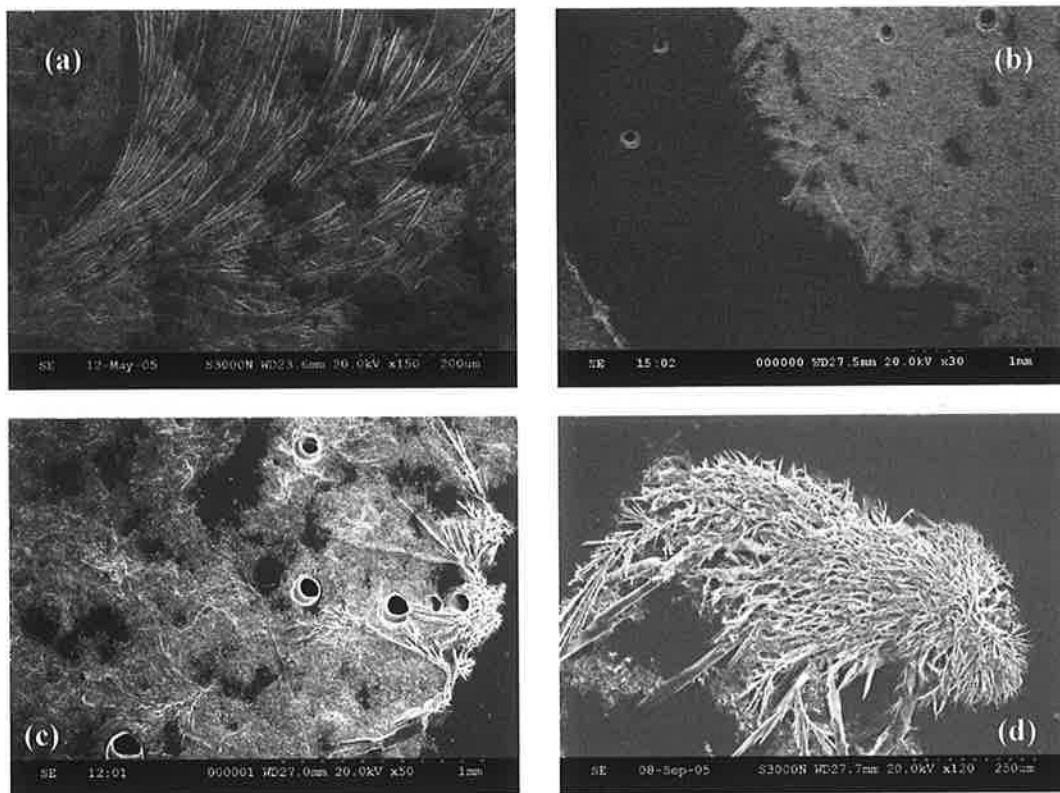


Figure 6.11 Low magnification SEM images of (a) nano2 (b) nano3 (c) nano4 and (d) nano7.

6.3.2.3 AFM

Atomic force microscopy (AFM) was used to further probe the nano-crystalline structure of these polymers. However, the heterogeneous nature of the materials made it difficult to obtain clear AFM images. SEM had shown that most of the crystalline structure was covered by amorphous polymer. Smooth rastering of the AFM tip across the crystalline rod surface was impeded by amorphous material and the crystalline nanostructures were not clearly observable. The effect of amorphous polymer on the AFM image of nanocrystalline material is shown in figure 6.12.

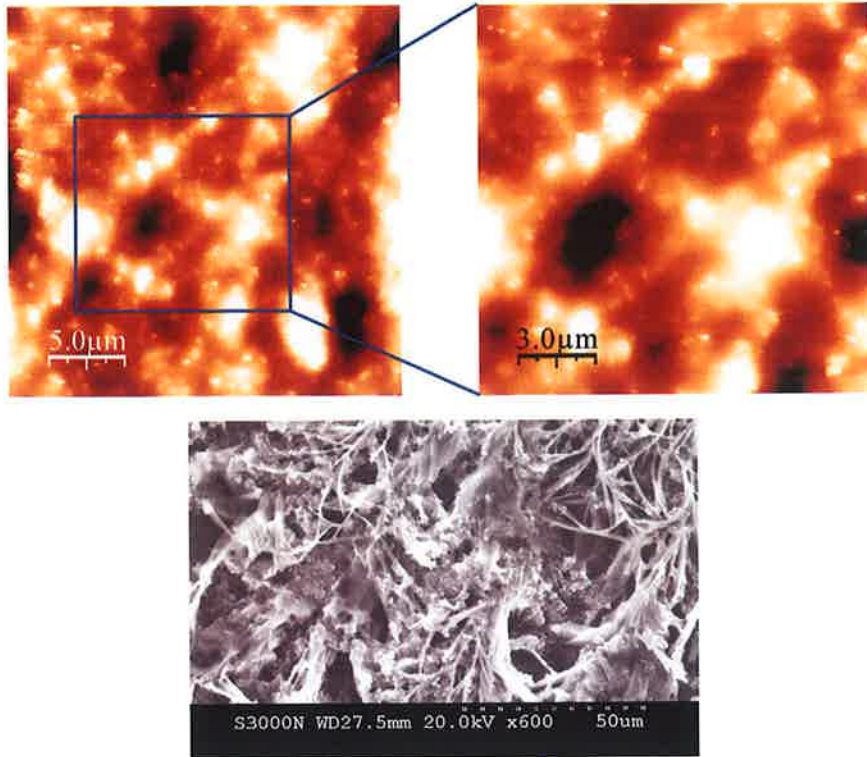


Figure 6.12 AFM (upper) and SEM (lower) images of sample nano2 showing crystalline structure underneath amorphous material.

To overcome this problem SEM was used to find regions in the stub where the crystalline material was not covered by amorphous polymer. These areas were noted and examined by AFM. AFM images showed that the crystalline rods were generally $<1\mu\text{m}$ in diameter (figure 6.13).

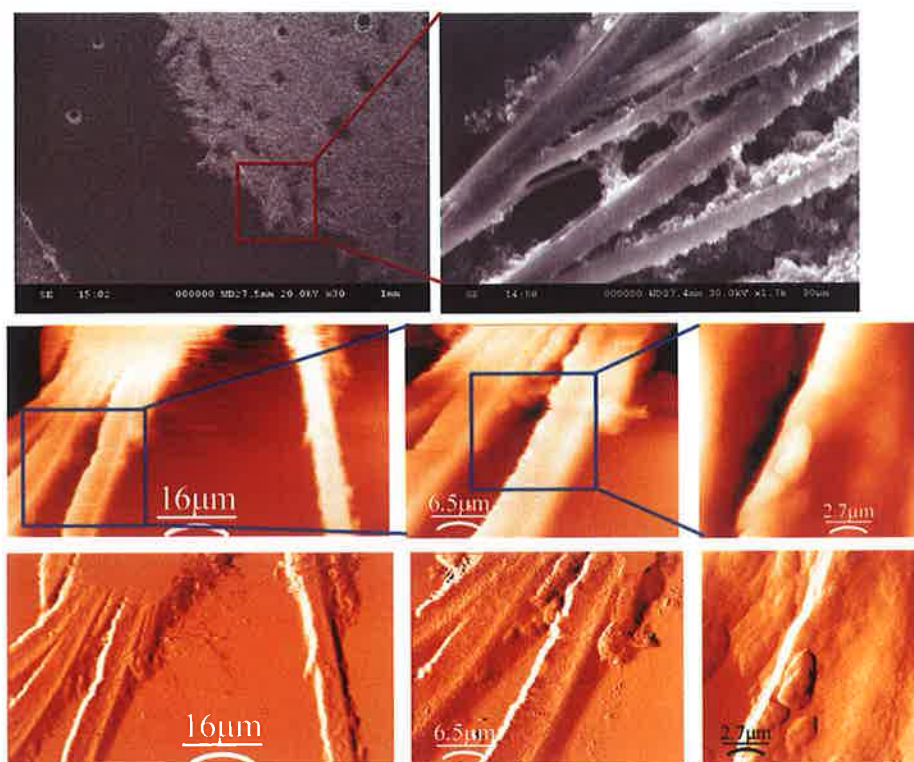


Figure 6.13 SEM (top), AFM (middle) and AFM derivative (bottom) images of sample nano4 showing crystalline rods $\sim 1 \mu\text{m}$ in diameter.

A more detailed examination of nanocrystalline rods using AFM was carried out on the highly crystalline nano7 sample. A much slower scan speed was used to obtain higher resolution AFM images, which clearly showed a number of rods of $\sim 1 \mu\text{m}$ diameter. It also showed that the larger rods, those $> 1 \mu\text{m}$, actually consisted of a number of sub micron-sized rods joined together.

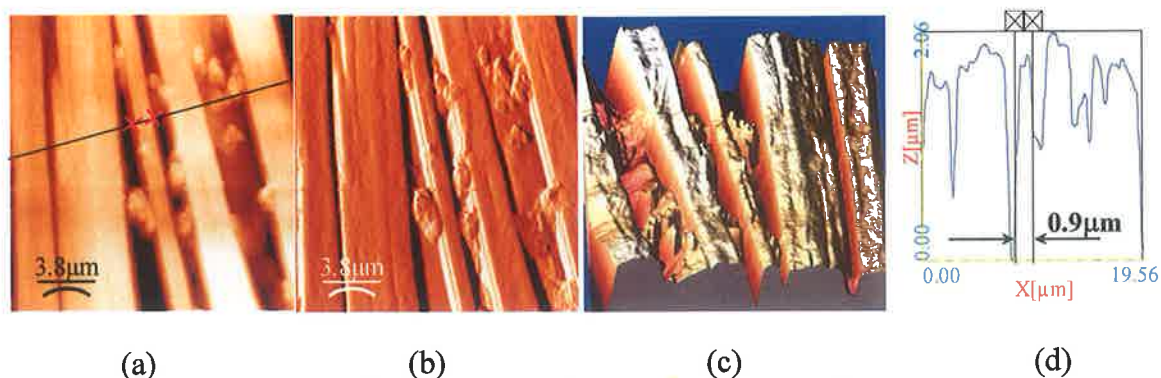


Figure 6.14 (a) Original AFM image, (b) derivative, (c) three-dimensional image and (d) cross-sectional size plot of nanorods in the highly crystalline sample nano7.

The fine structure of the amorphous material observed by AFM was found to consist of agglomerations of small spherical nanoparticles with a diameter of $< 100 \text{ nm}$. These

nanoparticles were also observable in some cases using SEM but were however at the limit of the resolution of the SEM equipment.

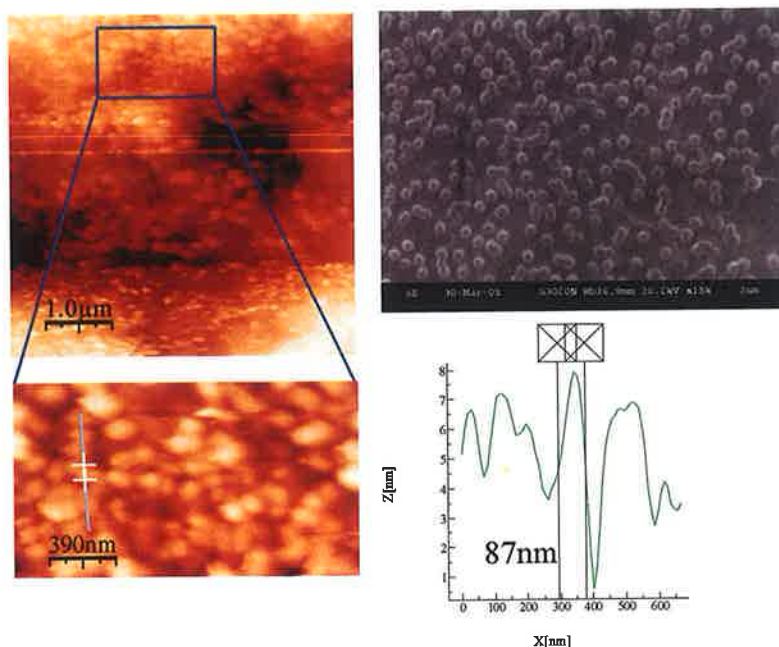


Figure 6.15 SEM (right top) and AFM (left) images and a cross-section from AFM (right bottom) showing spherical nano-crystalline particles of about 90-200 nm diameter.

A feature of the small scale preparations with a high oxidant concentration was the presence of highly crystalline flakes $\sim 1 \mu\text{m}$ in diameter. SEM and AFM images of a sample synthesised with four times the normal concentration of oxidant both showed the presence of crystalline flakes in an amorphous matrix and did not show any rod-like morphology.

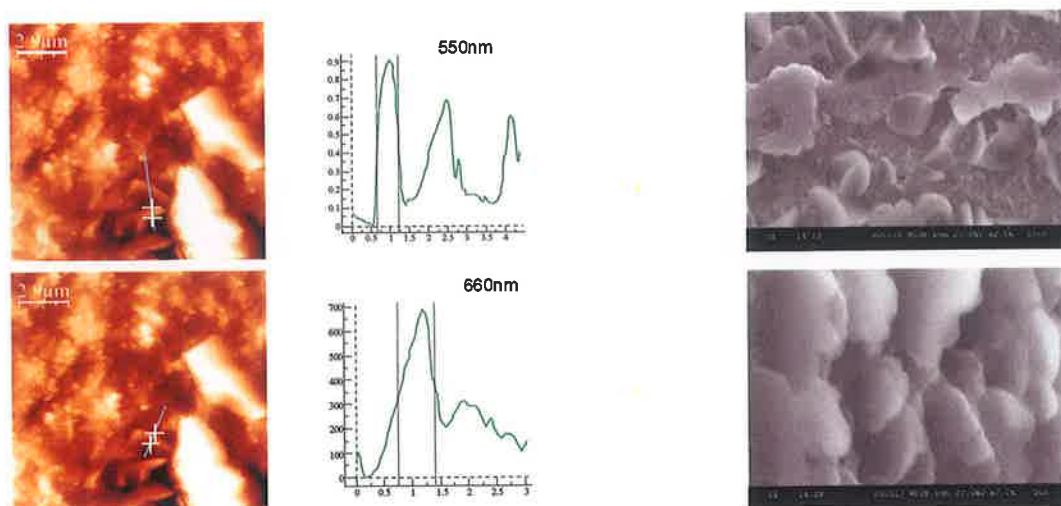


Figure 6.16 AFM (left), cross-sections (centre) and SEM (right) images showing the micro-crystalline flake morphology in samples grown with high oxidant concentrations.

6.3.2.4 Conductivity

Conductivity measurements were attempted on all samples using the 4-point probe apparatus described in Chapter 2. The pin spacing was 0.9 mm and currents ranging from 0.01-20 mA were applied. However, a stable, repeatable voltage, and therefore conductivity value, could not be obtained. This is probably due to the heterogeneous nature of these materials.

6.3.2.5 Dopant concentration (*y*-value)

The table below shows the *y*-values for all of the samples analysed by NMR relaxometry prepared by large-scale interfacial synthesis. A number of powder samples from the same preparation were analysed by CHN microanalysis and the resulting *y*-values were found to be within ~3 % of each other indicating while the samples are spatially heterogeneous the quantities used for microanalysis are statistically representative of the bulk material.

Table 6.3 Dopant concentration of polyaniline TFSA grown by large scale interfacial synthesis

Sample	%N	%F	<i>y</i> -value
Nano2	8.7	13.42	0.379
Nano3	8.62	10.34	0.294
Nano4	8.15	9.31	0.281
Nano7	8.53	13.65	0.395

6.3.2.6 NMR

The FFC-NMR measurements were carried out on the Stellar spinmaster FFC-NMR 2000 relaxometer using pre-polarised and non-polarised sequences. The magnetisation recovery curves were mono-exponential at all fields and at all temperatures for all dopant and crystallinity levels.

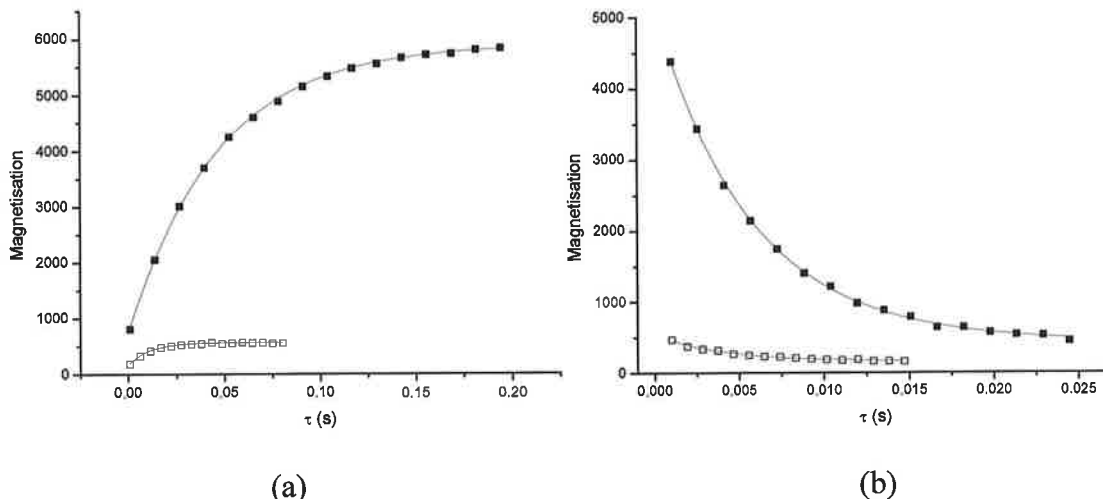


Figure 6.17 Mono-exponential magnetisation recovery curves of samples nano4 (\square) and nano7 (\blacksquare) at 298 K at (a) 10 MHz and (b) 0.1 MHz.

It is immediately apparent that T_2 is much larger for the highly crystalline materials and as a result the signal to noise ratio of the FID is much greater than for the less crystalline samples (figure 6.17). The data recorded is also of better quality than that obtained for amorphous preparations of similar dopant content, Chapter 5. The FID of mixed crystalline and amorphous polymer blends usually exhibit multi-exponentiality. However, due to efficient spin-diffusion between the crystalline and amorphous regions in polyaniline the FID is probably mono-exponential. The magnetisation was sampled by summing the intensity in the time range indicated by dashed lines in figure 5.4. The T_1 value obtained is insensitive to the interval used for this summation, although extending the interval to longer times (greater than 0.0003 s) increased the error in T_1 .

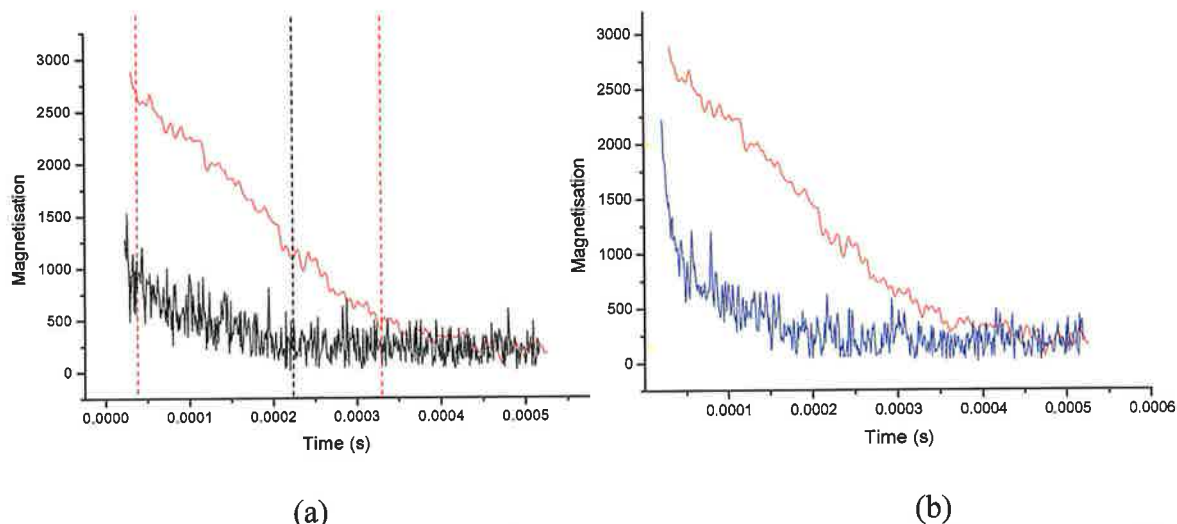


Figure 6.18 Free induction decays of (a) nano7 (-, y-value = 0.395) and the less crystalline nano4 (-, y-value = 0.281) and (b) nano7 (-) and an amorphous sample with similar dopant concentration TFSA2 (-, y-value = 0.389), each with 32 scans, showing monoexponential decays.

NMR relaxation profiles showed that the nano-crystalline samples had good reproducibility and stability. A number of NMR profiles were recorded over the temperature range (253 - 348 K) and the ambient temperature response (298 K) was rerecorded between each experiment to confirm sample stability. The samples remained stable over a number of weeks.

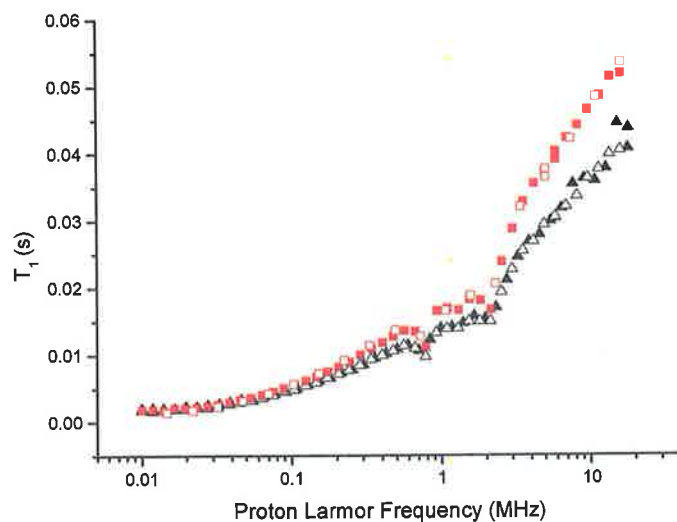


Figure 6.19 Relaxation profiles recorded at 298 K showing the stability of samples nano7 initially (■) and after 9 weeks (□), and for nano2 initially (▲) and after 3 weeks (△).

The samples with lower levels of crystallinity and with lower dopant levels (nano3 and nano4) showed little observable temperature dependence. This was as expected from previous experiments on low dopant concentration amorphous polyaniline.

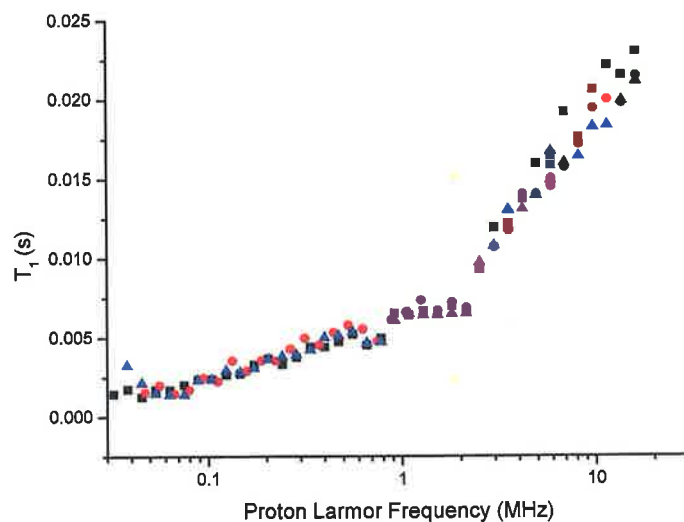


Figure 6.20 Relaxation profiles of low crystallinity content sample nano3 recorded at 298 K (■), 323 K (●), and 348 K (▲).

The samples with higher dopant concentrations and higher levels of crystallinity (nano7 and nano2) show temperature dependence at higher temperatures similar to that observed for highly doped amorphous polymers.

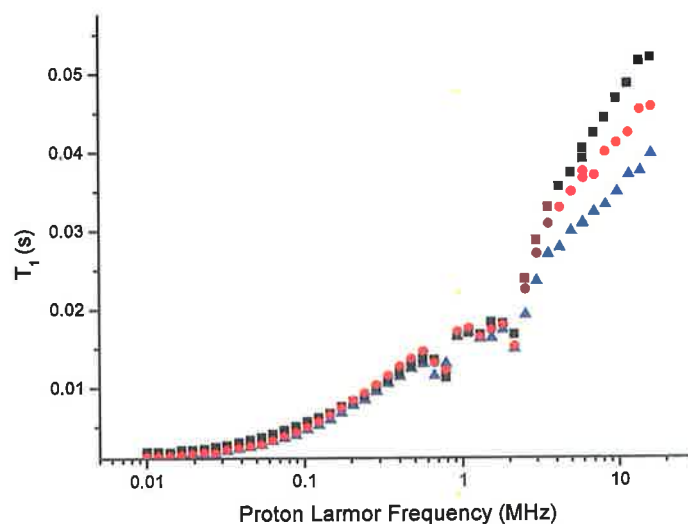


Figure 6.21 Relaxation profiles of sample nano7 recorded at 298 K (■), 323 K (●), and 348 K (▲).

As was observed for the amorphous polymers, the relaxation profiles are dependent on the dopant concentration as T_1 decreases across the frequency range with dopant concentration.

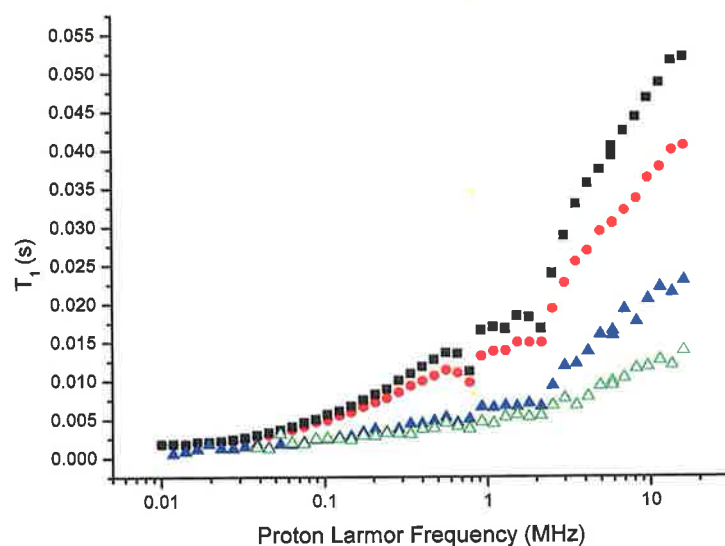


Figure 6.22 Relaxation profiles recorded at 298 K of samples nano2(●), nano3 (▲), nano4 (△) and nano7 (■).

6.4 Discussion

6.4.1 ^{19}F NMR

Triflic acid, the dopant used in this work, was chosen as it contains fluorine. As a result ^{19}F NMR relaxation times could be used as a probe for dopant motion. As was observed for amorphous polymers, in Chapter 5, the ^{19}F NMR response is insensitive to both dopant concentration and temperature change. The relaxation profiles do show a slight change from the amorphous response, but when the curves are fitted with the Cole-Cole spectral density function the correlation times and degree of correlation obtained are very similar ($\tau_{c\text{Amor}} = 3.6(8)\times 10^{-8}$ s $\tau_{c\text{Nano}} = 2.9(2)\times 10^{-8}$ s and $\delta_{\text{Amor}} = 0.36(4)$ $\delta_{\text{Nano}} = 0.35(2)$). The measured 29 ns correlation time for TFSA anion tumbling is again on the expected timescale for molecular tumbling in a moderately restricted environment at this temperature and a correlation value of 0.35 indicates a significantly correlated motion. Thus the anion motion is not restricted or controlled by the bulk crystallinity, or the dopant level.

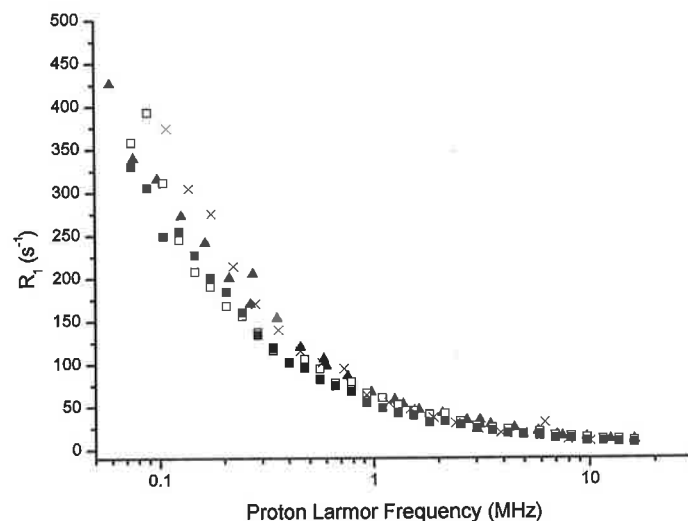


Figure 6.23 ^{19}F relaxation profiles of samples nano7 (■), nano3 (▲), and TFSA2 (X) at 298 K and sample nano7 (□) at 323 K.

6.4.2 ^1H NMR

6.4.2.1 *Quadrupolar Dips*

As was observed for the amorphous samples, the smooth gradual increase of T_1 with field strength is interrupted by three peaks at defined frequencies (0.74 MHz, 1.56 MHz and 2.30 MHz). These are ^{14}N quadrupolar dips and the affected frequency range is omitted from the data analysis which follows.

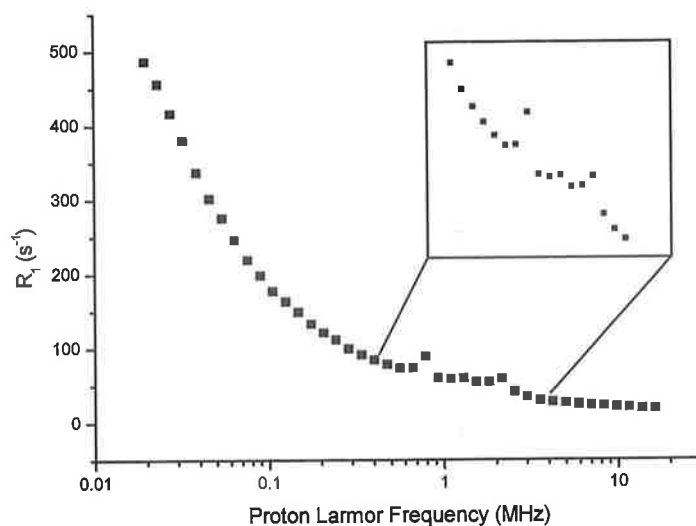


Figure 6.24 Relaxation profile of nano7 showing three quadrupolar dips (inset).

6.4.2.2 Effects of crystallinity on NMR response

It is currently accepted that conduction of ICP's is limited by charge carrier diffusion through the less doped amorphous regions. This FID measured for the amorphous sample with the Bruker minispec (Chapter 5) shows that there is a contribution to the NMR signal from the crystalline part for a mostly amorphous material. The FID recorded on the field-cycling magnet for the polyaniline TFSA samples from interfacial synthesis shows a large increase in signal intensity due to longer T_2 values associated with increasing crystallinity of the material.

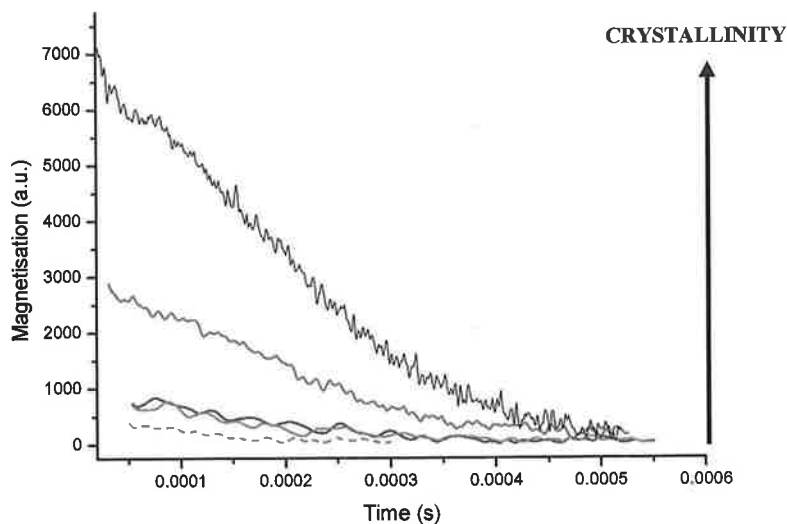


Figure 6.25 Free induction decays of semi-crystalline samples nano7 (-, y-value = 0.395), nano2 (-, y-value = 0.379) nano3 (-, y-value = 0.294), nano4 (-, y-value = 0.281) and amorphous sample TFSA4 (---, y-value = 0.399), each with 32 scans, showing the effect of increases in bulk crystallinity on the NMR signal.

6.4.2.3 Dimensionality

The crystalline or partially crystalline polyaniline TFSA samples were analysed in the same manner to the amorphous polymers from the previous chapter. A power-law spectral density function was applied successfully to fit the data. For the purposes of the fit the region containing the quadrupole dips was omitted from the data sets. The highly crystalline samples were fit accurately but due to the smaller signal-to-noise ratio and associated errors, analysing data with low dopant concentrations was more problematic.

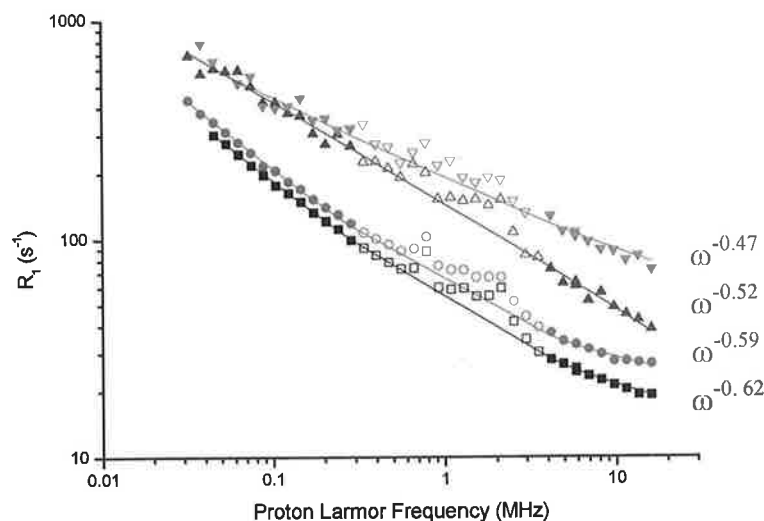


Figure 6.26 ^1H relaxation profiles for samples nano2 (\bullet), nano3 (\blacktriangle), nano4 (\blacktriangledown) and nano7 (\blacksquare) fit with the power-law function for fractal dimensionality. The regions containing quadrupole dips were omitted from the fits and are represented by open markers.

The samples exhibiting lower crystallinity (nano3 and nano4) share similar characteristics to amorphous samples with low dopant content from regime (i) (figures 5.24 and 5.25); low signal-to-noise and no temperature dependence of the power law. The samples with higher dopant content (nano2 and nano7) share similar characteristics with similarly doped amorphous materials, regime (ii) and (iii), such as high signal-to-noise and temperature dependence of the power law, despite having much higher bulk crystallinity.

Interpretation 1. Polaron transport through undoped regions.

As with the data from the amorphous samples, the power-law dependence of the ^1H profiles can be interpreted in two ways. In the first interpretation it is suggested that the $>\omega^{-1/2}$ behaviour arises from the relaxation of the nuclear spins coupling to electronic spins modulated by the motion of charge carriers through the undoped part of the material. The resulting dimensionalities for charge carrier motion plotted as a function of dopant mole fraction and overlaid with the equivalent results for the amorphous samples are presented in figure 6.27. Surprisingly, the values for the nanocrystalline polymers correspond very closely to those of the amorphous materials

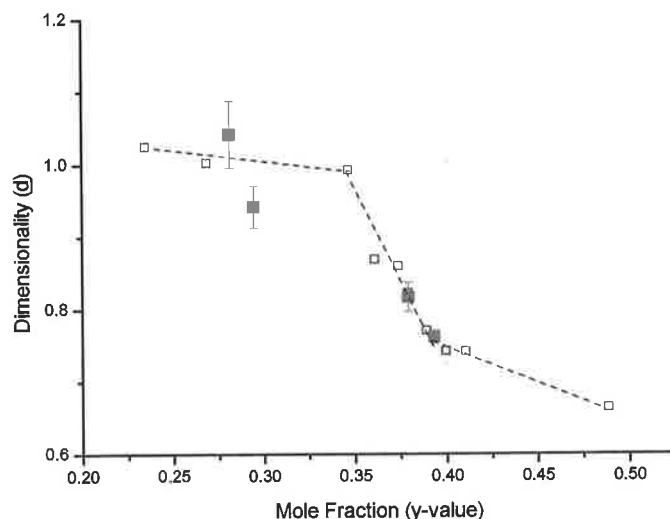


Figure 6.27 Spatial dimensionality, \bar{d} , as a function of dopant mole fraction from fits to spectral density functions for fractal dimensionality for the amorphous samples from the previous chapter (□) and the nanocrystalline samples (■).

The nanocrystalline samples have extensive crystalline nanostructure, detectable by SEM, but show similar NMR characteristics to the amorphous samples of comparable dopant levels. This indicates that the dimensionality of the charge carriers through the undoped, amorphous regions is not affected by the bulk crystallinity. It suggests that the improved conductivity observed in some of these materials is not due to increased diffusion through the amorphous regions, but probably is due to increased diffusion rates through the crystalline regions possibly arising from enhanced chain ordering. Due to the limitations of the synthesis fully crystalline polyaniline samples could not be prepared. Films of a fully crystalline, fully doped polyaniline material were synthesised using a self-stabilised dispersion technique by Lee et al [69] and were shown to have metallic-like conduction and a room-temperature conductivity of $>1000 \text{ Scm}^{-1}$. The temperature dependence and large increase in bulk conductivity suggests this material exhibits three-dimensional diffusion. This indicates that such a fully crystalline material does not have non-conducting regions to limit polaron motion. The NMR dispersion of such a motion might be expected to be frequency independent at low frequency.

Interpretation 2. Backbone fluctuations.

The second interpretation suggests that the NMR relaxation is due to ^1H - ^1H relaxation modulated by backbone fluctuations caused by polaron motion through the material.

The powers, or b-values, from the fits to the power law spectral density model can then be related to the structural (d_f) and dynamic (\bar{d}) dimensionality characteristics of the material. [168, 169] As in the last chapter \bar{d} can be assumed to be 4/3. [165] The resulting fractal dimensionalities, d_f , for backbone fluctuations were plotted as a function of dopant mole fraction and were overlaid with the equivalent results for the amorphous samples, figure 6.28.

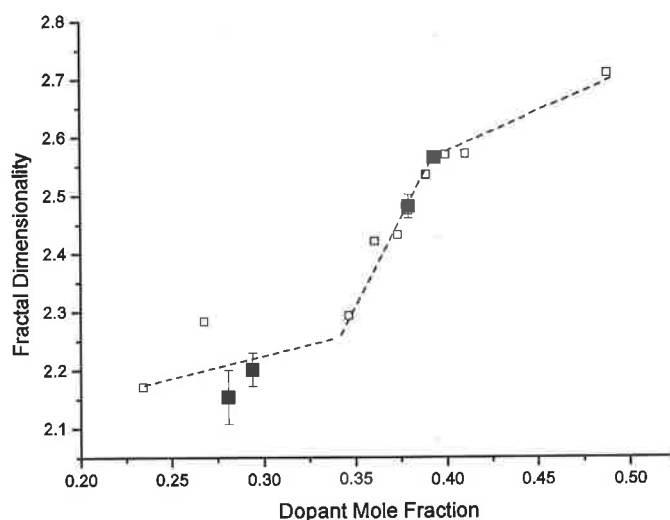


Figure 6.28 Fractal dimensionality, d_f , as a function of dopant mole fraction for the amorphous samples from the previous chapter (□) and the nanocrystalline samples (■)

For both amorphous and crystalline polymers as the y-value approaches 0.5, the distribution of the protons becomes uniform where the dimensionality is ~ 3 . This suggests that the dimensionality of the network is the same for both amorphous and crystalline phases, and is determined by the dopant level. Unfortunately attempts made to use EDAX and Auger spectroscopy to measure dopant levels in the crystalline and amorphous regions separately were inconclusive.

6.5 Conclusions

The aim of this project was to prepare pure nanocrystalline polyaniline to determine how changes in crystallinity affects the physical properties of these polymers. A number of synthetic approaches were used in an attempt to produce a highly crystalline material. The simplest was a modified aqueous polymerisation, which while producing the required yield of polymer showed no obvious crystalline morphology. Electrochemical methods proved less successful, as the polymer could not be grown in sufficient quantities for NMR analysis. Surfactant synthesis succeeded in producing large amounts of nano-structured polymer. However, the surfactant proved difficult to remove and attempted replacement with a TFSA anion proved ineffective.

The most successful route to nanocrystalline polymers was by interfacial synthesis. In this approach the polymer is grown at the interface of a monomer/organic solvent solution and oxidant/aqueous acid solution. SEM and AFM analysis showed that this route yielded materials with > 60 % of the sample consisting of crystalline rods of 0.1-2 μm diameter and millimetres long. However, the remaining part of the sample was amorphous. The relative concentration of the crystalline material could be increased with increasing acid concentration, but as triflic acid fumes strongly in air it is difficult to make accurate or highly concentrated acid solutions and a fully crystalline material could not be synthesised with this dopant.

A number of samples of varying crystallinity were synthesised, analysed by CHN microanalysis and NMR and compared with amorphous polymers of similar dopant levels. The T_2 of the samples increases greatly with increasing crystallinity. This indicates that the NMR response arises from the crystalline part of the material. However, when the T_1 profiles were examined they showed very similar behaviour to the amorphous materials; the low-dopant concentration samples showed no temperature response and poor data quality whereas the high dopant concentration samples the dimensionality increased with temperature. Therefore, the increase in T_2 may be explained as due to increased motion in the crystalline regions, which is averaged by efficient spin diffusion between regions of the polymer.

The T_1 profiles were fitted using a power-law spectral density function. This power law behaviour was interpreted as being due to relaxation by electronic spins of slow charge carrier dynamics through the undoped regions of the material or as

homonuclear dipolar interactions modulated by slow backbone fluctuations arising from doped chains. In both cases the extracted dimensionalities showed very similar behaviour to the amorphous materials. This indicates that the dimensionality is not governed by the bulk crystallinity but by the dopant concentration and that the dopant is just as likely to reside in the amorphous regions as the crystalline regions. It also suggests that the enhanced electrical properties of these materials are not due to increased diffusion through the undoped part of the polymer but to increased diffusion rates through the highly doped regions, possibly due to enhanced chain ordering. Contrary to our expectations, analysis of crystalline samples cannot be used to differentiate between the two interpretations.

Overall Conclusions and Future Work

It has been shown that field-cycling NMR is an effective analytical tool in the study of the mechanisms of transport in a number of solid conducting systems. A detailed mechanism for fluoride ion conduction in superionic PbSnF_4 was developed from ^{19}F NMR relaxometry data that is consistent with the diffraction and conductivity measurements. Using the fluoride jump distances and Arrhenius prefactors extracted from the analysis of the NMR data, a slower correlated motion was assigned to in-plane fluoride translational motion, while a fast correlated motion was assigned to non-translational out-of-plane fluoride jumps into nominally vacant sites. We propose that conductivity in PbSnF_4 is due to translational fluoride jumps in the conducting plane, facilitated by the fast exchange process that creates vacancies in the conducting plane which act as Frenkel defects.

Similar correlated charge carrier transport dynamics were observed in the high temperature phase of the superprotonic solid acid, $\text{Cs}_6(\text{HSO}_4)_3(\text{H}_2\text{PO}_4)_4$. Using dynamic and structural parameters extracted from the ^1H NMR data, an 'NMR' conductivity was calculated. While this is systematically greater than the conductivity obtained from impedance spectroscopy, the activation energy for conduction from NMR is in good agreement. The NMR analysis suggests that the conductivity increase, going from the low-temperature to the high-temperature superprotonic phase, is largely due to a large expansion of the lattice, and that the correlation time for proton motion is very weakly temperature dependent.

A number of doped polyaniline samples were synthesised with a range of dopant contents. Fitting the ^1H NMR analysis to a power law function showed that a change in the power with dopant content that could be interpreted in two ways. The first interpretation assumes that the power is related to the dimensionality of charge carriers through the undoped, less conducting part of the material. This dimensionality is inversely related to the conductivity which indicates that conductivity increase with a decrease in transport through the non-conducting regions. The second interpretation assumes that the power is related to the structural dimensionality of the backbone fluctuations of the polymer. This can be assigned to increases polymer motion with increasing dopant content. There is also a direct correlation to the conductivity

suggesting that conductivity increases as the homogeneity of the proton distribution, and hence doping, increases.

Nanocrystalline doped polyaniline was synthesised by a number of methods, of which interfacial synthesis proved most useful for our needs. A number of samples were synthesised with varying crystallinity levels which were analysed by microscopy and NMR. The ^1H NMR data resulted in very little change, with increasing crystallinity, to the trends observed in related amorphous samples. ^{19}F NMR was used to characterise dopant mobility in both amorphous and crystalline materials and it was shown that in both materials the anion is not directly involved in the conductivity.

The limited time and the vastness of the field of field solid conducting materials leaves scope for much future work. In the area of solid ionic conductors future work could involve investigation into related fluoride ion conductors such as BaSnF_4 and PbF_2 . Other possibilities including studies of conducting lithium solid electrolytes could be of tremendous scientific importance, as many of the electrolytes used today are based on lithium. There is also a large range of superprotonic conductors in the solid acid and perskovite family with well defined structures that would lend themselves well to study by field-cycling NMR. A more detailed study of crystalline conducting polymers and related carbon nanotube materials could be carried out by field-cycling methods, as this area is gaining commercial recognition in the field of biomedicine and consumer goods as well as fuel cell applications.

Bibliography

1. Pauli, W., Pauli exclusion principle, *Naturwiss* 1924, 12, 741.
2. Bloch, F., Nicodemus, D. and Staub, H. H., A Quantitative Determination of the Magnetic Moment of the Neutron in Units of the Proton Moment, *Physical Review* 1948, 74(9), 1025-1045.
3. Purcell, E. M., Spontaneous Emission Probabilities at Radio Frequencies, *Physical Review* 1946, 69(11-1), 681-681.
4. Bloembergen, N., Purcell, E. M. and Pound, R. V., Relaxation Effects in Nuclear Magnetic Resonance Absorption, *Physical Review* 1948, 73(7), 679-712.
5. Beckmann, P. A., Spectral Densities and Nuclear-Spin Relaxation in Solids, *Physics Reports-Review Section of Physics Letters* 1988, 171(3), 85-128.
6. Dissado, L. A. and Hill, R. M., Non-Exponential Decay in Dielectrics and Dynamics of Correlated Systems, *Nature* 1979, 279(5715), 685-689.
7. Havriliak, S. and Negami, S., A Complex Plane Analysis of Alpha-Dispersions in Some Polymer Systems, *Journal of Polymer Science Part C-Polymer Symposium* 1966(14PC), 99-&.
8. Cole, R. H., On the Analysis of Dielectric Relaxation Measurements, *Journal of Chemical Physics* 1955, 23(3), 493-499.
9. Gutowsky, H. S., Saika, A., Takeda, M. and Woessner, D. E., Proton Magnetic Resonance Studies on Natural Rubber .2. Line Shape and T1 Measurements, *Journal of Chemical Physics* 1957, 27(2), 534-542.
10. Chezeau, J. M., Strange, J. H. and Brot, C., Motional Disorder in Hexasubstituted Chloromethylbenzenes, *Journal of Chemical Physics* 1972, 56(3), 1380-&.
11. Koenig, S. H. and Brown, R. D., Field-Cycling Relaxometry of Protein Solutions and Tissue - Implications for Mri, *Progress in Nuclear Magnetic Resonance Spectroscopy* 1990, 22, 487-567.
12. Hallenga, K. and Koenig, S. H., Protein Rotational Relaxation as Studied by Solvent ^1H and ^2H Magnetic-Relaxation, *Biochemistry* 1976, 15(19), 4255-4264.

13. Davidson, D. W. and Cole, R. H., Dielectric Relaxation in Glycerol, Propylene Glycol, and Normal-Propanol, *Journal of Chemical Physics* 1951, 19(12), 1484-1490.
14. Beckmann, P., Methyl and Tertiarybutyl Reorientation in Molecular-Solids, *Chemical Physics* 1981, 63(3), 359-375.
15. Burnett, L. J. and Muller, B. H., Spin Relaxation and Molecular-Motion in Solid Ethane, *Journal of Magnetic Resonance* 1976, 23(2), 343-360.
16. Privalov, A. F., Lips, O. and Fujara, F., Dynamic processes in the superionic conductor LaF_3 at high temperatures as studied by spin-lattice relaxation dispersion, *Journal of Physics-Condensed Matter* 2002, 14(17), 4515-4525.
17. Focke, W. W., Wnek, G. E. and Wei, Y., Influence of Oxidation-State, pH, and Counterion on the Conductivity of Polyaniline, *Journal of Physical Chemistry* 1987, 91(22), 5813-5818.
18. Chiang, J. C. and Macdiarmid, A. G., Polyaniline - Protonic Acid Doping of the Emeraldine Form to the Metallic Regime, *Synthetic Metals* 1986, 13(1-3), 193-205.
19. Winokur, M., Moon, Y. B., Heeger, A. J., Barker, J., Bott, D. C. and Shirakawa, H., X-Ray-Scattering from Sodium-Doped Polyacetylene - Incommensurate-Commensurate and Order-Disorder Transformations, *Physical Review Letters* 1987, 58(22), 2329-2332.
20. Lee, C. E., Lee, C. H., Yoon, K. H. and Jin, J. I., NMR-Study of the PPV Conducting Polymers, *Synthetic Metals* 1995, 69(1-3), 427-428.
21. Pratt, F. L., Blundell, S. J., Lovett, B. W., Nagamine, K., Ishida, K., Hayes, W., Jestadt, T. and Monkman, A. P., Anisotropic polaron motion in conducting polymers studied by muon spin relaxation, *Synthetic Metals* 1999, 101(1-3), 323-324.
22. Su, W. P., Schrieffer, J. R. and Heeger, A. J., Soliton Excitations in Polyacetylene, *Physical Review B* 1980, 22(4), 2099-2111.
23. Shirakawa, H., Louis, E. J., Macdiarmid, A. G., Chiang, C. K. and Heeger, A. J., Synthesis of Electrically Conducting Organic Polymers - Halogen Derivatives of Polyacetylene, (Ch)X, *Journal of the Chemical Society-Chemical Communications* 1977(16), 578-580.

24. Chiang, C. K., Fincher, C. R., Park, Y. W., Heeger, A. J., Shirakawa, H., Louis, E. J., Gau, S. C. and Macdiarmid, A. G., Electrical-Conductivity in Doped Polyacetylene, *Physical Review Letters* 1977, 39(17), 1098-1101.
25. Funke, K., Jump Relaxation in Solid Electrolytes, *Progress in Solid State Chemistry* 1993, 22(2), 111-195.
26. Wagner C., S. W., *Zeitschrift Fur Physikalische Chemie* 1930, B11, 163.
27. Frenkel, J. Z., *Physical Chemistry B* 1935, 31, 163.
28. Kudo, T., Kishimoto, A., Oi, J. and Inoue, H., Synthesis of New W_3O_3 -Based Complex Oxides with Tunnels by a Chemical Mixing Process Using Peroxo-Polytungstates, *Solid State Ionics* 1990, 40-1, 567-571.
29. Boyce, J. B. and Huberman, B. A., Superionic Conductors - Transitions, Structures, Dynamics, *Physics Reports-Review Section of Physics Letters* 1979, 51(4), 189-265.
30. Norby, T., Solid-state protonic conductors: principles, properties, progress and prospects, *Solid State Ionics* 1999, 125(1-4), 1-11.
31. Grotthuss, C. J. T. v., *Annales de Chimie* 1806, 58, 54.
32. Haile, S. M., Boysen, D. A., Chisholm, C. R. I. and Merle, R. B., Solid acids as fuel cell electrolytes, *Nature* 2001, 410(6831), 910-913.
33. West, A. R., in *Solid State Chemistry and its Applications*, John Wiley and Sons, 1984.
34. Atkins, P. W., in *Physical Chemistry*, Oxford University Press, 1982.
35. Treptow, F., Jungbauer, A. and Hellgardt, K., Halide diffusion in polyaniline membranes, *Journal of Membrane Science* 2006, 270(1-2), 115-122.
36. Nagarale, R. K., Gohil, G. S. and Shahi, V. K., Sulfonated poly(ether ether ketone)/polyaniline composite proton-exchange membrane, *Journal of Membrane Science* 2006, 280(1-2), 389-396.
37. Hull, S., Superionics: crystal structures and conduction processes, *Reports on Progress in Physics* 2004, 67(7), 1233-1314.
38. Zhu, B., Fu, Q. X., Meng, G. Y., Jurado, J. F., Albinsson, I. and Mellander, B. E., $LiF-MgF_2$ composite electrolyte for advanced ceramic fuel cells: structure, electrical properties and applications, *Solid State Ionics* 2002, 148(3-4), 583-589.

39. de Souza, R. F., Padilha, J. C., Goncalves, R. S. and Dupont, J., Room temperature dialkylimidazolium ionic liquid-based fuel cells, *Electrochemistry Communications* 2003, 5(8), 728-731.
40. Sekhon, S. S., Krishnan, P., Singh, B., Yamada, K. and Kim, C. S., Proton conducting membrane containing room temperature ionic liquid, *Electrochimica Acta* 2006, 52(4), 1639-1644.
41. Kimmich, R. and Bachus, R., Nmr Field-Cycling Relaxation Spectroscopy, Transverse NMR Relaxation, Self-Diffusion and Zero-Shear Viscosity - Defect Diffusion and Reptation in Non-Glassy Amorphous Polymers, *Colloid and Polymer Science* 1982, 260(10), 911-936.
42. Noack, F., Nmr Field-Cycling Spectroscopy - Principles and Applications, *Progress in Nuclear Magnetic Resonance Spectroscopy* 1986, 18, 171-276.
43. Packard, M. and Varian, R., Free Nuclear Induction in the Earths Magnetic Field, *Physical Review* 1954, 93(4), 941-941.
44. Abragam, A. and Proctor, W. G., Experiments on Spin Temperature, *Physical Review* 1957, 106(1), 160-161.
45. Edmonds, D. T., Nuclear-Quadrupole Double-Resonance, *Physics Reports-Review Section of Physics Letters* 1977, 29(4), 234-290.
46. Anderson, A. G. and Redfield, A. G., Nuclear Spin-Lattice Relaxation in Metals, *Physical Review* 1959, 116(3), 583-591.
47. Satheesh, V., Galkin, A., Sykora, S. and Ferrante, G., Technical issues of fast field cycling NMR relaxometry, 2001,
48. Halle, B., Denisov, V. P. and Venu, K., in *Biological Magnetic Resonance*; (Berliner, L. J.), Kluwer/Plenum: New York, 1999.
49. de la Torre, J. G., Huertas, M. L. and Carrasco, B., Calculation of hydrodynamic properties of globular proteins from their atomic-level structure, *Biophysical Journal* 2000, 78(2), 719-730.
50. Kimmich, R. and Anorado, E., Field-cycling NMR relaxometry, *Progress in Nuclear Magnetic Resonance Spectroscopy* 2004, 44(3-4), 257-320.
51. Abragam, A., in *The Principles of Nuclear Magnetism*, Clarendon Press, Oxford, 1961.
52. Fukushima, E., Roeder S.B.W., in *Experimental Pulse NMR*, Addison-Wesley, Massachusetts, 1981.

53. Schroder, D. K., in *Semiconductor Material and Device Characterisation*, John Wiley and Sons, 1998.
54. Keithly Application Notes Series #2615, 2001,
55. Tubrandt, C. Z., *Electrochemistry* 1923, 29, 313.
56. Allen, P. C. and Lazarus, D., Effect of Pressure on Ionic-Conductivity in Rubidium Silver-Iodide and Silver-Iodide, *Physical Review B* 1978, 17(4), 1913-1927.
57. Denes, G., Yu, Y. H., Tyliczszak, T. and Hitchcock, A. P., Sn-K and Pb-L₃ Exafs, X-Ray-Diffraction, and ¹¹⁹Sn Mossbauer Spectroscopic Studies of Ordered Beta-PbSnF₄ and Disordered Pb_{1-x}Sn_xF₂ (X = 0.3, 0.4) Solid-Solutions and PbSn₄F₁₀ - High-Performance Fluoride-Ion Conductors, *Journal of Solid State Chemistry* 1993, 104(2), 239-252.
58. Eguchi, T. and Kuwano, J., Towards a Room-Temperature, Solid-State, Oxygen Gas Sensor, *Materials Research Bulletin* 1995, 30(11), 1351-1357.
59. Eguchi, T., Suda, S., Amasaki, H., Kuwano, J. and Saito, Y., Optimum design for the sensing electrode mixtures of PbSnF₄-based oxygen sensors for fast response at ambient temperature, *Solid State Ionics* 1999, 121(1-4), 235-243.
60. Tovar, L. L. G., Connor, P. A., Belliard, F., Torres-Martinez, L. M. and Irvine, J. T. S., Investigation of lead tin fluorides as possible negative electrodes for Li-ion batteries, *Journal of Power Sources* 2001, 97-8, 258-261.
61. Reau, J. M., Lucat, C., Portier, J., Hagenmuller, P., Cot, L. and Vilminot, S., Study of Structural and Electrical-Properties of a New Anion Conductor – PbSnF₄, *Materials Research Bulletin* 1978, 13(9), 877-882.
62. Donaldson, J. D. and Senior, B. J., Fluorostannates(2) - Non-Transition-Metal(2) Derivatives of Complex Tin(2) Fluoride Ions, *Journal of the Chemical Society a -Inorganic Physical Theoretical* 1967(11), 1821-&.
63. Collin, A., Denes, G., Le Roux, D., Madamba, M. C., Parris, J. M. and Salaun, A., Understanding the phase transitions and texture in superionic PbSnF₄ - The key to reproducible properties, *International Journal of Inorganic Materials* 1999, 1(5-6), 289-301.
64. Perez, G., Vilminot, S., Granier, W., Cot, L., Lucat, C., Reau, J. M. and Portier, J., About the Allotropic Transformations of PbSnF₄, *Materials Research Bulletin* 1980, 15(5), 587-593.

65. Castiglione, M., Madden, P. A., Berastegui, P. and Hull, S., The crystal structure of alpha-PbSnF₄ and its anion diffusion mechanism, *Journal of Physics-Condensed Matter* 2005, 17(6), 845-861.
66. Denes, G., Yu, Y. H., Tyliczszak, T. and Hitchcock, A. P., Sn-K, Pb-L₃, and Ba-L₃ EXAFS, X-Ray-Diffraction and ¹¹⁹Sn Mossbauer Spectroscopic Studies of Ordered PbSnF₄ and BaSnF₄ Fluoride Ionic Conductors with the Alpha-PbSnF₄ Structure, *Journal of Solid State Chemistry* 1991, 91(1), 1-15.
67. Brinkmann, D., NMR-Studies of Superionic Conductors, *Progress in Nuclear Magnetic Resonance Spectroscopy* 1992, 24, 527-552.
68. Mahajan, M. and Nageswar.Bd, Motional Narrowing of ¹⁹F Nuclear Magnetic Resonance in Lead Fluoride, *Chemical Physics Letters* 1971, 10(1), 29-&.
69. Hwang, T. Y., Engelsberg, M. and Lowe, I. J., Nuclear Magnetic-Resonance Study of ¹⁹F Diffusion in Lead Difluoride, *Chemical Physics Letters* 1975, 30(2), 303-305.
70. Hwang, T. Y., Lowe, I. J., Lau, K. F. and Vaughan, R. W., Further Nmr-Studies of Fluoride-Ion Motion in Doped Beta-PbF₂, *Journal of Chemical Physics* 1976, 65(3), 912-916.
71. Miller, J. R. and Mahendro.Pp, Spin-Lattice Relaxation in Pure and Europium-Doped BaF₂ Crystals at High and Low Temperatures, *Physical Review* 1968, 174(2), 369-&.
72. Privalov, A. F., Cenian, A., Fujara, F., Gabriel, H., Murin, I. V. and Vieth, H. M., The distribution of motional correlation times in superionic conductors: ¹⁹F nuclear magnetic resonance of tysonite-like LaF₃, *Journal of Physics-Condensed Matter* 1997, 9(43), 9275-9287.
73. Chaudhuri, S., Wang, F. and Grey, C. P., Resolving the different dynamics of the fluorine sublattices in the anionic conductor BaSnF₄ by using high-resolution MAS NMR techniques, *Journal of the American Chemical Society* 2002, 124(39), 11746-11757.
74. Ahmad, M. M., Yamada, K. and Okuda, T., Fluoride ion diffusion of superionic PbSnF₄ studied by nuclear magnetic resonance and impedance spectroscopy, *Journal of Physics-Condensed Matter* 2002, 14(30), 7233-7244.
75. *The Rietveld Method.* in *IUCR monographs on Crystallography* 5. 1993: Oxford University Press, New York.

76. Halle, B., Johannesson, H. and Venu, K., Model-free analysis of stretched relaxation dispersions, *Journal of Magnetic Resonance* 1998, 135(1), 1-13.
77. Boysen, D. A., Uda, T., Chisholm, C. R. I. and Haile, S. M., High-performance solid acid fuel cells through humidity stabilization, *Science* 2004, 303(5654), 68-70.
78. Haile, S. M., Fuel cell materials and components, *Acta Materialia* 2003, 51(19), 5981-6000.
79. Merle, R. B., Chisholm, C. R. I., Boysen, D. A. and Haile, S. M., Instability of sulfate and selenate solid acids in fuel cell environments, *Energy & Fuels* 2003, 17(1), 210-215.
80. Haile, S. M., Calkins, P. M. and Boysen, D., Superprotonic conductivity in beta-Cs₃(HSO₄)₂(H_x(P,S)O₄), *Solid State Ionics* 1997, 97(1-4), 145-151.
81. Haile, S. M., Lentz, G., Kreuer, K. D. and Maier, J., Superprotonic Conductivity in Cs₃(HSO₄)(H₂PO₄), *Solid State Ionics* 1995, 77, 128-134.
82. Chisholm, C. R. I. and Haile, S. M., Superprotonic behavior of Cs₂(HSO₄)₂(H₂PO₄) - a new solid acid in the CsHSO₄-CsH₂PO₄ system, *Solid State Ionics* 2000, 136, 229-241.
83. Baranov, A. I., Shuvalov, L. A. and Shchagina, N. M., Superior Conductivity and Phase-Transitions in CsHSO₄ and CsHSeO₄ Crystals, *Jetp Letters* 1982, 36(11), 459-462.
84. Chisholm, C. R. I. and Haile, S. M., Structure and thermal behavior of the new superprotonic conductor Cs₂(HSO₄)(H₂PO₄), *Acta Crystallographica Section B-Structural Science* 1999, 55, 937-946.
85. Haile, S. M. and Calkins, P. M., X-ray diffraction study of Cs₅(HSO₄)₃(H₂PO₄)₂, a new solid acid with a unique hydrogen-bond network, *Journal of Solid State Chemistry* 1998, 140(2), 251-265.
86. Chisholm, C., *Superprotonic Phase Transitions in Solid Acids*, 2003, Caltech: California.
87. Chisholm, C. R. I. and Haile, S. M., X-ray structure refinement of CsHSO₄ in phase II, *Materials Research Bulletin* 2000, 35(7), 999-1005.
88. Brown, I. D., Geometry of O-H...O Hydrogen-Bonds, *Acta Crystallographica Section A* 1976, 32(JAN1), 24-31.
89. Kreuer, K. D., Fast Proton Transport in Solids, *Journal of Molecular Structure* 1988, 177, 265-276.

90. Kreuer, K. D., Proton conductivity: Materials and applications, *Chemistry of Materials* 1996, 8(3), 610-641.
91. Murphy, E. J., Conduction in Single Crystals of Ammonium Dihydrogen Phosphate, *Journal of Applied Physics* 1964, 35(9), 2609-&.
92. Pollock, J. M. and Sharan, M., Conduction and Diffusion in Crystals Containing Hydrogen Bonds .2. Ammonium Dihydrogen Phosphate, *Journal of Chemical Physics* 1969, 51(8), 3604-&.
93. Sharon, M. and Kalia, A. K., Electrical-Conduction and Diffusion Studies in $\text{NH}_4\text{H}_2\text{PO}_4$ and KH_2PO_4 Single-Crystals, *Journal of Solid State Chemistry* 1977, 21(3), 171-183.
94. Baranov, A. I., Khiznichenko, V. P. and Shuvalov, L. A., High-Temperature Phase-Transitions and Proton Conductivity in Some Kdp-Family Crystals, *Ferroelectrics* 1989, 100, 135-141.
95. Komukae, M., Osaka, T., Makita, Y., Ozaki, T., Itoh, K. and Nakamura, E., Dielectric and Thermal Studies on New Phase-Transitions of CsHSO_4 , *Journal of the Physical Society of Japan* 1981, 50(10), 3187-3188.
96. Baranov, A. I., Merinov, B. V., Tregubchenko, A. V., Khiznichenko, V. P., Shuvalov, L. A. and Schagina, N. M., Fast Proton Transport in Crystals with a Dynamically Disordered Hydrogen-Bond Network, *Solid State Ionics* 1989, 36(3-4), 279-282.
97. Belushkin, A. V., Carlile, C. J. and Shuvalov, L. A., The Diffusion of Protons in the Superionic Conductor CsHSO_4 by Quasi-Elastic Neutron-Scattering, *Journal of Physics-Condensed Matter* 1992, 4(2), 389-398.
98. Chisholm, C. R. I., Merle, R. B., Boysen, D. A. and Haile, S. M., Superprotonic phase transition in $\text{CsH}(\text{PO}_3\text{H})$, *Chemistry of Materials* 2002, 14(9), 3889-3893.
99. Slade, R. C. T., Dickens, P. G., Claridge, D. A., Murphy, D. J. and Halstead, T. K., Ammonium Ion Motions in the Hexagonal Tungsten Trioxide Framework - a H-1-Nmr Study of $(\text{NH}_4)_x\text{WO}_3$, *Solid State Ionics* 1990, 38(3-4), 201-206.
100. Slade, R. C. T., Barker, J. and Strange, J. H., Protonic Conduction and H-1 Self-Diffusion in Nafion Film Studied by Ac Conductivity and Pulsed Field Gradient NMR Techniques, *Solid State Ionics* 1989, 35(1-2), 11-15.

101. Matsuo, Y., Takahashi, K., Hatori, J. and Ikehata, S., Proton dynamics in superionic phase of $Tl_3H(SO_4)_2$, *Journal of Solid State Chemistry* 2004, 177(11), 4282-4285.
102. Ishii, T. and Abe, T., Non-BPP ion dynamics - NMR- T_1 , *Solid State Ionics* 2002, 154, 203-208.
103. Lahajnar, G., Blinc, R., Dolinsek, J., Arcon, D. and Slak, J., 1D and 2D NMR study of ionic conductivity in $CsDSO_4$, *Solid State Ionics* 1997, 97(1-4), 141-144.
104. Yoshida, Y., Matsuo, Y. and Ikehata, S., 1H NMR and ^{77}Se NMR in $CsHSeO_4$, *Solid State Ionics* 2005, 176(31-34), 2457-2460.
105. Yamada, K., Sagara, T., Yamane, Y., Ohki, H. and Okuda, T., Superprotonic conductor CsH_2PO_4 studied by 1H , ^{31}P NMR and X-ray diffraction, *Solid State Ionics* 2004, 175(1-4), 557-562.
106. Hayashi, S. and Mizuno, M., Proton dynamics in $Cs_2(HSO_4)(H_2PO_4)$ studied by 1H NMR, *Solid State Ionics* 2005, 176(7-8), 745-754.
107. Hayashi, S. and Mizuno, M., Proton diffusion in the superprotonic phase of $CsHSO_4$ studied by 1H NMR relaxation, *Solid State Ionics* 2004, 171(3-4), 289-293.
108. Suzuki, K. and Hayashi, S., Proton dynamics in $Cs_3(HSO_4)_2(H_2PO_4)$ studied by 1H NMR, *Solid State Ionics* 2006, 177(33-34), 2873-2880.
109. Ito, T., Shirakawa, H. and Ikeda, S., Simultaneous Polymerization and Formation of Polyacetylene Film on Surface of Concentrated Soluble Ziegler-Type Catalyst Solution, *Journal of Polymer Science Part a-Polymer Chemistry* 1974, 12(1), 11-20.
110. Stejskal, J. and Gilbert, R. G., Polyaniline. Preparation of a conducting polymer (IUPAC technical report), *Pure and Applied Chemistry* 2002, 74(5), 857-867.
111. Mathew, R., Mattes, B. R. and Espe, M. P., A solid state NMR characterization of cross-linked polyaniline powder, *Synthetic Metals* 2002, 131(1-3), 141-147.
112. Bleier, H., Finter, J., Hilti, B., Hofherr, W., Mayer, C. W., Minder, E., Hediger, H. and Ansermet, J. P., Transparent Electrically Conductive Composite-Materials - Methods of Preparation and Their Application, *Synthetic Metals* 1993, 57(1), 3605-3610.

113. Heeger, A. J., Polyaniline with Surfactant Counterions - Conducting Polymer Materials Which Are Processible in the Conducting Form, *Synthetic Metals* 1993, 57(1), 3471-3482.
114. Echigo, Y., Asami, K., Takahashi, H., Inoue, K., Kabata, T., Kimura, O. and Ohsawa, T., Ion Rechargeable Batteries Using Synthetic Organic Polymers, *Synthetic Metals* 1993, 57(1), 3611-3616.
115. Paddeu, S., Ram, M. K., Carrara, S. and Nicolini, C., Langmuir-Schaefer films of a poly(o-anisidine) conducting polymer for sensors and displays, *Nanotechnology* 1998, 9(3), 228-236.
116. Jezzard, P., Carpenter, T. A., Hall, L. D., Clayden, N. J. and Jackson, P., Temperature Mapping in Solid Polymers Using the Temperature-Dependence of NMR Relaxation-Times, *Journal of Polymer Science Part B-Polymer Physics* 1992, 30(12), 1423-1425.
117. Trivedi, D. C., in Handbook of Organic Conducting Polymers, Nalwa, H. S., Editor, 1997, Wiley, Chichester, p. 505-572, 251-318.
118. Adams, P. N., Laughlin, P. J., Monkman, A. P. and Kenwright, A. M., Low temperature synthesis of high molecular weight polyaniline, *Polymer* 1996, 37(15), 3411-3417.
119. Kobayashi, T., Yoneyama, H. and Tamura, H., Oxidative-Degradation Pathway of Polyaniline Film Electrodes, *Journal of Electroanalytical Chemistry* 1984, 177(1-2), 293-297.
120. Armes, S. P. and Miller, J. F., Optimum Reaction Conditions for the Polymerization of Aniline in Aqueous-Solution by Ammonium Persulfate, *Synthetic Metals* 1988, 22(4), 385-393.
121. Macdiarmid, A. G. and Epstein, A. J., Secondary Doping in Polyaniline, *Synthetic Metals* 1995, 69(1-3), 85-92.
122. Ferry, A., Edman, L., Forsyth, M., MacFarlane, D. R. and Sun, J. Z., NMR and Raman studies of a novel fast-ion-conducting polymer-in-salt electrolyte based on LiCF_3SO_3 and PAN, *Electrochimica Acta* 2000, 45(8-9), 1237-1242.
123. Bhattacharya, A. and De, A., Conducting composites of polypyrrole and polyaniline - A review, *Progress in Solid State Chemistry* 1996, 24(3), 141-181.

124. Wessling, B., Dispersion as the link between basic research and commercial applications of conductive polymers (polyaniline), *Synthetic Metals* 1998, 93(2), 143-154.
125. Stafstrom, S., Bredas, J. L., Epstein, A. J., Woo, H. S., Tanner, D. B., Huang, W. S. and Macdiarmid, A. G., Polaron Lattice in Highly Conducting Polyaniline - Theoretical and Optical Studies, *Physical Review Letters* 1987, 59(13), 1464-1467.
126. Bredas, J. L., Chance, R. R. and Silbey, R., Comparative Theoretical-Study of the Doping of Conjugated Polymers - Polarons in Polyacetylene and Polyparaphenylene, *Physical Review B* 1982, 26(10), 5843-5854.
127. Angelopoulos, M., Asturias, G. E., Ermer, S. P., Ray, A., Scherr, E. M., Macdiarmid, A. G., Akhtar, M., Kiss, Z. and Epstein, A. J., Polyaniline - Solutions, Films and Oxidation-State, *Molecular Crystals and Liquid Crystals* 1988, 160, 151-163.
128. Javadi, H. H. S., Cromack, K. R., Macdiarmid, A. G. and Epstein, A. J., Microwave Transport in the Emeraldine Form of Polyaniline, *Physical Review B* 1989, 39(6), 3579-3584.
129. Nakajima, T. and Kawagoe, T., Polyaniline - Structural-Analysis and Application for Battery, *Synthetic Metals* 1989, 28(1-2), C629-C638.
130. Bonnell, D. A. and Angelopoulos, M., Spatially Localized Electronic-Structure in Polyaniline by Scanning Tunneling Spectroscopy, *Synthetic Metals* 1989, 33(3), 301-310.
131. Wang, F. S., Tang, J. S., Wang, L. X., Zhang, H. F. and Mo, Z. S., Study on the Crystallinity of Polyaniline, *Molecular Crystals and Liquid Crystals* 1988, 160, 175-184.
132. Pron, A., Genoud, F., Menardo, C. and Nechtschein, M., The Effect of the Oxidation Conditions on the Chemical Polymerization of Polyaniline, *Synthetic Metals* 1988, 24(3), 193-201.
133. Shacklette, L. W. and Baughman, R. H., Defect Generation and Charge Transport in Polyaniline, *Molecular Crystals and Liquid Crystals* 1990, 189, 193-212.
134. Thyssen, A., Borgerding, A. and Schultze, J. W., Formation and Electronic Conductivity of Polyaniline, *Makromolekulare Chemie-Macromolecular Symposia* 1987, 8, 143-157.

135. Kaplan, S., Conwell, E. M., Richter, A. F. and Macdiarmid, A. G., A Solid-State Nmr Investigation of the Structure and Dynamics of Polyanilines, *Synthetic Metals* 1989, 29(1), E235-E242.
136. Richter, A. F., Ray, A., Ramanathan, K. V., Manohar, S. K., Furst, G. T., Opella, S. J., Macdiarmid, A. G. and Epstein, A. J., N-15 Nmr of Polyaniline, *Synthetic Metals* 1989, 29(1), E243-E249.
137. Glowinkowski, S., Makrocka-Rydzik, M., Wanke, S. and Jurga, S., Molecular dynamics in polyethylene and ethylene-1-butene copolymer investigated by NMR methods, *European Polymer Journal* 2002, 38(5), 961-969.
138. Wilson, C. W. and Pake, G. E., Nuclear Magnetic Resonance Determination of Degree of Crystallinity in 2 Polymers, *Journal of Polymer Science* 1953, 10(5), 503-505.
139. Mansfield, M. L., Temperature-Dependent Changes in the Structure of the Amorphous Domains of Semicrystalline Polymers, *Macromolecules* 1987, 20(6), 1384-1393.
140. Travers, J. P., Chroboczek, J., Devreux, F., Genoud, F., Nechtschein, M., Syed, A., Genies, E. M. and Tsintavis, C., Transport and Magnetic-Resonance Studies of Polyaniline, *Molecular Crystals and Liquid Crystals* 1985, 121(1-4), 195-199.
141. McBrierty, V. J., Douglass, D. C. and Weber, T. A., Nuclear Magnetic-Relaxation and Molecular-Motion in Poly(Vinylidene Fluoride), *Journal of Polymer Science Part B-Polymer Physics* 1976, 14(7), 1271-1286.
142. Rouse, P. E., A Theory of the Linear Viscoelastic Properties of Dilute Solutions of Coiling Polymers, *Journal of Chemical Physics* 1953, 21(7), 1272-1280.
143. Schweizer, K. S., Mode-Coupling Theory of the Dynamics of Polymer Liquids - Qualitative Predictions for Flexible Chain and Ring Melts, *Journal of Chemical Physics* 1989, 91(9), 5822-5839.
144. Doi, M., Transition Behavior from De Gennes-Type Motion to Rouse of a Polymer-Chain in Fixed Network, *Journal of Physics a-Mathematical and General* 1975, 8(3), 417-426.
145. Fatkullin, N., Kimmich, R. and Weber, H. W., Spin-Lattice Relaxation of Polymers - the Memory-Function Formalism, *Physical Review E* 1993, 47(6), 4600-4603.

146. Ullman, R., Nuclear Magnetic Relaxation of Polymer Solutions, *Journal of Chemical Physics* 1965, 43(9), 3161-&.
147. Bovey, F. A. and Jelinski, L. W., The Observation of Chain Motion in Macromolecules by ^{13}C and ^2H Nuclear Magnetic-Resonance Spectroscopy, *Journal of Physical Chemistry* 1985, 89(4), 571-583.
148. Sariciftci, N. S., Kolbert, A. C., Cao, Y., Heeger, A. J. and Pines, A., Magnetic resonance evidence for metallic state in highly conducting polyaniline, *Synthetic Metals* 1995, 69(1-3), 243-244.
149. Lee, K., Cho, S., Park, S. H., Heeger, A. J., Lee, C. W. and Lee, S. H., Metallic transport in polyaniline, *Nature* 2006, 441(7089), 65-68.
150. Clark, W. G., Tanaka, K., Brown, S. E., Menon, R., Wudl, F., Moulton, W. G. and Kuhns, P., High field NMR studies of conduction electron dynamics in metallic polypyrrole-PF₆, *Synthetic Metals* 1999, 101(1-3), 343-343.
151. McBrierty, V. J. and Packer, K. J., in *Nuclear Magnetic Resonance in Solid Polymers*, Cambridge University Press, 1979.
152. Demco, D. E., Johansson, A. and Tegenfeldt, J., Proton spin diffusion for spatial heterogeneity and morphology investigations of polymers, *Solid State Nuclear Magnetic Resonance* 1995, 4(1), 13-38.
153. Buda, A., Demco, D. E., Bertmer, M., Blumich, B., Reining, B., Keul, H. and Hocker, H., Domain sizes in heterogeneous polymers by spin diffusion using single-quantum and double-quantum dipolar filters, *Solid State Nuclear Magnetic Resonance* 2003, 24(1), 39-67.
154. Geppi, M., Harris, R. K., Kenwright, A. M. and Say, B. J., A method for analysing proton NMR relaxation data from motionally heterogeneous polymer systems, *Solid State Nuclear Magnetic Resonance* 1998, 12(1), 15-20.
155. Nechtstein, M., *Electron Spin Dynamics*, in Handbook of Conducting Polymers, Reynolds, J. R., Editor, 1998, Dekker.
156. Mabboux, P. Y., Beau, B., Travers, J. P. and Nicolau, Y. F., Non-exponential NMR relaxation in heterogeneously doped conducting polymers, *Synthetic Metals International Conference on Science and Technology of Synthetic Metals* 1997, 84(1-3), 985-986.

157. Beau, B., Travers, J. P. and Banka, E., NMR evidence for heterogeneous disorder and quasi-1D metallic state in polyaniline CSA, *Synthetic Metals International Conference on Science and Technology of Synthetic* 1999, 101(1-3), 772-775.
158. Kahol, P. K., Kumar, K. K. S., Geetha, S. and Trivedi, D. C., Effect of dopants on electron localization length in polyaniline, *Synthetic Metals* 2003, 139(2), 191-200.
159. Devreux, F. and Lecavelier, H., Evidence for Anomalous Diffusion in a Conducting Polymer, *Physical Review Letters* 1987, 59(22), 2585-2587.
160. Mizoguchi, K., Nechtschein, M., Travers, J. P. and Menardo, C., Spin Dynamics in the Conducting Polymer, Polyaniline, *Physical Review Letters* 1989, 63(1), 66-69.
161. Alexander, S. and Orbach, R., Density of States on Fractals - Fractons, *Journal De Physique Lettres* 1982, 43(17), L625-L631.
162. Epstein, A. J., Macdiarmid, A. G. and Pouget, J. P., Spin Dynamics and Conductivity in Polyaniline, *Physical Review Letters* 1990, 65(5), 664-664.
163. Wang, Z. H., Scherr, E. M., Macdiarmid, A. G. and Epstein, A. J., Transport and EPR Studies of Polyaniline - a Quasi-One-Dimensional Conductor with 3-Dimensional Metallic States, *Physical Review B* 1992, 45(8), 4190-4202.
164. Wang, Z. H., Li, C., Scherr, E. M., Macdiarmid, A. G. and Epstein, A. J., 3 Dimensionality of Metallic States in Conducting Polymers - Polyaniline, *Physical Review Letters* 1991, 66(13), 1745-1748.
165. Havlin, S. and Benavraham, D., Diffusion in Disordered Media, *Advances in Physics* 1987, 36(6), 695-798.
166. Tagowska, M., Palys, B. and Jackowska, K., Polyaniline nanotubules-anion effect on conformation and oxidation state of polyaniline studied by Raman spectroscopy, *Synthetic Metals* 2004, 142(1-3), 223-229.
167. Anorado, E. and Pusiol, D. J., ¹⁴N nuclear quadrupole dips in the proton spin-lattice relaxation dispersion in the smectic-C phase of HpAB, *Physical Review Letters* 1996, 76(21), 3983-3986.
168. Korb, J. P. and Bryant, R. G., The physical basis for the magnetic field dependence of proton spin-lattice relaxation rates in proteins, *Journal of Chemical Physics* 2001, 115(23), 10964-10974.

169. Korb, J. P., Van-Quynh, A. and Bryant, R., Low-frequency localized spin-dynamical coupling in proteins, *Comptes Rendus De L Academie Des Sciences Serie Ii Fascicule C-Chimie* 2001, 4(11), 833-837.
170. Mizoguchi, K., Nechtschein, M. and Travers, J. P., Spin Dynamics and Conductivity in Polyaniline - Temperature-Dependence, *Synthetic Metals* 1991, 41(1-2), 113-116.
171. Wang, J. P., Zou, B. S., Hong, X. Y. and Collard, D. M., Photoinduced vibrational absorptions from poly(3-octylthiophene)/Fe₂O₃ nanoparticle composite, a time-resolved FTIR study, *Synthetic Metals* 2000, 113(3), 223-226.
172. Huang, J. X., Virji, S., Weiller, B. H. and Kaner, R. B., Polyaniline nanofibers: Facile synthesis and chemical sensors, *Journal of the American Chemical Society* 2003, 125(2), 314-315.
173. Huang, J., Virji, S., Weiller, B. H. and Kaner, R. B., Nanostructured polyaniline sensors, *Chemistry-a European Journal* 2004, 10(6), 1315-1319.
174. Kraeutler, B. and Bard, A. J., Heterogeneous Photocatalytic Preparation of Supported Catalysts - Photodeposition of Platinum on TiO₂ Powder and Other Substrates, *Journal of the American Chemical Society* 1978, 100(13), 4317-4318.
175. Li, X. W., Wang, G. C., Li, X. X. and Lu, D. M., Surface properties of polyaniline/nano-TiO₂ composites, *Applied Surface Science* 2004, 229(1-4), 395-401.
176. Xia, H. S. and Wang, Q., Ultrasonic irradiation: A novel approach to prepare conductive polyaniline/nanocrystalline titanium oxide composites, *Chemistry of Materials* 2002, 14(5), 2158-2165.
177. Feng, W., Bai, X. D., Lian, Y. Q., Liang, J., Wang, X. G. and Yoshino, K., Well-aligned polyaniline/carbon-nanotube composite films grown by in-situ aniline polymerization, *Carbon* 2003, 41(8), 1551-1557.
178. Li, G. C., Pang, S. P., Peng, H. R., Wang, Z. B., Cui, Z. L. and Zhang, Z. K., Templateless and surfactantless route to the synthesis of polyaniline nanofibers, *Journal of Polymer Science Part a-Polymer Chemistry* 2005, 43(17), 4012-4015.

179. Wei, Z. X., Wan, M. X., Lin, T. and Dai, L. M., Polyaniline nanotubes doped with sulfonated carbon nanotubes made via a self-assembly process, *Advanced Materials* 2003, 15(2), 136-+.
180. Stejskal, J., Trchova, M., Fedorova, S., Sapurina, I. and Zemek, J., Surface polymerization of aniline on silica gel, *Langmuir* 2003, 19(7), 3013-3018.
181. Li, J., Fang, K., Qiu, H., Li, S. P., Mao, W. M. and Wu, Q. Y., Micromorphology and conductive property of the pellets prepared by HCl-doped polyaniline nanofibers, *Synthetic Metals* 2004, 145(2-3), 191-194.
182. Zuppiroli, L., Beuneu, F., Mory, J., Enzel, P. and Bein, T., The Low-Field Conductivity of Zeolite-Encapsulated Molecular Wires, *Synthetic Metals* 1993, 57(2-3), 5081-5087.
183. Martin, C. R., Nanomaterials - a Membrane-Based Synthetic Approach, *Science* 1994, 266(5193), 1961-1966.
184. Misoska, V., Price, W., Ralph, S. and Wallace, G., Electrochemical synthesis of pyrrole through a polystyrene opal matrix, *Synthetic Metals* 2001, 121(1-3), 1501-1502.
185. Langer, J. J., Framski, G. and Golczak, S., Polyaniline micro- and nanofibrils, *Synthetic Metals* 2001, 121(1-3), 1319-1320.
186. Langer, J. J., Framski, G. and Joachimiak, R., Polyaniline nano-wires and nano-networks, *Synthetic Metals* 2001, 121(1-3), 1281-1282.
187. Li, Z. F. and Ruckenstein, E., Intercalation of conductive polyaniline in the mesostructured V_2O_5 , *Langmuir* 2002, 18(18), 6956-6961.
188. Ferrer-Anglada, N., Gorri, J. A., Muster, J., Liu, K., Burghard, M. and Roth, S., Electrical transport and AFM microscopy on V_2O_5 -x-polyaniline nanorods, *Materials Science & Engineering C-Biomimetic and Supramolecular Systems* 2001, 15(1-2), 237-239.
189. Gan, L. M., Zhang, L. H., Chan, H. S. O. and Chew, C. H., Preparation of Conducting Polyaniline-Coated Barium-Sulfate Nanoparticles in Inverse Microemulsions, *Materials Chemistry and Physics* 1995, 40(2), 94-98.
190. Wang, Z., Chen, M. A. and Li, H. L., Preparation and characterization of uniform polyaniline nano-fibrils using the anodic aluminum oxide template, *Materials Science and Engineering a-Structural Materials Properties Microstructure and Processing* 2002, 328(1-2), 33-38.

191. Sun, L. F., Liu, H. B., Clark, R. and Yang, S. C., Double-strand polyaniline, *Synthetic Metals* 1997, 84(1-3), 67-68.
192. Li, W. G., McCarthy, P. A., Liu, D. G., Huang, J. Y., Yang, S. C. and Wang, H. L., Toward understanding and optimizing the template-guided synthesis of chiral polyaniline nanocomposites, *Macromolecules* 2002, 35(27), 9975-9982.
193. Cho, M. S., Park, S. Y., Hwang, J. Y. and Choi, H. J., Synthesis and electrical properties of polymer composites with polyaniline nanoparticles, *Materials Science & Engineering C-Biomimetic and Supramolecular Systems* 2004, 24(1-2), 15-18.
194. Stejskal, J., Kratochvil, P. and Helmstedt, M., Polyaniline dispersions .5. Poly(vinyl alcohol) and poly(N-vinylpyrrolidone) as steric stabilizers, *Langmuir* 1996, 12(14), 3389-3392.
195. Park, S. Y., Cho, M. S. and Choi, H. J., Synthesis and electrical characteristics of polyaniline nanoparticles and their polymeric composite, *Current Applied Physics* 2004, 4(6), 581-583.
196. Kim, S. W., Shim, S. C., Kim, D. Y. and Kim, C. Y., Synthesis and properties of novel triphenylamine polymers containing ethynyl and aromatic moieties, *Synthetic Metals* 2001, 122(2), 363-368.
197. Hopkins, A. R., Sawall, D. D., Villahermosa, R. M. and Lipeles, R. A., Interfacial synthesis of electrically conducting polyaniline nanofiber composites, *Thin Solid Films* 2004, 469-70, 304-308.
198. Banerjee, P. and Mandal, B. M., Blends of HCl-doped polyaniline nanoparticles and poly(vinyl chloride) with extremely low percolation threshold - A morphology study, *Synthetic Metals* 1995, 74(3), 257-261.
199. Reghu, M., Yoon, C. O., Yang, C. Y., Moses, D., Heeger, A. J. and Cao, Y., Superlocalization of the Electronic Wave-Functions in Conductive Polymer Blends at Concentrations near the Percolation-Threshold, *Macromolecules* 1993, 26(26), 7245-7249.
200. Chan, H. S. O., Gan, L. M., Chew, C. H., Ma, L. R. and Seow, S. H., Characterization of Chemically and Electrochemically Prepared Polyanilines in Inverse Microemulsions, *Journal of Materials Chemistry* 1993, 3(11), 1109-1115.

201. Kim, B. J., Oh, S. G., Han, M. G. and Im, S. S., Synthesis and characterization of polyaniline nanoparticles in SDS micellar solutions, *Synthetic Metals* 2001, 122(2), 297-304.
202. Samuelson, L., Liu, W., Nagarajan, R., Kumar, J., Bruno, F. F., Cholli, A. and Tripathy, S., Nanoreactors for the enzymatic synthesis of conducting polyaniline, *Synthetic Metals* 2001, 119(1-3), 271-272.
203. Moulton, S. E., Innis, P. C., Kane-Maguire, L. A. P., Ngamna, O. and Wallace, G. G., Polymerisation and characterisation of conducting polyaniline nanoparticle dispersions, *Current Applied Physics* 2004, 4(2-4), 402-406.
204. Hassan, P. A., Sawant, S. N., Bagkar, N. C. and Yakhmi, J. V., Polyaniline nanoparticles prepared in rodlike micelles, *Langmuir* 2004, 20(12), 4874-4880.
205. Oh, S. G. and Im, S. S., Electroconductive polymer nanoparticles preparation and characterization of PANI and PEDOT nanoparticles, *Current Applied Physics* 2002, 2(4), 273-277.
206. Han, D. X., Chu, Y., Yang, L. K., Liu, Y. and Lv, Z. X., Reversed micelle polymerization: a new route for the synthesis of DBSA-polyaniline nanoparticles, *Colloids and Surfaces a-Physicochemical and Engineering Aspects* 2005, 259(1-3), 179-187.
207. Morrin, A., Wilbeer, F., Ngamna, O., Moulton, S. E., Killard, A. J., Wallace, G. G. and Smyth, M. R., Novel biosensor fabrication methodology based on processable conducting polyaniline nanoparticles, *Electrochemistry Communications* 2005, 7(3), 317-322.
208. Zhang, X. Y. and Manohar, S. K., Polyaniline nanofibers: chemical synthesis using surfactants, *Chemical Communications* 2004(20), 2360-2361.
209. Sarno, D. M., Manohar, S. K. and MacDiarmid, A. G., Controlled interconversion of semiconducting and metallic forms of polyaniline nanofibers, *Synthetic Metals* 2005, 148(3), 237-243.
210. Kim, B. J., Oh, S. G., Han, M. G. and Im, S. S., Preparation of polyaniline nanoparticles in micellar solutions as polymerization medium, *Langmuir* 2000, 16(14), 5841-5845.
211. Xia, H. S. and Wang, Q., Synthesis and characterization of conductive polyaniline nanoparticles through ultrasonic assisted inverse microemulsion polymerization, *Journal of Nanoparticle Research* 2001, 3(5-6), 401-411.

212. Li, G. C., Peng, H. R., Wang, Y., Qin, Y., Cui, Z. L. and Zhang, Z. K., Synthesis of polyaniline nanobelts, *Macromolecular Rapid Communications* 2004, 25(18), 1611-1614.
213. Kros, A., Linhardt, J. G., Bowman, H. K. and Tirrell, D. A., From giant vesicles to filaments and wires: Templates for conducting polymers, *Advanced Materials* 2004, 16(8), 723-+.
214. Chiou, N. R. and Epstein, A. J., Polyaniline nanofibers prepared by dilute polymerization, *Advanced Materials* 2005, 17(13), 1679-+.
215. Li, W. G. and Wang, H. L., Oligomer-assisted synthesis of chiral polyaniline nanofibers, *Journal of the American Chemical Society* 2004, 126(8), 2278-2279.
216. Zhang, X. Y., Goux, W. J. and Manohar, S. K., Synthesis of polyaniline nanofibers by "nanofiber seeding", *Journal of the American Chemical Society* 2004, 126(14), 4502-4503.
217. Zhang, L. J., Long, Y. Z., Chen, Z. J. and Wan, M. X., The effect of hydrogen bonding on self-assembled polyaniline nanostructures, *Advanced Functional Materials* 2004, 14(7), 693-698.
218. Qiu, H. J., Wan, M. X., Matthews, B. and Dai, L. M., Conducting polyaniline nanotubes by template-free polymerization, *Macromolecules* 2001, 34(4), 675-677.
219. He, C., Tan, Y. W. and Li, Y. F., Conducting polyaniline nanofiber networks prepared by the doping induction of camphor sulfonic acid, *Journal of Applied Polymer Science* 2003, 87(9), 1537-1540.
220. Zhong, W. B., Deng, J. Y., Yang, Y. S. and Yang, W. T., Synthesis of large-area three-dimensional polyaniline nanowire networks using a "soft template", *Macromolecular Rapid Communications* 2005, 26(5), 395-400.
221. McCarthy, P. A., Huang, J. Y., Yang, S. C. and Wang, H. L., Synthesis and characterization of water-soluble chiral conducting polymer nanocomposites, *Langmuir* 2002, 18(1), 259-263.
222. Liang, L., Liu, J., Windisch, C. F., Exarhos, G. J. and Lin, Y. H., Direct assembly of large arrays of oriented conducting polymer nanowires, *Angewandte Chemie-International Edition* 2002, 41(19), 3665-3668.

223. He, H. X., Zhu, J. S., Tao, N. J., Nagahara, L. A., Amlani, I. and Tsui, R., A conducting polymer nanojunction switch, *Journal of the American Chemical Society* 2001, 123(31), 7730-7731.
224. Tang, Z. Y., Liu, S. Q., Wang, Z. X., Dong, S. J. and Wang, E. K., Electrochemical synthesis of polyaniline nanoparticles, *Electrochemistry Communications* 2000, 2(1), 32-35.
225. Huang, J. X. and Kaner, R. B., Nanofiber formation in the chemical polymerization of aniline: A mechanistic study, *Angewandte Chemie-International Edition* 2004, 43(43), 5817-5821.
226. Gao, H. X., Jiang, T., Han, B. X., Wang, Y., Du, J. M., Liu, Z. M. and Zhang, J. L., Aqueous/ionic liquid interfacial polymerization for preparing polyaniline nanoparticles, *Polymer* 2004, 45(9), 3017-3019.
227. Wang, X., Zhuang, J., Peng, Q. and Li, Y. D., A general strategy for nanocrystal synthesis, *Nature* 2005, 437(7055), 121-124.
228. Hurley, F. H. and Wier, T. P., Electrodeposition of Metals from Fused Quaternary Ammonium Salts, *Journal of the Electrochemical Society* 1951, 98(5), 203-206.
229. Welton, T., Room-temperature ionic liquids. Solvents for synthesis and catalysis, *Chemical Reviews* 1999, 99(8), 2071-2083.
230. Jaeger, D. A. and Wang, J. K., Micellar Effects on the Regiochemistry of a Diels-Alder Reaction, *Tetrahedron Letters* 1992, 33(43), 6415-6418.
231. Fischer, T., Sethi, A., Welton, T. and Woolf, J., Diels-Alder reactions in room-temperature ionic liquids, *Tetrahedron Letters* 1999, 40(4), 793-796.
232. Sheldon, R., Catalytic reactions in ionic liquids, *Chemical Communications* 2001(23), 2399-2407.
233. Anderson, J. L., Armstrong, D. W. and Wei, G. T., Ionic liquids in analytical chemistry, *Analytical Chemistry* 2006, 78(9), 2892-2902.
234. Sun, Y., Cabovska, B., Evans, C. E., Ridgway, T. H. and Stalcup, A. M., Retention characteristics of a new butylimidazolium-based stationary phase, *Analytical and Bioanalytical Chemistry* 2005, 382(3), 728-734.
235. Buzzeo, M. C., Hardacre, C. and Compton, R. G., Use of room temperature ionic liquids in gas sensor design, *Analytical Chemistry* 2004, 76(15), 4583-4588.

236. Galinski, M., Lewandowski, A. and Stepniak, I., Ionic liquids as electrolytes, *Electrochimica Acta* 2006, 51(26), 5567-5580.
237. Seddon, K. R., Room-temperature ionic liquids: Neoteric solvents for clean catalysis, *Kinetics and Catalysis* 1996, 37(5), 693-697.
238. Antony, J. H., Dolle, A., Mertens, D., Wasserscheid, P., Carper, W. R. and Wahlbeck, P. G., C-13 NMR relaxation rates in the ionic liquid 1-methyl-3-nonylimidazolium hexafluorophosphate, *Journal of Physical Chemistry A* 2005, 109(30), 6676-6682.
239. Singh, A. K. and Mehrotra, N. K., Correlation of mutual viscosity and NMR spin-lattice relaxation time with dielectric relaxation time in some benzaldehydes, *Japanese Journal of Applied Physics Part 1-Regular Papers Brief Communications & Review Papers* 2005, 44(7A), 5236-5239.
240. Jacquemin, J., Husson, P., Padua, A. A. H. and Majer, V., Density and viscosity of several pure and water-saturated ionic liquids, *Green Chemistry* 2006, 8(2), 172-180.
241. Harris, K. R., Woolf, L. A. and Kanakubo, M., Temperature and pressure dependence of the viscosity of the ionic liquid 1-butyl-3-methylimidazolium hexafluorophosphate, *Journal of Chemical and Engineering Data* 2005, 50(5), 1777-1782.
242. Tokuda, H., Hayamizu, K., Ishii, K., Susan, M. and Watanabe, M., Physicochemical properties and structures of room temperature ionic liquids. 2. Variation of alkyl chain length in imidazolium cation, *Journal of Physical Chemistry B* 2005, 109(13), 6103-6110.

Appendix 1 – Ionic Liquids

A1.1 Introduction

Ionic liquids are derived from surfactants and typically consist of a large organic cation such as pyridinium, imidazolium or quaternary ammonium ions (figure A1.1) and an anion such as a halide, BF_4^- or CF_3SO_3^- . [228] They are defined as salts with a melting temperature below the boiling point of water (373 K). Many ionic liquids have a melting point far below this temperature and some are in the liquid state at room temperature. The latter are referred to as room temperature ionic liquids (RTILs) and much of the recent work on ionic liquids has been concerned with these materials. [229] Ionic liquids also have a wide liquid range (~ 300 K), and have high thermal, electrochemical and chemical stability. The physical properties of ionic liquids are influenced by many factors such as molecular weight and stoichiometry, anionic and cationic charges and charge distribution. One of the main points of interest of these compounds is the variability of their physicochemical properties as function of cationic and anionic components and the ease with which these may be varied.

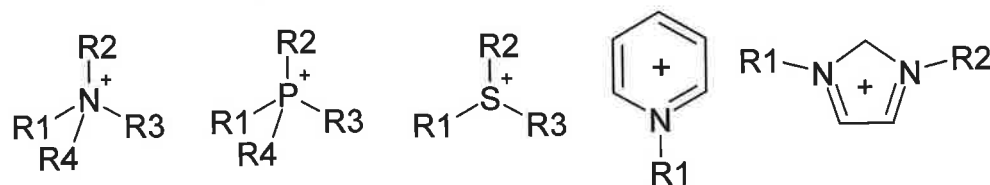


Figure A1.1 Cations commonly used in ionic liquids.

Ionic liquids have found use in many branches of chemical research including synthesis, separation and electrochemistry. One of the most extensively utilised applications of these materials was their use as replacements for organic solvents in chemical syntheses. The main advantages of ionic liquids over the traditional solvents are their extremely low vapour pressure, wide solubility, miscibility, non-volatility or flammability and low toxicity. It has been reported that the use of ionic liquids in Diels-Alder, Friedel-Crafts [230, 231] and metal-catalysed reactions [232] can give rise to greater yields, higher reaction rates and improved product selectivity.

Ionic liquids have also shown promise in separation applications. Methylimidazole based compounds have been used as low-polarity stationary phases for GC and showed good thermal stability and good sample retention properties. [233] Similar

materials have been used in HPLC experiments where they showed decreased band tailing and band broadening and improved resolution. They have also been used as solvents for liquid-liquid extractions, as they can give rise to pH-dependent liquid/liquid partitioning, and also as matrices for mass spectrometry due to their excellent vacuum stability and solubilising properties. [234]

One of the most recent applications of ionic liquids is in sensor devices, which use ionic liquids as sensing materials for organic vapours and are based on the variable viscosity of ionic liquid membranes with increased dissolution of analytes in the membrane. [235] Similar materials have also found use in electrochemical devices as electrolytes, photochemical solar cells and capacitors. [236]

Most of the research in this field, including the present work, has focused on imidazolium-based ionic liquids. This class of ionic liquids possess all of the properties desired in these compounds, good stability, low vapour pressure, wide solubility, miscibility, non-volatility or flammability, low toxicity, low cost and the anions are easily exchanged by either lewis acid or anion metathesis routes. These compounds are generally synthesised from 1-methylimidazole, 1-ethyl-3-methylimidazole or a similar related compound. One drawback of these imidazole based compounds is they tend to be hygroscopic. This problem can be overcome by preparing ionic liquids using dialkylimidazolium cations with water stable anions such as nitrates, sulphates and tetrafluoroborates. [229, 237]

A1.2 Experimental

A1.2.1 Synthesis

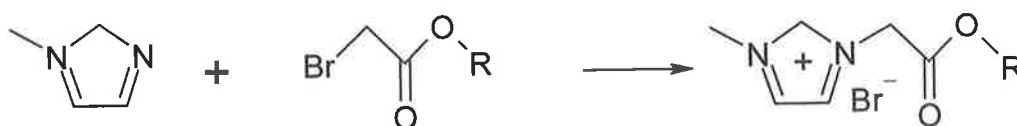


Figure A1.2 Synthesis of 3-Methyl-1-(alkyl)imidazolium bromide.

A range of compounds was prepared by our collaborators in Dr Nick Gathergoods group in the School of Chemical Sciences in DCU. The synthesis was similar for each compound and the general synthetic route was as follows. To a stirred solution of 10mmol 1-methylimidazole in 15ml of dry diethyl ether at 268 K under nitrogen, 12mmol of alkyl bromoacetate was added dropwise. The reaction mixture was stirred vigorously at 268 K for 90 mins and left overnight at room temperature. The diethyl

ether phase was carefully removed and the ionic liquid was washed with diethyl ether, the residual solvent was removed in vacuo, and the product was dried at 333 K to yield a viscous liquid.



Figure A1.3 Anion Exchange reaction of 3-Methyl-1-(alkyl)imidazolium bromide to form 3-Methyl-1-(alkyl)imidazolium NTf₂⁻

To form the trifluoromethane sulfonimide salt (NTf₂⁻) an anion exchange reaction (Br⁻ to NTf₂⁻) was set up. 2.5mmol of the ionic liquid from the first step was dissolved in 5ml water and 3mmol of lithium trifluoromethane sulfonimide (LiNTf₂) was added and stirred vigorously at room temperature overnight. The product was washed with water, any solvent was removed by rotary evaporation and the product was dried yielding a viscous liquid.

A number of compounds were synthesised with varying chain lengths, anions and number of oxygen atoms in the aliphatic backbone. The following compounds were synthesised:

Table A1.1 Table of structures and physical characteristics of the ionic liquids in this study

Label	Cation Structure	Appearance	Anion
4CO-Tf		Yellow viscous oil	NTf ₂ ⁻
10C-Tf		Yellow viscous oil	NTf ₂ ⁻
10CO-Tf		Brown, viscous oil	NTf ₂ ⁻
5C-Br		Yellow viscous oil	Br ⁻
5C-Tf		Pale yellow viscous oil	NTf ₂ ⁻
7CO-Br		Yellow waxy oil	Br ⁻
7CO-Tf		Yellow viscous oil	NTf ₂ ⁻

A1.2.3 NMR relaxometry

All ¹H relaxation measurements were carried out on the Stellar spinmaster FFC-NMR 2000 relaxometer using pre-polarised and non-polarised sequences. The magnetisation recovery curves were mono-exponential for all samples at all fields and at all temperatures.

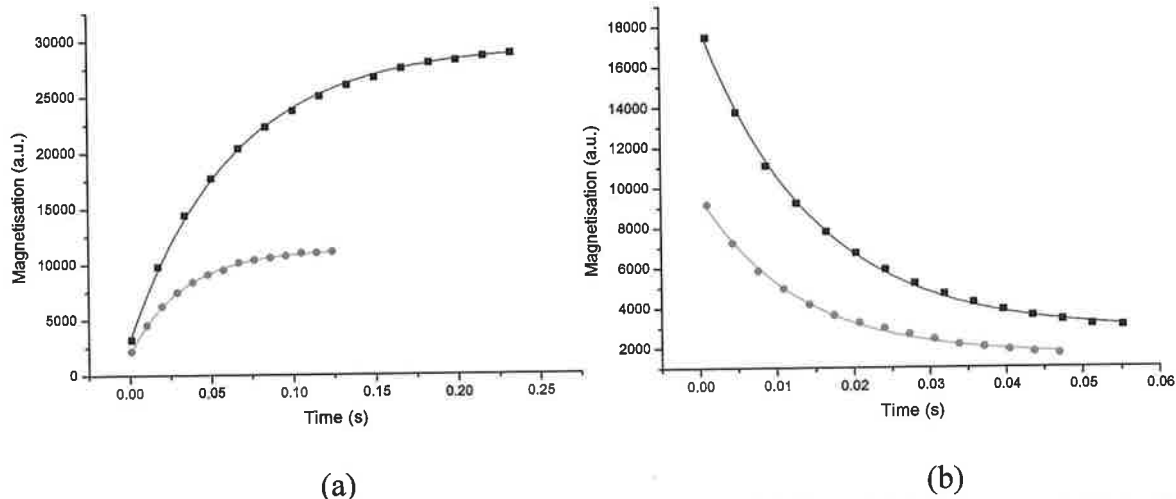


Figure A1.4 Magnetisation recovery curves recorded at 298 K at (a) 16MHz and (b) 0.1MHz for ionic liquids 10C-Tf (●) and 10CO-Tf (■).

A1.3 Results

Approximately 1 cm³ of each sample was placed in a 10 mm ID NMR tube under nitrogen and sealed. In order to test the thermal stability of the samples, a relaxation profile of each sample was collected initially at 298 K. The sample was heated and cooled in order to obtain profiles at different temperatures and after each heating/cooling cycle the profile at 298 K was recorded and was found to show no significant change from the original profile recorded at this temperature.

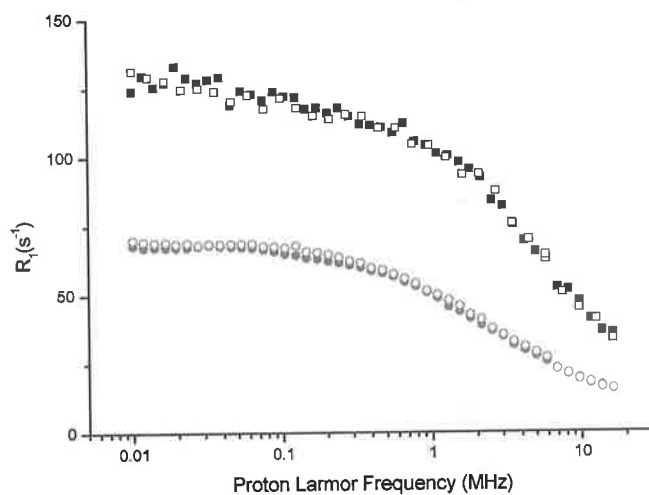


Figure A1.5 ¹H NMR profiles at 298K showing the stability of samples 10C-Tf (●○) and 7CO-Br (■□) initially (solid marks) and after heating the sample to 348 K (open marks) for a number of hours.

Relaxation profiles, over the ^1H frequency range 20-0.01MHz, were recorded for each sample at a number of temperatures. All of the samples, regardless of cation structure or anion type showed similar changes in the behaviour of their relaxation profiles with increasing temperature. The T_1 increased considerably with temperature across the field range from 298-348 K demonstrating that the systems are in the extreme narrowing dynamic regime.

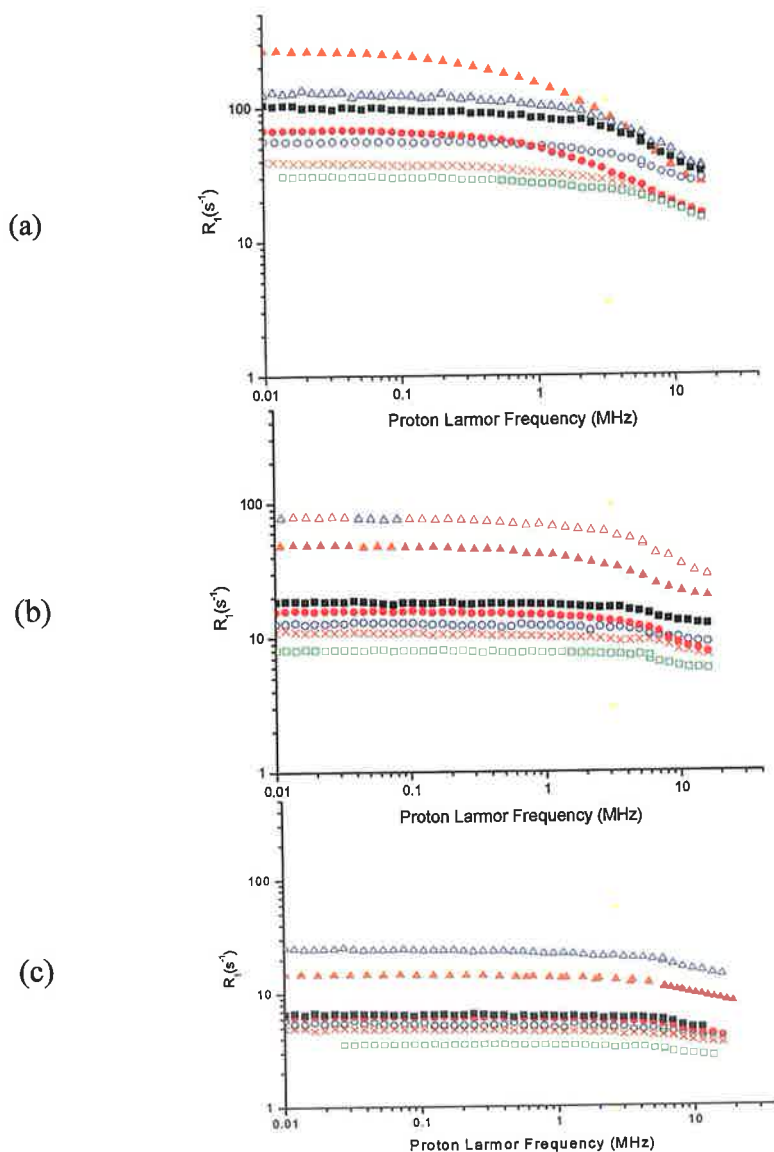


Figure A1.6 Relaxation profiles of samples 4CO-Tf (\square), 10C-Tf (\bullet), 10CO-Tf (\blacksquare) 5C-Br (\blacktriangle), 5C-Tf (\times), 7CO-Br (\circ) and 7CO-Tf (\triangle) at (a) 298, (b) 323 and (c) 348 K.

Several relationships between the structure and the NMR response were apparent. These are important as many of the physicochemical properties of ionic liquids are

related to the structure and dynamics of the cation and also on the nature of the anion. The ionic liquids 10CO-Tf and 10C-Tf are very similar with the same anion and imidazolium head group. Their aliphatic backbones are similar, however unlike 10C-Tf which contains a decane group, 10CO-Tf has three carbamoyl groups in the backbone. The effect of this modification to the cation structure is that the ^1H relaxation rate is greater for 10CO-Tf across the field range at all temperatures.

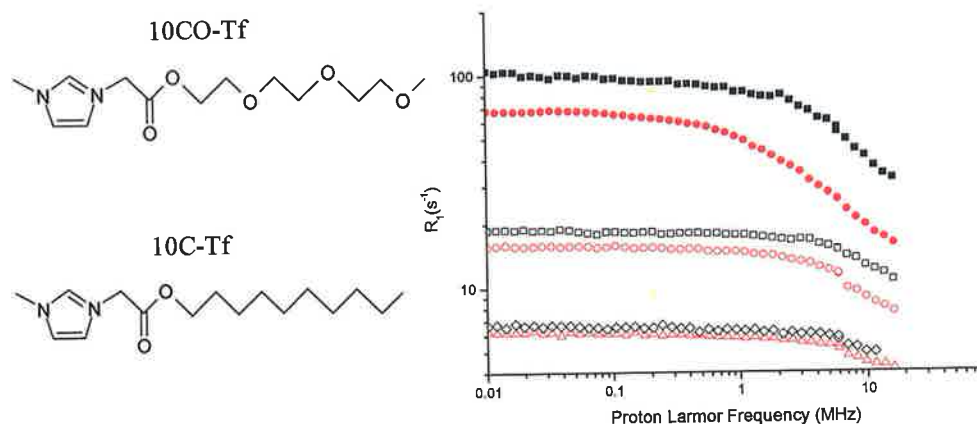


Figure A1.7 Relaxation profiles showing the temperature dependence of ^1H relaxation for samples 10CO-Tf ($\blacksquare\blacksquare\blacklozenge$) and 10C-Tf ($\bullet\circ\triangle$) recorded at 298, 323 and 348 K, respectively.

For the ionic liquids with similar anions (NTf_2^-) and carbomoyl groups in the aliphatic backbone (samples 10CO-Tf, 7CO-Tf and 4CO-Tf) a decrease in the backbone chain length resulted in a decrease in relaxation rate (R_1). This relationship was noted at all temperatures at which relaxation profiles were recorded.

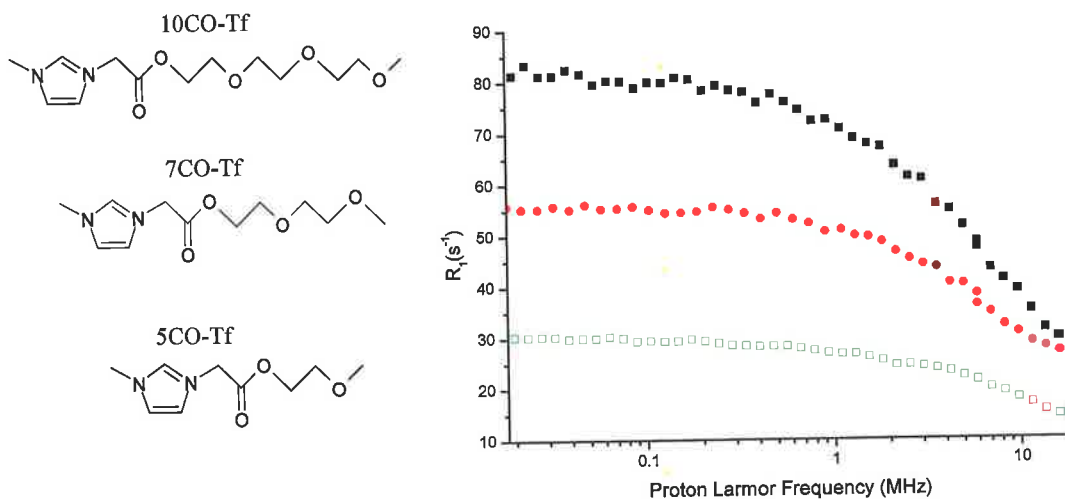


Figure A1.8 Relaxation profiles of samples 10CO-Tf (■), 7CO-Tf (●) and 4CO-Tf(□) recorded at 298 K.

A similar relationship was also observed for samples with the NTf_2^- anion and an alkyl chain (samples 5C-Tf and 10C-Tf). A decrease in the backbone chain length resulted in a decrease in relaxation rate (R_1) and this relationship was also apparent at all temperatures at which relaxation profiles were recorded.

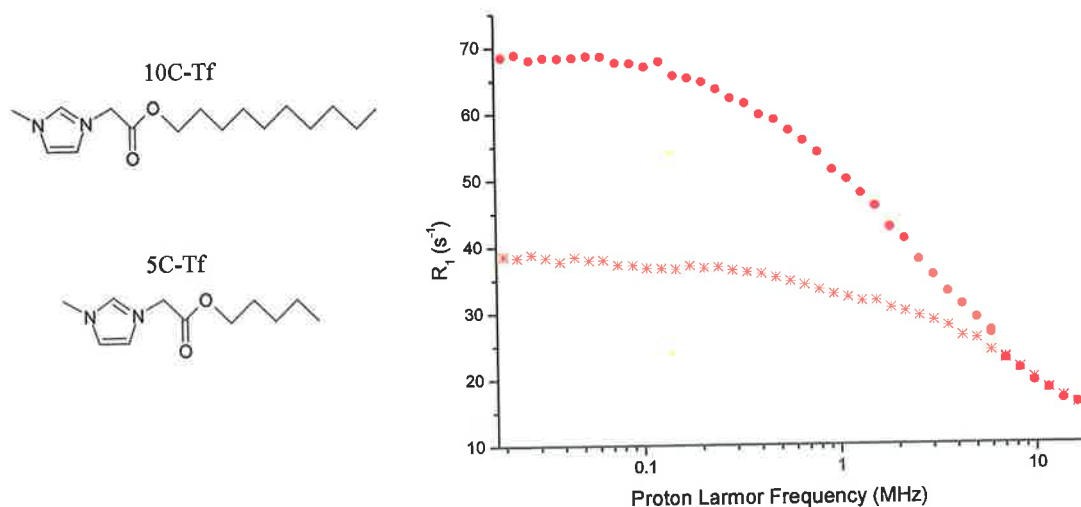


Figure A1.9 Relaxation profiles of samples 10C-Tf (●), and 5C-Tf (×), recorded at 298 K.

The physicochemical properties may also be altered by changing the anion, which can be accomplished by an anion exchange reaction. For both 7CO- and 5C- samples a higher relaxation rate was observed at all temperatures for the bromide than for the NTf_2^- salt (figure A1.10).

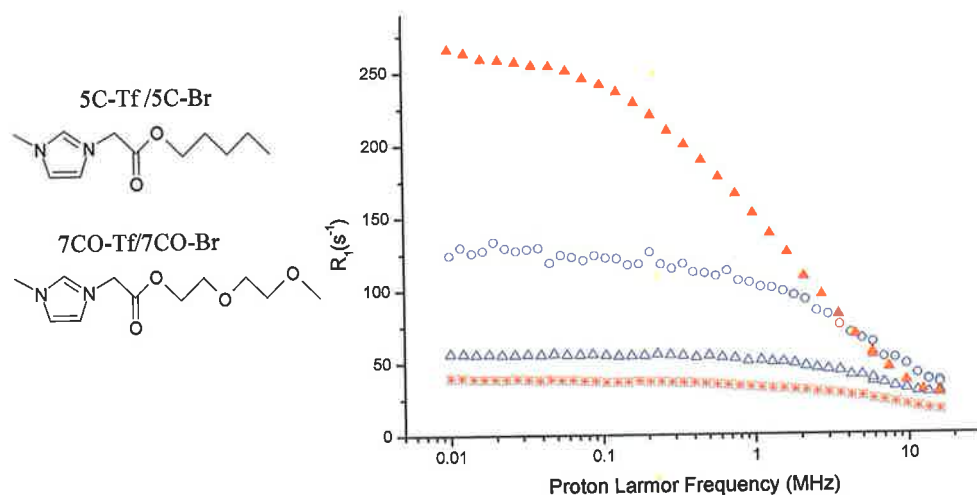


Figure A1.10 ^1H NMR profiles, recorded at 298 K, showing the dependence of the NMR response on the anion, for 7CO-Br (\circ), 7CO-Tf (Δ), 5C-Br (\blacktriangle) and 5C-Tf ($*$).

A1.4 Discussion

The NMR profiles were fitted with a multi-Lorentzian model derived from the Bloembergen-Purcell-Pound (BPP) spectral density function, as described earlier in this thesis. Fitting the NMR data to this model indicates there are two independent ^1H motions. However, the fits were poor, indicating that a better model for the spectral density is required.

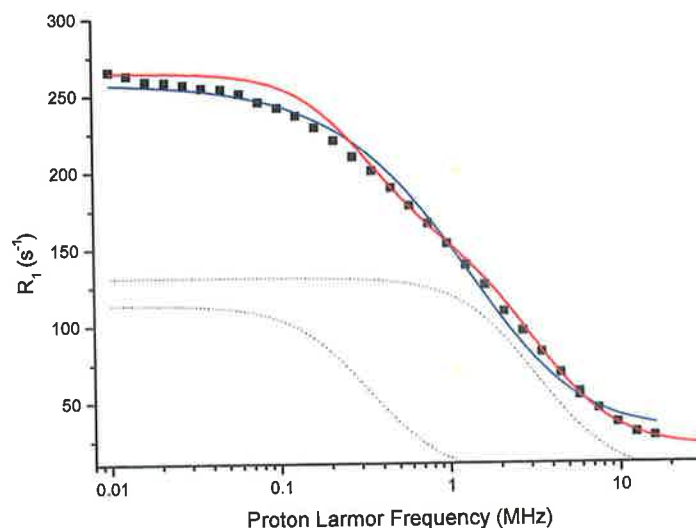


Figure A1.11 ^1H NMR profiles of sample 5C-Br (\blacksquare) at 298 K fitted with BPP (-) and multi-Lorentzian (-) spectral density functions. Also shown are the contributions from the two components in the multi-Lorentzian fit (\cdots).

The relaxation curves were then analysed using a Cole-Cole model as described elsewhere in this thesis to that used earlier in this thesis. All of the NMR data could be fitted using this model and correlation times (τ_c), dipolar coupling constants (β values) and correlation co-efficients (δ values) were extracted.

$$T_{1d}^{-1} = \beta_{HH} \left(\left(\frac{2}{\omega} \sin\left(\frac{\sigma\pi}{2}\right) \left[\frac{(\omega\tau_c)\delta}{1 + (\omega\tau_c)^{2\delta} + \left(2\cos\left(\frac{\delta\pi}{2}\right)(\omega\tau_c)^\delta}\right)} \right] \right) + \left(\frac{1}{\omega} \sin\left(\frac{\sigma\pi}{2}\right) \left[\frac{(2\omega\tau_c)\delta}{1 + (2\omega\tau_c)^{2\delta} + \left(2\cos\left(\frac{\delta\pi}{2}\right)(2\omega\tau_c)^\delta}\right)} \right] \right) \right) \quad [\text{A1.1}]$$

Table A1.2 Table of correlation parameters extracted from Cole-Cole fits of relaxation profiles of ionic liquids at multiple temperatures.

	Temp (K)	β ($\times 10^8$ s $^{-2}$)	τ ($\times 10^{-8}$ s)	δ
10C-Tf	297	17.6(2)	3.61(1)	0.94(6)
	323	12.1(5)	1.02(2)	0.97(7)
	348	6.3(8)	0.62(2)	0.97(7)
10CO-Tf	297	101(2)	1.01(9)	0.96(5)
	323	10.2(4)	0.85(5)	0.98(1)
	348	3.79(5)	0.82(4)	0.97(4)
5C-Br	297	44.1(6)	6.56(5)	0.92(6)
	323	17.2(2)	2.26(7)	0.96(1)
	348	1.6(4)	0.65(8)	0.96(9)
7CO-Tf	297	110(5)	1.75(4)	0.95(4)
	323	71.5(5)	0.82(1)	0.96(5)
	348	24.9(4)	0.74(3)	0.96(5)
7CO-Br	297	16.1(5)	2.03(3)	0.94(4)
	323	6.4(1)	0.93(5)	0.96(8)
	348	2.5(5)	0.92(2)	0.97(4)
5C-Tf	297	248(4)	1.41(2)	0.92(1)
	308	22.9(6)	0.78(5)	0.92(5)
	323	22.3(6)	0.69(2)	0.95(6)
	338	20.8(5)	0.21(5)	0.95(5)
	348	8.9(7)	0.20(4)	0.98(4)
4CO-Tf	297	268(4)	0.59(2)	0.96(5)
	323	12.6(1)	0.49(6)	0.97(7)
	348	1.3(2)	0.31(3)	0.98(1)

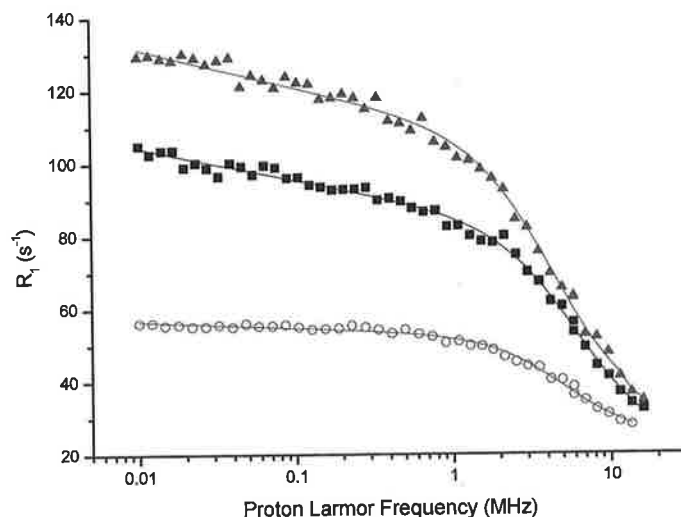


Figure A1.12 ^1H NMR profiles, recorded at 298 K, for samples 7CO-Br (\circ), 7CO-Tf (Δ) and 10CO-Tf (\blacksquare) fitted with a Cole-Cole spectral density function.

Using the dipolar coupling constants obtained from these fits ^1H - ^1H internuclear distances were calculated. Most of the samples show similar behaviour; a surprisingly large increase in the average internuclear spacing obtained, of $\sim 20\%$ over the measured temperature range.

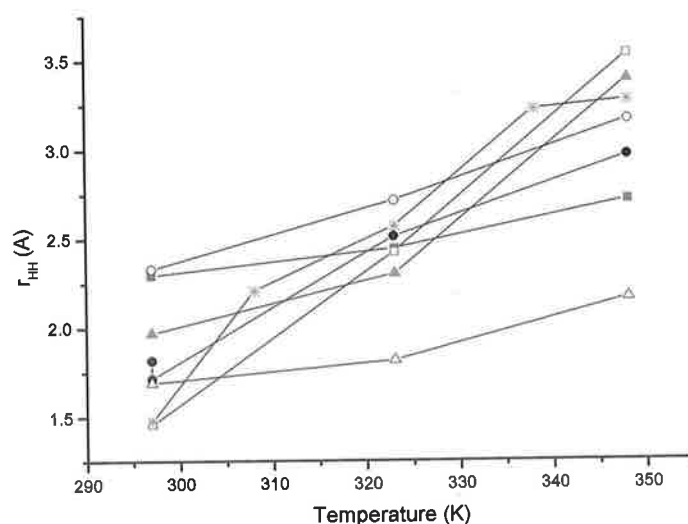


Figure A1.13 Temperature dependence of the ^1H - ^1H internuclear distance from the Cole-Cole fits of samples 4CO-Tf (\square), 10C-Tf (\bullet), 10CO-Tf (\blacksquare), 5C-Br (\blacktriangle), 5C-Tf (\times), 7CO-Br (\circ) and 7CO-Tf (Δ).

The correlation times generally decrease with increasing temperature as expected for a thermally activated process. Similar effects have been observed in ^{13}C NMR relaxation experiments on ionic liquids and other viscous liquids and glasses by Antony. [15, 16]

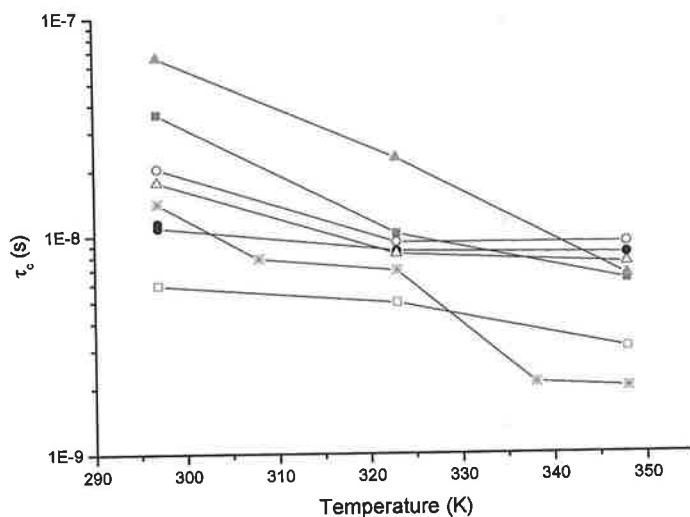


Figure A1.14 Temperature dependence of the correlation time from the Cole-Cole fits of samples 4CO-Tf (□), 10C-Tf (●), 10CO-Tf (■), 5C-Br (▲), 5C-Tf (X), 7CO-Br (○) and 7CO-Tf (Δ).

Dynamic parameters extracted by NMR relaxometry can be interpreted in terms of changes in viscosity [238, 239] using the Stokes-Einstein-Debye relationship:

$$\tau = \frac{4\pi\eta r^3}{k_B T} \quad [\text{A1.1}]$$

where τ is the dielectric dispersion time ($\tau_c = \tau/3$), r is the radius of the molecule and η is the viscosity. The internuclear distances and correlation times extracted from the NMR analysis were used to calculate the viscosity of all samples at a number of temperatures. The resulting viscosities showed good agreement with the trend in viscosity of similar liquids measured traditional methods in the literature (~110-10 mPa s from 300-380 K for bmim[NTf₂], a short chain imidazolium based RTIL). [12]

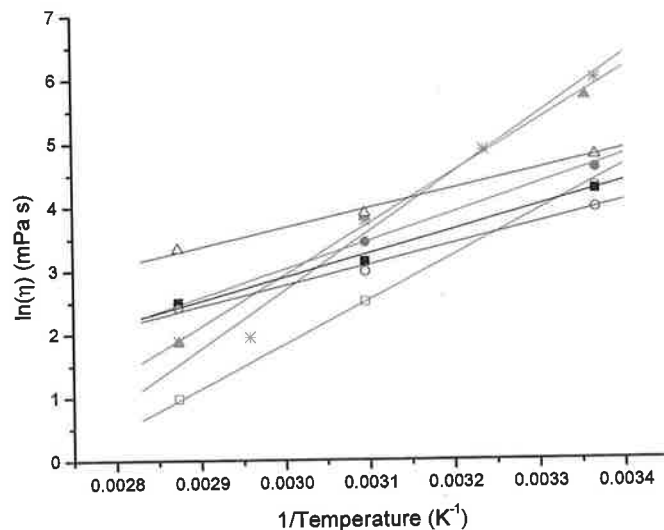


Figure A1.15 Temperature dependence of the viscosities derived from the NMR profiles of (□), 10C-Tf (●), 10CO-Tf (■) 5C-Br (▲), 5C-Tf (X), 7CO-Br (○) and 7CO-Tf (Δ) fitted with an Arrhenius function.

The viscosity of ionic liquids has previously been shown to display an Arrhenius-like temperature dependence [240, 241] according to the equation:

$$\eta = \eta_{\infty} \exp\left(+\frac{E_{Act}}{RT}\right) \quad [A1.2]$$

Where E_{Act} is the activation energy of the thermally activated process and η_{∞} is the viscosity at infinite temperature. An empirical extension of the Arrhenius law, the Vogel-Fulcher-Tamman (VFT) equation, has been used by some authors to interpret the temperature dependence of viscosity in ionic liquids with small symmetric cations [10, 12]. The relationship is described as:

$$\eta = A \exp\left(+\frac{B}{T-T_0}\right) \quad [A1.3]$$

where A (mPa s), B (K) and T_0 (K) are constants. However, in this case the viscosity data derived from NMR data fits to a simple Arrhenius model. This is possibly due to the small data sets recorded (figure A1.15).

Table A1.3 NMR derived viscosities, activation energies and prefactors from the Arrhenius analysis

	Temp (K)	4CO-Tf	10C-Tf	10CO-Tf	5C-Br	5C-Tf	7CO-Br	7CO-Tf
η_{NMR} (mPa s)	297	51.6	97.4	70.1	300.4	398.1	118.2	52
	308					130.9		
	323	11.2	30.8	23.1	45.7	43.3	48.7	19.5
	338					6.9		
	348	2.6	11.8	12.1	6.3	6.5	27.9	11.1
E_{Act} (kJ mol ⁻¹)		49(2)	35(1)	29(2)	63(7)	73(5)	24(2)	25 (4)
n_{∞} (mPa s)		9.2(1) $\times 10^{-08}$	6.4(1) $\times 10^{-05}$	4.5(6) $\times 10^{-04}$	1.8(2) $\times 10^{-09}$	4.5(5) $\times 10^{-11}$	6.6(2) $\times 10^{-03}$	1.4(2) $\times 1^{-03}$

The main result from this work is the observation that the viscosities calculated from NMR data generally increase with chain length for ionic liquids with oxygen atoms in the backbone. However, this is not observed for the alkyl analogues. A similar result was observed by Tokuda *et al* studying [Rmim][(CF₃SO₂)₂N] ionic liquids at 303 K by traditional bulk viscosity measurement techniques. [242]

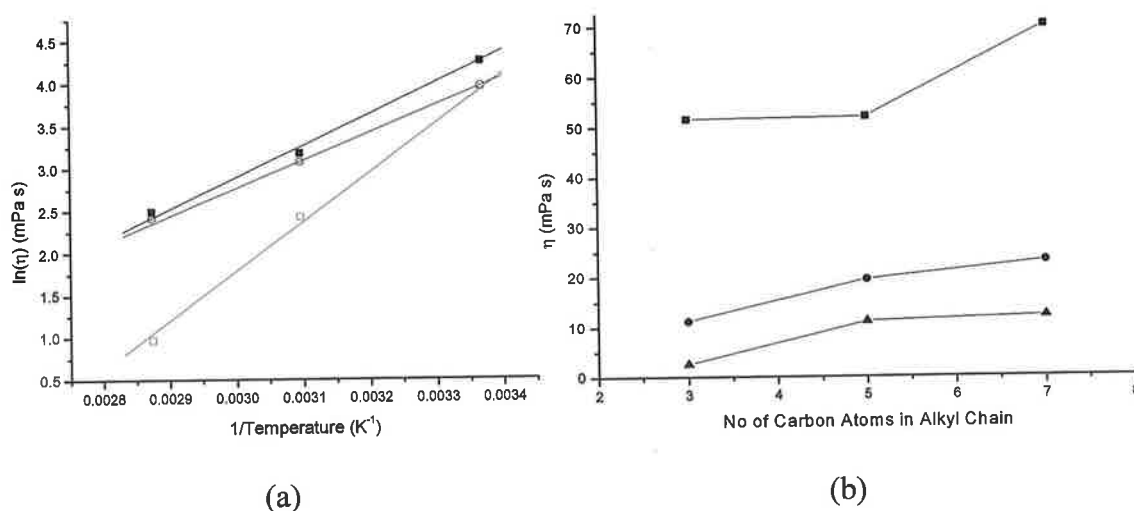


Figure A1.16 (a) Temperature dependence of NMR viscosity for samples 4CO-Tf (\square), 7CO-Tf (Δ) and 10CO-Tf (\blacksquare) and (b) dependence of NMR viscosity on the number of carbons in carbamoyl chain for the same samples

Another result is that the type of anion has very little effect on the activation energy of the temperature activated change in viscosity. Br⁻ and NTf₂⁻ analogues of samples 5C- and 7CO- were compared and showed very similar viscosity changes with anion type.

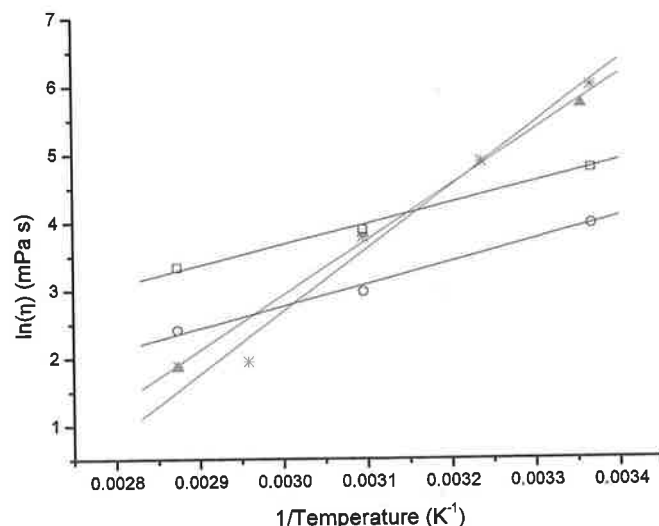


Figure A1.17 Temperature dependence of the viscosities of samples 5C-Br (▲), 5C-Tf (X), 7CO-Br (○) and 7CO-Tf (Δ).

Table A1.4 Trends in the behaviour of ionic liquids analysed by NMR methods.

By Comparing	Change	R_1	η_{NMR}	E_a
10C-/10CO-Tf	$\text{CH}_2 \rightarrow \text{CO}$	Increase	Decrease	Decrease
4-/7-/10CO-Tf	$n(\text{CO})$	Increase	Increase	Decrease
5-/10C-Tf	$n(\text{CH}_2)$	Increase	297/323 K Decrease 348 K Increase	Decrease
5C- and 7CO-	$\text{NTf}_2 \rightarrow \text{Br}$	Increase	5C No change 7CO Increase	No change No change

A1.5 Conclusions

The aim of this part of the project was to examine whether field-cycling relaxometry is a suitable tool for the analysis of ionic liquids. In summary it can be seen from this preliminary study that FFC-NMR can be used as a probe of proton dynamics and molecular motion in ionic liquids. Analysis of the NMR profiles using a Cole-Cole spectral density model yielded correlation times and internuclear distances for molecular motions, which were sensitive to the identity of both the anion and cation. Using the correlation times and internuclear distances from the NMR fits physical properties such as diffusion rates and viscosity can be approximated. The resulting viscosities showed good agreement with the trend in viscosity of similar liquids measured traditional methods in the literature.

Appendix 2 – Publications

To be submitted to ACS.

Conductivity and fluoride ion dynamics in α - PbSnF_4 , NMR and diffraction studies.

*Eoin Murray,^a Dermot Brougham,^{a, b, *} Jovan Stankovic^c and Isaac Abrahams^c*

a. School of Chemical Sciences, Dublin City University, Glasnevin, Dublin 9, Ireland.

b. National Institute for Cellular Biotechnology, School of Chemical Sciences, Dublin City University, Glasnevin, Dublin 9, Ireland.

c. Centre for Materials Research, School of Biological and Chemical Sciences, Queen Mary, University of London, Mile End Road, London, E1 4ND, United Kingdom.

*Dermot.brougham@dcu.ie

ABSTRACT:

Fast-field cycling ^{19}F NMR relaxometry has been applied to investigate fluoride ion dynamics in the layered anionic conductor PbSnF_4 . Two dynamic processes, on different timescales, are observed to modulate the ^{19}F T_1 values. By considering the temperature dependencies of the NMR relaxometry, conductivity and diffraction data together we propose the following mechanism for fluoride transport. The slower process is due to anion exchange between anions on equivalent sites (F2) in the

conducting fluoride plane, which lies between Sn and Pb layers. This is a diffusive process related directly to the mechanism of electrical conduction. The activation barriers for this motion agree closely with those determined from the temperature dependence of the DC conductivity. The faster process is due to non-diffusive exchange between the occupied sites (F2) and nominally vacant sites (F1), which lie between Sn planes. This process does not directly limit conductivity, but it does generate vacancies in the F2 sites and partial occupancy of the F1 sites. Above 340 K the fast process shows an increase in activation energy, as increased occupancy of F1 sites necessitates the formation of a Frenkel defect on a significant proportion of the F1 sites prior to an F2-F1 jump. In this temperature range the slow process shows a decrease in the activation energy, also observed in the conductivity data, which is due to increased numbers of vacancies in the F2 sites, which facilitate alternative diffusive pathways through the conducting fluoride plane.

KEYWORDS;

PbSnF₄, superionic conductors, fluoride conductor, NMR, relaxometry, diffraction

INTRODUCTION:

PbSnF₄, is a member of the MSnF₄ family (M = Pb, Sn and Sr) of layered anionic conducting solids. The conduction mechanisms across this family are of interest due to their high conductivities. PbSnF₄ has the highest ambient temperature anionic conductivity, 10⁻³ S cm⁻¹, of any known material and has been studied using a range of techniques focusing on structural, thermal, electrical and dynamic properties.¹⁻³ Technologically PbSnF₄ is a viable electrolyte in solid-state oxygen sensors, as the

alternative oxides have low room temperature conductivity, which limits the sensor response time.

α -PbSnF₄ was first reported by Donaldson and Senior,¹ while Reau *et al*⁴ were the first to experimentally determine its conductivity. The reported activation energy for conduction in PbSbF₄ is between 0.41 to 0.52 eV.¹ More recently, Reau and Chadwick,⁴ and Ahmad⁵ observed a discontinuity in the temperature dependence of the conductivity at around 350K and reported barriers to conductivity of 22 kJmol⁻¹ (0.23 eV) in the low temperature range, and 30 kJmol⁻¹ (0.31 eV) in the high temperature range. Several authors have reported phase transitions or other anomalous behaviour between 340-350K in PbSnF₄. Reau⁴ suggested a transition from a monoclinic (α) to a tetragonal (β) phase. Denes *et al*⁶ had previously shown that there are no symmetry changes, or phase transition at this temperature.

In a recent detailed neutron diffraction study Castiglione and Hull⁷ confirmed that PbSnF₄ has the fluorite structure and is tetragonal, in the space group $P4/nmm$, over the temperature range 298 – 591 K. This is a common structure for fast ion conductors, other notable examples include δ -Bi₂O₃ and the stabilised zirconias including Zr_{1-x}Y_xO_{2-x/2} and Zr_{1-x}Ca_xO_{2-x}. The PbSnF₄ structure may be described as being based on an ordered cubic close packed (ccp) array of cations (Sn²⁺ and Pb²⁺), resulting in a layered tetragonal structure (Fig.1). In the ideal fluorite structure, fluoride ions fully occupy all the available tetrahedral interstices in the ccp lattice, with octahedral interstices remaining vacant. In α -PbSnF₄, the room temperature distribution of fluoride ions was found⁷ to deviate from the ideal fluorite structure with three quarters of the fluoride ions located in two crystallographic sites F2 (4f) and F3 (2b) corresponding to those in the ideal fluorite structure and the remaining fluoride ions located in an octahedral site F4 (2c) between the Sn and Pb layers. Ions

located in the F4 site were found to be preferentially coordinated to the Sn atoms. The remaining tetrahedral site (F1) between adjacent Sn layers shows no measurable occupancy at 298 K. The structure remains tetragonal above 340K, but there is increased fluoride disorder, with greater anion density linking the F2 and F4 sites.

While critical in determining the structure of the fluoride sub-lattice, diffraction studies can only provide spatially and temporally averaged atomic positions. Furthermore, refinement of the diffraction data is difficult due to large anisotropic thermal parameters and partial site-occupancies. ^{19}F NMR spectroscopy is sensitive to the fluoride motions and has been used by to determine the mechanism of conductivity in some members of the MSnF_4 group. In particular, T_1 relaxometry and ^{19}F and ^{119}Sn MAS NMR was used recently ⁸ to determine that conductivity in BaSnF_4 is due to two-dimensional fluoride motion between the Ba and Sn layers, with exchange between the static and mobile sub-lattices occurring on a much slower (millisecond) timescale. These sub-lattices are identifiable in the ^{19}F spectrum. Previous NMR studies of PbSnF_4 show that, unlike BaSnF_4 , rapid fluoride motion makes identification of the mobile and rigid sub-lattices difficult even at room temperature. Second moment analysis⁵, of data from the temperature range 160 – 295 K, yielded a barrier of 18.5 kJmol^{-1} (0.193 eV), which is somewhat less than is obtained from conductivity indicating that local motions contribute to the line narrowing. Yamada and coworkers have also published ⁹ conductivity, impedance spectroscopy and ^{19}F , ^{119}Sn and ^{87}Rb NMR data on RbSn_2F_5 . This analysis conclusively demonstrated that this material exhibits two-dimensional fluoride conduction. A discontinuity in the temperature dependence of the conductivity was observed at 368 K.

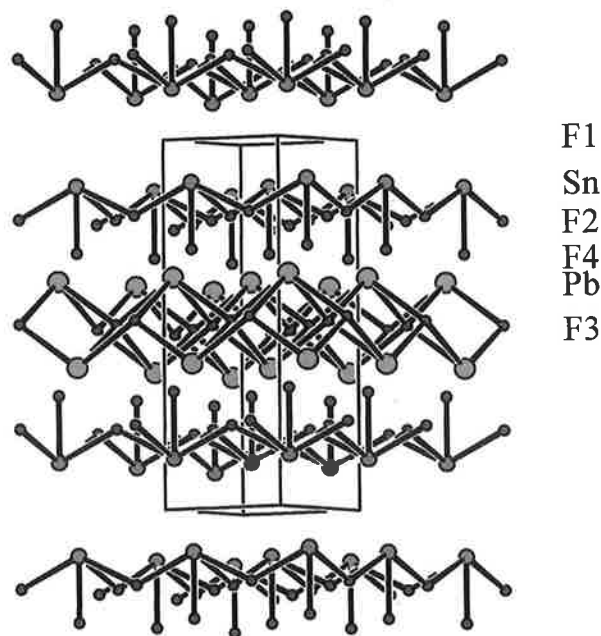


Figure 1 Structure of PbSnF_4 showing the cation layers and the four fluoride sites; F1 vacant; F2 and F4 (mobile) between the Sn and Pb layers; and F3 (static) between two Pb layers.

Using field-cycling NMR techniques the magnetic field dependence of the spin-lattice relaxation time, $T_1(\omega)$, can be measured. For each temperature, the field-cycling relaxation rate, $R_1(\omega) = 1/T_1(\omega)$, profile maps out the spectral density for the motional ^{19}F spin system in the frequency range from several kHz to about 10 MHz [Kimmich]. Thus $R_1(\omega)$ is sensitive to dynamic processes with correlation times that range from 10^{-5} to 10^{-9} s. Interpretation of fixed frequency NMR relaxometry data requires a model for the spectral density functions. The BPP formalism¹⁰ which assumes a single random dynamic process is normally adopted, and the process is assumed to be Arrhenius activated. By taking this approach, dynamic information (activation energies and pre-factors) can be extracted obtained from analysis of the temperature dependence of the relaxation, $R_1(T)$, but their physical interpretation may be compromised. The advantages of field-cycling relaxometry are that (i) the number

and shape of the spectral density functions are apparent from the relaxation profile; and (ii) the adherence of the dynamics to Arrhenius, or other activation models, can be tested by recording profiles at a number of temperatures, $R_1(\omega, T)$. A field-cycling NMR study has been reported for the high temperature fluoride conductor, LaF_3 .¹¹ Slow and fast motions were observed within the fluoride sublattices which did not conform to the BPP formalism.

In this paper we report the first study of field-cycling ^{19}F NMR relaxometry in layered fluoride ion conductors. We demonstrate that the technique provides insight into the transport mechanism beyond that obtainable from other techniques. The proposed mechanism is validated by the excellent agreement of the dynamic and structural parameters obtained from the NMR analysis, with those obtained from conductivity measurements and diffraction analysis, respectively. This approach may lead to greater understanding of the role of lattice vacancies in the conduction mechanisms of this important class of layered anionic conductors.

EXPERIMENTAL METHODS

Preparation

PbSnF_4 was prepared by conventional solid state methods. Stoichiometric amounts of SnF_2 and PbF_2 were ground as a slurry in methylated spirits using an agate mortar and pestle. After drying the mixture was sealed in an evacuated pyrex tube and heated in a tube furnace at 523 K for *ca* 18 h. After cooling, the sample was reground as a slurry in methylated spirits and dried at 353 K for 3 h. The dry sample was then resealed in a Pyrex glass tube and heated for a further 18h at 523 K, before being cooled to room temperature.

X-ray diffraction

X-ray powder diffraction data were collected at room temperature on an automated Philips PW1050/30 X-ray diffractometer, using Ni filtered CuK α radiation ($\lambda = 1.5418 \text{ \AA}$), in flat plate $\theta/2\theta$ geometry. Data were collected in the range 5-120° 2θ , in steps of 0.02°, with a scan time of 7 s per step. Calibration was with an external Si standard. The structure of PbSnF₄ was refined using data in the range 20 to 120° 2θ by the Rietveld method using the GSAS suite of programs.¹² The structure described by Castiglione *et al*⁷ was used as a starting model for refinement.

Neutron diffraction

Neutron diffraction data were collected on the Polaris diffractometer at the ISIS facility, Rutherford Appleton Laboratory, UK. Data were collected on back-scattering and low angle detectors over the respective time of flight ranges 1.0 to 20 and 0.5 to 20 ms. 200 μA or greater were collected in each case. The samples were contained in cylindrical 11 mm vanadium cans located in front of the back-scattering detectors. The structure of PbSnF₄ was refined using data in the range 20 to 120° 2θ by the Rietveld method using the GSAS suite of programs.¹² The structure described by Castiglione *et al*⁷ was used as a starting model for refinement.

Field-cycling NMR relaxometry

¹⁹F spin-lattice relaxation data was recorded in the range from 10kHz-18MHz on a Stelar FFC2000 [stelar] operating at a ¹⁹F measuring frequency of 9.81 MHz. Standard field cycling experiments were applied. A field slew rate of 20MHz/ms was used in all cases with a switching time of 1ms, to allow the electromagnet to settle. A digitisation rate of 1 MHz was used, the dead time of the spectrometer is about 24 μs . The FID was sampled with 512 points in the time range 25-540 μs after the 90° pulse which was of 7 μs duration. The relaxation rates, R_1 , were determined from the magnetisation recovery curves by least squares fitting. The R_1 values were not

sensitive to time window applied to the FID. The ^{19}F field range 18-75 MHz was accessed with a Bruker WP80 electromagnet. In a typical experiment c. 1 g of polycrystalline PbSnF_4 was used. The sample temperature was controlled using a thermostatted flow of dried air that ensured temperature precision within 1K over the full temperature range, 228-423K. Temperatures were calibrated externally using a Cu-Al thermocouple in a 10mm NMR tube.

RESULTS

Crystallography

Crystallographic and refinement parameters are summarised in Table 1. The refined structural parameters are presented in Table 2, with the corresponding fitted X-ray diffraction profile in Fig. 1. Significant contact distances are given in Table 3. The data show a much higher level of purity than in the previous sample. Fig. 2 shows detail of the fitted diffraction data. There are still small amounts of the monoclinic phase present suggesting some loss of SnF_2 . However, the amount of this impurity is estimated to be quite low.

Table 1 Crystal and Refinement Parameters for PbSnF_4

Chemical formula	PbSnF_4
Formula weight	401.88
Crystal system	Tetragonal
Space group	$P4/nmm$

Unit cell dimensions	$a = 4.2158(4) \text{ \AA}$ $c = 11.396(1) \text{ \AA}$
Volume	$202.53(5) \text{ \AA}^3$
Z	2
Density (calculated)	6.592 g cm^{-3}
Absorption coefficient μ (CuK α)	130.13 mm^{-1}
F(000)	336
Sample description	Beige powder
R-factors *	$R_p = 0.1131, R_{wp} = 0.0897,$ $R_{ex} = 0.0308, R_F2 = 0.1405$
Total no. of variables	30
No of profile points used	4999

* For definition of R-factors see reference 3

Table 2 Final Refined Parameters for PbSnF₄

Atom	Mult.	x	y	z	$U_{iso} (\text{\AA}^2)^a$
Pb	2	0.25	0.25	0.3742(7)	0.003(2)
Sn	2	0.25	0.25	0.8630(9)	0.007(3)
F(1)	4	0.75	0.25	0.237(6)	0.090(9)
F(2)	2	0.75	0.25	0.5	0.090(9)
F(3)	2	0.25	0.25	0.658(6)	0.090(9)

Table 3 Significant contact distances (\AA) in PbSnF₄, at 298 K

Pb-F(2)	2.800(6)	Pb-F(4)	3.079(2)
---------	----------	---------	----------

Sn-F(2)	2.321(4)	Sn-F(4)	2.0062(9)
F(1)-F(2)	2.476*	F(2)-F(2)	2.992(1)
F(2)-F(3)	3.237(8)	F(2)-F(4)	2.388(5)

*not refined on basis of scattering; set to ideal position

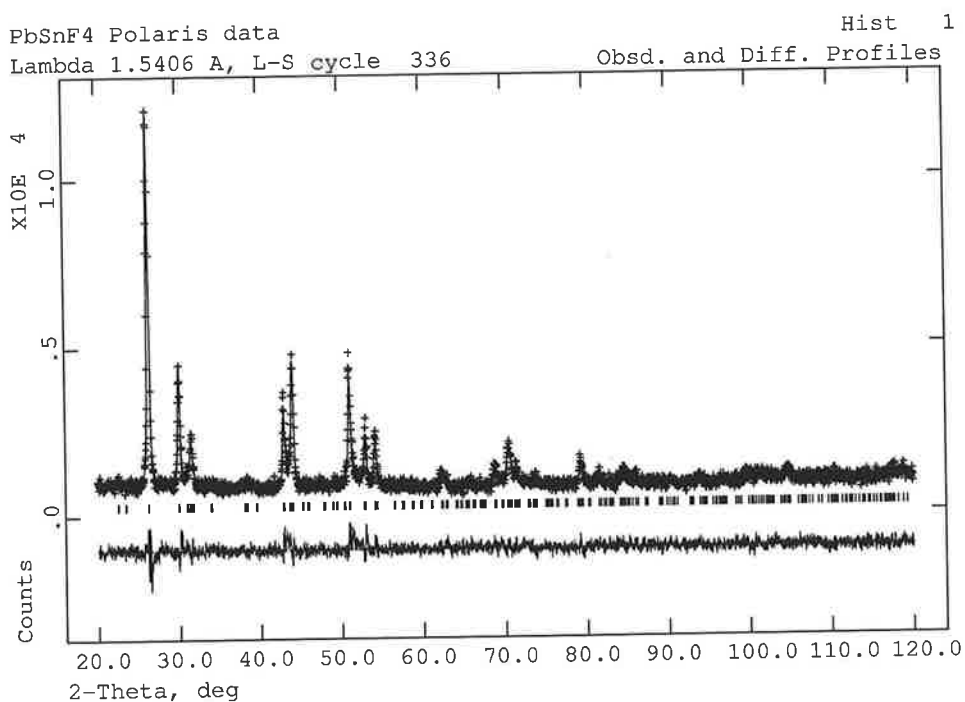


Figure 2. Fitted X-ray diffraction profile for PbSnF₄, showing observed (points), calculated (line) and difference (lower) profiles. Reflection positions are indicated by markers.

Both Sn and Pb are in their subvalent state and exhibit asymmetric coordination environments as a result of stereochemical distortion from the lone pairs of electrons on these atoms. As is often seen, the degree of stereochemical distortion is more pronounced in Sn, which may essentially be described as five coordinate with one short and four longer bonds, constituting a capped square pyramidal coordination

environment (Fig.2a). Pb shows distorted cubic coordination with four short and four longer bonds to fluoride ions (Fig. 2b).

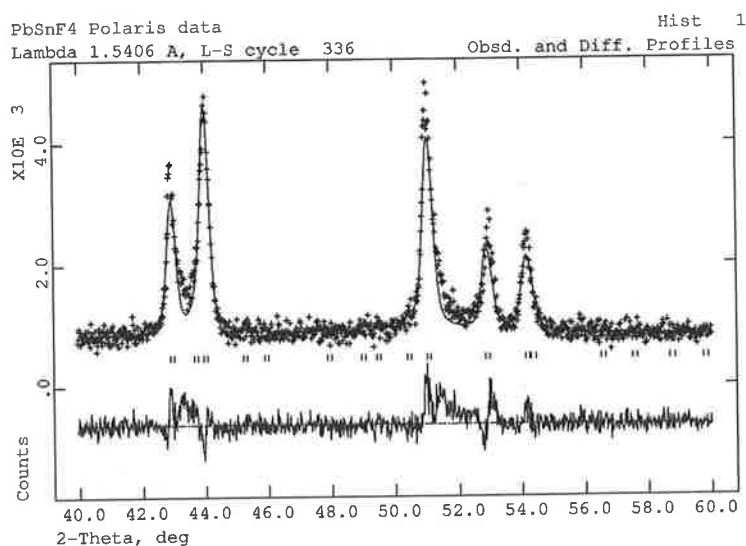
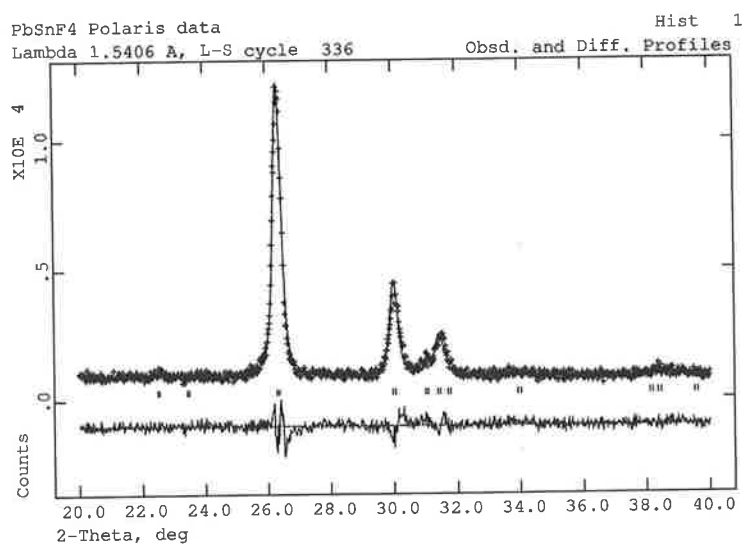


Figure 3. Detail of fitted X-ray diffraction profile for PbSnF4, (a) 20 to 40° 2 θ and (b) 40 to 60° 2 θ . Observed (points), calculated (line) and difference (lower) profiles are shown. Reflection positions are indicated by markers.

NMR

Field-cycling NMR profiles for samples A and B were collected at various temperatures in the range from 228 K to 423 K. For both samples, the magnetisation recovery curves were mono-exponential at all fields and at all temperatures. Data at selected temperatures for sample B are presented in Fig. 8. This sample showed significant dependence of spin-lattice relaxation on temperature across the ^{19}F frequency range 0.01-20 MHz. Visual inspection of the data indicates a broad dispersion, which moves to higher frequencies with increasing temperature (Fig. 8a). At temperatures above 273 K, a second spectral density contribution becomes visible at the lower end of the accessible frequency range. This dispersion is also observed to move to higher frequency as with increasing temperature. Comparison of the NMR profiles for samples A and B (supplementary information) reveals that the overall shape of the profiles is very similar and the curves are almost superimposable at all temperatures.

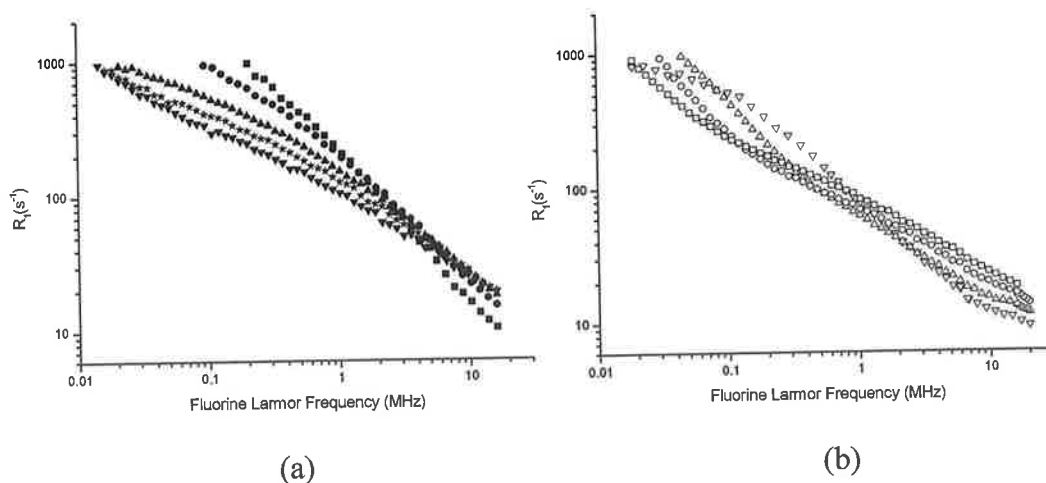


Figure 4. ^{19}F NMR data for sample b, showing the change in relaxation at (a) reduced temperature (\blacksquare 228 K, \bullet 248 K, \blacktriangle 263 K, $*$ 273 K, \blacktriangledown 283 K), and (b) elevated temperatures (\square 298 K, \circ 323 K, \triangle 373 K and \triangledown 423 K).

It is possible to measure R_1 values above 1000 s^{-1} by field-cycling techniques. However,, given the magnetic field slew rate used, 20 MHz ms^{-1} , the conservative approach of removing all R_1 values in excess of this value ($T_1 < 1 \text{ ms}$) was adopted to avoid possible systematic errors.

DISCUSSION

¹⁹F NMR relaxation data analysis

The observation of mono-exponential relaxation at all frequencies and temperatures strongly supports the assumption that the measured relaxation rates are representative of the bulk material and that all motional fluoride ions are at a common spin temperature due to fast spin diffusion [ref]. In analysing the data, it was assumed that the relaxation is driven by modulation of the homonuclear dipolar ^{19}F - ^{19}F interactions arising from anion dynamics. Calculations based on the crystallographic data [ref] show that, given the low isotopic abundance and weaker gyromagnetic ratios of these nuclei, the heteronuclear dipolar ^{19}F - ^{117}Sn , ^{19}F - ^{119}Sn and ^{19}F - ^{207}Pb interactions are too weak to contribute significantly to the observed fast ^{19}F relaxation. The Bloembergen, Purcell and Pound (BPP) theory of relaxation in polycrystalline solids can therefore be applied and the spin-lattice relaxation rate, R_1 , is given by:

$$R_1 = \frac{1}{T_1} = \frac{9}{8} \left(\frac{\mu_0}{4\pi} \right)^2 \gamma_F^4 \hbar^2 I(I+1) \frac{1}{r_{FF}^6} [J_1(\omega) + J_2(2\omega)] \quad [1]$$

Where, μ_0 is the vacuum permeability, γ_F the gyromagnetic ratio for the ^{19}F nucleus, r_{FF} is the fluoride ion jump distance, and $J(\omega)$ is the spectral density at frequency, ω .

It is possible to fit the NMR data successfully using spectral density functions based on a multi-Lorentzian or a modified Lorentzian model. However,, the only approach

that fits the NMR data at all temperatures and which is consistent with the known crystallography and the temperature dependence of the DC conductivity is a two-process model. In this, it is assumed that there are two dynamic processes driving the observed relaxation at all temperatures above 263 K. It is possible to generate a good fit to all of the data, when it is assumed that the faster motion, which lies within the frequency window at all temperatures, takes a non-Lorentzian form. The Cole-Cole spectral density function¹³ was applied. This function was developed for dielectric spectroscopy and has been previously used to interpret NMR relaxation data [ref]. This phenomenological approach effectively applies a stretched Lorentzian model, with a parameter, δ , which is usually interpreted as either the extent of correlation of the motion, or the width of the distribution of correlation times. For $\delta = 1$, the Cole-Cole equation reduces to a simple Lorentzian function, while $\delta = 0$ corresponds to the highest degree of correlation possible;

$$J_{CC}(\omega, \tau_c, \delta) = \frac{2}{\omega} \sin\left(\frac{\delta\pi}{2}\right) \left[\frac{(\omega\tau_c)^\delta}{1 + (\omega\tau_c)^{2\delta} + \{2\cos(\delta\pi/2)\}(\omega\tau_c)^\delta} \right]$$

[2]

where τ_c is the correlation time, defined as the mean time between fluoride ion hops, or the inverse of the hopping rate, τ_c^{-1} . For the faster motion in PbSnF₄ the δ value is very weakly temperature dependent below 340 K and the data in this temperature range can be fitted by fixing the δ value to the average value, 0.68, without significantly altering the extracted rates τ_c^{-1} . Above 340 K the δ value decreases significantly with temperature, and it is not possible to fit the data assuming a constant δ value. This is indicative of either an increase in the extent of correlation in the motional process, or of the width of the distribution of barriers.

Having modelled the faster process in this way, the slower process (only observed above 263 K) can be successfully modelled with a simple Lorentzian spectral density contribution. This indicates uncorrelated motion of the fluoride anions over a single barrier.

Fluoride ion dynamics

The correlation times, τ_c , extracted using the two-process model indicate that there are two motions on distinctly different timescales. The correlation times for the slow motion range between 2×10^{-5} s and 5×10^{-7} s over the temperature range, while for the fast motion the correlation times range from 1×10^{-7} s to 9×10^{-8} s.

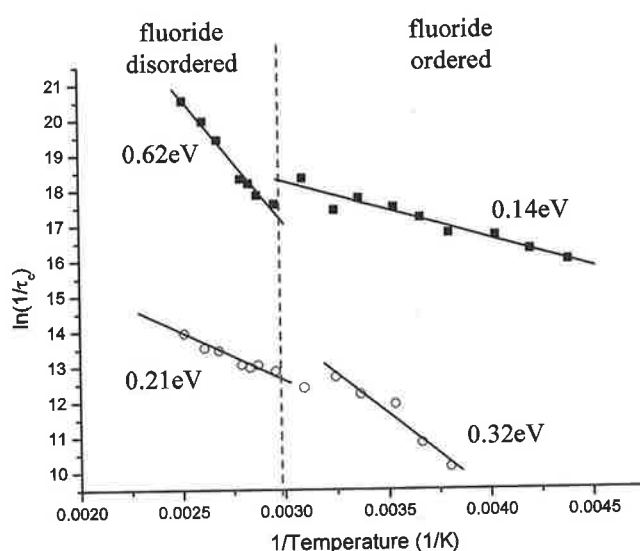


Figure 5 Arrhenius plot of $\ln(\tau_c)$ against reciprocal temperature, extracted using the two-process model analysis of the NMR data for sample b. The solid curves are fits linear fits to the data points. The dashed line indicates the temperature at which the fluoride sublattice disorder increases.

Arrhenius behaviour is observed for both processes (Fig. 16), with a discontinuity evident at around 340 K. This is very close to the temperature where changes in the

activation energy for conductivity were reported ⁷. The activation energies and pre-factors obtained from fitting the data, from above and below the critical temperature, to linear functions, are given in Table 4.

Table 4. Dynamic information from Arrhenius analysis of the rate data from the two-process model, above and below 340K, where the fluoride sublattice is disordered and ordered, respectively.

	E_{act} (kJmol ⁻¹)	E_{act} (eV)	τ_0^{-1} (s ⁻¹)
<i>Fast, disordered</i>	59(3)	0.62(3)	5.29(3)x10 ¹⁶
<i>Fast, ordered</i>	13(1)	0.14(1)	1.15(1)x10 ¹⁰
<i>Slow, disordered</i>	20(2)	0.21(2)	4.69(6)x10 ⁸
<i>Slow, ordered</i>	30(3)	0.32(3)	4.46(2)x10 ¹⁰

It is very interesting to note that the activation energy for DC conductivity observed in PbSnF₄ were 30 kJ mol⁻¹ below 350 K and 22 kJ mol⁻¹ above that temperature. ⁵ This numerical agreement with the NMR derived data in table 4 and the observation of the same transitional temperature range (340-350 K) by both techniques, strongly suggests that the slower motion observed on a microscopic level by NMR is directly related to the mechanism of bulk conductivity. This assignment also means that the faster motion, observed by NMR, does not correspond to a translational motion of anions through the lattice, instead it must be a local exchange process.

The Arrhenius pre-factor, or attempt frequency, derived from the NMR analysis, for the slower (Lorentzian) motion in the ordered-lattice temperature range is $\tau_0^{-1} = 4.46 \times 10^{10} \text{ s}^{-1}$. This is slightly lower than the picosecond vibrational timescale of an ion

trapped in a normal lattice site, however low pre-factors are not unusual in superionic systems and there has been much speculation on their causes.¹⁴ Significantly, the pre-factor is smaller, by more than three orders of magnitude, than that expected for the generation of a Frenkel defect.¹⁴ This strongly suggests that even when the fluoride lattice is relatively ordered, there are large numbers of vacancies available, a situation consistent with the presence of a faster independent process generating the required vacancies. Above 350 K, where the fluoride lattice is disordered, the pre-factor for the slower process is smaller at $\tau_0^{-1} = 4.69 \times 10^8 \text{ s}^{-1}$. This may be due to additional broadening of the potential well for anion dynamics, associated with an increase in disorder. The barrier to this slower motion is lower as might be expected.

The pre-factor for the faster (Cole-Cole) motion in the ordered-lattice temperature range, $\tau_0^{-1} = 1.15 \times 10^{10} \text{ s}^{-1}$, is also close to the timescale expected for anion motion into a pre-existing vacancy. Above 350 K, the pre-factor for this motion is much larger at $\tau_0^{-1} = 5.29 \times 10^{16} \text{ s}^{-1}$, and the activation energy is higher. This strongly suggests that, for the non-translational fluoride exchange process, the onset of fluoride disorder is associated with the requirement for defect generation.¹⁴

The dipolar coupling constants are strongly dependent on the fluorine-fluorine internuclear distance, r_{FF} . For systems where the dynamic processes driving relaxation are fully understood, NMR relaxation analysis is the most accurate method for measuring inter-nuclear distances. Unlike diffraction analysis where a model for all of the atomic positions is refined against the measured diffraction pattern, NMR relaxation provides a direct measurement of the physical separation of the different

fluoride ion minima. The variation in the r_{FF} values, and the fluorine-fluorine contact distances from crystallography ⁷, with temperature are shown in Figure 6.

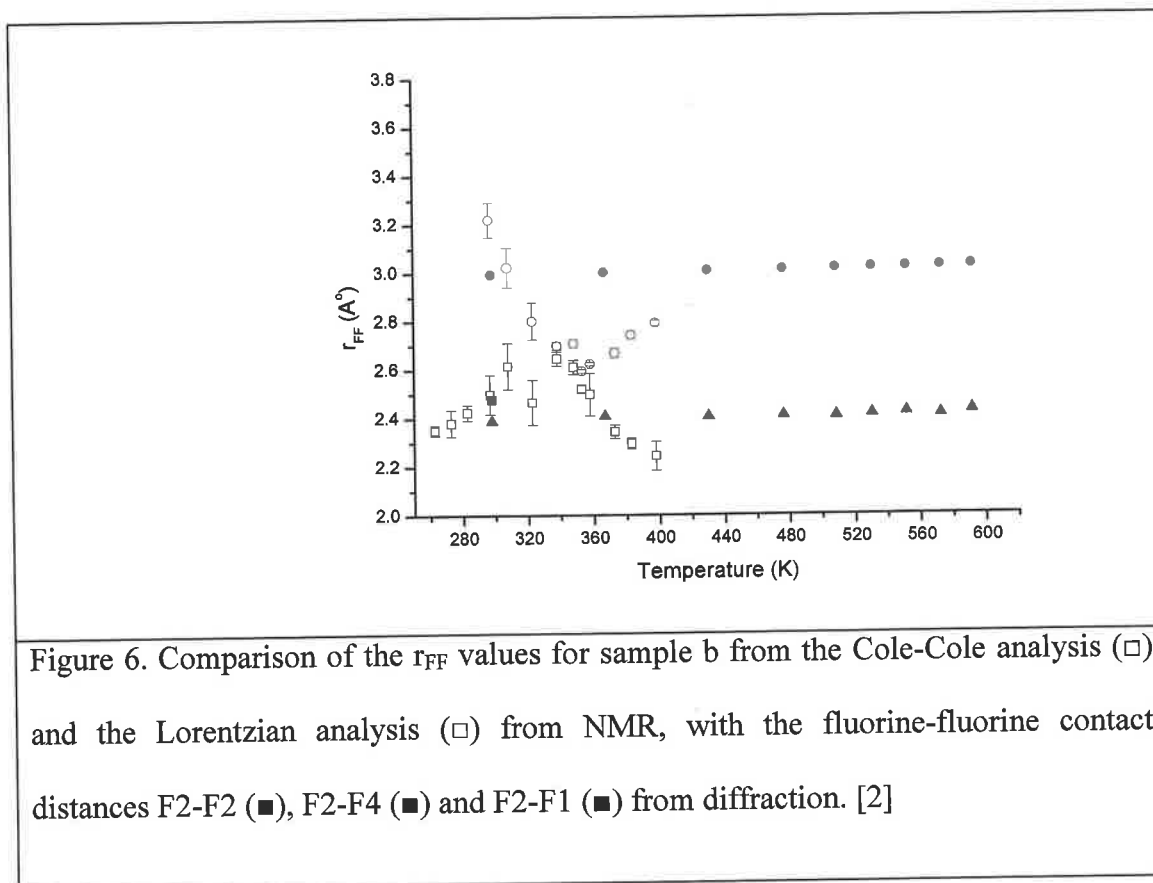


Figure 6. Comparison of the r_{FF} values for sample b from the Cole-Cole analysis (□) and the Lorentzian analysis (○) from NMR, with the fluorine-fluorine contact distances F2-F2 (■), F2-F4 (▲) and F2-F1 (●) from diffraction. [2]

Figure 6 clearly illustrates that the assumption, of relaxation due to homonuclear ^{19}F - ^{19}F dipolar interactions only, is valid as the crystallographic F-F distances are well reproduced. The variation in r_{FF} apparent from the NMR data is far greater than can be accounted for by thermal expansion of the lattice. Given the large anisotropic thermal parameters required to fit the diffraction data, one could assume that there is considerable uncertainty as to the exact position of the minimum. In summary, the r_{FF} value for the slower motion is $3.0 \pm 0.2 \text{ \AA}$, in the ordered-lattice temperature range, and reduces to $2.7 \pm 0.2 \text{ \AA}$ at higher temperature. For the faster motion, the r_{FF} value is $2.4 \pm 0.2 \text{ \AA}$ over the full temperature range. By comparing the crystallographic and NMR data recorded at 298 K, we can confidently assign the slow (Lorentzian) motion

to F2-F2 in-plane anion hops. As the temperature increases the r_{FF} values decrease to a value between the F2-F2 and F2-F4 crystallographic contact distances, reflecting the increased anion disorder in the motional fluoride plane (F2 and F4) at higher temperature. From the r_{FF} values at 298 K, the fast (Cole-Cole) anion motion could be assigned either to F2-F4 *in-plane*, or to F2-F1 *out-of-plane*, hops. As the temperature is increased there is an apparent initial increase in the r_{FF} value, although with the onset of fluoride disorder at 340K, it reduces back to a value slightly less than the F2-F4 and F2-F1 contact distances.

The pre-factor for the faster motion, at temperatures where the fluoride lattice is ordered, is consistent with assigning the faster process to F2-F1 hops, as F2-F4 motion would require generation of a defect. The F1 site is nominally vacant and the inter-fluorine distance is short, which is consistent with a very fast process. This assignment is also consistent with the observations from diffraction,⁷ which show that the F1 partial occupancy is very low, but increases with temperature and becomes detectable at temperatures above 700 K. F1 occupancies below 5% would be difficult to model in the diffraction analysis. Indeed low occupancies are expected, given that the F1 residence time would be expected to be very short, given that the barrier to reverse F1-F2 hops must be significantly lower than for F2-F1 hops.

The faster motion (F2-F1) appears as a broad dispersion in the ^{19}F NMR data. This could be due to a correlated process, or a distribution of barrier heights, both of which are consistent with partial F1 occupancy. The presence of a fluoride ion on this site will perturb the nearby Sn lone pairs, altering the electron density in the locality of the occupied site. The r_{FF} values associated with this process increase with temperature up

to 340K, to a value 0.2 Å larger than the crystallographic contact distance and then reduce back to a value about 0.2 Å less than that value. It should be noted that this crystallographic distance is not refined, as the contribution to the scattering is negligible, instead the values are fixed close to the ideal fluorite site. In the absence of any possible crystallographic confirmation one could speculate that the apparent systematic reduction in r_{FF} , above 340 K, is due to the formation of anion interstitials as part of the Frenkel F2-F1 process, which are closer to the F2-F2 plane than the formal F1 fluorite site location.

The good agreement between the extracted fluorine jump distance and the crystallographic structure, strongly suggests that the fluoride atoms in the F3 sites are not part of the dynamic fluoride lattice, and that our experiments are not sensitive to their relaxation. We deduce that the T_2 of this rigid sub-lattice is very short, so this ^{19}F magnetisation contribution dephases completely during the short switching time required for field stabilisation at the detection field. In BaSnF_4 the timescale for exchange between the mobile and static lattices was shown by NMR ¹¹ to be milliseconds. Processes on this ultra-slow timescale fall outside the dynamic range of the field-cycling experiment.

Mechanism for fluoride ion dynamics

A consistent picture of the fluoride dynamics emerges from the NMR study. There are two processes on different timescales which modulate the ^{19}F relaxation times in the accessible temperature and frequency range. There is a slower uncorrelated motion and a faster correlated motion. The barriers to both of these motions change at ~ 340 K which matches a transition seen in the published conductivity data. The

barrier to the faster motion increases while the barrier to the slower motion decreases indicating an increase in disorder in the anion layer, which accounts for the increased conductivity at higher temperature.

In the low temperature regime, the slower, motion may be unambiguously assigned to F2-F2 exchange on the basis of the anion hop distance at room temperature. The pre-factor associated with this motion is close to that expected for an anion motion into a pre-existing vacancy. In this temperature range, the anion hop distances for the faster correlated motion are consistent with F2-F1 or F2-F4 jump distances. However,, the faster process does not directly limit conductivity, while F2-F4 hops should be translational. In addition, the F2-F4 jump would require the formation of a Frenkel defect, which is not consistent but the low pre-factor obtained. We therefore assign the faster process to F2-F1 jumps. The occupancy of the F1 site remains low due to fast F1-F2 return jumps. Thus the F2-F1 motion gives rise to vacancies on the F2 site through formation of an anion Frenkel defect.

At 340 K a clear transition is observed for both motional processes. The faster correlated process shows an increase in activation energy and an increase in the extent of correlation. As a consequence, the pre-factor for this process increases significantly, since increased occupancy of F1 sites necessitates the formation of a Frenkel defect on a significant proportion of the F1 sites prior to an F2-F1 jump.

In the high temperature range, there is a reduction in the activation energy and the pre-factor for the slower Lorentzian process, which is still associated with F2-F2 dynamics. However, in this temperature range there is now a significant concentration

of vacancies on the F2 site. The mechanism for motion in the conducting plane now involves F2-F2 and F2-F4 hops, the barrier to the process is lower as an alternative pathway is now accessible and the pre-factor is lower, as is expected for anion motion over a flatter potential energy surface.¹⁴ This interpretation is supported by a change in the jump distance to a value intermediate between the F2-F2 and F2-F4 crystallographic distances. While the diffraction data is consistent with the observation of partial occupancies of F2 and F4 sites at elevated temperatures,⁷ which was interpreted as being due to shared anion density. In summary, the observed transition in conductivity to a phase of lower activation energy at 350 K is correlated with F2-F4 mixing of the translational anion motions which arises due to an excess of F2 vacancies driven by an increasing number of rapid correlated F2-F1 hops.

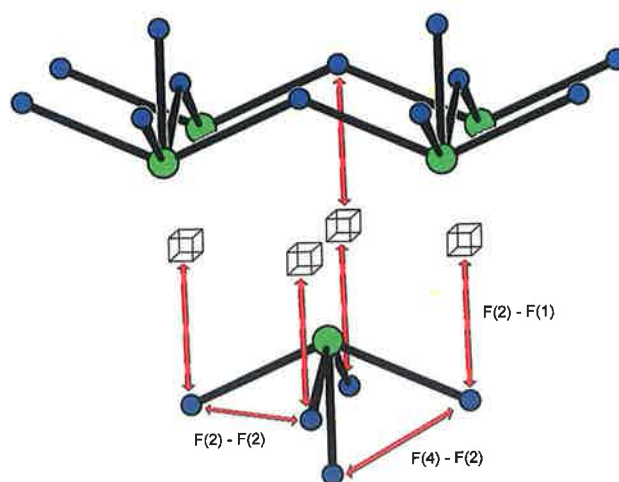


Figure 7 Pb-Sn layer of PbSnF₄ showing F2-F2 and F2-F4 translational motions and F2-F1 local hops

Applicability of the two-process model to PbSnF₄

It is also possible to fit the data using a “multi-Lorentzian” or model free approach¹⁵, however the fits obtained are less stable and the extracted rate and distance information does not concur with the diffraction data for PbSnF₄. In the temperature range from 263 to 350K, three Lorentzian spectral density components are required, while outside this range only two are needed. Close to these change over temperatures there are discontinuities in the temperature dependence of the rate data, indicating that this model is not valid. The two process model is also preferable as it requires fewer assumptions about the structure and fewer fitting parameters. Most importantly the two-process model is preferred as it is the only model that can provide quantitative agreement between the extracted dynamic (activation energy) and structural (fluoride jump distance) information with that obtained from independent conductivity measurements and crystallography.

Analysis of sample a using the two-process model yielded rates and fluoride jump distance very similar to that for sample b, see supplementary information. This agreement, for samples with a different fraction of the SnF₂ deficient phase, indicates that phase purity is not required to extract meaningful dynamic information. It is likely therefore that the second phase does not contribute significantly to the conductivity, fluorine dynamics or NMR relaxation. It is likely that the ¹⁹F T₂ values are very short for the magnetisation contribution from the SnF₂-deficient domains, as is the case for the static F3 sublattice in the main PbSnF₄ phase. In separate experiments we observed very short ¹⁹F T₂ values when studying the related salt BaF₂, which made it very difficult to study by field-cycling methods.

CONCLUSION

From the NMR analysis we can propose a detailed mechanism for conduction that is consistent with the diffraction and conductivity measurements. The data conformed very well to a model comprising a Cole-Cole spectral density function for fast correlated motions and a Lorentzian spectral density function for a slower process in the fluoride sublattice. Using the fluoride jump distances and Arrhenius prefactors extracted from the analysis, the faster motion was assigned to non-translational fluoride jumps from the F2 position to the vacant F1 sites. The slower motion was assigned to F2-F2 translational motion which, at higher temperatures, was mixed with F2-F4 jumps. The proposed mechanism indicates that conductivity in PbSnF_4 is due to translational diffusion in the F2-F4 plane which is assisted by fast F2-F1 hops creating vacancies in the F2 sublattice which act as Frenkel defects. The quenching of the highly disordered lattice, associated with a loss of mobility through the F4 sites, results in a decrease in conductivity of about 0.7 Scm^{-1} by room temperature.

SUPPLEMENTARY MATERIAL

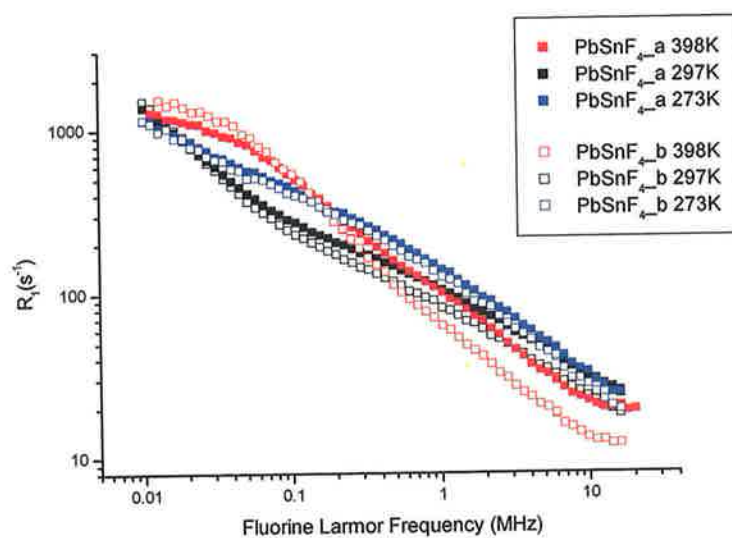


Figure ^{19}F FFC-NMR data for samples a and b at 273K, 297K and 398K.

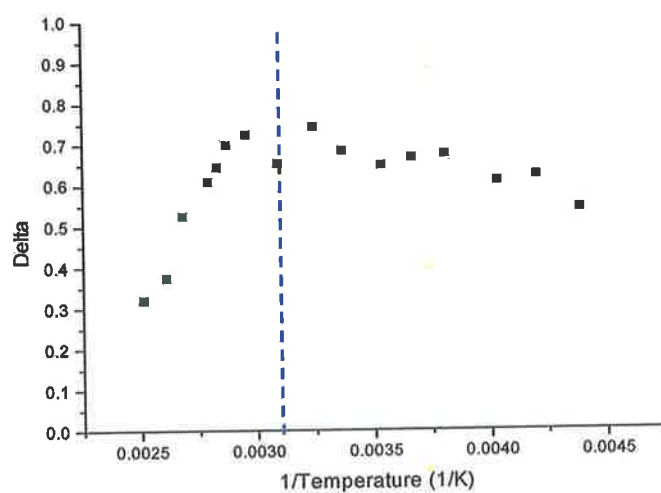


Figure Plot of the δ -value extracted from the cole-cole part of the cole-cole/Lorentzian model fits of NMR profiles of $\text{PbSnF}_4\text{_b}$ showing the discontinuity at $\sim 340\text{K}$

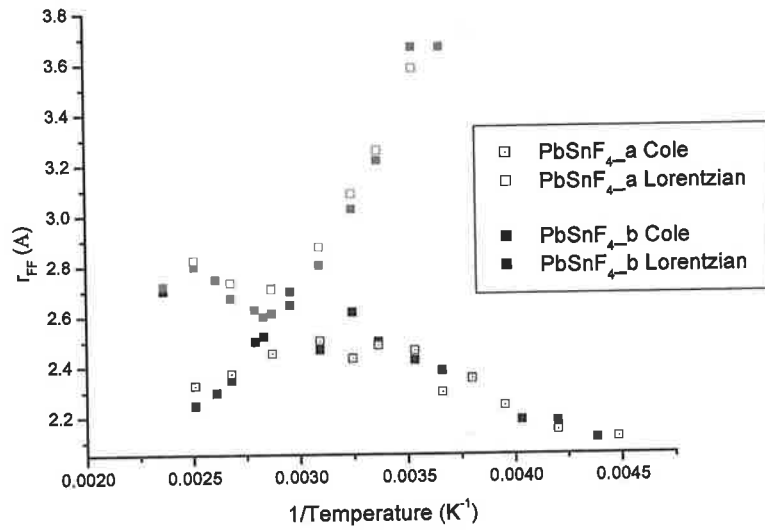


Figure 3.21 Arrhenius plot of (a) τ_c^{-1} and (b) r_{FF} determined for samples $PbSnF_4_a$ (\bullet, \blacksquare) and $PbSnF_4_b$ (\circ, \square), from the analysis of the NMR data using the two-process model.

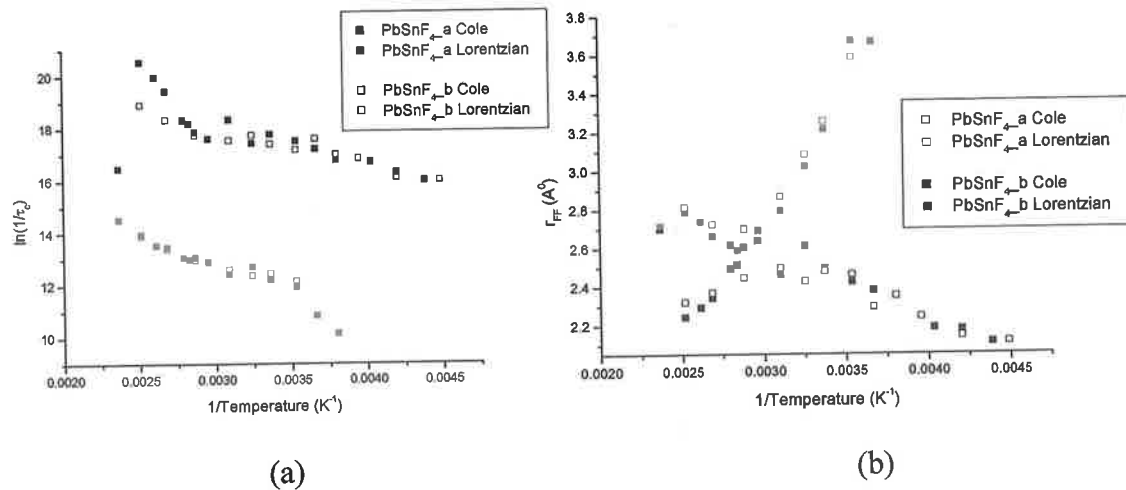


Figure 18 Plot of (a) τ_c and (b) β extracted from samples $PbSnF_4_a$ and $PbSnF_4_b$ using the Cole-Lorentzian model

ACKNOWLEDGMENT

EM gratefully acknowledges the financial support of the Irish Research Council for Science, Engineering and Technology Embark scholarship funded by the National Development Plan. DB acknowledges Enterprise Ireland Research Innovation Fund (basic research grant, SC/2002/336) and the Higher Education Authority for the Republic of Ireland for support in equipment purchase.

REFERENCES

1. Donaldson J D and Senior B J 1967 *J. Chem. Soc. A* 1821
2. Collin A, Denes G, Le Roux D, Madamba M C, Parris J M and Salaun A 1999 *Int. J. Inorg. Mater.* 1 289
3. G. Denes, Y. H. Yu, T. Tyliczszak, and A. P. Hitchcock, *Journal of Solid State Chemistry*, 104, 239-252, (1993),
4. Jean-Mauricie Reau, Claude Lucat, Josik Portier et Paul Hagenmuller, *Mat. Res. Bull. Vol.13*, pp.877-882, (1978),
5. Ahmad MM Yamada K, Okuda T, *J. Phys.: Condens. Matter* 14 (2002) 7233–7244
6. G. Denes, Y. H. Yu, T. Tyliczszak, and A. P. Hitchcock, *Journal of Solid State Chemistry*, 104, 239-252, (1993),
7. M. Castiglione, P.A. Madden, P. Berastegui and S. Hull, *J. Phys.: Condens. Matter.*, 17 (2005) 845
8. grey
9. Yamada K, Ahmad MM, Ogiso Y, *et al.*, Two dimensional fluoride ion conductor RbSn₂F₅ studied by impedance spectroscopy and F-19, Sn-119, and Rb-87 NMR *Eur. Phys. J., B* 40 (2): 167-176.
10. Bloembergen, E.M. Purcell, R.V. Pound "Relaxation Effects in Nuclear Magnetic Resonance Absorption" *Physical Review* (1948) v73. 7:679-746

11. Privalov A. F., Lips O, Fujara F., Dynamic processes in the superionic conductor LaF₃ at high temperatures as studied by spin-lattice relaxation dispersion. *J. Phys.: Condens Matter*, 14 (17): 4515-4525
12. "The Rietveld Method" ed. R.A.Young, IUCR monographs on Crystallography 5, p 21, Oxford University Press, New York (1993).
13. Cole KS and Cole RH, *J Chem Phys* 9 (1941) 341
14. Boyce JB and Huberman BA *Phys Rep* 51 1979 189
15. Halle B, Johannesson H and Venu K *J Mag Res* 135 (1998) 1



NMRD of polyaniline-based conducting polymers[☆]

E. Murray^a, D.F. Brougham^{b,*}

^a School of Chemical Sciences, Dublin City University, Dublin 9, Ireland

^b National Institute for Cellular Biotechnology, School of Chemical Sciences, Dublin City University, Dublin 9, Ireland

Received 28 June 2004; received in revised form 11 January 2005; accepted 30 June 2005
Available online 7 November 2005

Abstract

Nuclear magnetic resonance dispersion (NMRD) is a technique for measuring NMR relaxation times, which is commonly used to study dynamics in condensed matter. In this paper, we present NMRD profiles, for polyanilines doped with trifluoromethanesulfonic acid (TFSA), recorded as a function of temperature and dopant concentration. This work demonstrates that NMRD can be used to characterise the critical processes that determine the conductivity of the materials. The NMRD profile of the bulk polymer is sensitively dependent on the concentration of the dopant, while the response of the dopant is insensitive to concentration. Complete analysis of the NMRD profiles of these ICPs will give important information, including the rates of spin diffusion and of charge transport between dopant-rich domains.
© 2005 Elsevier B.V. All rights reserved.

Keywords: Nuclear magnetic resonance spectroscopy; Conduction; Dopant

1. Introduction

The aim of this project is to use NMRD to study polymer dynamics and charge transport in the both the doped and undoped forms of the ICP polyaniline–TFSA. Nuclear magnetic resonance dispersion (NMRD) is a technique used to measure the longitudinal relaxation time (T_1) as a function of NMR resonance frequency. NMRD can be used to study dynamics in condensed matter as T_1 is determined by fluctuations in local fields. For normal polymers, these fluctuations usually arise due to molecular motions. So, the NMRD response of an undoped polymer is driven by chain motion and the NMRD profile (T_1 versus frequency plot) should be a stretched-Lorentzian; the width of which is directly related to rate of molecular dynamics. In the case of intrinsically conducting polymers, ICP's, charge carrier motion may also affect the polymer relaxation. Thus, it is our hypothesis that NMRD can be used to characterise the critical processes that determine the conductivity of the materials. Through this work we hope to improve the

understanding of the charge transport mechanisms in this very important class of materials, specifically we are probing the interaction between the conducting (nano)domains and the bulk polymer.

Polyaniline (PAni) was the first ICP to achieve worldwide commercial availability. It has achieved significant importance among conducting polymers due to its ease of processability, environmental stability and of course high conductivity. The 'doped' (protonated) form is green coloured (hence emeraldine) and has conductivity on a semiconductor level of the order of 10 S cm^{-1} (depending on dopant), many orders of magnitude higher than that of common polymers.

The dopant used in this study, trifluoromethanesulfonic acid (TFSA) (Fig. 1), was chosen due to the fact its anion contains no protons to interfere with ^1H signal from the polymer backbone, while ^{19}F NMRD can be used to study the mobility of dopant.

It is thought that the dopants are not homogeneously distributed through the polymer, but rather are concentrated in domains separated by regions of lower conductivity [1]. Thus, the charge transport mechanism is limited by the flow of charge between domains. The domains are relaxation sinks, linked at a molecular level to the entire polymer by the process of spin diffusion. Thus, the doped regions determine the NMRD response of the polymer.

[☆] Based on presentation at the International Conference on Synthetic Metals, Wollongong, Australia, June 28–July 2, 2004 (ICSM 2004).

* Corresponding author.

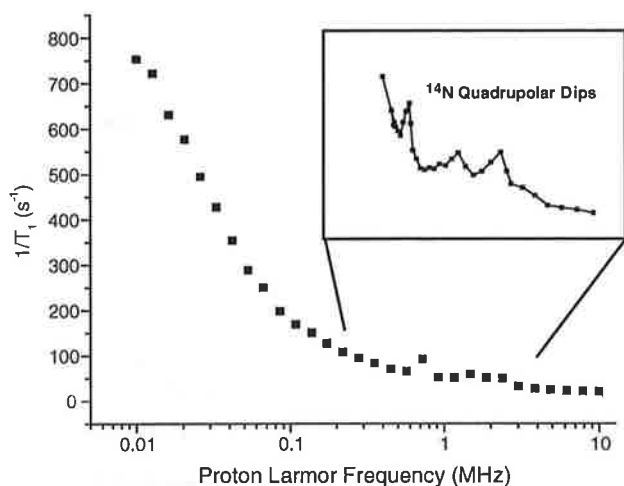


Fig. 4. ^1H NMRD of PANi-TFSA at 24 °C showing ^{14}N quadrupolar dips.

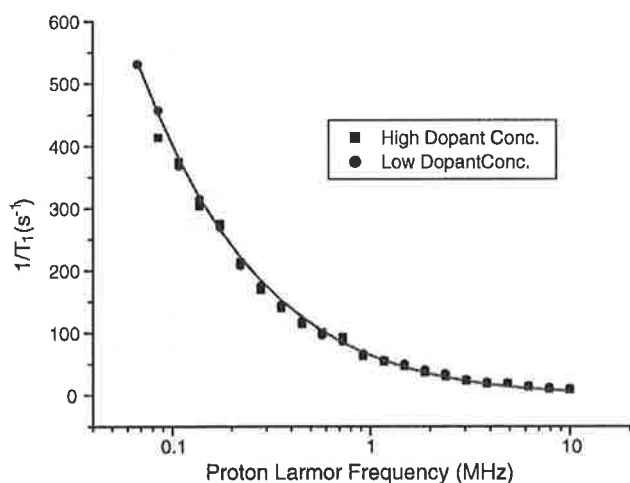


Fig. 5. ^{19}F NMRD profile, at 24 °C, of both high and low dopant concentration PANi-TFSA fitted with the Cole-Cole distribution model.

(Eqs. (1) and (2)).

$$\frac{1}{T_1} = C_{\text{dip}} \frac{1}{r^6} (aJ_\omega + bJ_{2\omega}) \quad (1)$$

$$J_{\text{cc}}(\omega, \tau_c, \delta) = \frac{2}{\omega} \sin\left(\frac{\delta\pi}{2}\right) \times \left[\frac{(\omega\tau_c)^\delta}{1 + (\omega\tau_c)^{2\delta} + \{2 \cos(\delta\pi/2)\}(\omega\tau_c)^\delta} \right] \quad (2)$$

where C_{dip} is dipole-dipole constant, J_{cc} the spectral density, ω the angular frequency (rad/s), τ_c the correlation time and δ is the degree of correlated motion and distribution of correlation times. Using the Cole-Cole distribution model to fit the ^{19}F data of PANi-TFSA, we found a correlation time, τ_c , of $3.69(8) \times 10^{-8}$ s and a value of 0.386(8) for δ . A τ_c of 37 ns for TFSA anion

tumbling is on the expected timescale for molecular tumbling in a moderately restricted environment at this temperature. The δ value is indicative of a significant degree of correlation of the dopant reorientational motion. The fact that both curves can be fitted with the same parameters demonstrates that the anions are in very similar environments irrespective of the dopant level.

There are two possible explanations for this; either the dopant is homogeneously distributed through the material and is relatively dilute, i.e. the anion environment is determined by the polymer backbone and partial de-doping does not affect the anion motional characteristics. Alternatively dopants may reside in domains of comparable size and dopant density, in which case the decrease in conductivity on de-doping is due to a decrease in the number of domains, with a resulting increase in the inter-domain separation. This is consistent with the observations of domains from EFM microscopy [7], XRD and EPR [1] of other workers.

Future work will involve measuring the temperature dependence of τ_c , which will allow the determination of the barrier height of the to motion. We are also developing a model to fit the profiles of the polymer backbone.

4. Conclusions

^1H NMRD can be used to probe the magnetic coupling of the polymer backbone of ICPs to dopant-rich domains, which act as NMR relaxation sinks. The coupling processes are interesting as they are related to the mechanisms of conduction in these materials. ^{19}F NMRD data suggest that conductivity is limited by the extent of inter-domain communication.

Acknowledgments

EM gratefully acknowledges the financial support of the Irish Research Council for Science, Engineering and Technology Embark scholarship funded by the National Development Plan. DB acknowledges Enterprise Ireland Research Innovation Fund and the Higher Education Authority for the Republic of Ireland for support in equipment purchase. The authors would like to thank Gordon Wallace and Peter Innis of the Intelligent Polymer Research Institute, University of Wollongong for their helpful comments and insights.

References

- [1] J. Too, S.M. Long, Phys. Rev. B: Solid State 57 (1998) 9567.
- [2] P.K. Kahol, K.K. Satheesh Kumar, S. Geetha, D.C. Trivedi, Synth. Met. 139 (2003) 191.
- [3] E. Anordo, G. Galli, G. Ferrante, Appl. Magn. Reson. 20 (2001) 365.
- [4] E. Anordo, D.J. Puiol, Phys. Rev. Lett. 76 (1996) 3983.
- [5] P.A. Beckmann, Phys. Rep. 171 (3) (1988) 85.
- [6] K.S. Cole, R.H. Cole, J. Chem. Phys. 19 (1951) 1484.
- [7] J.N. Barisci, R. Stella, G.M. Spinks, G.G. Wallace, Synth. Met. 124 (2001) 407.

Appendix 3 – Presentations and Posters

- *NMR Studies of Conducting Polymers* Eoin Murray* and Dermot Brougham, a talk given at Materials, Energy and Design Conference, DIT, Dublin, Ireland 2006
- *Charge-carrier Dynamics in Polyaniline using NMR Relaxometry*, Eoin Murray* and Dermot Brougham a poster presented at IRCSET National Symposium, Dublin, Ireland, 2005
- *Charge-carrier Dynamics in Conducting Polymers using Field-cycling NMR Relaxometry* Eoin Murray* and Dermot Brougham a poster presented at the 4th Conference on Field Cycling NMR Relaxometry 2005, Torino, Italy
- *NMRD and Charge Transport Study of Polyaniline Conducting Polymers*, Eoin Murray* and Dermot Brougham a poster presented at the IRCSET National Symposium, Dublin, Ireland, 2004
- *NMR Studies of Conducting Polymers*, Eoin Murray* and Dermot Brougham a poster presented at the ICSM, Wollongong, Australia, 2004.